Enzyme cascade reactions on 3D DNA scaffold with dynamic shape transformation

LIN PENG

Kyoto University

ACKNOWLEDGEMENTS

The studies in this thesis have been carried out under the direction of Professor Takashi Morii at the Graduate School of Energy Science, Kyoto University, during October 2017 to June 2021. The studies focus on the exploration of the biochemical mechanisms of DNA scaffolding effects on assembled enzymes, and the investigation of natural metabolic pathways based on a dynamic three-dimensional DNA scaffold.

I would like to take this opportunity to express my sincere appreciation to all the people who helped and encouraged me throughout my PhD study.

First of all, I would like to express my deep gratitude to my advisor, Professor Takashi Morii, for his tireless guidance and continuous encouragement throughout my whole PhD education. His dedication and unwavering enthusiasm for science keep me constantly engage with my research. Especially, his keen interest, innovative ideas, fruitful discussions and valuable suggestions help me think and do better in every step of the project. The excellent example he set as a scientist and mentor greatly impacts not only my work but also throughout my life, I am forever grateful for that.

I would like to express my sincere appreciation to Dr. Eiji Nakata for his kind guidance, helpful suggestions and encouragement in all the time of my research. His meticulous scrutiny, scientific approaches and sense of responsibility inspired me to study hard for each knowledge and work better in the project. I would like to acknowledge Dr. Shun Nakano for his help, encouragement and scholarly advice. I am very grateful for Professor Isao Saito for his valuable suggestions, fruitful discussions and great encouragement. I would like to thank Dr. Arivazhagan Rajendran for his helpful suggestions and insightful comments. And I would like to express my sincere gratitude to Dr. Huyen Dinh for her guidance, timely suggestions and collaborations in my research. I am very grateful to have her as a guider, coworker, friend, and sister throughout these years.

I would like to express my sincere gratitude and appreciation to my thesis committee members, Professor Masato Katahira and Professor Takashi Sagawa for their fruitful discussions and valuable suggestions in the writing and revising this thesis. I would like to express my thanks to Professor Masahiro Kinoshita for his collaboration works, fruitful discussions and valuable suggestions in my project.

My gratitude also goes to all the lab members, past and present, for their help and advice. I thank Dr. Thang Minh Nguyen for his help during my early time in experiments. I am thankful for all my good colleagues in the lab, Shunsuke Tajima, Hiroaki Konishi, Zhengxiao Zhang, Shiwei Zhang, Kiran Kumar Krishna Murthy, Geralbaatar Khongorzul, Taki Seko, Kouhei Muroi, Yuki Morita, Wanqing Hou, Taiga Baba, Yaqi Zhang, Mei Nakabayashi, Futa Komatsubara, and Yuya shibano. Especially, I thank Yuki Morita for her support in the experiments. I would like to acknowledge our secretary Yukie Kajikawa, and our technician Chiemi Nakata, for their kindness, help, sharing, and encouragement. My gratitude also goes to Yasuko Morii for her kindness and encouragement. I thank Dr. Masayuki Saimura for his experimental support.

I am deeply grateful to my parents Lin Yuning and Lin Shuying, my sisters, Lin Yan and Lin Ru, for their great supports, high standards and continuous encouragement throughout these years. Especially, I thank my mother for giving me the endless love and courage. I thank all my friends for their encouragement and sharing. I would like to acknowledge China Scholarship Council (CSC) for the PhD scholarship.

LIN PENG

Laboratory of Biofunctional Chemistry

Department of Fundamental Energy Science

Graduate School of Energy Science

Kyoto University

June 2021

Table of Contents

Chapter 3

Dynamic shape transformation of a DNA scaffold and its application for an enzyme nanocarrier

Chapter 4

Inter-enzyme distance dependency of the efficiency of cascade reaction with a faster downstream enzyme

Chapter 5

A Dynamic DNA scaffold with fast transformation kinetics and its application for the assembly of unstable enzyme

Chapter 6

CHAPTER 1

General Introduction

1.1. Spatial organization of nature systems

Living organisms have evolved over millions of years to build the complex metabolic network containing thousands of enzymatic reactions for their survival.[1] Biological systems face the challenges of unfavorable enzyme kinetics, low concentration of reactants, toxic intermediates and competing reactions when implementing the biochemical reactions. To address these obstacles, nature has developed the compartmentalization to spatially arrange enzymes in cells for efficient enzyme cascade reactions (Figure 1.1).[2] The strategies of compartmentalization include membrane-bound organelles (e.g. mitochondria, chloroplasts and peroxisome), bacterial microcompartments (BMC), and multi-enzyme complexes, in which the organization of enzymes often relies on the specific scaffold (e.g. proteins and membrane). [3]
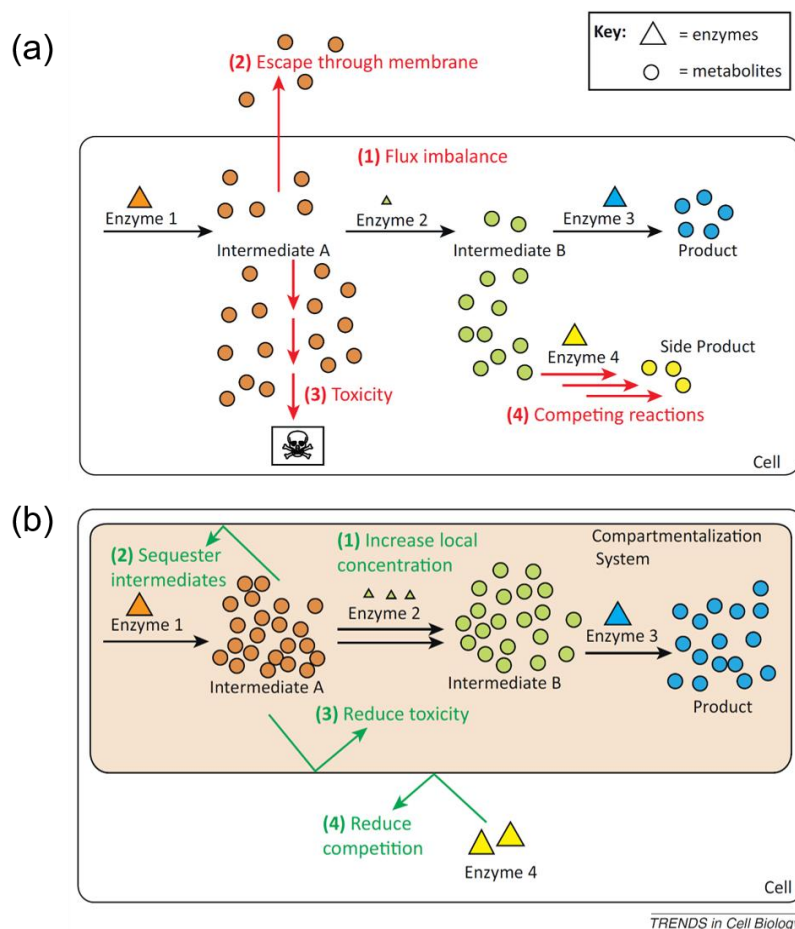
Figure 1.1. Nature's strategies to address the challenges. (a) The challenges that nature systems face in cells. (b) Cells utilize compartmentalization to solve the challenges.[2] Adapted by permission from Ref. 2. Copyright © 2012 Elsevier Ltd.

As the best studied bacterial microcompartments (BMC), carboxysome plays a central role in carbon fixation in cyanobacteria. Enzyme ribulose 1,5-bisphosphate carboxylase/oxygenase (RuBisCO) alone is inefficient with the properties of weak turnover rate and low specificity. By packing with carbonic anhydrase (CA) in the carboxysome, the reaction efficiency of RuBisCO is improved. In the cascade reaction of CA and RuBisCO, first enzyme CA converts bicarbonate HCO_3^- to CO_2, which is subsequently consumed by downstream RuBisCO in the carbon fixing reaction. The diffusion of negatively charged HCO_3^- into the protein shell is promoted by the positively charged pores of carboxysome, while the concentration of uncharged CO_2 is increased in the compartment, which enhances the RuBisCO reactivity in the carbon fixation.(Figure 1.2a).[4,5]

Substrate channeling is the transportation of the intermediates from one enzyme active site to the next without the release into solution.[6] The classic example of substrate channeling is tryptophan synthase. This $\alpha_2\beta_2$ tetrameric enzyme complex catalyzes a two-step cascade reaction that converts indole 3-glycerol-phosphate and serine to tryptophan. The intermediate indole is directly transferred through the 25 Å long hydrophobic tunnel bridging the two active sites (Figure 1.2b).[6-8] Such hydrophobic tunnel is also found in carbamoyl-phosphate synthase that channels carbamates to neighboring active site.[9] Another mechanism of intramolecular substrate channeling is electrostatic guidance as shown in the malate dehydrogenase-citrate synthase (MD-CS) complex.[10] The intermediate oxaloacetate is channeled by the electrostatic tunnel connected with CS, enabling the high fluxes of MD-CS enzyme pair in Krebs cycle.[6,10,11]

Membrane is one of the crucial scaffolds for proteins in cells. The embedded proteins in lipid bilayers may serve as channels, receptors, energy transducers, and enzymes.[12] For example, cyanobacterial thylakoid possesses a unique structure carrying

both photosynthetic and respiratory electrons transfer chains, which allows the performance of both oxygenic photosynthesis and aerobic respiration in the same cellular compartment (Figure 1.2c).[13] As another typical example, mammalian cytochromes P450 on the membrane of endoplasmic reticulum or mitochondria are an important class of enzymes involved in the biotransformation of many endo- and exogenous compounds.[14] Interestingly, the structural properties of membrane like the dynamic hydration layer on the surface may play a functional role in maintaining the interaction of protein and phospholipid, thus modulating the enzyme activity.[15]
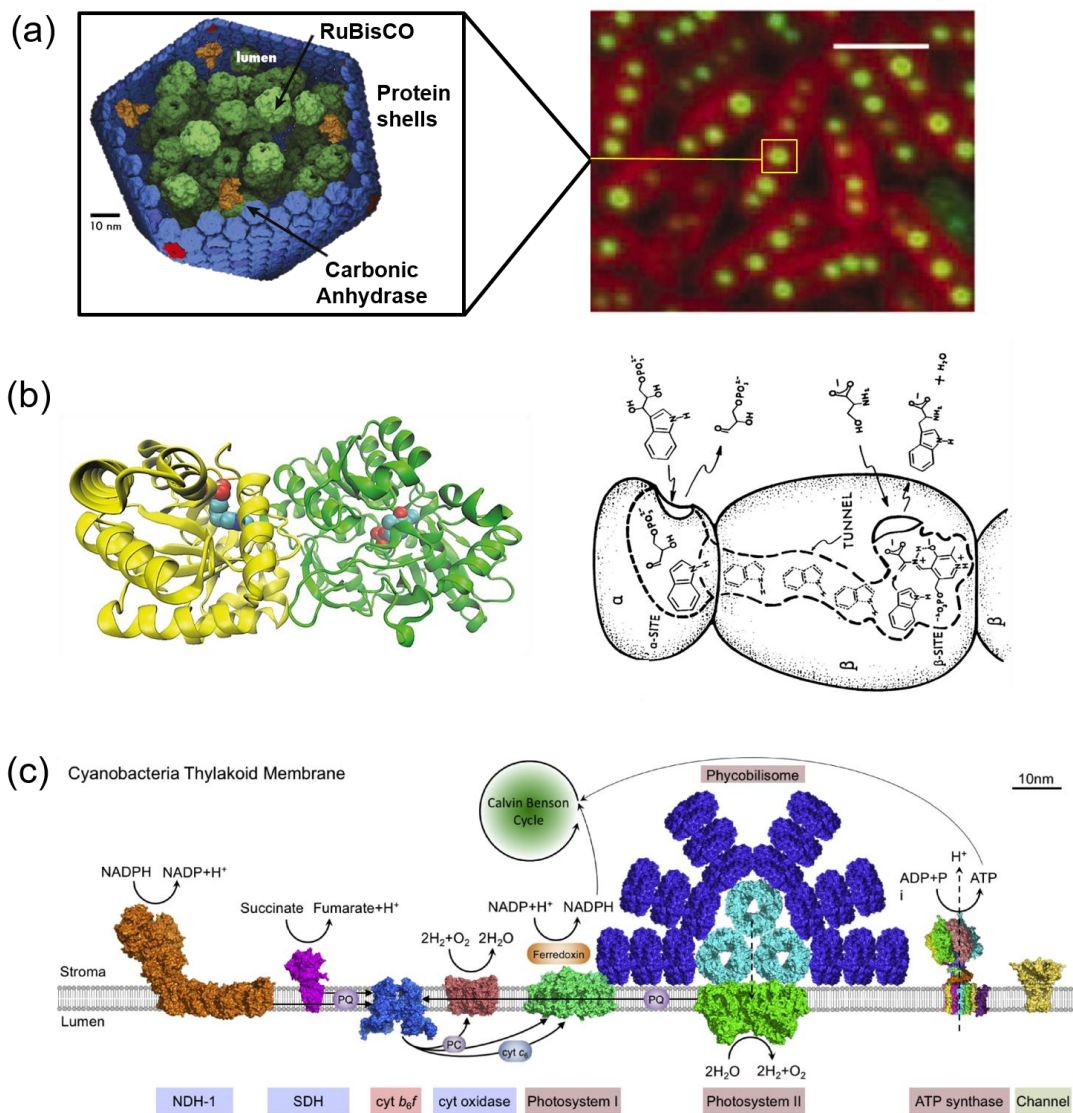
Figure 1.2. Spatial organization in nature systems. (a) Left: an illustration of carboxysome. Enzymes RuBisCO and carbonic anhydrase (CA) are packed inside carboxysome.[4] Right: carboxysomes in cyanobacteria. scale bar: 2 μm.[5] (b) Left: the crystal structure of tryptophan

synthase (PDB ID: 1A5S). The *α*-subunit and *β*-subunit are shown in yellow and green, respectively.[6] Adapted from by the permission from Ref. 6. Copyright © 2016 Springer Nature. Right: an illustration of the substrate channeling in tryptophan synthase.[8] Adapted by permission from Ref. 8. Copyright © 2012 Elsevier Ltd. (c) Model of cyanobacterial thylakoid membrane.[13]

1.2. Artificial metabolic pathways inspired by the nature system

Inspired by nature, artificial enzyme cascade reactions have been constructed based on a wide ranges of carriers, such as polymersomes,[16] lipids,[17] proteins,[18] and graphene oxides.[19] Klermund *et al.* compartmentalized the three-step reaction in a polymersome to synthesize CMP-*N*-acetylneuraminic acid (CMP-Neu5Ac). It was found that the incorporation of the outer membrane protein F (OmpF) into membrane could restrain the cross-inhibitions in enzyme cascade reactions. The overall throughput was enhanced 2.2-time compared to the reaction by free enzymes (Figure 1.3a).[16] Zhang *et al.* utilized the bacterial microcompartment shell protein EutM from *Salmonella enterica* as the carriers of enzymes by SpyTag-SpyCatcher strategy. Alcohol dehydrogenase (ADH) and amine-dehydrogenase (AmDH) were coimmobilized on the scaffold to convert alcohols to chiral amines in a highly enantioselective manner (Figure 1.3b).[18] The artificial metabolic pathways implemented on the above carriers exhibit great potential in the biosynthesis of value-added chemicals,[18-20] however, further applications are limited by the low enzyme loading yields and the difficulties to control over the spatial arrangement and stoichiometry of enzymes.

The past two decades have witnessed the rapid development of DNA nanotechnology and its applications.[21] Given the predominant advantages of structural programmability and accurate addressability, DNA structures are considered as the ideal platforms for the assembly of various macromolecules.[22] Enzyme cascades have been constructed on DNA scaffold with the precise control over the loading numbers and positions.[23] As one of the typical examples applied in biosynthesis, Lim *et al.* applied a

CRISPR/Cas-based strategy to organize five enzymes comprising the violacein synthesis pathway on a DNA scaffold at the nanoscale. A notable increase in violacein production demonstrated the benefits of DNA scaffolding (Figure 1.3c).[24]
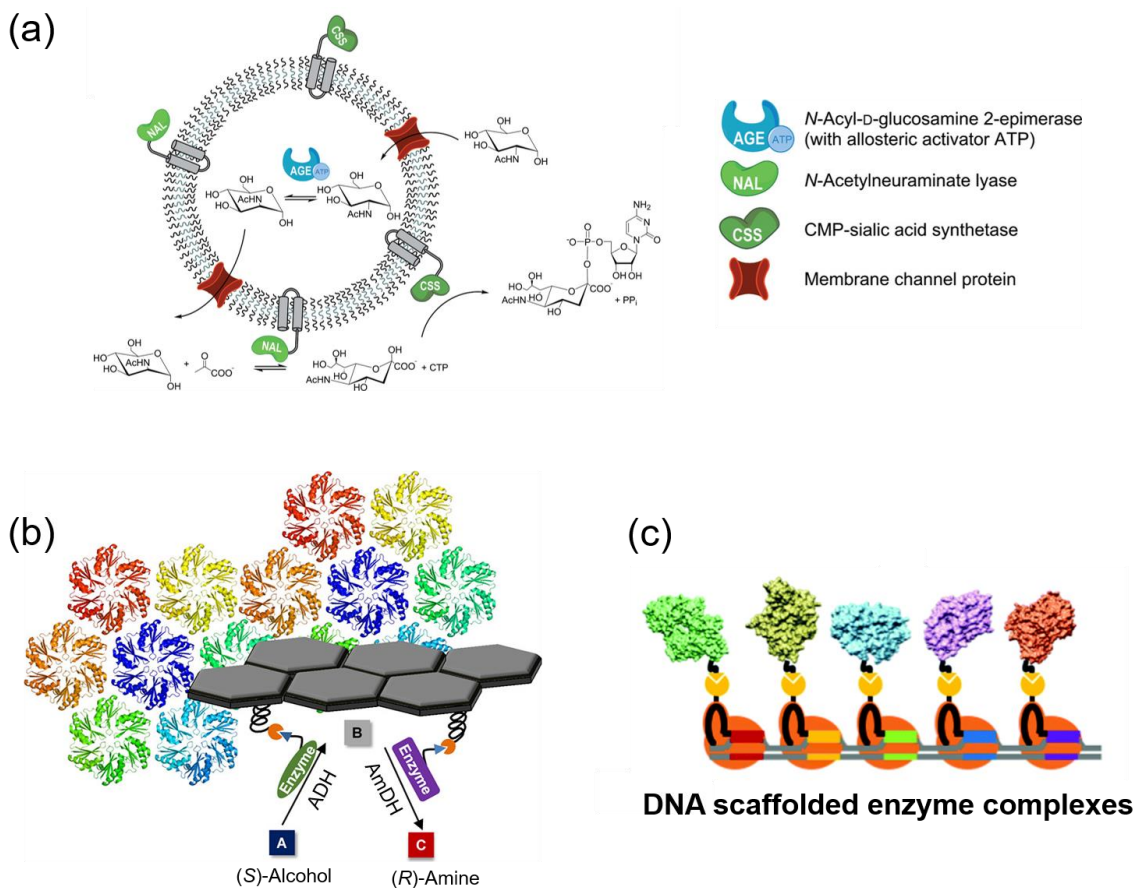
Figure 1.3. Enzyme cascades assembled on various carriers for the biosynthesis of value-added chemicals. (a) Enzyme cascade reaction compartmentalized in a polymersome for the synthesis of CMP-*N*-acetylneuraminic acid (CMP-Neu5Ac).[16] Adapted with permission from Ref. 16. Copyright © 2017 American Chemical Society. (b) Coimmobilization of alcohol dehydrogenase (ADH) and amine-dehydrogenase (AmDH) on EutM-SpyCatcher protein scaffolds for the synthesis of chiral amine.[18] Adapted with permission from Ref. 18. Copyright © 2018 American Chemical Society. (c) Scheme of the CRISPR/Cas-directed programmable assembly of five enzymes on a DNA scaffold to convert L-tryptophan into violacein.[24] Adapted from Ref. 24 with the permission from the Royal Society of Chemistry.

1.3. DNA nanotechnology and its applications

In the early 80s, Seeman pioneered the idea that DNA can be the building blocks of higher-order structures for its predictable Watson-Crick base paring. A Holliday-junction with four-arm formed by single-stranded oligoneucleotides was constructed (Figure 1.4a).[25] Subsequently, DNA was used in the construction of increasingly complex shapes and lattices,[26] such as 2D nanogrids, three-helix bundle and DNA octahedron assembled and visualized by atomic force microscopy (AFM) and/or transmission electron microscopy (TEM) (Figure 1.4b).[27–29] However, these assembly processes faced the challenges of scalability and programmability.

In 2006, Rothemund created DNA origami method that folds a long, single-stranded DNA template (7-kilobase) into desired two-dimensional (2D) shapes with the aid of over 200 short oligonucleotides (staple strands). Non-periodic structures, such as square, rectangle, star and smiley face were obtained (Figure 1.4c).[30] Featuring the preparation simplicity, structural programmability and high folding yield, DNA origami technique plays an important role in the development of structural DNA nanotechnology. In 2009, Douglas *et al.* extended DNA origami method to build custom three-dimensional structures formed as pleated layers of DNA helices in the honeycomb lattices, providing a general route to the construction of complex 3D DNA nanostructures (Figure 1.4d).[31] By using the software caDNAno,[32] the staple sequences for folding newly designed DNA structures can be generated quickly. After that, a number of DNA structures with complexity were constructed, such as DNA box with controllable lid, DNA nanoflask, DNA bundle with bends and hollow DNA sphere (Figure 1.4e).[33–36]
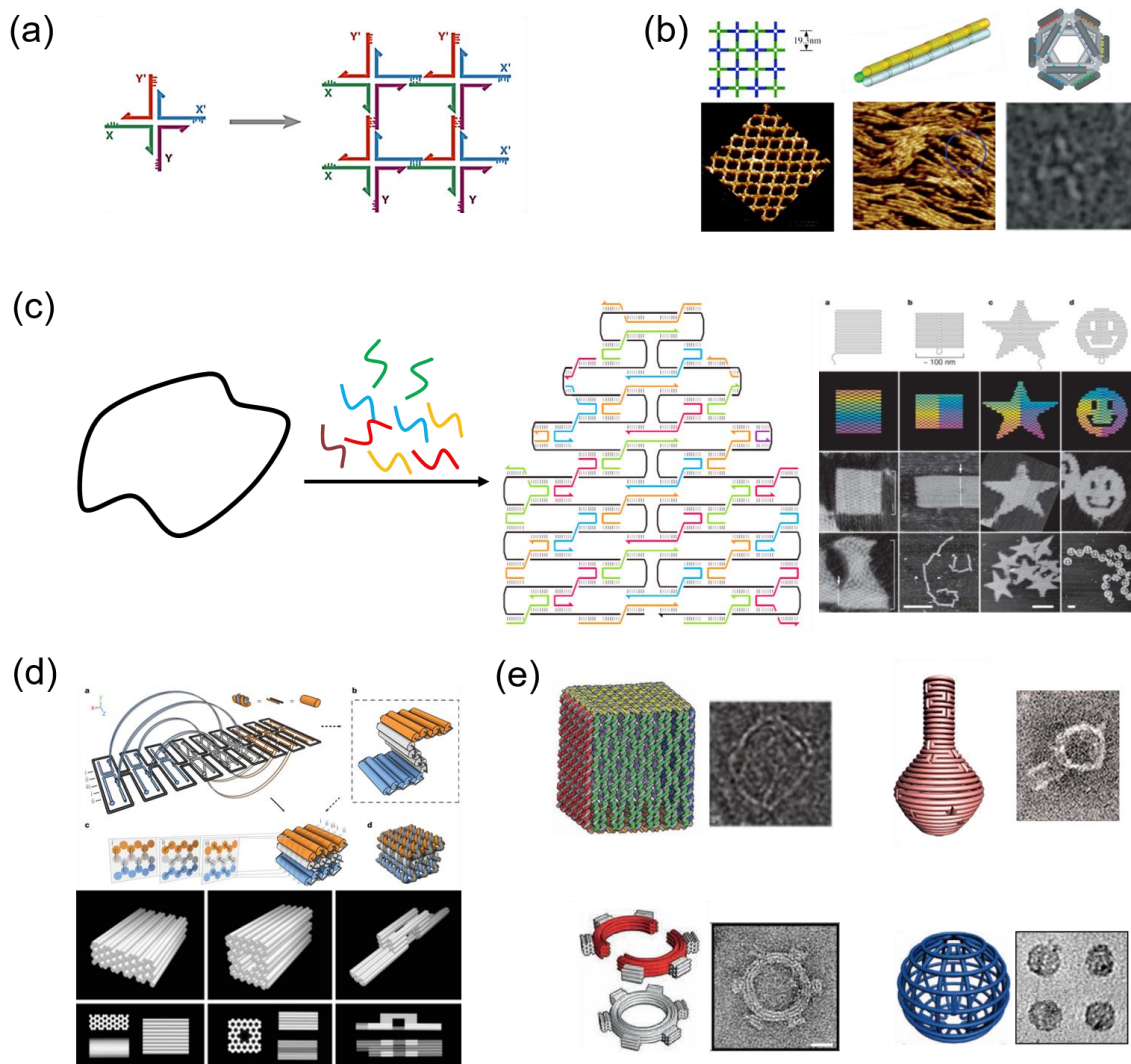
Figure 1.4. DNA nanotechnology and DNA structures. (a) Four-arm Holiday junctions with sticky ends self-assemble into 2D DNA arrays.[25] Adapted by permission from Ref. 25. Copyright © 1982 Elsevier Ltd. (b) Left: self-assembly of 2D nanogrids with corrugated design.[27] Middle: a three-helix bundle consisting of three double helical DNA domains.[28] Adapted by permission from Ref. 28. Copyright © 2005 American Chemical Society. Right: DNA octahedron involving twelve struts connected by six flexible joints.[29] Adapted from by the permission from Ref. 29. Copyright © 2004 Springer Nature. (c) DNA origami using a 7-kb single-stranded DNA template that folds into arbitrary shapes with the aid of DNA staple strands.[30] Adapted from by permission from Ref. 30. Copyright © 2006 Springer Nature. (d) Design and folding of three-dimensional DNA origami shapes.[31] Adapted from by the permission from Ref. 31. Copyright © 2009 Springer Nature. (e) 3D DNA origami structures. Top left: a DNA origami cube ant its Cryo-EM image.[33] Adapted from by the permission from Ref. 33. Copyright © 2009 Springer Nature. Top right: DNA nanoflask and its TEM image.[34] Bottom left: a curving DNA origami bundle and its TEM image.[35] Bottom right: 3D DNA spherical structure and its TEM image.[36]

Besides the static DNA structures, the dynamic DNA nanotechnology enables the construction of various reconfigurable DNA origami structures induced by the hybridization of short DNA,[37–39] aptamer-molecule interactions,[40] temperature,[41] pH,[42] ion,[43] and electric field[44] with controlled translational, rotational or more sophisticated movement, exhibiting great potential for applications in drug delivery, biosensing, diagnosis, and biocatalysis (Figure 1.5).[45] The tailored properties of DNA devices create the novel ways to deliver the drugs into cells. Douglas *et al.* constructed a logic-gated DNA origami nanorobot in hexagonal barrel form, which was opened by antigen proteins like platelet-derived growth factor (PDGF) and selectively transported antibody to the targeting cells (Figure 1.5c).[46] Amir *et al.* used a modified structure of this DNA nanorobot[46] to build a dynamic DNA structure able to interact with each other in cockroach with logical outputs.[47] Li *et al.* incorporated the nucleolin-binding aptamer to a DNA nanotube that carried thrombin. Nucleolin expressed by tumor-associated endothelials acted as a trigger of the aptamer locks and opened the tube, which subsequently exposed thrombin in the blood to result in tumor necrosis.[48]

In addition to drug delivery, dynamic DNA origami structures displayed attractive applications in biocatalysis to regulate the inter-enzyme distance, enzyme-substrate interaction, or encapsulation/release of enzymes. Here, the typical examples of controlling individual enzyme behavior on DNA scaffold were listed. Grossi *et al.* built a DNA nanovault with reversible opening/closing process induced by DNA strand displacements. It was demonstrated that closing the vault significantly reduced the enzyme activity of alpha-chymotrypsin (aCt) encapsulated in the vault (Figure 1.5d).[49] Juul *et al.* introduced a temperature-controlled system to encapsulate or release the enzyme horseradish peroxidase (HRP) using a preassembled and covalently closed 3D DNA cage structure. This system allowed the entrance or release of HRP at 37 ℃, with residing HRP in the central cavity of the cage at 4 ℃ (Figure 1.5e).[50] Ijäs *et al.*

9

constructed a solution pH-responsive DNA origami nanocapsule that can be loaded with horseradish peroxidase (HRP) and reversibly opened and closed by changing the solution pH from 6.4 to 7.8 (Figure 1.5f).[51]
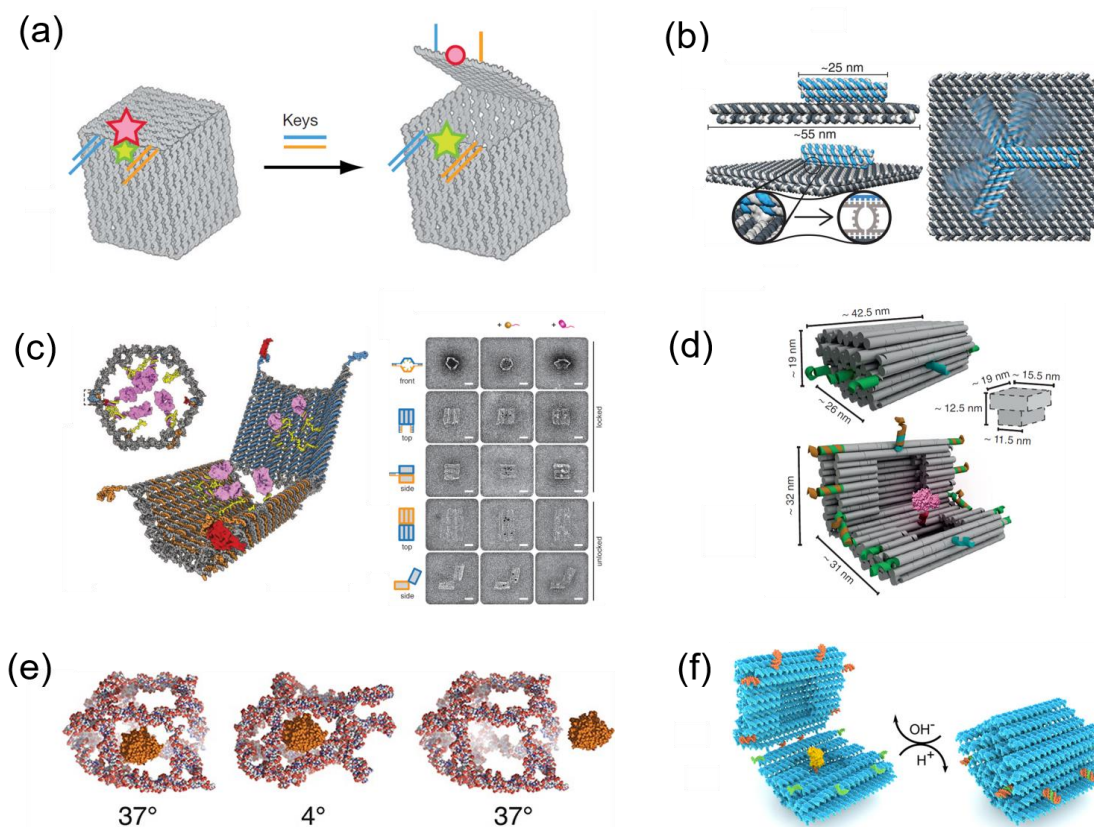
Figure 1.5. Dynamic DNA origami devices and applications. (a) Illustration of the box with controllable lid initiated by a toehold-strand displacement reaction.[33] Adapted from by the permission from Ref. 33. Copyright © 2009 Springer Nature. (b) A DNA origami structure with controllable rotation by electric field.[44] (c) Left: front view of closed DNA nanorobot equipped with antibody. Middle: perspective view of opened nanorobot. Right: typical TEM images of DNA nanorobot encapsulated with gold nanoparticles (gold) or antibody (magenta), scale bar: 20 nm.[46] (d) A DNA vault for controlling enzyme activity. The reversible transition of DNA vault between the open states and the closed states was induced by toehold-mediated strand displacement.[49] (e) A DNA cage for capture and release of enzyme horseradish peroxidase (HPR) triggered by temperature.[50] Adapted with permission from Ref. 50 Copyright © 2013 American Chemical Society. (f) A HRP loaded DNA origami nanocapsule reversibly opened and closed with different buffer pH.[51]

1.4. Overview of the strategies to assemble proteins on DNA scaffolds

Featuring the tremendous self-assembly properties and addressability, DNA scaffolds provide ideal platforms for the assembly of functional macromolecules like proteins.[52] To locate proteins of interest (POI) on DNA structures, various strategies have been developed, which are commonly divided into the noncovalent conjugation method and the covalent conjugation method.[53–56] The noncovalent conjugation can be realized by DNA-protein interaction, such as biotin-avidin,[57] Ni-NTA-Hexahistidine,[58] antigen-antibody,[59] aptamer binding,[60] and DNA binding protein-DNA interactions (Figure 1.6).[61] The noncovalent methods give flexible and reversible conjugations, resulting in low binding yields.
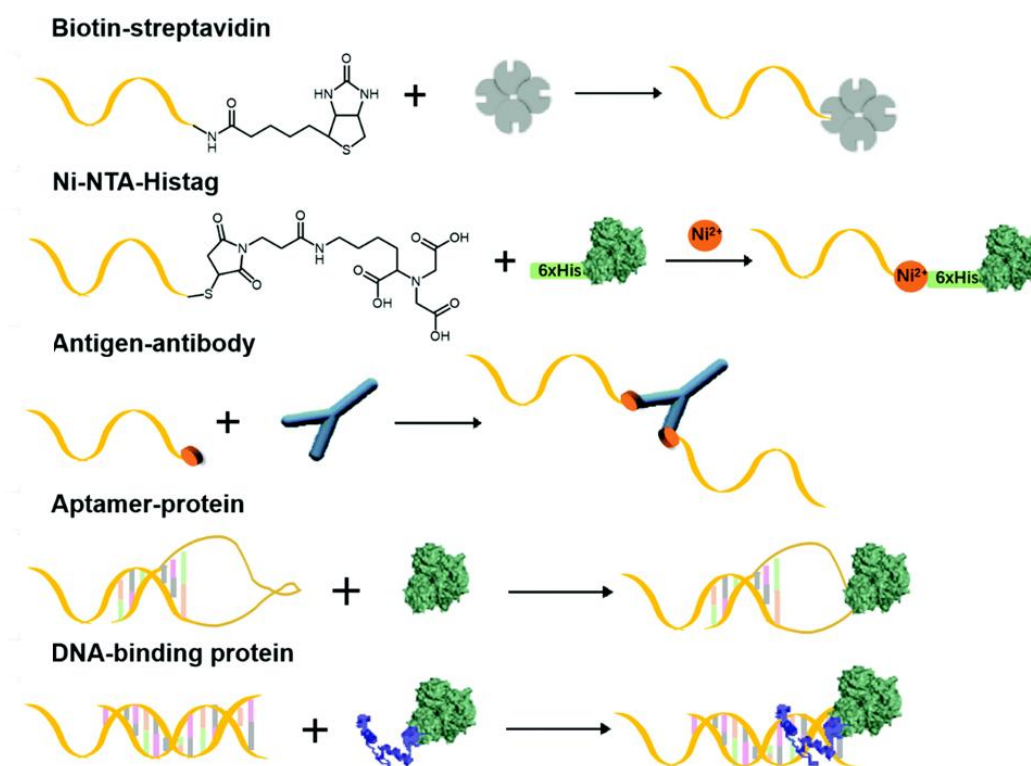
Figure 1.6. Typical methods for the noncovalent protein-DNA conjugation.[56] Adapted from Ref. 56 with the permission from the Royal Society of Chemistry.

On the other hand, the covalent strategies render irreversible conjugations, including non-specific covalent methods and specific covalent methods (Figure 1.7). The non-specific covalent methods can be realized by small molecular cross-linkers like N-succinimidyl 3-(2-pyridyldithio)-propionate (SPDP)[62] or sulfo-succinimidyl-4-(N-maleimidomethyl)-cyclohexane-1-carboxylate (Sulfo-SMCC).[63] However, the chemical modification processes may hamper the catalytic ability of enzymes.[56] The specific covalent conjugation can be achieved by a self-labeling protein tag, which is fused to POI to react with a small molecule-modified oligonucleotide incorporated in DNA scaffold.[64] SNAP-tag (human O^6-alkylguanine-DNA-alkyltransferase, hAGT)[65] and Halo-tag (Haloalkane dehalogenase)[66] are the most commonly used tag proteins. SNAP-tag reacts with its substrate O^6-benzylguanine (BG), while Halo-tag reacts with 5-chlorohexane (CH) derivatives.[65,66] The orthogonality of these reactions enables the simultaneous assembly of multiple enzymes.[56]
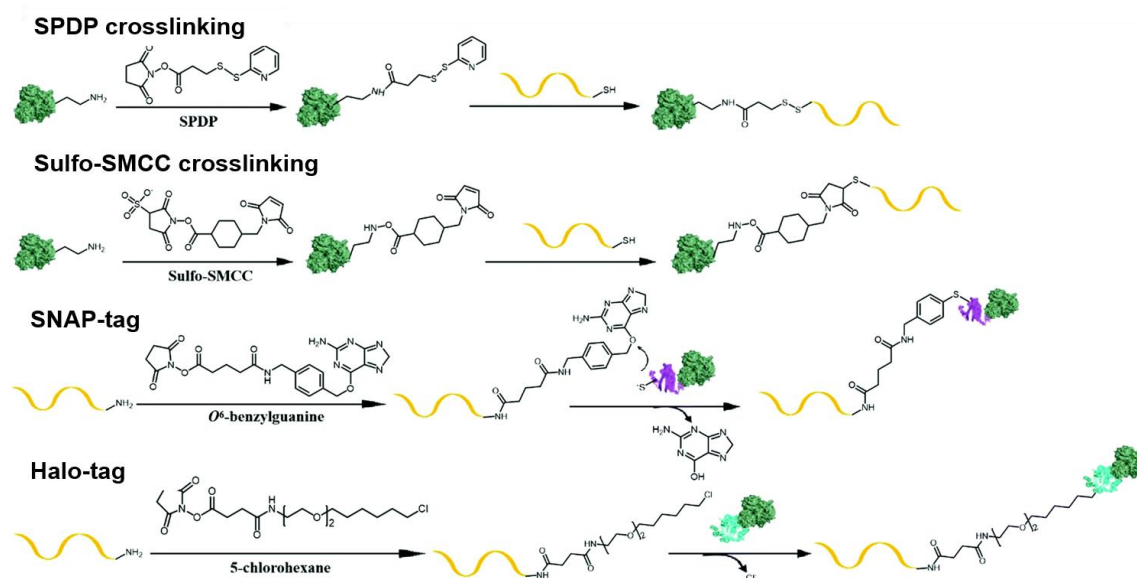
Figure 1.7. Typical methods for the covalent protein-DNA conjugation.[56] Adapted from Ref. 56 with the permission from the Royal Society of Chemistry.

In the Morii lab, the modular adaptor method for specifically locating the POI on DNA scaffold was developed. In the first generation, sequence-specific DNA binding proteins were utilized to locate proteins on DNA scaffold through a noncovalent interaction. Two types of well-characterized zinc finger proteins zif268[67] and AZP4[68], were utilized as orthogonal adaptors to bind specific DNA sequence on the DNA scaffold. A cyan fluorescent protein variant (Cerulean)[69] and a yellow fluorescent protein variant (YPet)[69] were fused to the C terminal of zif268 and AZP4, respectively, via linkers to give zif268-Cer and AZP4-YPet, which bound to the DNA origami scaffold with the binding efficiencies of over 50% and 30%, respectively (Figure 1.8a).[70]

The basic leucine zipper (bZIP) protein GCN4[71] was used as an adaptor to locate the dimeric protein on DNA scaffold. A dimeric enzyme xylitol dehydrogenase (XDH)[72] from *Pichia stipitis* was fused to the C-terminal of GCN4 through a glycine-glycine-serine (GGS) linker to give adaptor-fused enzyme G-XDH, which was then assembled on DNA scaffold with four binding sites in the central activity in over 80% binding yield (Figure 1.8b). Notably, G-XDH showed higher activity than the wild type of XDH.[73]
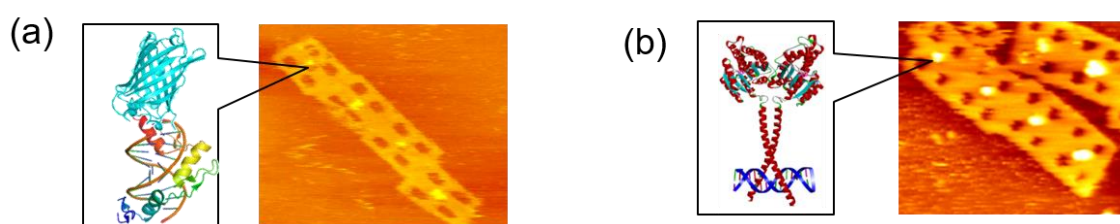
Figure 1.8. Assembly of POIs on DNA scaffold using DNA binding protein. (a) Left: molecular model of a complex of protein zif268-Cer (zif268 fused Cerulean) and a hairpin DNA. Right: AFM image of zif268-Cer located on the central cavity of DNA scaffold.[70] (b) Left: molecular model of a complex of G-XDH (GCN4 fused xylitol dehydrogenase) and a hairpin DNA. Right: AFM image of G-XDH located on the central cavity of DNA scaffold.[73] Adapted by permission from Ref. 73. Copyright © 2014 Elsevier Ltd.

To realize the rapid and stable location of POI on DNA scaffold specifically through covalent linkage in high loading yield, the modular adaptor comprising a self-ligating protein tag and a DNA binding protein was developed.[74-77] SNAP-tag was fused to the C-terminal of the DNA-binding protein zif268[67] to obtain a modular adaptor ZF-SNAP which rapidly formed a stable covalent bond with O^6-benzylguanine (BG) modified-DNA sequence incorporated in the DNA scaffold.[74] As a typical application, the enhanced green fluorescent protein (EGFP) was fused to the C-terminal of ZF-SNAP to give ZF-SNAP-EGFP, which was then attached on a DNA scaffold specifically with over 90% binding yield (Figure 1.9a and Figure 1.9b).[74] Besides the fluorescent protein, a monomeric enzyme xylose reductase (XR) was fused to ZF-SNAP to obtain ZS-XR that specifically loaded on a three-well DNA scaffold with a high binding yield (Figure 1.9c).[75]
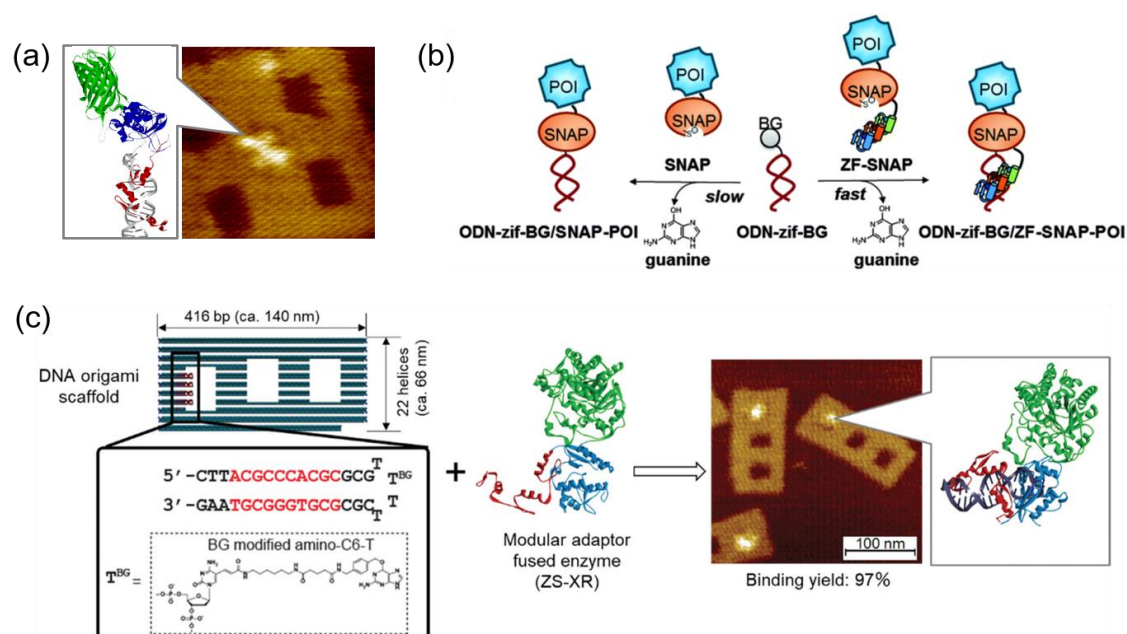
Figure 1.9. Assembly of POIs on DNA scaffold by modular adaptor. (a) Left: molecular model of a complex of ZF-SNAP-EGFP and a hairpin DNA. Right: AFM image of ZF-SNAP-EGFP assembled on the DNA scaffold.[74] (b) A scheme representing the formation of the covalent bond between the SNAP tag and O^6-benzylguanine (BG) with fast kinetics.[74] Adapted from Ref. 74 with the permission from the Royal Society of Chemistry. (c) A scheme representing the binding process of modular adaptor enzyme ZS-XR (ZF-SNAP fused xylose reductase) on a 2D DNA scaffold.[54] Adapted from Ref. 54 with the permission from the Royal Society of Chemistry.

In order to assemble several types of functional proteins on the same DNA scaffold, various modular adaptors with orthogonality were developed.[76,77] The orthogonal modular adaptors candidates were constructed based on the three types of DNA-binding proteins (zif268,[67] AZP4,[68] and GCN4[71]) and the three types of protein tags (SNAP-tag,[65] Halo-tag,[66] and CLIP-tag[78]). The orthogonality and binding yield of three modular adaptors (ZF-SNAP, AZ-Halo, and AZ-CLIP) were evaluated (Figure 1.10). The coassembly yield of these modular adaptors reached 90% at the ambient temperatures within 30 min estimated by AFM images. The mild conditions and fast binding is of great significance of loading unstable enzymes on DNA scaffold.[76,77]
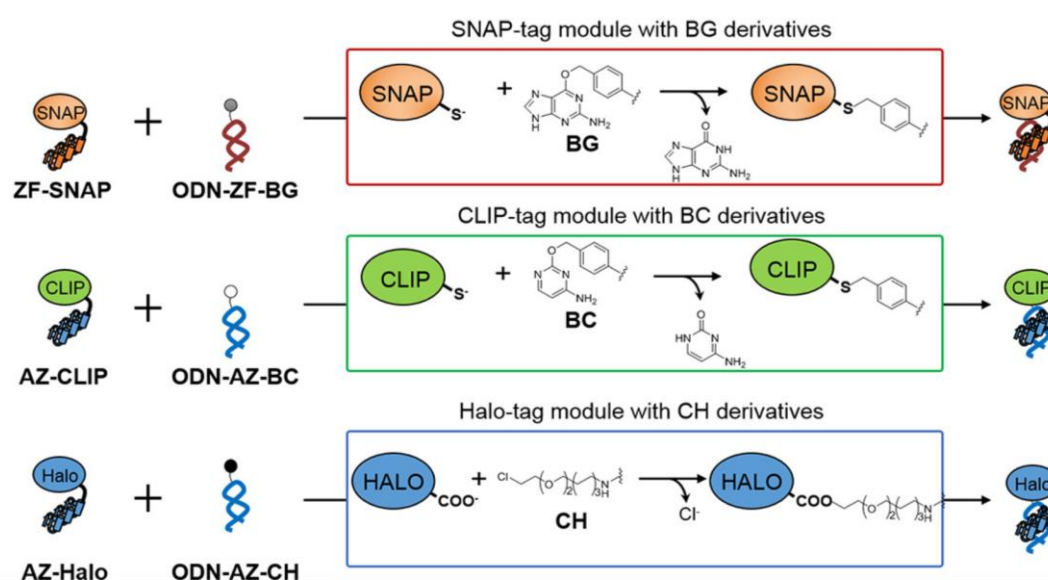
Figure 1.10. Illustration representing the binding reactions between the modular adaptors and the substrates incorporated in the ODN.[76] Adapted with permission from Ref. 76. Copyright © 2017 American Chemical Society.

1.5. Overview of DNA scaffolded enzyme systems and DNA scaffolding effect

Integrating the structural predictability of DNA with the diverse conjugation strategies has enabled the construction of higher order bio-hybrid structures of DNA and enzymes. Artificial enzyme cascades have been implemented on 2D to 3D DNA scaffolds.[79] Here, several typical examples were reviewed and discussed. Wilner *et al.* activated the glucose oxidase/horseradish peroxidase (GOx/HRP) enzyme cascade on topologically programmed DNA scaffolds. The efficiency of GOx/HRP on two-hexagon scaffold with the inter-enzyme distance of ~ 6 nm was 1.2-fold higher than that on four-hexagon system (~ 23 nm) (Figure 1.11a).[80] Fu *et al.* organized GOx/HRP on a rectangular DNA scaffold by changing the inter-enzyme distance from 10 nm to 65 nm to observe a drastic enhancement of activity at a distance of 10 nm (Figure 1.11b).[81]

The simple dynamic DNA device and three-dimensional DNA structures were also applied to investigate the enzyme cascade reaction of GOx/HRP. A DNA tweezer built by Xin *et al.*, could switch between open and closed states driven by a DNA strand displacement reaction (Figure 1.11c).[82] The observed higher overall enzyme reaction efficiency of GOx/HRP in the closed state was attributed to the shorter distance of two enzyme-modified DNA arms.[82] A DNA nanoreactor which was fabricated by gluing two separate origami units equipped with GOx and HRP (GOx-origami and HRP-origami) via the hybridization of 32 short bridging DNA sequences.[83] Additionally, GOx/HRP was positioned in an intact DNA cage obtained by connecting the two separate half cages through the complementary DNA sequences (Figure 1.11d).[84]

Besides GOx/HRP, two-step reaction consisting of gluocose-6-phosphate dehydrogenase (G6pDH) and malic dehydrogenase (MDH) was conducted on a DNA double-crossover (DX) tile scaffold with NAD^+-tethered poly(T)$_{20}$ oligonucleotide facilitating the transportation of NADH (Figure 1.11e).[85] And a three-enzyme pathway involving MDH, oxaloacetate decarboxylase (OAD), and lactate dehydrogenase (LDH)

16

was located in a triangular pattern on a three-point star DNA scaffold with optimized geometric organizations to enhance the production of lactate (Figure 1.11f).[86]
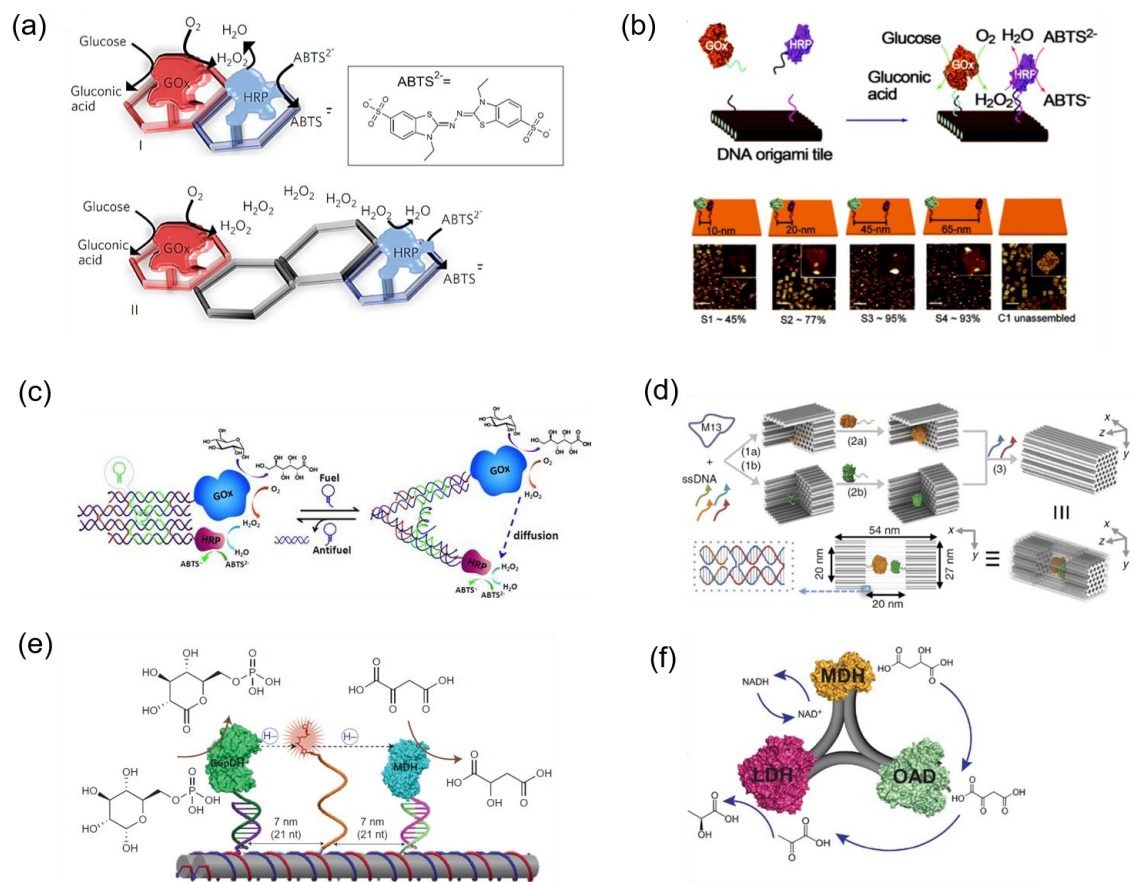
Figure 1.11. Enzyme cascade reactions on DNA scaffold. (a) Assembly of the glucose oxidase and horseradish peroxidase (GOx and HRP) on the two-hexagon and four-hexagon scaffolds.[80] Adapted from by the permission from Ref. 80. Copyright © 2009 Springer Nature. (b) Enzymes GOx and HRP assembled on DNA scaffold with the variation of interenzyme distances from 65 nm to 10 nm.[81] Adapted with permission from Ref. 81. Copyright © 2012 American Chemical Society. (c) A DNA double crossover (DX) consisting of two arms for the attachement of GOx and HRP.[82] (d) The encapsulation of GOx (orange) and HRP (green) in a DNA nanocage.[84] (e) Arrangement of gluocose-6-phosphate dehydrogenase and malic dehydrogenase (G6pDH and MDH) on a DNA DX tile.[85] Adapted from by the permission from Ref. 85. Copyright © 2014 Springer Nature. (f) The assembly of MDH, oxaloacetate decarboxylase (OAD), and lactate dehydrogenase (LDH) pathway on a triangular DNA scaffold.[86]

In the Morii lab, D-xylose metabolic pathway or carbonic anhydrase/RubisCO (CA/RuBisCO) enzyme cascade was investigated on 2D DNA scaffolds. The modular adaptor method was applied to stably locate enzymes on scaffold with the precise control over enzyme stoichiometry and inter-enzyme distance. ZS-XR (modular adaptor ZF-SNAP fused xylose reductase) and G-XDH (adaptor GCN4 fused xylitol dehydrogenase) were arranged on a three-well DNA scaffold with the alteration of inter-enzyme distance from 98 nm to 10 nm, it was found the highest efficiency appeared at a distance of 10 nm and the intermediates (xylitol and NAD^+) transferred to the downstream enzyme following Brownian motion (Figure 1.12).[75]
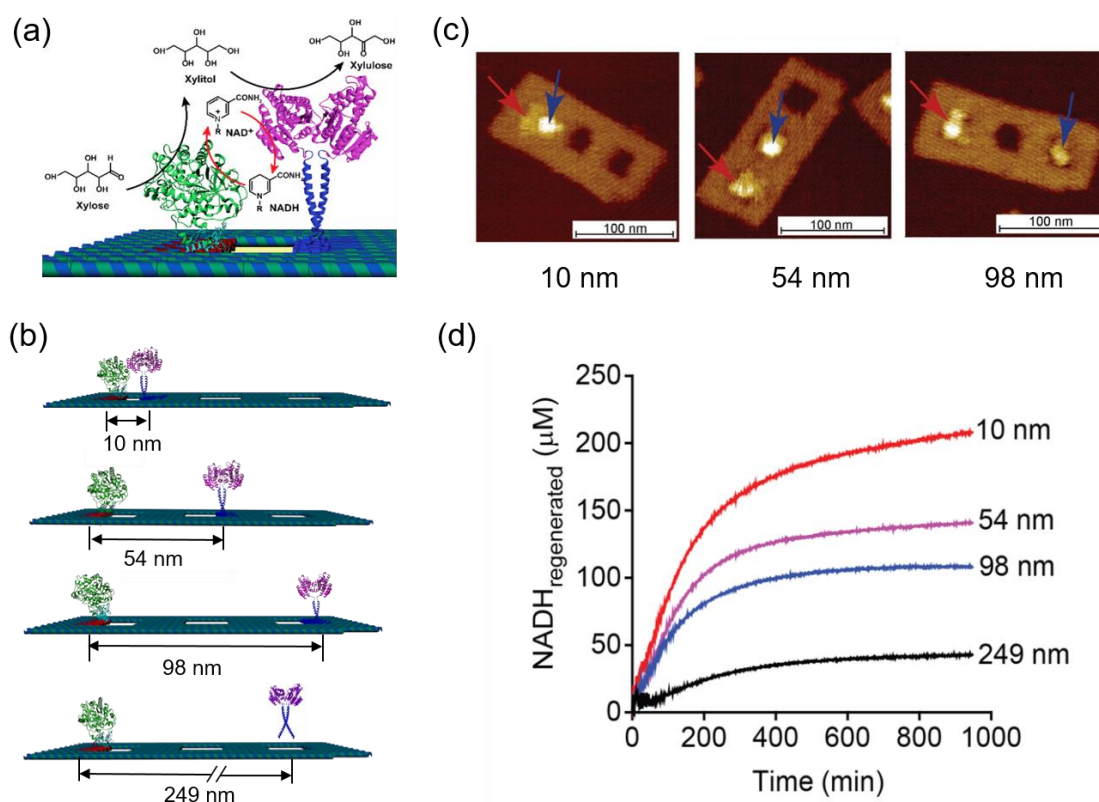
Figure 1.12. Enzyme cascade reactions of xylose reductase/xylitol dehydrogenase (XR-XDH) on the DNA scaffold. (a) Scheme of cascade reactions of XR/XDH on a 2D DNA scaffold. (b) The variation of inter-enzyme distances of XR and XDH on the DNA scaffold. (c) AFM images of ZS-XR and G-XDH coassembled on the DNA scaffold with the inter-enzyme distances of 10 nm, 54 nm and 98 nm, scale bar: 100 nm. (d) The regenerated NADH of enzyme cascade reactions with different inter-enzyme distance.[75] Adapted with permission from Ref. 75. Copyright © 2016 American Chemical Society.

The enzyme cascade reaction XR/XDH was extended to realize the three-step reaction, in which xylulose kinase (XK) converted xylulose to xylulose-5-phosphate by utilizing ATP on the same 2D DNA scaffold. The produced ADP in the system that coassembled the third enzyme within 10 nm was higher than that with 50 nm. However, the distance dependency was observed to a smaller extent than that observed for the XR/XDH system, indicating that the kinetic parameters of upstream and downstream enzymes were the critical factor on the inter-enzyme distance dependence of cascade reaction efficiency (Figure 1.13).[76]
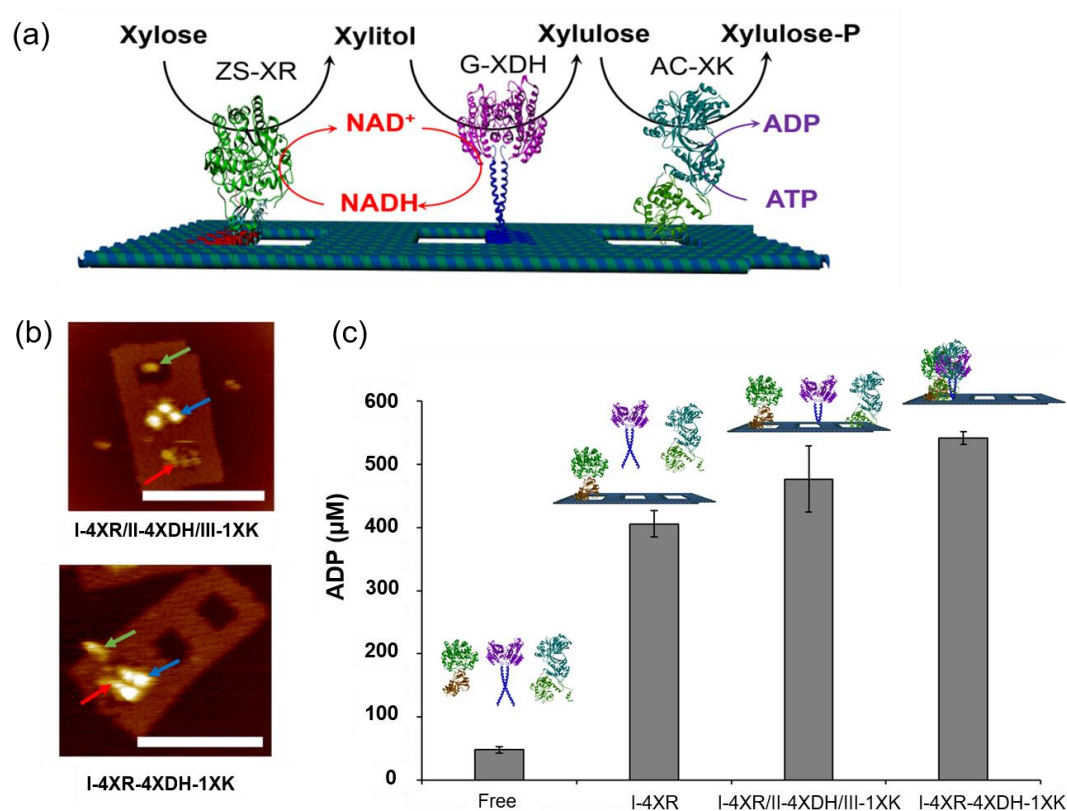
Figure 1.13. Xylose reductase/xylitol dehydrogenase/xylulose kinase (XR/XDH/XK) cascade reactions on DNA scaffold (a) Scheme of enzyme cascade reactions of XR/XDH/XK on a 2D DNA scaffold. (b) Top: AFM image of I-4XR/II-4-XDH/III-XK (4 binding sites for ZS-XR, 4 binding sites for G-XDH and 1 binding site for XK locating in Cavity I, Cavity II and Cavity III, respectively), scale bar: 100 nm; bottom: AFM image of I-4XR/I-4XDH-I-XK (4 bindig sites for ZS-XR, 4 binding sites for G-XDH and 1 binding site for AC-XK locating in Cavity I), scale bar: 100 nm. (c) Comparison of ADP production from the enzyme cascades after 24-h reaction.[76] Adapted with permission from Ref. 76. Copyright © 2017 American Chemical Society.

To mimic the spatial arrangement of carbonic anhydrase (CA) and ribulose 1,5-bisphosphate carboxylase/oxygenase (RuBisCO) in the carboxysome, enzymes ZS-CA (modular adaptor ZF-SNAP fused CA) and G-RuBisCO (adaptor GCN4 fused RuBisCO) were coassembled on a 2D DNA scaffold with five cavities. The co-assembly of CA and RuBisCO on DNA scaffold decreased the RuBisCO activity, suggesting that the proximity of CA and RuBisCO may be not the critical factor for enhancing the activity of RuBisCO in carboxysome (Figure 1.14).[87] This result was consistent with the previous report, where RuBisCO and CA were coencapsulated in an engineered protein cage with insignificant kinetic effect of enzyme cascade reaction.[88]
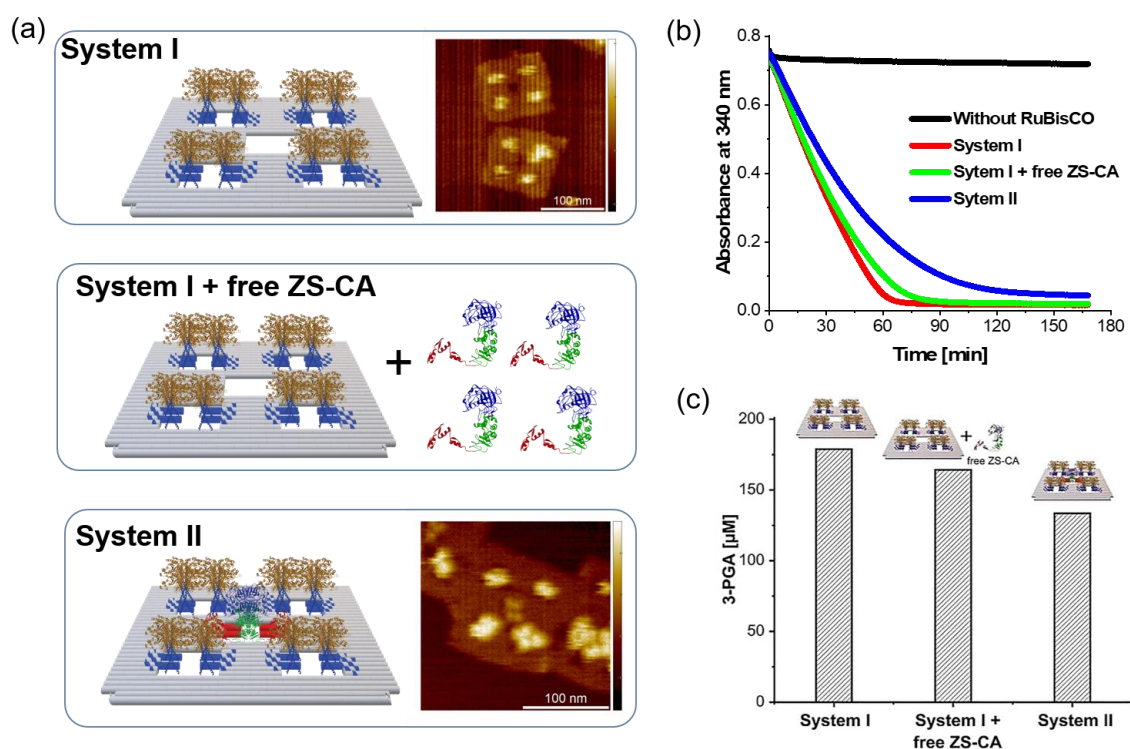
Figure 1.14. Carbonic anhydrase and RuBisCO (CA/RuBisCO) enzyme cascade reactions on DNA scaffold. (b) Illustration of the enzyme reaction systems. Top: G-RuBisCO assembled on the DNA scaffold; middle: free ZS-CA with DNA scaffolded G-RuBisCO; bottom: G-RuBisCO coassembled with ZS-CA on the DNA scaffold. (c) Time course of A340 of enzyme reactions. (d) Comparison of the enzyme activities of RuBisCO by the production of 3-phosphoglycerate (3-PGA).[87]

In addition to the enzyme cascade reaction efficiency is improved on DNA scaffold, the enhanced activities of DNA tethered individual-enzyme have also been reported for various DNA-enzyme complexes.[89,90] Several mechanisms were proposed to illustrate the improved catalytic ability. Zhao *et al.* observed 4-10-fold higher turnover numbers of five DNA cage encapsulated enzymes (HRP, GOx, MDH, G6pDH and LDH) than the respective free enzymes. It was hypothesized that the ordered hydration layer formed by the negatively charged DNA cage stabilized the enzymes and contributed to the catalytic enhancement (Figure 1.15a).[84] Rudiuk *et al.* conjugated *β*-lactamase with a branched complexes containing up to four λDNA (48.5 kbp). The microenvironment composed of giant and ordered DNA molecules was attributed to the increased catalytic activity without modifying the affinity of enzyme for the substrate (Figure 1.15b).[91] Lin *et al.* assembled HRP on a triangular DNA scaffold to study the substrate-scaffold interactions by using various substrates. Substrates were captured by DNA scaffold through electrostatic interactions or other interactions, leading to the enrichment of substrate and reduced K_m (Figure 1.15c).[92,93] Timm *et al.* observed the activity enhancement of oxidoreductase Gre2 or BM3 (reductase domain of the monooxygenase P450) on a DNA scaffold. It was suggested that large, highly charged DNA scaffold reduced the adsorption of enzymes on the reaction vessels.[94]

Besides the above factors, pH environment was regarded as a critical factor resulting in the improved enzyme activity on DNA scaffold. Zhang *et al.* suggested that activity enhancement of enzymes (GOx and HRP) located on DNA scaffolds derived from the lower pH of the negatively charged DNA scaffold surface compared with the bulk solution, which provided more optimal pH for GOx or HRP (Figure 1.15d).[95] The local pH change might be one of the reasons causing the catalytic enhancement, however, the illustrations relevant to local pH of DNA scaffold surface were limited to the specific enzymes (GOx or HRP), which exhibited similar pH dependence with an

increased maximal turnover rate under more acidic conditions.[95,96] Therefore, questions are put forth whether the mechanism of pH environment can be applied to other enzymes with different pH preferences and what is the critical factor resulting in the enhanced activity of the scaffolded enzymes.
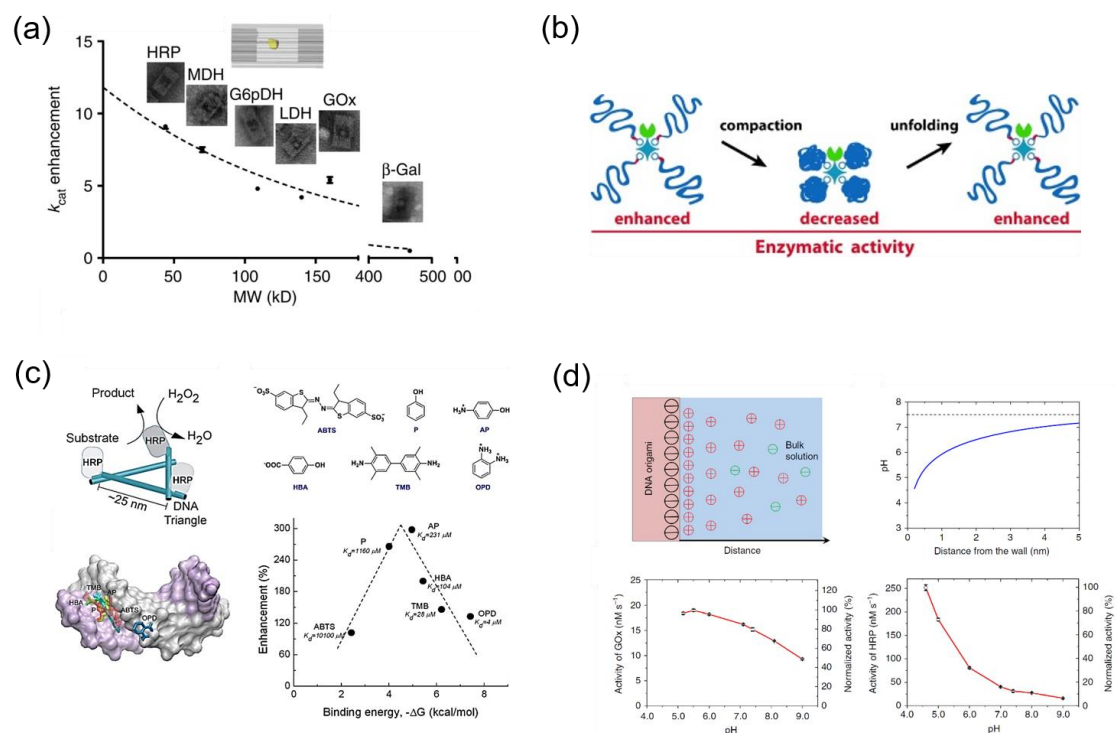
Figure 1.15. Mechanisms of the catalytic enhancement of DNA scaffolded enzymes. (a) Kcat enhancement of different enzymes encapsulated in DNA nanocage.[84] (b) DNA-protein multibranch conjugates underwent the compaction or unfolding.[91] (c) Top left: the assembly of HRP on the triangular DNA scaffold; top right: various substrates of HRP; bottom left: molecular model of HRP substrates binding sites on DNA scaffold; bottom right: the enhancement of HRP activity as a function of the predicted substrate-DNA binding energy.[92] Adapted with permission from Ref. 92. Copyright © 2013 American Chemical Society. (d) Influence of DNA scaffold on the enzymatic activity. Top left: scheme presenting the distribution of positive ions near the surface of DNA origami scaffold; top right: pH-distance profile near DNA origami; bottom left: pH-activity profile of GOx in 1 mM glucose; bottom right: pH-activity profile of HRP in 200 uM H_2O_2 and 2 mM ABTS.[95]

1.6. Aim of this research

To understand and mimic the spatial organization of enzymes in the cell, a dynamic three-dimensional DNA origami scaffold to assemble individual or multiple enzymes was constructed. Chemical mechanisms of the catalytic enhancement by scaffolded enzymes were investigated to evaluate the effects of DNA scaffold surface on the activity of assembled enzymes. The 3D DNA scaffold with dynamic shape transformation was applied for natural metabolic pathway like D-xylose metabolic pathways to understand how the enzyme kinetics, spatial arrangement and confined 3D DNA space affect the enzyme cascade reaction efficiency. Understanding the chemistry behind the catalytic activity of these scaffolded enzymes accelerate the wide applications of artificial metabolic systems.

The DNA scaffold with large enveloping capacity constructed in this work would be applicable to a wide range of enzymes to improve their catalytic properties. The efficient dynamic shape transformation of DNA scaffold is expected to be applied for the construction of more sophisticated metabolic pathways, drug delivery, biosensing, biocatalytic and diagnostic tools.

1.7. References

1. Hossain, G. S. *et al.* Rewriting the metabolic blueprint: advances in pathway diversification in microorganisms. *Front. Microbiol.* **9**, (2018).

2. Chen, A. H. & Silver, P. A. Designing biological compartmentalization. *Trends Cell Biol.* **22**, 662–670 (2012).

3. Agapakis, C. M., Boyle, P. M. & Silver, P. A. Natural strategies for the spatial optimization of metabolism in synthetic biology. *Nat. Chem. Biol.* **8**, 527–535 (2012).

4. Bonacci, W. *et al.* Modularity of a carbon-fixing protein organelle. *Proc. Natl. Acad. Sci.* **109**, 478–483 (2012).

5. Savage, D. F., Afonso, B., Chen, A. H. & Silver, P. A. Spatially ordered dynamics of the bacterial carbon fixation machinery. *Science* **327**, 1258–1261 (2010).

6. Wheeldon, I. *et al.* Substrate channelling as an approach to cascade reactions. *Nat. Chem.* **8**, 299–309 (2016).

7. Schneider, T. R. *et al.* Loop closure and intersubunit communication in tryptophan synthase. *Biochemistry* **37**, 5394–5406 (1998).

8. Dunn, M. F. Allosteric regulation of substrate channeling and catalysis in the tryptophan synthase bienzyme complex. *Arch. Biochem. Biophys.* **519**, 154–166 (2012).

9. Miles, E. W., Rhee, S. & Davies, D. R. The molecular basis of substrate channeling. *J. Biol. Chem.* **274**, 12193–12196 (1999).

10. Wu, F. & Minteer, S. Krebs cycle metabolon: structural evidence of substrate channeling revealed by cross-linking and mass spectrometry. *Angew. Chem., Int. Ed.* **54**, 1851–1854 (2015).

11. Guynn, R. W., Gelberg, H. J. & Veech, R. L. Equilibrium constants of the malate dehydrogenase, citrate synthase, citrate lyase, and acetyl coenzyme A hydrolysis reactions under physiological conditions. *J. Biol. Chem.* **248**, 6957–6965 (1973).

12. Berg, J. M., Tymoczko, J. L., & Stryer, L. *Biochemistry*. WH Freeman, New York, 2019.

13. Liu, L. N. Distribution and dynamics of electron transport complexes in cyanobacterial thylakoid membranes. *Biochim. Biophys. Acta-Bioenerg.* **1857**, 256–265 (2016).

14. Šrejber, M. *et al.* Membrane-attached mammalian cytochromes P450: an overview of the membrane's effects on structure, drug binding, and interactions with redox partners. *J. Inorg. Biochem.* **183**, 117–136 (2018).

15. Laage, D., Elsaesser, T. & Hynes, J. T. Water dynamics in the hydration shells of biomolecules. *Chem. Rev.* **117**, 10694–10725 (2017).

16. Klermund, L., Poschenrieder, S. T. & Castiglione, K. Biocatalysis in polymersomes: improving multienzyme cascades with incompatible reaction steps by compartmentalization. *ACS Catal.* **7**, 3900–3904 (2017).

17. Walde, P. & Ichikawa, S. Enzymes inside lipid vesicles: preparation, reactivity and applications. *Biomol. Eng.* **18**, 143–177 (2001).

18. Zhang, G., Quin, M. B. & Schmidt-Dannert, C. Self-assembling protein scaffold system for easy in vitro coimmobilization of biocatalytic cascade enzymes. *ACS Catal.* **8**, 5611–5620 (2018).

19. Zhao, F., Li, H., Jiang, Y., Wang, X. & Mu, X. Co-immobilization of multi-enzyme on control-reduced graphene oxide by non-covalent bonds: an artificial biocatalytic system for the one-pot production of gluconic acid from starch. *Green Chem.* **16**, 2558–2565 (2014).

20. Wei, Q., He, S., Qu, J. & Xia, J. Synthetic multienzyme complexes assembled on virus-like particles for cascade biosynthesis in cellulo. *Bioconjug. Chem.* **31**, 2413–2420 (2020).

21. Hong, F., Zhang, F., Liu, Y. & Yan, H. DNA origami: scaffolds for creating higher order structures. *Chem. Rev.* **117**, 12584-12640 (2017).

22. Tapio, K. & Bald, I. The potential of DNA origami to build multifunctional materials. *Multifunct. Mater.* **3**, (2020).

23. Rajendran, A., Nakata, E., Nakano, S. & Morii, T. Nucleic-acid-templated enzyme cascades. *ChemBioChem* **18**, 696–716 (2017).

24. Lim, S., Kim, J., Kim, Y., Xu, D. & Clark, D. S. CRISPR/Cas-directed

programmable assembly of multi-enzyme complexes. *Chem. Commun.* **56**, 4950–4953 (2020).

25. Seeman, N. C. Nucleic acid junctions and lattices. *J. Theor. Biol.* **99**, 237–247 (1982).

26. Seeman, N. C. & Sleiman, H. F. DNA nanotechnology. *Nat. Rev. Mater.* **3**, (2017).

27. Yan, H., Park, S. H., Finkelstein, G., Reif, J. H. & LaBean, T. H. DNA-templated self-assembly of protein arrays and highly conductive nanowires. *Science* **301**, 1882–1884 (2003).

28. Park, S. H. *et al.* Three-helix bundle DNA tiles self-assemble into 2D lattice or 1D templates for silver nanowires. *Nano Lett.* **5**, 693–696 (2005).

29. Shih, W. M., Quispe, J. D. & Joyce, G. F. A 1.7-kilobase single-stranded DNA that folds into a nanoscale octahedron. *Nature* **427**, 618–621 (2004).

30. Rothemund, P. W. K. Folding DNA to create nanoscale shapes and patterns. *Nature* **440**, 297–302 (2006).

31. Douglas, S. M. *et al.* Self-assembly of DNA into nanoscale three-dimensional shapes. *Nature* **459**, 414–418 (2009).

32. Douglas, S. M. *et al.* Rapid prototyping of 3D DNA-origami shapes with caDNAno. *Nucleic Acids Res.* **37**, 5001–5006 (2009).

33. Andersen, E. S. *et al.* Self-assembly of a nanoscale DNA box with a controllable lid. *Nature* **459**, 73–76 (2009).

34. Han, D. *et al.* DNA origami with complex curvatures in three-dimensional space. *Science* **332**, 342–346 (2011).

35. Dietz, H., Douglas, S. M. & Shih, W. M. Folding DNA into twisted and curved nanoscale shapes. *Science* **325**, 725–730 (2009).

36. Han, D. *et al.* DNA gridiron nanostructures based on four-arm junctions. *Science* **339**, 1412–1415 (2013).

37. Zadegan, R. M. *et al.* Construction of a 4 Zeptoliters switchable 3D DNA box origami. *ACS Nano* **6**, 10050–10053 (2012).

38. Zhang, D. Y. & Winfree, E. Control of DNA strand displacement kinetics using toehold exchange. *J. Am. Chem. Soc.* **131**, 17303–17314 (2009).

39. Zhang, D. Y. & Seelig, G. Dynamic DNA nanotechnology using strand-displacement reactions. *Nat. Chem.* **3**, 103–113 (2011).

40. Rangel, A. E., Hariri, A. A., Eisenstein, M. & Soh, H. T. Engineering aptamer switches for multifunctional stimulus-responsive nanosystems. *Adv. Mater.* (2020).

41. Turek, V. A. *et al.* Thermo-responsive actuation of a DNA origami flexor. *Adv. Funct. Mater.* **28**, 1–7 (2018).

42. Kim, S. H. *et al.* Reversible regulation of enzyme activity by pH-responsive encapsulation in dna nanocages. *ACS Nano* **11**, 9352–9359 (2017).

43. Marras, A. E. *et al.* Cation-activated avidity for rapid reconfiguration of dna nanodevices. *ACS Nano* **12**, 9484–9494 (2018).

44. Kopperger, E. *et al.* A self-assembled nanoscale robotic arm controlled by electric field. *Science* **359**, 296–301 (2018).

45. Deluca, M., Shi, Z., Castro, C. E. & Arya, G. Dynamic DNA nanotechnology: toward functional nanoscale devices. *Nanoscale Horizons* **5**, 182–201 (2020).

46. Douglas, S. M., Bachelet, I. & Church, G. M. A logic-gated nanorobot for targeted transport of molecular payloads. *Science* **335**, 831–834 (2012).

47. Amir, Y., Ben-Ishay, E., Levner, D., Ittah, S., Abu-Horowitz, A., & Bachelet, I. Universal computing by DNA origami robots in a living animal. *Nat. Nanotechnol.* **9**, 353-357 (2014).

48. Li, S. *et al.* A DNA nanorobot functions as a cancer therapeutic in response to a molecular trigger in vivo. *Nat. Biotechnol.* **36**, 258–264 (2018).

49. Grossi, G., Dalgaard Ebbesen Jepsen, M., Kjems, J. & Andersen, E. S. Control of enzyme reactions by a reconfigurable DNA nanovault. *Nat. Commun.* **8**, (2017).

50. Juul, S. *et al.* Temperature-controlled encapsulation and release of an active enzyme in the cavity of a self-assembled DNA nanocage. *ACS Nano* **7**, 9724–9734 (2013).

51. Ijäs, H., Hakaste, I., Shen, B., Kostiainen, M. A. & Linko, V. Reconfigurable DNA origami nanocapsule for pH-controlled encapsulation and display of cargo. *ACS Nano* **13**, 5959-5967 (2019).

52. Chandrasekaran, A. R., Anderson, N., Kizer, M., Halvorsen, K., & Wang, X. Beyond the fold: emerging biological applications of DNA origami. *ChemBioChem* **17**, 1081-1089 (2016).

53 Yang, Y. R., Liu, Y. & Yan, H. DNA Nanostructures as programmable biomolecular scaffolds. *Bioconjug. Chem.* **26**, 1381–1395 (2015).

54. Ngo, T. A. *et al.* Protein adaptors assemble functional proteins on DNA scaffolds. *Chem. Commun.* **55**, 12428–12446 (2019).

55. Jaekel, A., Stegemann, P. & Saccà, B. Manipulating enzymes properties with DNA nanostructures. *Molecules* **24**, (2019).

56. Kong, G. *et al.* DNA origami-based protein networks: from basic construction to emerging applications. *Chem. Soc. Rev.* **50**, 1846–1873 (2021).

57. Mallik, L. *et al.* Electron microscopic visualization of protein assemblies on flattened DNA origami. *ACS Nano* **9**, 7133–7141 (2015).

58. Shen, W., Zhong, H., Neff, D. & Norton, M. L. NTA directed protein nanopatterning on DNA origami nanoconstructs. *J. Am. Chem. Soc.* **131**, 6660–6661 (2009).

59. Yamazaki, T., Heddle, J. G., Kuzuya, A. & Komiyama, M. Orthogonal enzyme arrays on a DNA origami scaffold bearing size-tunable wells. *Nanoscale* **6**, 9122–9126 (2014).

60. Chhabra, R. *et al.* Spatially addressable multiprotein nanoarrays templated by aptamer-tagged DNA nanoarchitectures. *J. Am. Chem. Soc.* **129**, 10304–10305 (2007).

61. Valero, J., Pal, N., Dhakal, S., Walter, N. G. & Famulok, M. A bio-hybrid DNA rotor-stator nanoengine that moves along predefined tracks. *Nat. Nanotechnol.* **13**, 496–503 (2018).

62. Ge, Z. *et al.* Constructing submonolayer DNA origami scaffold on gold electrode for wiring of redox enzymatic cascade pathways. *ACS Appl. Mater. Interfaces* **11**,

13881–13887 (2019).

63. Zhao, S. *et al.* Efficient intracellular delivery of RNase a using DNA origami carriers. *ACS Appl. Mater. Interfaces* **11**, 11112–11118 (2019).

64 Saccà, B. *et al.* Orthogonal protein decoration of DNA origami. *Angew. Chem., Int. Ed.* **122**, 9568-9573 (2010).

65. Keppler, A. *et al.* A general method for the covalent labeling of fusion proteins with small molecules *in vivo*. *Nat. Biotechnol.* **21**, 86–89 (2003).

66. Los, G. V. Halo-tag: a novel protein labeling technology for cell imaging and protein analysis. *ACS Chem. Biol.* **3**, 373-382 (2008).

67. Pavletich, N. P. & Pabo, C. Zinc finger-DNA recognition : crystal structure of a zif268-DNA complex at 2.1 A. *Science* **252**, 809–818 (1991).

68. Greisman, H. A. & Pabo, C. O. A general strategy for selecting high-affinity zinc finger proteins for diverse DNA target sites. *Science* **275**, 657–661 (1997).

69. Shaner, N. C., Steinbach, P. A., & Tsien, R. Y. A guide to choosing fluorescent proteins. *Nat. Methods* **2**, 905-909 (2005).

70. Nakata, E. *et al.* Zinc-finger proteins for site-specific protein positioning on DNA-origami structures. *Angew. Chem., Int. Ed.* **51**, 2421–2424 (2012).

71. Ellenberger, T. E., Brandl, C. J., Struhl, K. & Harrison, S. C. The GCN4 basic region leucine zipper binds DNA as a dimer of uninterrupted α helices: crystal structure of the protein-DNA complex. *Cell* **71**, 1223–1237 (1992).

72. Watanabe, S., Kodaki, T. & Makino, K. Complete reversal of coenzyme specificity of xylitol dehydrogenase and increase of thermostability by the introduction of structural zinc. *J. Biol. Chem.* **280**, 10340–10349 (2005).

73. Ngo, T. A., Nakata, E., Saimura, M., Kodaki, T. & Morii, T. A protein adaptor to locate a functional protein dimer on molecular switchboard. *Methods* **67**, 142–150 (2014).

74. Nakata, E., Dinh, H., Ngo, T. A., Saimura, M. & Morii, T. A modular zinc finger adaptor accelerates the covalent linkage of proteins at specific locations on DNA nanoscaffolds. *Chem. Commun.* **51**, 1016–1019 (2015).

75. Ngo, T. A., Nakata, E., Saimura, M. & Morii, T. Spatially organized enzymes drive cofactor-coupled cascade reactions. *J. Am. Chem. Soc.* **138**, 3012–3021 (2016).

76. Nguyen, T. M., Nakata, E., Saimura, M., Dinh, H. & Morii, T. Design of modular protein tags for orthogonal covalent bond formation at specific DNA sequences. *J. Am. Chem. Soc.* **139**, 8487–8496 (2017).

77. Nguyen, T. M. *et al.* Rational design of a DNA sequence-specific modular protein tag by tuning the alkylation kinetics. *Chem. Sci.* **10**, 9315–9325 (2019).

78. Gautier, A. *et al.* An engineered protein tag for multiprotein labeling in living cells. *Chem. Biol.* **15**, 128–136 (2008).

79. Linko, V. *et al.* DNA-based enzyme reactors and systems. *Nanomaterials* **6**, 139 (2016).

80. Wilner, O. I. *et al.* Enzyme cascades activated on topologically programmed DNA scaffolds. *Nat. Nanotechnol.* **4**, 249–254 (2009).

81. Fu, J., Liu, M., Liu, Y., Woodbury, N. W. & Yan, H. Interenzyme substrate diffusion for an enzyme cascade organized on spatially addressable DNA nanostructures. *J. Am. Chem. Soc.* **134**, 5516–5519 (2012).

82. Xin, L., Zhou, C., Yang, Z. & Liu, D. Regulation of an enzyme cascade reaction by a DNA machine. *Small* **9**, 3088–3091 (2013).

83. Linko, V., Eerikäinen, M. & Kostiainen, M. A. A modular DNA origami-based enzyme cascade nanoreactor. *Chem. Commun.* **51**, 5351–5354 (2015).

84. Zhao, Z. *et al.* Nanocaged enzymes with enhanced catalytic activity and increased stability against protease digestion. *Nat. Commun.* **7**, (2016).

85. Fu, J. *et al.* Multi-enzyme complexes on DNA scaffolds capable of substrate channelling with an artificial swinging arm. *Nat. Nanotechnol.* **9**, 531–536 (2014).

86. Liu, M., Fu, J., Qi, X., Wootten, S., Woodbury, N. W., Liu, Y., & Yan, H. A three-enzyme pathway with an optimised geometric arrangement to facilitate substrate transfer. *ChemBioChem*, **17**, 1097-1101 (2016).

87. Dinh, H. *et al.* Reaction of ribulose biphosphate carboxylase/oxygenase assembled on a DNA scaffold. *Bioorganic Med. Chem.* **27**, 115120 (2019).

88. Frey, R., Mantri, S., Rocca, M. & Hilvert, D. Bottom-up construction of a primordial carboxysome mimic. *J. Am. Chem. Soc.* **138**, 10072 (2016).

89. Zhang, Y., Ge, J. & Liu, Z. Enhanced activity of immobilized or chemically modified enzymes. *ACS Catal.* **5**, 4503–4513 (2015).

90. Ellis, G. A. *et al.* Artificial multienzyme scaffolds: pursuing *in vitro* substrate channeling with an overview of current progress. *ACS Catal.* **9**, 10812–10869 (2019).

91. Rudiuk, S., Venancio-Marques, A. & Baigl, D. Enhancement and modulation of enzymatic activity through higher-order structural changes of giant DNA-protein multibranch conjugates. *Angew. Chem., Int. Ed.* **124**, 12866–12870 (2012).

92. Lin, J. L. & Wheeldon, I. Kinetic enhancements in DNA-enzyme nanostructures mimic the sabatier principle. *ACS Catal.* **3**, 560–564 (2013).

93. Gao, Y. *et al.* Tuning enzyme kinetics through designed intermolecular interactions far from the active site. *ACS Catal.* **5**, 2149–2153 (2015).

94. Timm, C. & Niemeyer, C. M. Assembly and purification of enzyme-functionalized DNA origami structures. *Angew. Chem., Int. Ed.* **54**, 6745–6750 (2015).

95. Zhang, Y., Tsitkov, S. & Hess, H. Proximity does not contribute to activity enhancement in the glucose oxidase-horseradish peroxidase cascade. *Nat. Commun.* **7**, (2016).

96. Xiong, Y., Huang, J., Wang, S. T., Zafar, S. & Gang, O. Local environment affects the activity of enzymes on a 3D molecular scaffold. *ACS Nano* **14**, 14646–14654 (2020).

CHAPTER 2

Evaluation of the role of DNA surface for enhancing the activity of scaffolded enzymes

2.1. Introduction

Enzymes have been widely applied in the fields of chemical, medical and food industries.[1] Immobilizing the enzymes of interest on the surface of carrier provides the simplest yet useful method for practical enzyme applications.[2] Immobilized enzymes often display higher activity and stability than the free form, however, the exact mechanism for the high activity is still under debate.[3] Enhancement of the stability and/or catalytic activity of immobilized enzymes were observed for a broad range of carriers, such as protein,[4] lipid,[5] silica,[6] graphene oxide,[7] polymers[8] and DNA-based materials.[9] Understanding the origin of enhanced activity of immobilized enzymes accelerate the logical design of effective catalysts.

Among the carriers for immobilizing enzymes, DNA scaffolds, such as DNA origami, attract great interest as enzyme templates by the structural programmability and accurate addressability.[10,11] A series of individual- or multi-enzyme systems have been located on DNA structures with control over the positions and stoichiometry of enzymes.[12–14] While these studies illustrate increasing yields of coupled enzyme reactions, enhanced activities of single type of DNA scaffolded enzymes have been reported.[15–17] Several mechanisms were proposed to describe the increased catalytic ability. Compared to the other enzyme carriers, high, negative surface charge density is a distinctive character of DNA nanostructures. It was hypothesized to form the ordered hydration layer that contributed to the catalytic enhancement by stabilizing the structure of enzyme[15] or the micro-environment that increased catalytic activity without modifying the affinity of enzyme for the substrate.[16] Furthermore, the catalytic enhancement of DNA scaffolded enzymes could be caused by more general factor like reduction of the adsorption on the reaction vessels.[17] It was also suggested that substrates were attracted to the negatively charged surface of DNA nanostructure through electrostatic interaction, leading to the enrichment of substrates near the surface

and enzymes.[18]

Besides the above factors, modulation of the local pH environment by the highly negative charges on DNA scaffold surface was proposed as a critical factor to increase enzyme activity on DNA scaffold.[19,20] However, such a local pH change could limit the general application of DNA nanostructures for scaffolding enzymes because the enzymes are built up with their own optimal pH preferences. The relevance to the local pH environment of DNA scaffold could be limited to a few enzymes tested so far, which exhibited the similar pH dependence with an increased maximal turnover rate in more acidic conditions.[19,20]

In this chapter, two types of enzyme with the optimal activity at pH 6 or 8 equally displayed significant catalytic enhancements on the DNA scaffold. The neutral or net negative charge of their substrates and cofactors indicated that the surface-substrate or -cofactor electrostatic attractive interaction could not account for the increase in activities of assembled enzymes. The large scaffold with high density of DNA helices improved the enzyme stability and reduced the adsorption on reaction vessels, however, these factors alone are insufficient to explain the observed high activity of scaffolded enzyme. By using a ratiometric pH indicator, a lower local pH shift of 0.8 was observed near the DNA scaffold. The postulated local pH change near the DNA scaffold surface unlikely plays a general role in enhancing the activity of scaffolded enzymes. Instead, the ordered hydration layer of DNA scaffold surface might be the important factor affecting the activity of assembled enzymes, which was further investigated by applications of various salts and hydrophilic or hydrophobic substrates to the reaction.

34

2.2. Results and discussions

2.2.1. Construction and characterization of DNA scaffold

A square pyramidal DNA scaffold derived from the open state of DNA robot[21] was constructed by DNA origami.[10,11] The scaffold consisted of two boat forms that were covalently attached in the rear by single-stranded scaffold hinges with the dimensions of 70 nm × 45 nm × 17.5 nm. Three connecting hinges (single-stranded DNA) spanning two domains of DNA scaffold were utilized to fold the fully open state. The different views of DNA scaffold were shown in Figure 2.1. The constructed DNA scaffold features its large enveloping capacity and rigid structure.
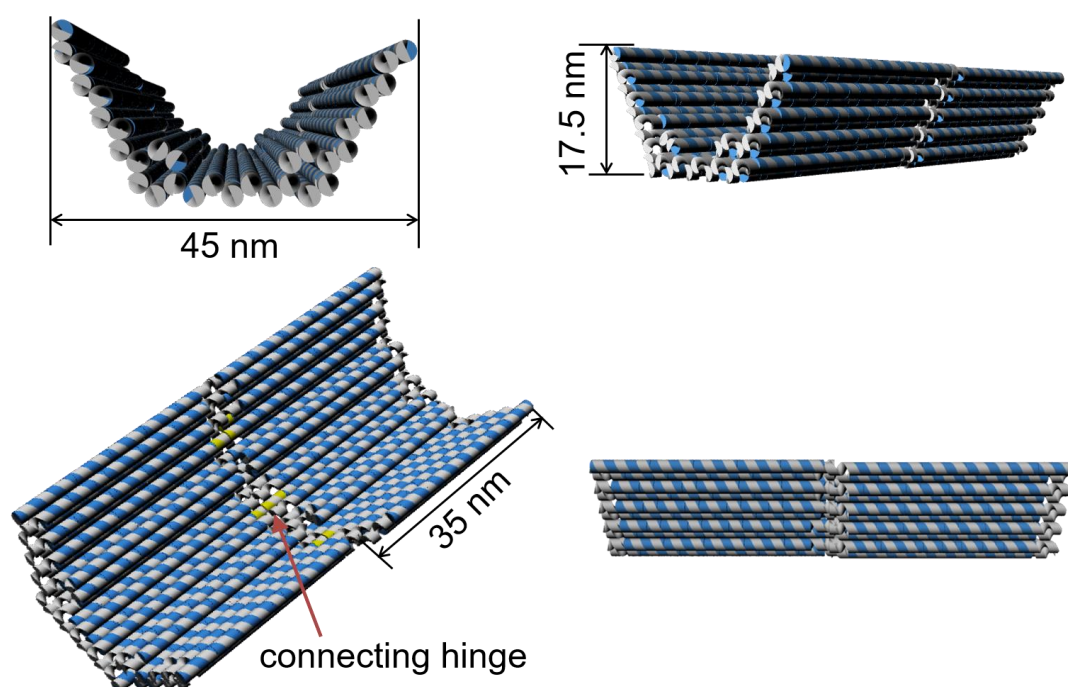
Figure 2.1. DNA scaffold in different views with designed dimensions. The single-stranded DNA in gold indicated the connecting hinge to fold the fully open state. Scaffold model was constructed by using Autodesk Maya (Autodesk® Maya® 2015, student version).

Size exclusion chromatography (Sephacryl S-400) was used to remove the excess amount of staple strands. The formation of DNA scaffold was verified by agarose gel electrophoresis, in which over 90% of each DNA scaffold migrated as a monomeric band. The recovery yield of DNA scaffold after purification was estimated

35

to be 82% by the quantification of DNA in the agarose gel band (Figure 2.2). The extinction coefficient of DNA scaffold was determined to be 1.2×10^8 $M^{-1}cm^{-1}$ (Materials and Methods). The purified DNA scaffold was also characterized by atomic force microscopy (AFM) with 94% well-formed yield (282/300) and transmission electron microscopy (TEM), the measured long and narrow sides by TEM were 66.3 ± 4.2 nm and 45.2 ± 3.5 nm, respectively, which were well consistent with the designed dimensions (Figure 2.3 and Figure 2.4). Some unrecognized structures appeared in TEM images, which most likely formed during the negative staining procedure used for TEM imaging by 2% phosphotungstic (pH 1.0), resulting in structural distortion or collapse of the macromolecular assemblies caused by the air-drying and imaging of conventional specimens under the vacuum conditions of TEM.[22]
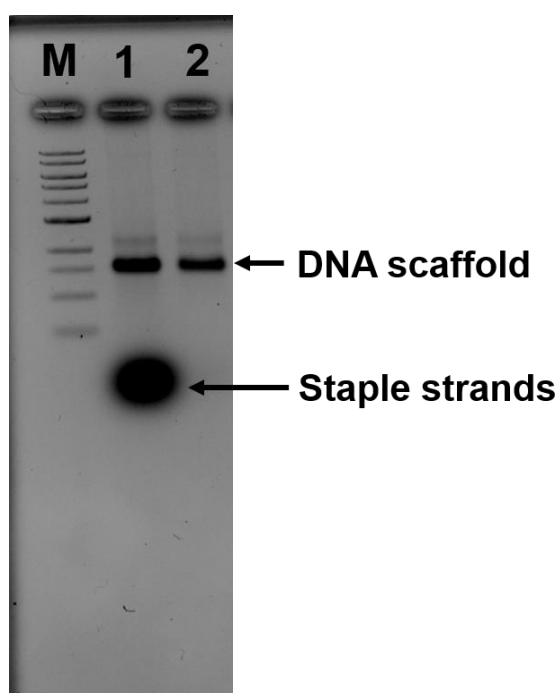
Figure 2.2. Agarose gel electrophoretic analysis of the DNA scaffold before and after the purification. The gel was stained with ethidium bromide (EtBr) and visualized by using Molecular Imager FX pro (Biorad). Lane M: 1 kb DNA marker, Lane 1: DNA scaffold (20 nM before purification). Lane 2: DNA scaffold after purification by using 500 μL volume of Sephacryl S-400 in Ultrafree-MC-DV column. Gel electrophoresis conditions: 1% agarose in 1 × TAE buffer with 12.5 mM $MgCl_2$, 50 V, 2 h.
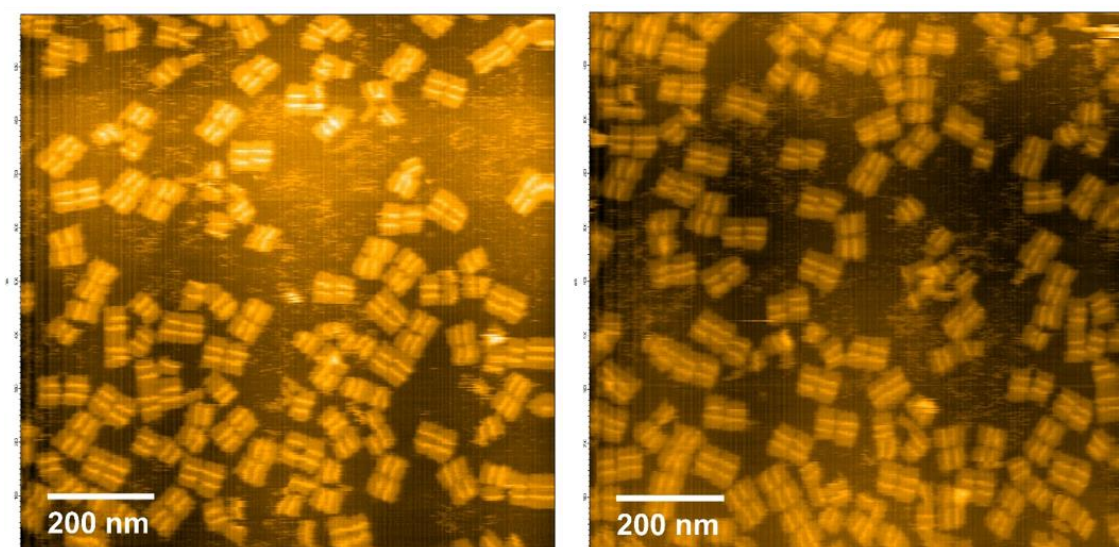
Figure 2.3. AFM images of DNA scaffold, scale bar: 200 nm. The well-formed yield of DNA scaffold was estimated to be 94% (282/300) by AFM images.
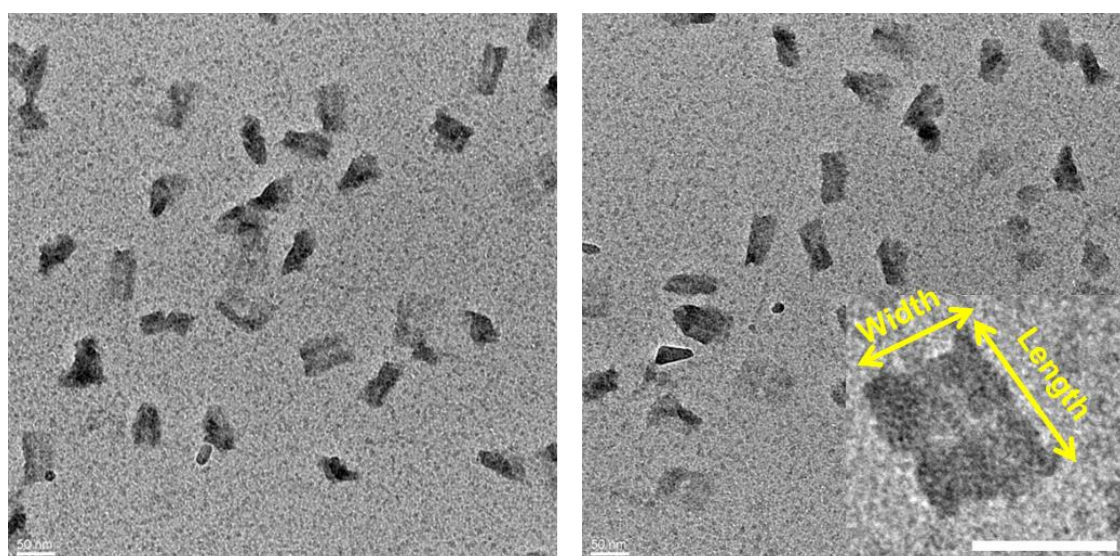
Figure 2.4. TEM images of DNA scaffold, scale bar: 50 nm. The measured width and length of typical DNA scaffold by TEM were 66.3 ± 4.2 nm and 45.2 ± 3.5 nm, respectively.

2.2.2. Assembly of enzyme ZS-XR or HG-XDH on DNA scaffold and quantification of enzyme loading yields

A mutant of xylose reductase (XR) and native xylitol dehydrogenase (XDH) derived from *Pichia stipitis*, both of which have been applied in a recombinant *Saccharomyces cerevisiae* mutant to convert xylose to ethanol,[23,24] were chosen as targeted enzymes for further assembly and study. The modular adaptor method[25–28] was applied to stably locate the enzymes at specific positions on DNA scaffold through the covalent linkage. Enzyme ZS-XR was constructed as previous reported,[26] it was obtained by fusing the monomeric xylose reductase (XR) to a modular adaptor (ZF-SNAP) consisting of the zinc finger protein zif268 binding to the specific DNA sequence and a self-ligating tag protein (SNAP-tag) reacting with a substrate benzylguanine (BG) incorporated in the DNA sequence. Similarly, to construct a modular adaptor fused enzyme HG-XDH, xylitol dehydrogenase was fused to the C-terminal of modular adaptor Halo-GCN4 containing the basic leucine zipper protein (GCN4)[29] binding to the specific DNA sequence and protein tag Halo-tag[30] reacting with its substrate 5-chlorohexane derivatives (CH) incorporated in the DNA sequence (Figure 2.5).

DNA scaffold was designed with three binding sites (hairpin DNAs) containing the target DNA sequence modified with BG for ZS-XR or three binding sites modified with CH for HG-XDH.[27-28] The DNA scaffold with corresponding binding sites was incubated with ZS-XR or HG-XDH at a molar ratio of 1:10 at 4 °C for 1 h, followed by the purification with gel filtration (Toyopearl HW55F) to remove the unbound proteins to give the purified DNA scaffolded ZS-XR (sXR) or DNA scaffolded HG-XDH (sXDH). For the detailed experimental procedure, see the Materials and Methods. The loading yields of enzymes on DNA scaffold were quantitated by AFM images. ZS-XR was assembled on DNA scaffold specifically with average 2.54 molecules of monomer

($N_{\text{ZS-XR}}$ = 2.54) locating on each scaffold (Figure 2.6 and Table 2.1). HG-XDH was positioned on DNA scaffold with average 2.51 molecules of dimer ($N_{\text{HG-XDH}}$ = 2.51) on each scaffold (Figure 2.7 and Table 2.1).
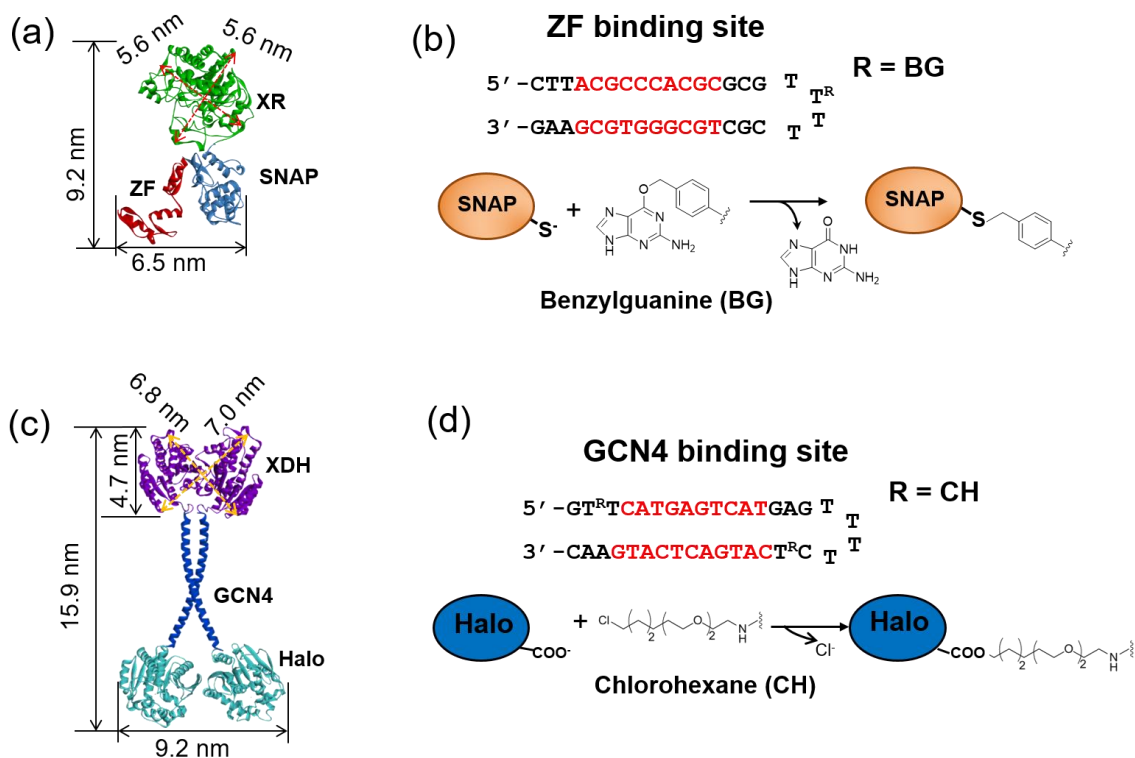
Figure 2.5. Molecular models of enzymes and binding reactions. (a) Molecular model of enzyme ZS-XR containing zif268 (PBD ID: 1ZAA), SNAP-tag (PBD ID: 3KZY) and XR (PDB ID: 3TJL).[26] (b) Zif268 binding site (hairpin DNA) and SNAP-tag reacting with its substrate benzylguanine (BG).[26] (c) Molecular model of enzyme HG-XDH containing Halo-tag (PDB ID: 1CQW), GCN4 (PBD ID: 1DGC) and XDH (PDB ID: 1ZEM). (d) GCN4 binding site (hairpin DNA) and Halo-tag reacting with its substrate chlorohexane (CH). Molecular models were constructed by using Discovery Studio (version 3.1, Accelrys Inc.).
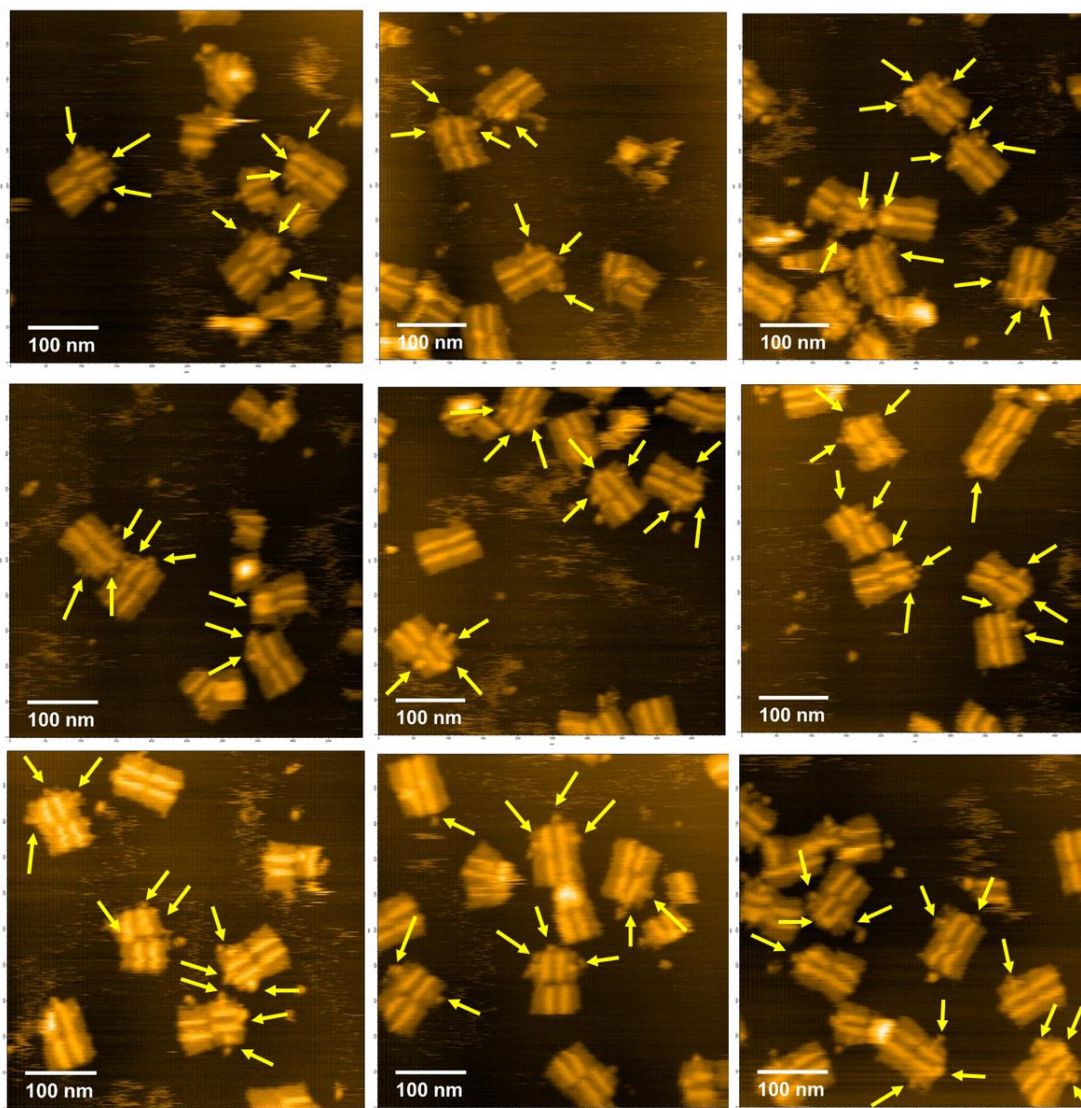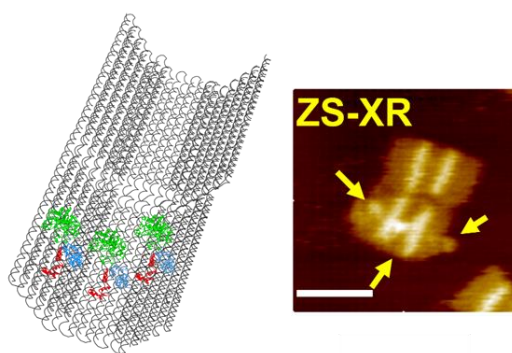
Figure 2.6. Scheme and AFM images of ZS-XR assembled on the DNA scaffold with three binding sites (sXR), scale bar: 100 nm. The arrows indicate enzyme ZS-XR. An average number of ZS-XR bound to each DNA scaffold was estimated to be 2.54 molecules of monomer (253 well-formed DNA scaffolds were counted as shown in Table 2.1).
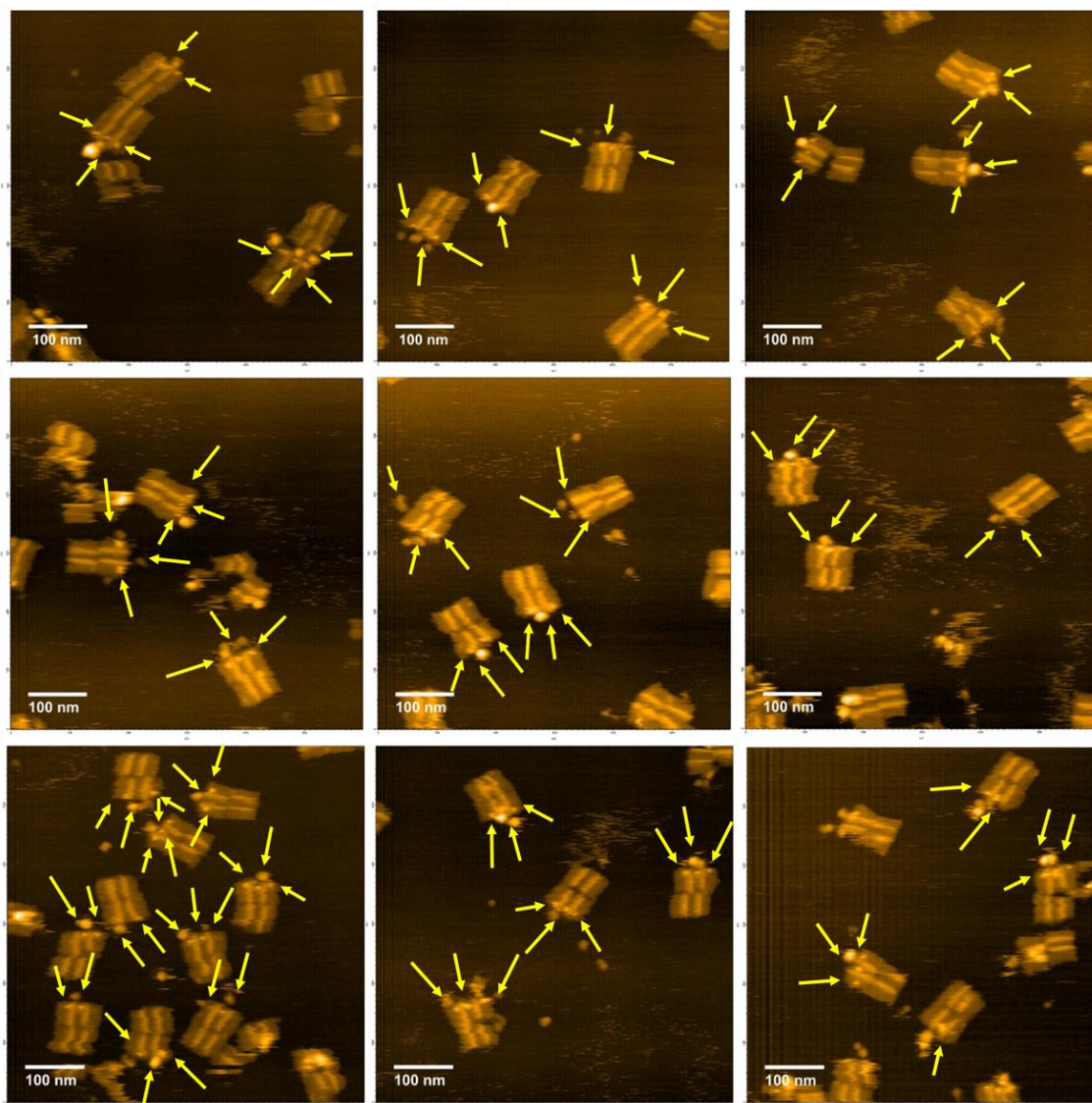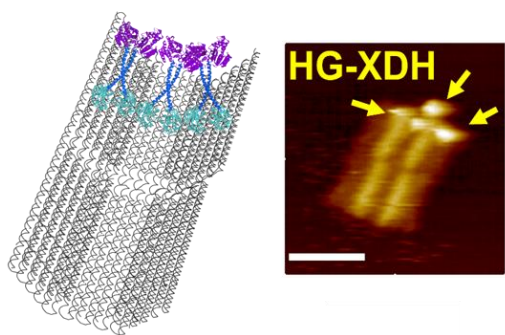
Figure 2.7. Scheme and AFM images of HG-XDH assembled on the DNA scaffold with three binding sites (sXDH), scale bar: 100 nm. The arrows indicated the enzyme HG-XDH. An average number of HG-XDH bound to each DNA scaffold was estimated to be 2.51 molecules of dimer (376 well-formed DNA scaffolds were counted as shown in Table 2.1).

To confirm the assembly yield of HG-XDH on DNA scaffold from the counting results, volume analysis of AFM images was conducted.[26] It was observed that the AFM cantilever deformed the modular adaptor Halo-GCN4 and enzyme XDH during the AFM analysis with the plausible XDH domain locating outside DNA scaffold. Therefore, volume analysis was conducted only for the plausible XDH domain existing next to the DNA scaffold. Firstly, free enzyme XDH was independently characterized by AFM and volume analysis was performed. The frequency distribution of molecule volumes of XDH showed that the volume of one dimer of XDH was 260 ± 127 nm^3 (Figure 2.8a-c). Typical AFM image of scaffolded HG-XDH and the volume analysis process were shown in Figure 2.8d-f. The frequency distribution of molecule volume showed three fractions centered at 408 ± 110 nm^3 (30%), 715 ± 212 nm^3 (55%) and 1300 ± 275 nm^3 (15%), respectively, which corresponded to two dimers, three dimers and four dimers of XDH, respectively. In average, 2.85 dimers of XDH were loaded on each DNA scaffold ($2 \times 15\% + 3 \times 55\% + 4 \times 15\% = 2.85$), which derived from the volume analysis of DNA scaffold bound with proteins. Considering 88.4% DNA scaffolds were observed to bind with HG-XDH (Table 2.1), the actual number of bound HG-XDH was calculated as follows: $N'_{\text{HG-XDH}} = 88.4\% \times 2.85 = 2.52$ (molecules of HG-XDH dimer on each DNA scaffold), which was well consistent with that derived from the value obtained by direct counting ($N_{\text{HG-XDH}} = 2.51$).

These results indicated that enzymes were loaded on the predesigned positions of DNA scaffold with high assembly efficiency and the enzyme loading yields derived from counting were accurate. The concentration of DNA-enzyme complexes was quantitated by using a NanoDrop spectrophotometer at 260 nm and calculated by the determined extinction coefficient of DNA scaffold ($\varepsilon_{\text{DNA scaffold}} = 1.2 \times 10^8$ M^{-1}cm^{-1}). The detail was shown in the Materials and Methods.
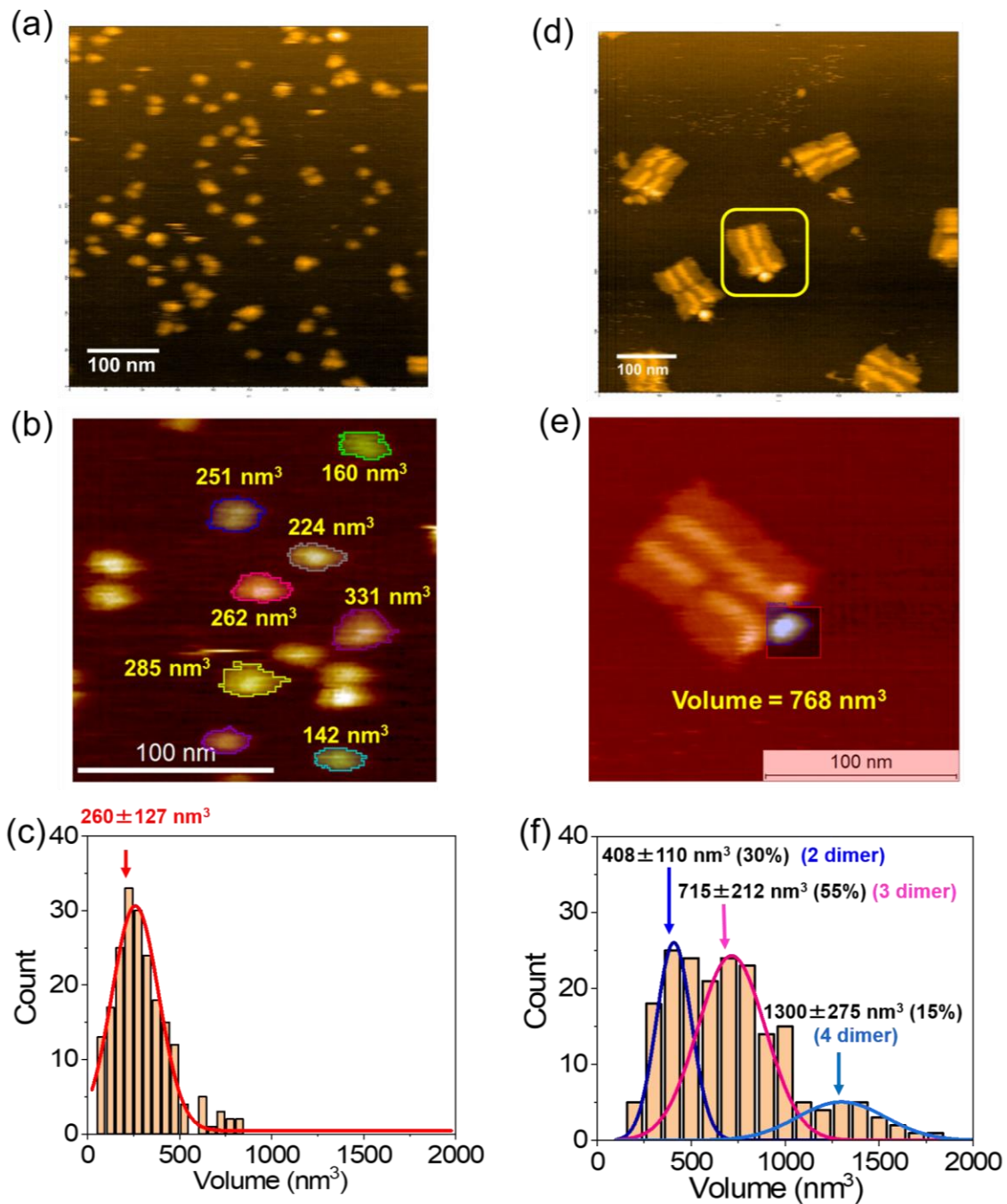
Figure 2.8. Volume analysis of AFM images. (a) AFM image of free enzyme XDH on mica surface, scale bar: 100 nm. (b) Volume analysis of free enzyme XDH, scale bar: 100 nm. (c) Frequency distribution of free XDH volume (215 particles were counted), the volume of XDH (dimer) was estimated to be 260 ± 127 nm^3. (d) Typical AFM image of scaffolded HG-XDH (sXDH), scale bar: 100 nm. (e) On the AFM analysis of sXDH, a plausible XDH portion of HG-XDH tended to locate near the outside of scaffold, while modular adaptor Halo-GCN4 of HG-XDH retained on the DNA scaffold, scale bar: 100 nm. (f) Frequency distribution of XDH volumes of sXDH (195 DNA scaffold assembled with HG-XDH analyzed).

Table 2.1. Average number of assembled enzyme on DNA scaffold

Scaffolded enzyme	Modular adaptor enzymes	Number of well-formed DNA scaffold	Numbers and yields of enzymes on modified sites			Average assembly yield
			Three-binding	Two-binding	One-binding	
sXR	ZS-XR	253	187 [73.9%]	28 [11.1%]	26 [10.3%]	2.54[a]
sXDH	HG-XDH	376	295 [78.4%]	22 [5.8%]	16 [4.2%]	2.51[b]

[a] Calculated from the average assembly yield of ZS-XR on DNA scaffold

$N_{ZS-XR} = 3 \times 73.9\% + 2 \times 11.1\% + 1 \times 10.3\% + 0 \times 4.7\% = 2.54$ (molecules of ZS-XR monomer on each DNA scaffold)

[b] Calculated from the average assembly yield of HG-XDH on DNA scaffold

$N_{HG-XDH} = 3 \times 78.4\% + 2 \times 5.8\% + 1 \times 4.2\% + 0 \times 11.4\% = 2.51$ (molecules of HG-XDH dimer on each DNA scaffold)

2.2.3. Activity of enzymes in free and scaffolded forms

The reaction of enzyme ZS-XR or HG-XDH at pH7.0 was analyzed by monitoring the consumption or production of NADH spectrophotometrically at 340 nm. ZS-XR converts its substrate xylose to xylitol by utilizing a cofactor NADH. The initial reaction velocity (V_{ini}) of scaffolded ZS-XR (sXR) was almost 4-fold higher than free ZS-XR in the presence of DNA scaffold without its binding sites (ZS-XR + Scaffold), ZS-XR attached to a BG-modified oligodeoxyribonucleotide (ZS-XR + ODN), or free ZS-XR (Free ZS-XR) (Figure 2.9). HG-XDH converts its substrate xylitol to xylulose by consuming a cofactor NAD$^+$. The initial reaction velocity of scaffolded HG-XDH (sXDH) was also increased by over 4 times than free HG-XDH in the presence of DNA scaffold without its binding sites (HG-XDH + Scaffold), HG-XDH attached to a CH-modified ODN (HG-XDH + ODN), or free HG-XDH (Free HG-XDH) (Figure 2.10).

The catalytic enhancements were observed for both DNA scaffolded enzymes compared with the respective free enzymes under the same enzyme concentration. The neutral or net negative charge of their substrates (xylose or xylitol) and cofactors

(NADH or NAD$^+$) indicated that neither the surface-scaffold nor cofactor electrostatic attractive interaction accounted for the increase in activities of DNA assembled enzymes.
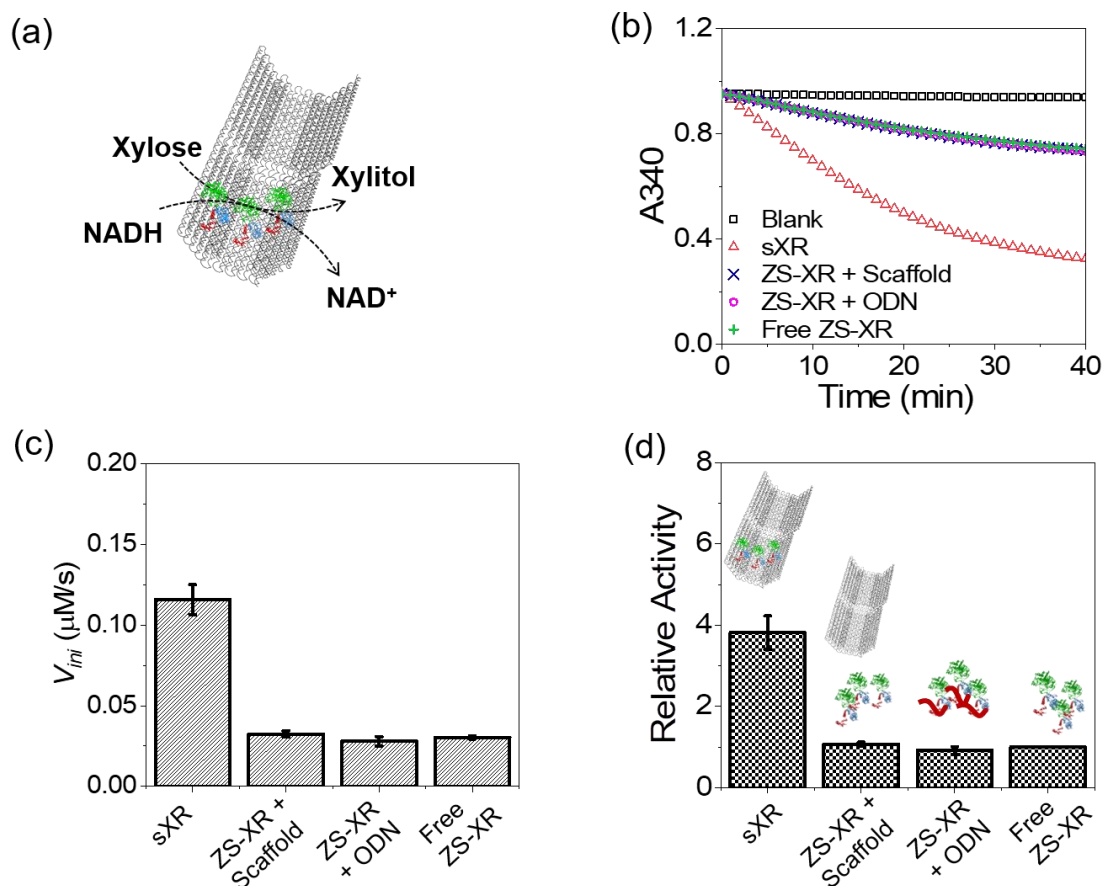
Figure 2.9. Catalytic activities of ZS-XR loaded on the DNA scaffold and free ZS-XR. (a) Scheme of ZS-XR enzyme reaction. (b) Time course of absorbance at 340 nm (A340) of enzyme reactions of scaffolded ZS-XR (sXR), free ZS-XR in the presence of DNA scaffold without its binding sites (ZS-XR + Scaffold), ZS-XR attached with a BG-modified oligodeoxynucleotide (ZS-XR + ODN) and free ZS-XR in solution (Free ZS-XR). (c) Comparison of initial reaction velocity of each enzyme reaction. (d) Relative activity of enzyme reactions, in which enzyme activity of Free ZS-XR was set to 1. Enzyme reactions were carried out by 5 nM (monomer) ZS-XR or sXR reacting with 200 mM xylose and 300 μM NADH in the buffer (pH 7.0) containing 40 mM Tris-HCl, 20 mM acetic acid, 12.5 mM MgCl$_2$, 5 μM BSA, 0.002% Tween20, 1 μM ZnCl$_2$ and 100 mM NaCl at 25 °C. Data in (c) and (d) were the averages of three independent repetitions, error bars indicated the S.D. of the repetitions.
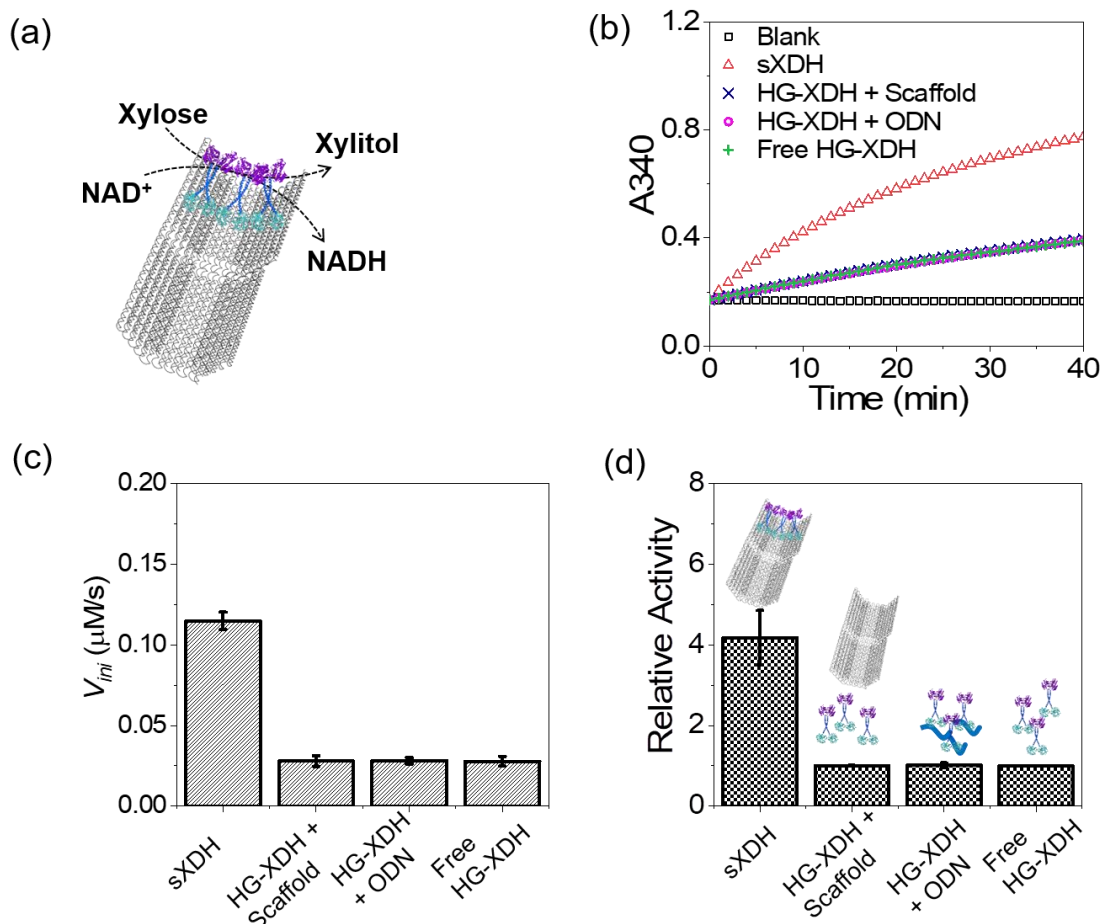
Figure 2.10. Catalytic activities of HG-XDH loaded on the DNA scaffold and free HG-XDH. (a) Scheme of HG-XDH enzyme reaction. (b) Time course of absorbance at 340 nm (A340) of enzyme reactions of scaffolded HG-XDH (sXDH), free HG-XDH in the presence of DNA scaffold without its binding sites (HG-XDH + Scaffold), HG-XDH modified with a CH modified oligodeoxynucleotide (HG-XDH + ODN) and free HG-XDH in solution (Free HG-XDH). (c) Comparison of initial reaction velocity of each enzyme reaction. (d) Relative activity of enzyme reactions, in which enzyme activity of Free HG-XDH was set to 1. Enzyme reactions were carried out by 5 nM (dimer) HG-XDH or sXDH reacting with 300 mM xylitol and 2 mM NAD^+ in the buffer (pH 7.0) containing 40 mM Tris-HCl, 20 mM acetic acid, 12.5 mM $MgCl_2$, 5 μM BSA, 0.002% Tween20, 1 μM $ZnCl_2$ and 100 mM NaCl at 25 ℃. Data in (c) and (d) were the averages of three independent repetitions, error bars indicated the S.D. of the repetitions.

2.2.4. pH dependent activity of enzymes in free and scaffolded forms

As depicted in Figure 2.11 and Figure 2.12, the pH activity profiles of the free and DNA scaffolded enzymes exhibited almost identical behavior. Free ZS-XR and scaffolded ZS-XR (sXR) possessed the same optimal pH value at 6.0, while both free HG-XDH and scaffolded HG-XDH (sXDH) had a pH optimum at 8.0. Enzyme ZS-XR and HG-XDH displayed different pH preferences (2.0-unit pH differences), indicating that local pH modulated by DNA scaffold surface might not be the critical factor to enhance the activity of scaffolded enzymes. The optimal pH value of anchored enzymes was not altered by the immobilization process, which might be due to the biocompatibilities of DNA-based materials and the covalent modular adaptor conjugation strategy that maintained the conformations and catalytic properties of enzymes.
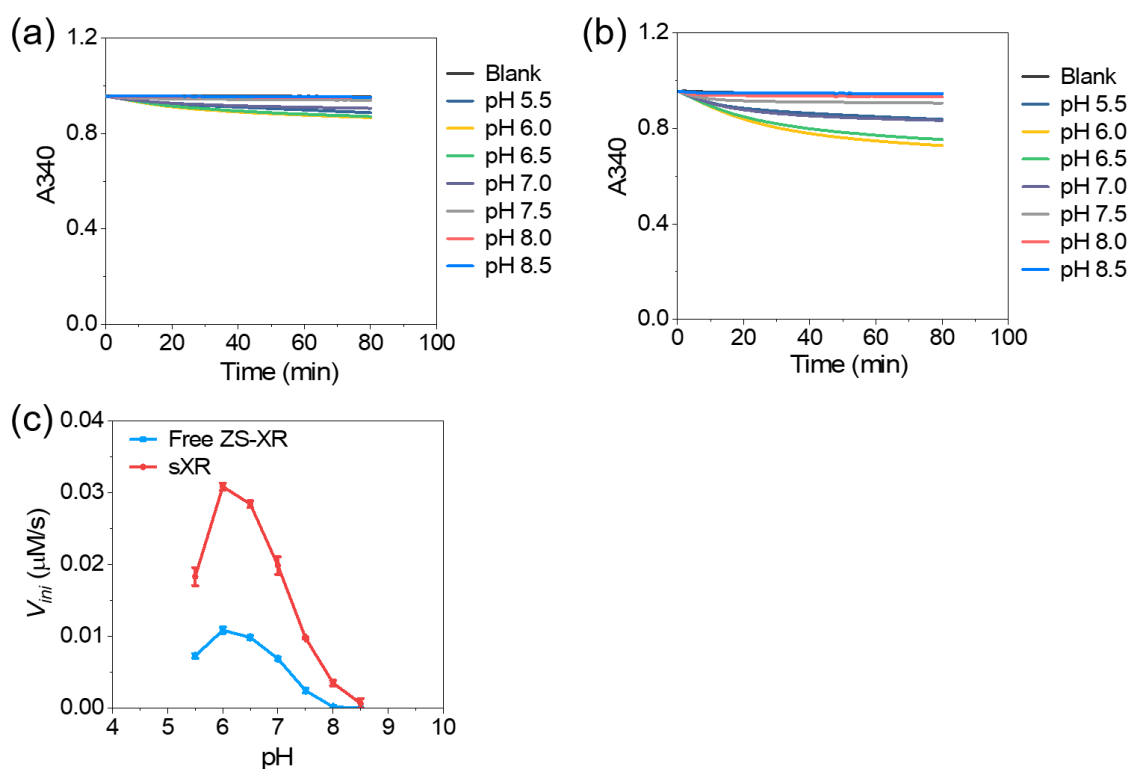
Figure 2.11. Reactions of free ZS-XR and scaffolded ZS-XR (sXR) at various pH conditions. (a) Time course of A340 of free ZS-XR reaction in the buffer with different pH (5.5 to 8.5). (b) Time course of A340 of sXR reaction in the buffer with different pH (5.5 to 8.5). (c) Effect of pH on the initial reaction velocity of free ZS-XR and sXR enzyme reactions. Enzyme reactions

were carried out by 2 nM (monomer) ZS-XR or sXR reacting with 200 mM xylose and 300 μM NADH in 40 mM Good's buffer with different pH (MES, pH 5.5 to 6.5; HEPES, pH 7.0 to 8.0; HEPPS, pH 8.5) containing 12.5 mM MgCl$_2$, 5 μM BSA, 0.002% Tween20, 1 μM ZnCl$_2$ and 100 mM NaCl at 25 °C. Data in (c) were the averages of three independent repetitions, error bars indicated the S.D. of the repetitions.
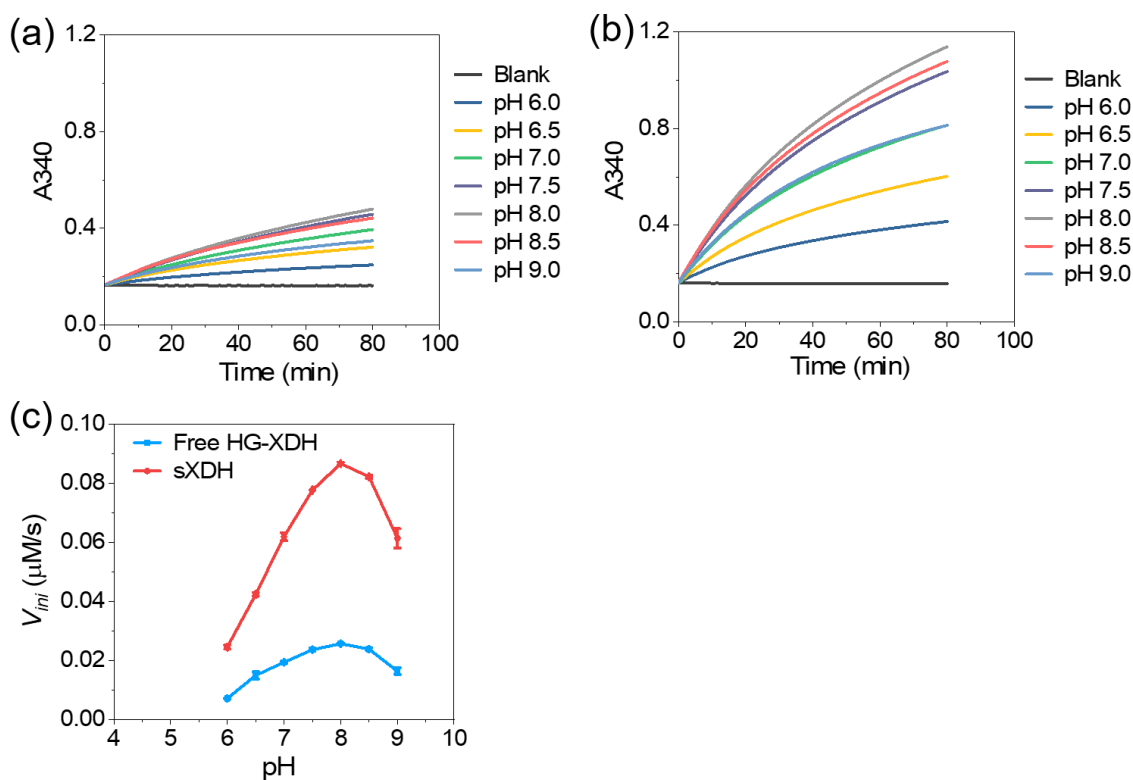
Figure 2.12. Reactions of free HG-XDH and scaffolded HG-XDH (sXDH) at various pH conditions. (a) Time course of A340 of free HG-XDH reaction in the buffer with different pH (6.0 to 9.0). (b) Time course of A340 of sXDH reaction in the buffer with different pH (6.0 to 9.0). (c) Effect of pH on the initial reaction velocity of free HG-XDH and sXDH enzyme reactions. Enzyme reactions were carried out by 2.5 nM (dimer) HG-XDH or sXDH reacting with 300 mM xylitol and 2 mM NAD$^+$ in 40 mM Good's buffer with different pH (MES, pH 5.5 to 6.5; HEPES, pH 7.0 to 8.0; HEPPS, pH 8.5; CHES, 9.0) containing 12.5 mM MgCl$_2$, 5 μM BSA, 0.002% Tween20, 1 μM ZnCl$_2$ and 100 mM NaCl at 25 °C. Data in (c) were the averages of three independent repetitions, error bars indicated the S.D. of the repetitions.

2.2.5. Stability of enzymes in free and scaffolded forms

The stabilities of enzymes in free and scaffolded forms were investigated by measuring the residual activity of enzymes after incubation at ambient temperature. A solution of 6 nM free ZS-XR or scaffolded ZS-XR (sXR) was incubated with 5 μM bovine serum albumin (BSA) at 25 °C in the low-binding tubes. After 15 min, remaining activities evaluated by the initial reaction velocity of free ZS-XR and sXR were 32% and 60%, respectively. Even considering the instability of free ZS-XR,[23] the tolerance of sXR against deactivation after the pre-incubation is not the sole determinant for the higher activity of sXR over free ZS-XR (Figure 2.13a). sXDH also showed higher residual activity under the same incubation conditions with the remaining activity of free HG-XDH and sXDH being 63% and 75%, respectively, after 12-h incubation (Figure 2.13b). The higher residual activity of DNA scaffolded enzyme can be attributed to the prevention of adsorption of enzymes on the tube surface,[17] as found in the case where BSA is added to the aqueous solution.[31,32] Indeed, the above enzyme reactions were evaluated in the presence of 5 μM BSA (Figure 2.9 – Figure 2.13) because BSA was effective on retaining the activity of free HG-XDH in a concentration dependent manner up to 5 μM (Figure 2.14).

Figure 2.13. Stability of enzymes in free and scaffolded forms incubated with BSA. (a) Initial reaction velocities of free ZS-XR and sXR after the indicated incubation time with BSA. 6 nM (monomer) free ZS-XR or sXR was incubated with 5 μM BSA and 0.002% Tween20 in a buffer (pH 7.0) containing 40 mM Tris-HCl, 20 mM acetic acid and 12.5 mM $MgCl_2$ at 25 °C prior to

the assay of catalytic activity. Enzyme reactions were carried out by 2.5 nM (monomer) free ZS-XR or sXR reacting with 200 mM xylose and 300 μM NADH in the buffer (pH 7.0) containing 40 mM Tris-HCl, 20 mM acetic acid, 12.5 mM $MgCl_2$, 5 μM BSA, 0.002% Tween20, 1 μM $ZnCl_2$ and 100 mM NaCl at 25 °C. (b) Initial reaction velocities of free HG-XDH and sXDH after the indicated incubation time with BSA. 6 nM (dimer) free HG-XDH or sXDH was incubated with 5 μM BSA and 0.002% Tween20 in a buffer (pH 7.0) containing 40 mM Tris-HCl, 20 mM acetic acid and 12.5 mM $MgCl_2$ at 25 °C prior to the assay of catalytic activity. Enzyme reactions were carried out by 2.5 nM (dimer) free HG-XDH or sXDH reacting with 300 mM xylitol and 2 mM NAD^+ in the buffer (pH 7.0) containing 40 mM Tris, 20 mM acetic acid, 12.5 mM $MgCl_2$, 5 μM BSA, 0.002% Tween20, 1 μM $ZnCl_2$ and 100 mM NaCl at 25 °C. Data were the averages of three independent repetitions, error bars indicated the S.D. of the repetitions.
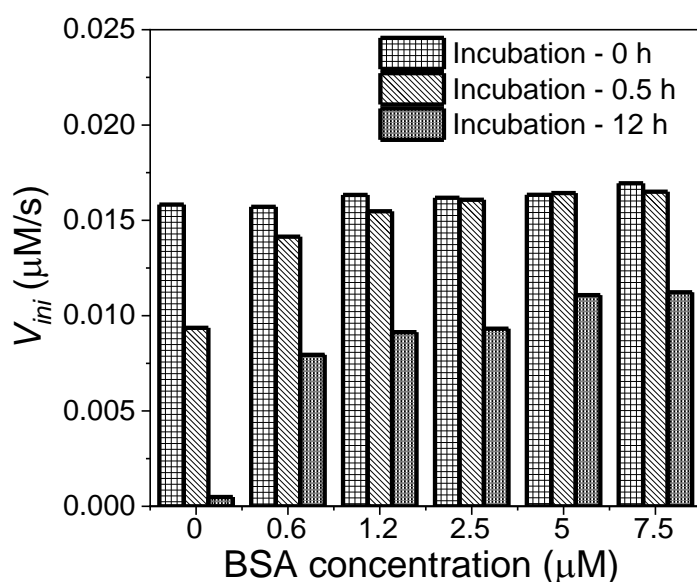
Figure 2.14. Concentration dependent effects of BSA on the residual activity of free HG-XDH against the pre-incubation time. Free HG-XDH (6 nM) was incubated with 0 to 7.5 μM BSA in a buffer (pH 7.0) containing 40 mM Tris-HCl, 20 mM acetic acid and 12.5 mM $MgCl_2$ at 25 °C prior to the assay of catalytic activity. Enzyme reactions were carried out by 2.5 nM free HG-XDH (dimer) reacting with 300 mM xylitol and 2 mM NAD^+ in the buffer (pH 7.0) containing 40 mM Tris-HCl, 20 mM acetic acid, 12.5 mM $MgCl_2$, 5 μM BSA, 0.002% Tween20, 1 μM $ZnCl_2$ and 100 mM NaCl at 25 °C.

To test whether the DNA scaffold could also prevent the enzyme deactivation, both the free and scaffolded enzymes were pre-incubated in the absence of BSA before starting reactions. Free ZS-XR and sXR incubated for 30 min without BSA retained 17% and 30%, respectively, of the original activity (Figure 2.15a). Free HG-XDH and sXDH incubated for 30 min without BSA likewise retained 62% and 86%, respectively, of its original activity. After 12 h, free HG-XDH almost completely lost the activity, while sXDH retained 40% of its original activity (Figure 2.15b). These results indicated that the scaffold with high DNA helix packing density further protected the embedded enzyme against adsorption or deactivation even in the presence of BSA (Figure 2.13). The ordered hydration layer formed by negatively charged DNA scaffold surface was suggested to stabilize the enzyme configuration.[15] However, the actual mechanism by which the ordered hydration layer stabilizes enzyme remains to be elucidated. In the case of HG-XDH, the dimeric form of XDH could be further stabilized upon binding the specific DNA sequence on the scaffold. However, the stabilizing effect alone cannot explain the 4-fold higher catalytic activity of scaffolded enzymes over the free enzymes.

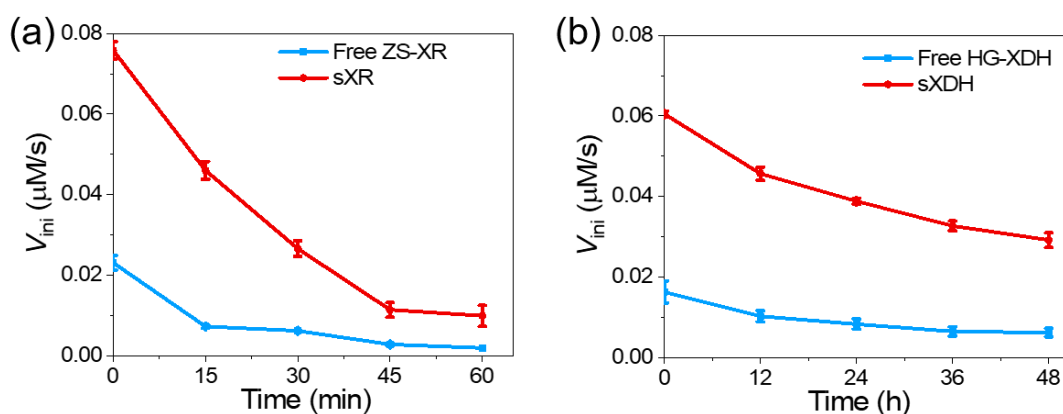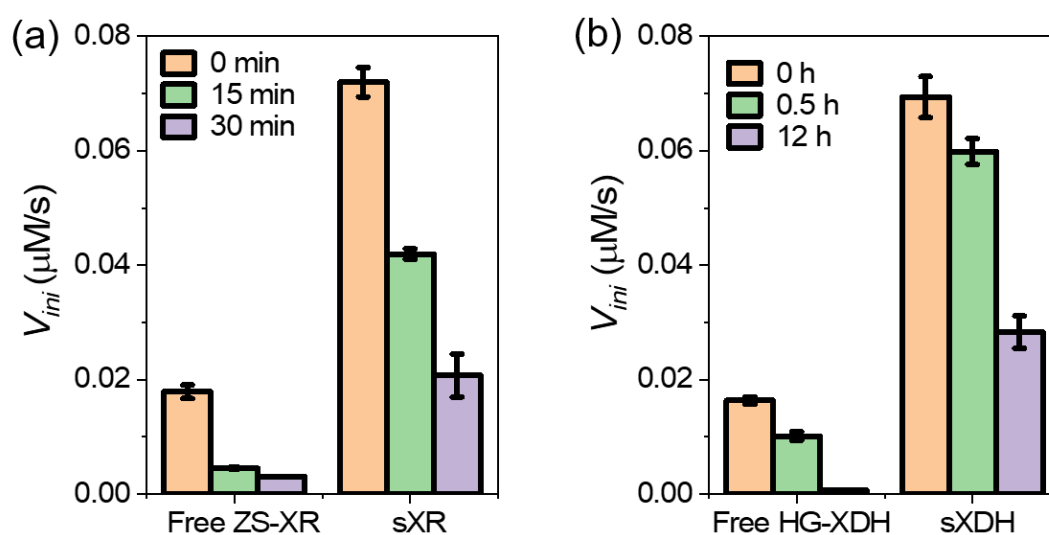**Figure 2.15.** Stability of enzymes in free and scaffolded forms incubated without BSA. (a) Residual activities of free ZS-XR and scaffolded ZS-XR (sXR) against the pre-incubation time without the addition of BSA. Free ZS-XR or sXR (6 nM) was incubated at 25 °C in a buffer (pH 7.0) containing 40 mM Tris-HCl, 20 mM acetic acid and 12.5 mM $MgCl_2$ prior to the assay of

catalytic activity. Enzyme reactions were carried out by 2.5 nM (monomer) free ZS-XR or sXR reacting with 200 mM xylose and 300 μM NADH in the buffer (pH 7.0) containing 40 mM Tris-HCl, 20 mM acetic acid, 12.5 mM MgCl$_2$, 5 μM BSA, 0.002% Tween20, 1 μM ZnCl$_2$ and 100 mM NaCl at 25 °C. (b) Residual activities of free HG-XDH and scaffolded HG-XDH (sXDH) against the pre-incubation time without the addition of BSA. Free HG-XDH or sXDH (6 nM) was incubated at 25 °C in a buffer (pH 7.0) containing 40 mM Tris-HCl, 20 mM acetic acid and 12.5 mM MgCl$_2$ prior to the assay of catalytic activity. Enzyme reactions were carried out by 2.5 nM (dimer) free HG-XDH or sXDH reacting with 300 mM xylitol and 2 mM NAD$^+$ in the buffer (pH 7.0) containing 40 mM Tris-HCl, 20 mM acetic acid, 12.5 mM MgCl$_2$, 5 μM BSA, 0.002% Tween20, 1 μM ZnCl$_2$ and 100 mM NaCl at 25 °C. Data were the averages of three independent repetitions, error bars indicated the S.D. of the repetitions.

2.2.6. Evaluation of local pH on the surface of DNA scaffold by SNARF derivatives

To assess the local pH environment of DNA scaffold, it was constructed with nine hybridization sites (protruding single-stranded DNA) for the attachment of dual-emission ratiometric pH indicator SNARF derivative.[33-35] Maleimido-modified SNARF derivative (SNARF-mal) was first conjugated to thiol-modified single-stranded DNA (ODN-thiol) to obtain ODN-SNARF. The preparation detail was shown in Materials and Methods. After that, ODN-SNARF was used for the further conjugation with DNA scaffold via hybridization with the protruding DNA sequence. The SNARF derivative was loaded on the DNA scaffold either facing near the surface (sSNARF-n) or locating 6.7 nm away from the surface (sSNARF-f), which roughly corresponded to the distance between enzyme and surface of DNA scaffold (Figure 2.16).

It was reported that the low lying n-π* transition of the maleimide ring would significantly reduce the quantum yield of fluorophore. By the addition of a thiol group, the emission of fluorophore was restored.[36,37] To achieve the similar properties with ODN-SNARF, SNARF-mal was modified with β-mercaptoethanol that provided thiol group to obtain SNARF-mal-ME (Figure 2.16b).
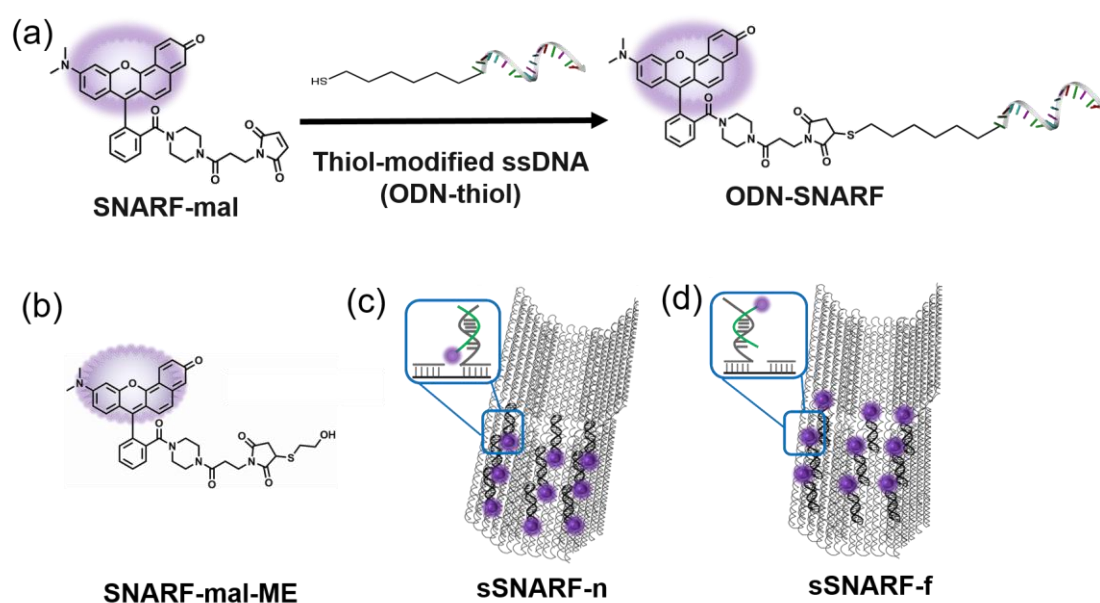
Figure 2.16 Local pH environment of DNA scaffold surface assessed by SNARF derivative. (a) Scheme representing the preparation of ODN-SNARF. (b) Structure of *β*-mercaptoethanol-modified SNARF-mal (SNARF-mal-ME). (c) Scheme representing SNARF derivative facing near DNA scaffold surface (sSNARF-n). (d) Scheme representing SNARF locating 6.7 nm far apart from the DNA scaffold surface (sSNARF-f).

The fluorescence emission spectra of SNARF-mal-ME, sSNARF-n and sSNARF-f were monitored upon the excitation at the wavelength of 534 nm in the buffer with different final pH ranging from 4.6 to 9.5. The spectra exhibited fluorescence emission peaks at 600 m and 652 nm, respectively. As the pH of the solution increased from pH 4.1 to pH 9.5, emission intensities recorded at 600 nm decreased, whereas the emission intensities recorded at 652 nm increased (Figure 2.17a-c). The ratio of fluorescence emission intensity at 600 nm over 652 nm was plotted against the buffer pH to deduce pH titration curves (Figure 2.17d). The large error bars in the acidic region presumably resulted from the weak and fluctuated fluorescence intensities at 652 nm under the acidic condition (pH 4.6 – 5.9), in which SNARF-mal-ME displayed lower ratio value at pH 4.6 compared with sSNARF-n and sSNARF-f. In the curve fitting to the equation shown in Materials and Methods, the maximum ratio

was fixed to the same value (R_{max} = 1.9). The pKa values of SNARF-mal-ME, sSNARF-n and sSNARF-f were 6.3 ± 0.1, 7.1 ± 0.1 and 6.8 ± 0.1, respectively. The pKa value of SNARF derivative shifted higher by 0.8 near the DNA scaffold surface or 0.5 at 6.7 nm away from the surface.
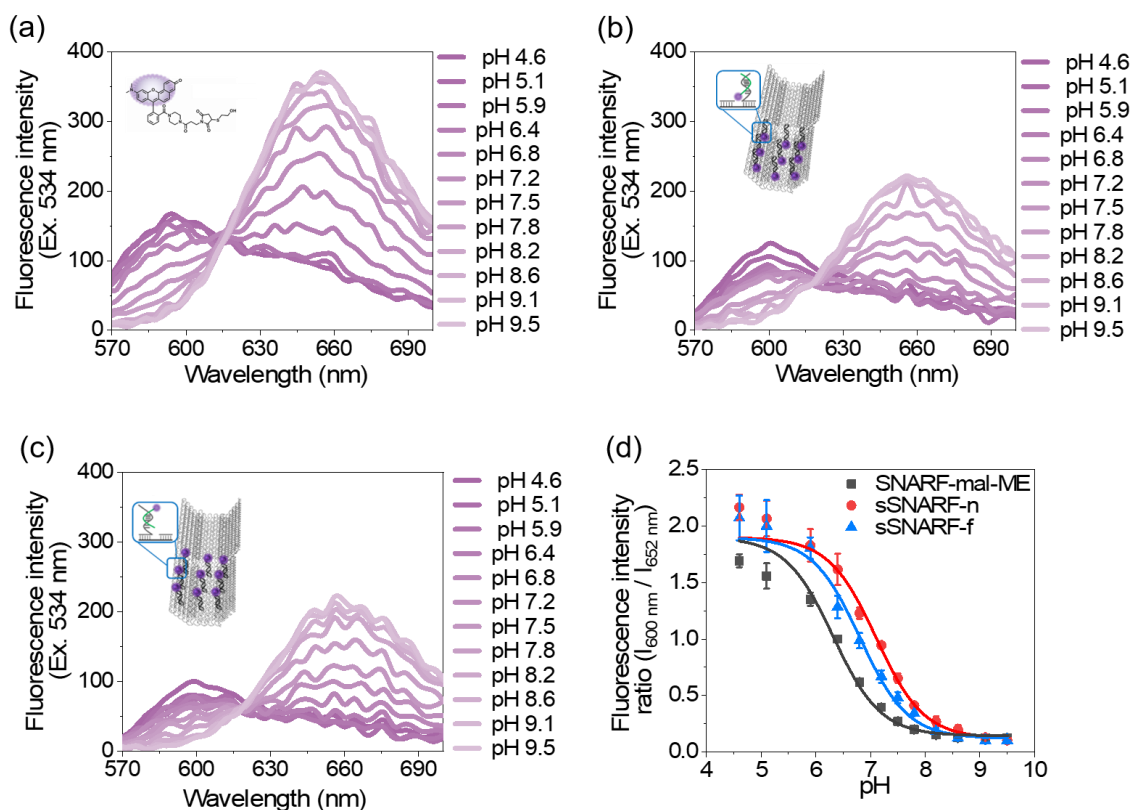
Figure 2.17. Titration of fluorescence emissions for SNARF-mal-ME, sSNARF-n and sSNARF-f by buffer pH. (a) Fluorescence emission spectra of SNARF-mal-ME in the buffer with different pH (4.6 to 9.5). (b) Fluorescence emission spectra of sSNARF-n in the buffer with different pH (4.6 to 9.5). (c) Fluorescence emission spectra of sSNARF-f in the buffer with different pH (4.6 to 9.5). Fluorescence emission of 45 nM SNARF-mal-ME, sSNARF-n or sSNARF-f was monitored upon excitation at 534 nm in the buffer with different final pH (4.6 to 9.5) containing 0.002% Tween20 and 12.5 mM MgCl$_2$ at 25 °C. (d) Plots of the fluorescence emission intensity ratio ($I_{600\ nm}/I_{652nm}$) against the buffer pH for SNARF-mal-ME, sSNARF-n and sSNARF-f. 40 mM Acetate buffer or Good's buffer was used in the presence of 12.5 mM MgCl$_2$ (acetate buffer: pH 4.6 and pH 5.1; MES buffer: pH 5.9 – pH 6.8; HEPES buffer: pH 7.2 – pH 8.2; CHES buffer: pH 8.6 – pH 9.5). Data in (d) were the averages of three independent repetitions, error bars indicated the S.D. of the repetitions.

By using the titration curve of SNARF-mal-ME as the standard of bulk buffered solution, local pH near the surface of DNA scaffold and near the enzyme loaded position in the reaction buffer (pH 7.0) was deduced to be 6.2 and 6.5, respectively (Materials and Methods). The lower local pH might derive from the large and negatively charged surface of DNA scaffold which attracts the protons (Figure 2.18a).[19] Based on the pH profiles of enzyme activity, the local pH near the enzyme would result in at most 25% enhancement of the catalytic activity for sXR and 30% reduction for sXDH since ZS-XR and HG-XDH displayed the optimal pH at 6.0 and 8.0, respectively (Figure 2.18b). Therefore, the postulated modulation of enzyme activity by the lower pH shift near DNA scaffold surface[19] unlikely explains the catalytic enhancements of both scaffolded enzymes.
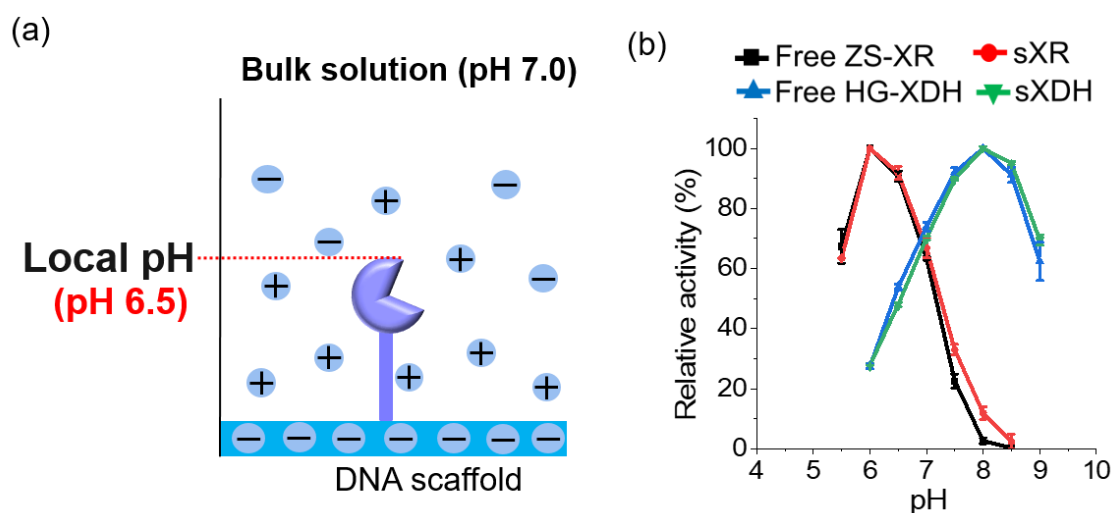
Figure 2.18. (a) Local pH of DNA scaffold surface assessed by SNARF pH indicator. (b) pH profiles of enzymes in free and DNA scaffolded forms, the enzyme reaction conditions were shown in the captions of Figure 2.11 and Figure 2.12. Data in (b) were the averages of three independent repetitions, error bars indicated the S.D. of the repetitions.

2.2.7. Evaluation of the chemistry of ordered hydration layer on the DNA scaffold surface by studying the enzyme reactions with hydrophilic or hydrophobic substrates

To understand the origins of the catalytic enhancement of DNA assembled enzymes, the contribution of the interaction between DNA carrier surface and enzyme must be considered further. It has been shown that a layer of water, whose density and orientational structures are substantially different from those of bulk water, is formed near a surface emanating strong electric field like the DNA scaffold surface.[38-40] The formation of such ordered hydration layer is a plausible candidate for the general factor to enhance the catalytic activity of the enzyme scaffolded on DNA nanostructure. It has been proposed by Zhao *et al.* that the ordered hydration layer formed by the DNA nanocage might stabilize enzymes and increase the catalytic ability.[15] Besides the stabilization effect, the ordered hydration shell with hydrophilic properties increasing the local concentration of hydrophilic substrate of enzyme and enhancing the activity of DNA scaffolded enzyme was further hypothesized in this chapter (Figure 2.19).
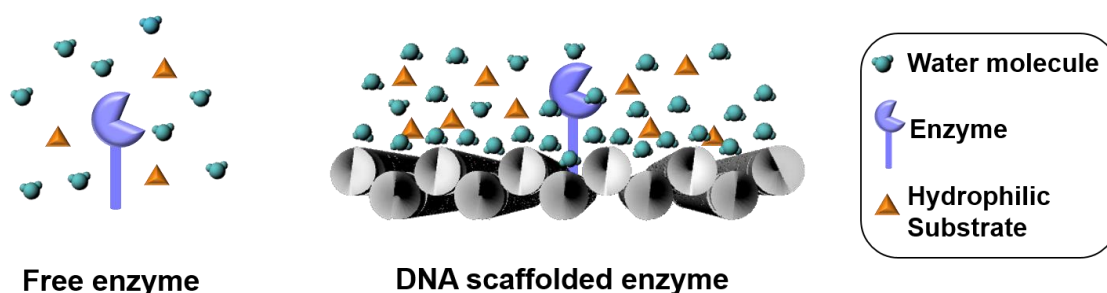
Figure 2.19. Scheme representing the hypothesis that ordered hydration layer of DNA scaffold surface increases the local concentration of hydrophilic substrate of enzyme.

To test this hypothesis, the effect of various substrates with hydrophilicity or hydrophobicity on the activity of free and scaffolded ZS-XR was investigated. The enzyme reactions were conducted with hydrophilic substrates D-xylose (Log P = - 2.7) or D,L-glyceraldehyde (Log P = -1.6), or hydrophobic substrates 4-nitrobenzaldehyde (Log P = 1.3), ethyl benzoylformate (Log P = 1.7), or o-chloroacetophenone (Log P = 1.9). The structures and properties of xylose reductase substrates were shown in Figure 2.20. The K_m values of free ZS-XR for xylose, D,L-glyceraldehyde and 4-nitrobenzaldehyde were determined to be 256.4 mM, 1.9 mM and 0.3 mM, respectively. The k_{cat} values of free ZS-XR for xylose, D,L-glyceraldehyde and 4-nitrobenzaldehyde were 124.6 min^{-1}, 158.4 min^{-1} and 480 min^{-1}, respectively (Table 2.2). The k_{cat}/K_m values of XR for o-chloroacetophenone and ethyl benzoylformate were 20.4 $mM^{-1}min^{-1}$ and 16.1 $mM^{-1}min^{-1}$, respectively.[41,42]

D-xylose

Chemical Formula: $C_5H_{10}O_5$
Molecular Weight: 150.13
Log P: -2.7

D,L-glyceraldehyde

Chemical Formula: $C_3H_6O_3$
Molecular Weight: 90.08
Log P: -1.6

4-nitrobenzaldehyde

Chemical Formula: $C_7H_5NO_3$
Molecular Weight: 151.12
Log P: 1.3

Ethyl Benzoylformate

Chemical Formula: $C_{10}H_{10}O_3$
Molecular Weight: 178.19
Log P: 1.7

o-chloroacetophenone

Chemical Formula: C_8H_7ClO
Molecular Weight: 154.59
Log P: 1.9

Figure 2.20. Structures and properties of xylose reductase substrates. The chemical formula, molecular weight and Log P value were shown. The higher Log P value indicated the higher hydrophobicity.

Compared with xylose, the enzyme reactions with D,L-glyceraldehyde, ethyl benzoylformate and *o*-chloroacetophenone displayed slower initial reaction velocities and reduced reaction efficiencies, while 4-nitrobenzaldehyde displayed faster enzyme reaction, as shown in the time courses of A340 of enzyme reactions (Figure 2.21). The fold enhancement was calculated from the initial reaction velocity of scaffolded ZS-XR (sXR) divided by that of free ZS-XR (Figure 2.22a and Figure 2.22b). Hydrophilic substrate D,L-glyceraldehyde showed comparable fold enhancement with xylose, while the hydrophobic substrates ethyl benzoylformate and *o*-chloroacetophenone reduced the fold enhancement from 3.5-fold to 1.8-fold and 2.0-fold, respectively. The hydrophobic substrate 4-nitrobenzaldehyde showed similar fold enhancement with xylose and D,L-glyceraldehyde despite the properties of hydrophobicity (Log P = 1.3). Considering the low K_m value (0.3 mM) and high k_{cat} value (480 min^{-1}) of ZS-XR for 4-nitrobenzaldehyde, the effect of ordered hydration layer reducing the hydrophobic substrate may be alleviated due to the high substrate affinity and high catalytic efficiency (Table 2.2).

The activity fold enhancements of DNA scaffolded enzymes were plotted by the Log P values of substrates. It was found that the fold enhancements were decreased when the reactions were proceeded with substrates with high hydrophobicity like ethyl benzoylformate (Log P = 1.7) and *o*-chloroacetophenone (Log P = 1.9) (Figure 2.22c), which supported the hypothesis. While further evaluation with a variety of substrates is necessary to obtain a more evident tendency, understanding the role of ordered hydration layer on DNA scaffolded enzymes is an attractive direction to explore the working mechanisms of the catalytic enhancements.
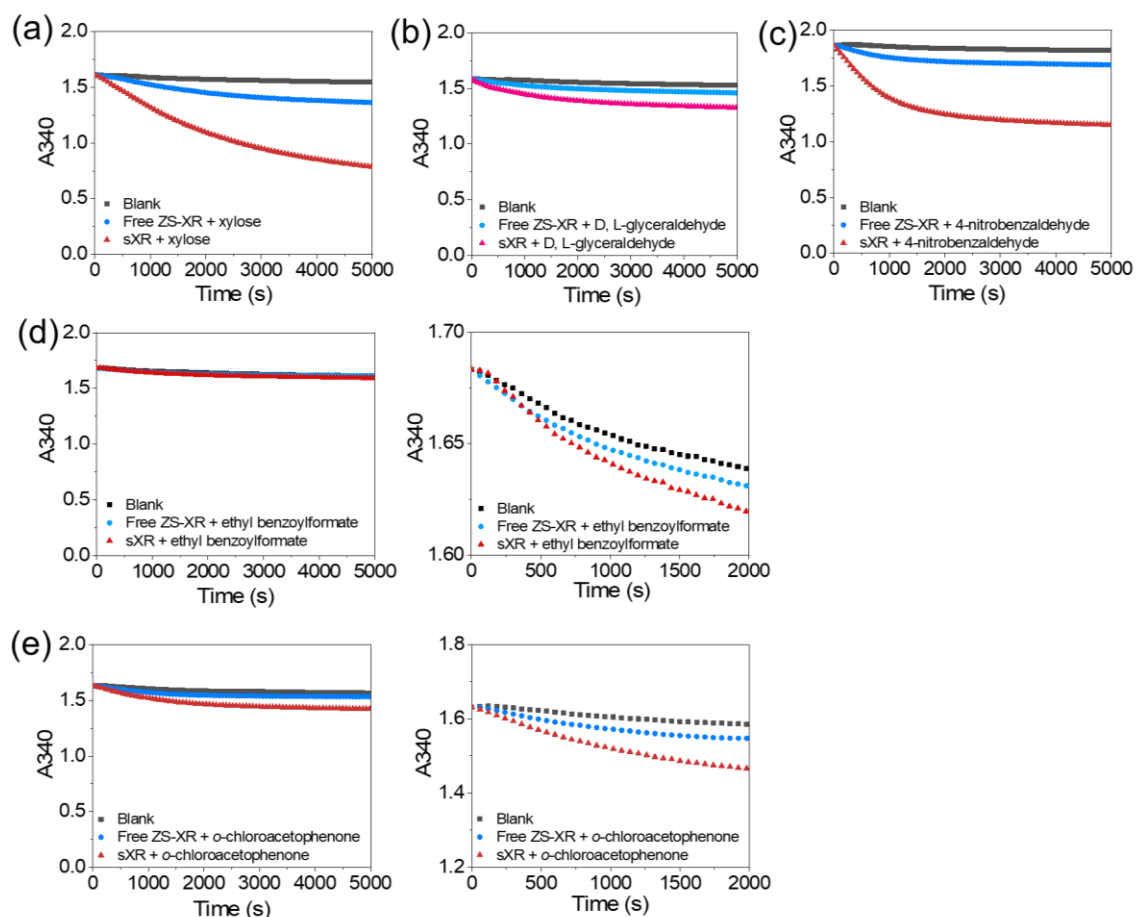
Figure 2.21. Free ZS-XR and scaffolded ZS-XR (sXR) enzyme reactions with various substrates. (a) Time course of A340 of enzyme reactions with 50 mM xylose. (b) Time course of A340 of enzyme reactions with 15 mM D,L-glyceraldehyde. (c) Time course of A340 of enzyme reactions with 1 mM 4-nitrobenzaldehyde. (d) Time course of A340 of enzyme reactions with 2 mM ethyl benzoylformate, the enlarged figure was shown in right side. (e) Time course of A340 of enzyme reactions with 2 mM o-chloroacetophenone. The enlarged figure was shown in right side. Enzyme reactions were carried out by 5 nM (monomer) free ZS-XR or sXR reacting with 500 μM NADH in the buffer (pH 7.0) containing 40 mM Tris-HCl, 20 mM acetic acid, 12.5 mM MgCl₂, 5 μM BSA, 0.002% Tween20, 1 μM ZnCl₂, 100 mM NaCl and 5% ethanol at 25 °C.

Fig.2.22. Fold enhancement of sXR with various substrates. (a) Initial reaction velocity of free ZS-XR and sXR enzyme reactions with different substrates. (b) Activity fold enhancement of sXR compared with free ZS-XR. D,L-glyceraldehyde was abbreviated as D,L-Gly; 4-nitrobezaldehyde was abbreviated as 4-NBA; ethyl benzoylformate was abbreviated as Ethyl BF; *o*-chloroacetophenone was abbreviated as *o*-CH. The enzyme reaction conditions were indicated in the caption of Figure 2.21. (c) Plot of activity fold enhancement of sXR versus the hydrophobicity of substrates (Log P values). Data were the averages of three independent repetitions, error bars indicated the S.D. of the repetitions.

Table 2.2. Kinetic parameters of XR for different substrates

Substrate	K_m (mM)	k_{cat} (min^{-1})	k_{cat}/K_m (mM^{-1}min^{-1})
D-Xylose	256.4	124.6	0.5
D, L-glyceraldehyde	1.9	158.4	83.4
4-nitrobenzaldehyde	0.288	480.0	1666.7
o-chloroacetophenone			20.4[*]
ethyl benzoylformate			16.1[*]

Measurement of kinetic parameters for xylose, D, L-glyceraldehyde and 4-nitrobenzaldehyde were shown in Materials and Methods.

* The k_{cat}/K_m values of ethyl benzoylformate and *o*-chloroacetophenone were taken from the references.[41,42]

2.2.8. Evaluation of the chemistry of ordered hydration layer on the DNA scaffold surface by studying the effect of salts

To further test the hypothesis that ordered hydration layer formed by the highly negative charged of DNA scaffold surface will enrich the local concentration of hydrophilic substrates and increase the enzyme activity of DNA scaffolded enzyme, the effect of various salts on the activities of ZS-XR or HG-XDH in free and scaffolded forms was investigated. Four types of salts (Na_2SO_4, NaCl, CsCl and NaBr) were studied, in which Na^+ and Cl^- are usually considered as indifferent ions in terms of Hofmeister series, anions on the left of Cl^- like SO_4^{2-} are more hydrated than Cl^- and are known as kosmotropes, and anions on the right of Cl^- like Br^- are more hydrated than Cl^- and are known as chaotropes.[43] Cation Cs^+ is known as a water breaker which is weakly hydrated.[44]

Compared with the control reaction (without the addition of salts), the addition of 0.5 M NaCl, CsCl and NaBr reduced the initial reaction velocities of both free ZS-XR and scaffolded ZS-XR (sXR) (Figure 2.23a), the activity fold enhancement of sXR with 0.5 M NaCl or CsCl was comparable with that of control, while decreased from 3.7-fold to 2.6-fold with 0.5 M NaBr (Figure 2.23b). 0.5 M Na_2SO_4 did not affect the initial reaction velocities of free ZS-XR and sXR, and maintained the similar fold enhancement with control. Free ZS-XR with 1 M NaCl, CsCl and NaBr retained 69%, 58% and 33% of its original activity, respectively, while sXR retained 54%, 50% and 14% of its original activity, respectively (Figure 2.23c). The activity fold enhancements were reduced from 3.7-fold to 2.9-fold, 3.2-fold, and 1.6-fold, respectively (Figure 2.23d). Water molecules are highly packed in the restraint area between the enzyme surface and the highly negative charged DNA surface. The hydrophilic substrate of xylose reductase (xylose) is more concentrated in the restraint area than that near the surface of enzyme in bulk solution. Upon addition of the salt, concentration of the

hydrophilic substrate is lowered while that of the hydrophobic substrate increases in the restraint area due to the destruction of the ordered hydration layer. This might explain for the results that NaCl, CsCl or NaBr in high concentration decreased the activity fold enhancement of sXR.
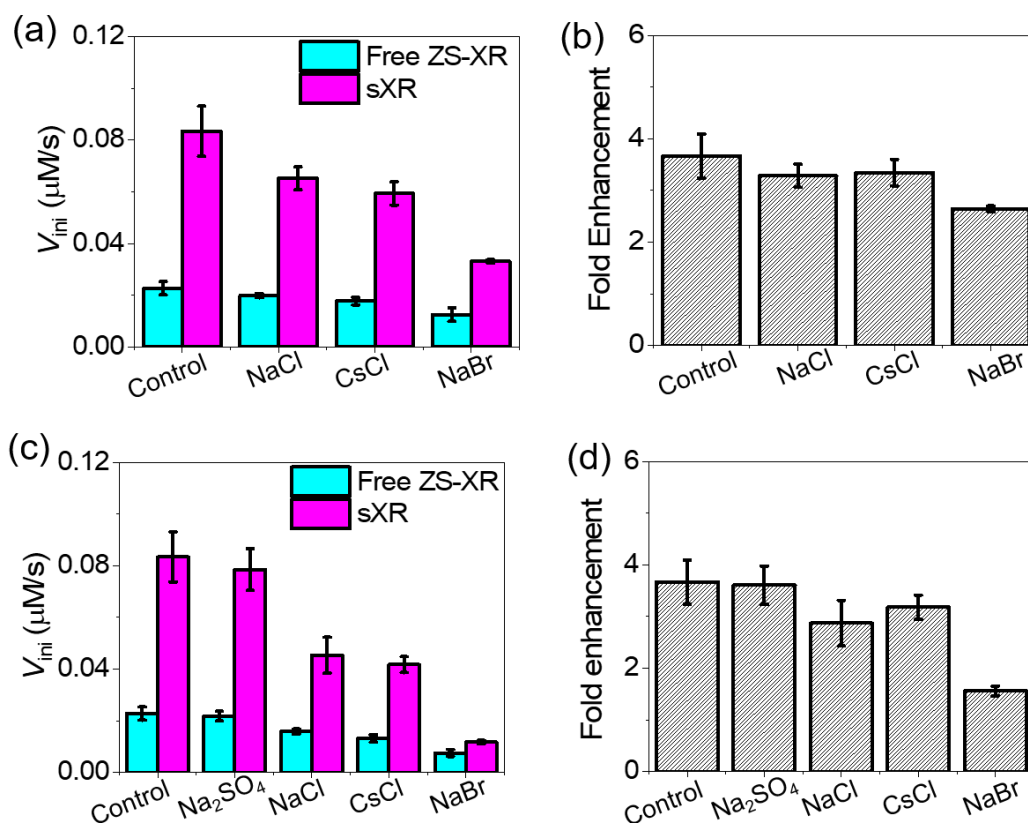
Figure 2.23. The effect of salts on free and scaffolded ZS-XR enzyme activity. (a) Initial reaction velocities of free ZS-XR or sXR enzyme reactions with 0.5 M salt, control indicated the reaction without the addition of salts. (b) Fold enhancement of sXR activity over free ZS-XR in the absence or presence of 0.5 M salt. (c) Initial reaction velocities of free ZS-XR or sXR enzyme reactions with 1 M salt, control indicated the reaction without the addition of salts. (d) Fold enhancement of sXR activity over free ZS-XR in the absence or presence of 1 M salt. Enzyme reactions were carried out by 2.5 nM (monomer) free ZS-XR or sXR reacting with 200 mM xylose and 300 μM NADH in the buffer (pH 7.0) containing 40 mM Tris-HCl, 20 mM acetic acid, 12.5 mM $MgCl_2$, 5 μM BSA, 0.002% T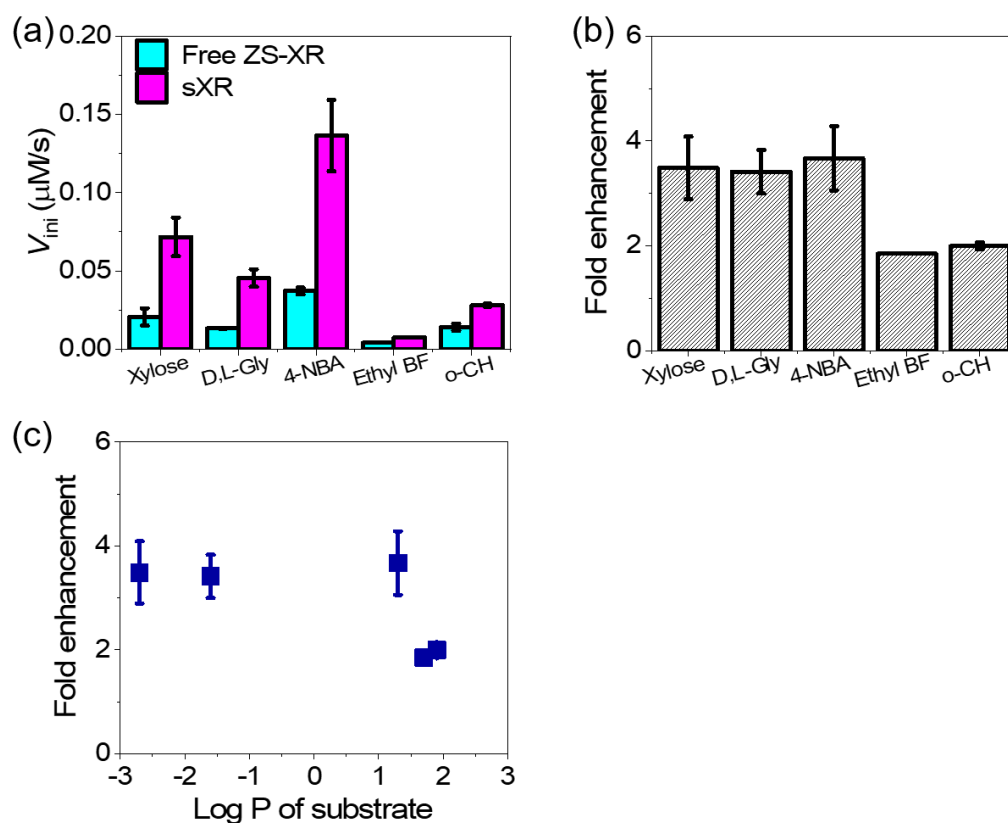ween20, 1 μM $ZnCl_2$ and 100 mM NaCl at 25 °C. Data were the averages of three independent repetitions, error bars indicated the S.D. of the repetitions.

Addition of 0.5 M NaCl, CsCl or NaBr reduced the initial reaction velocities of free HG-XDH and scaffolded HG-XDH (sXDH) (Figure 2.24a). 0.5 M NaCl or CsCl slightly increased the activity fold enhancement, while 0.5 M NaBr increased fold enhancement from 4.1-fold to 6.9-fold (Figure 2.24b). The addition of 0.5 M Na_2SO_4 slightly increased the initial reaction velocities of both free and scaffolded enzymes, while maintained the comparable activity fold enhancement of sXDH with control reactions. Free HG-XDH with 1 M NaCl, CsCl or NaBr maintained 52%, 66%, or 9% of its activity, while sXDH retained 71%, 83%, or 27% of its original activity (Figure 2.24c). The activity fold enhancements of sXDH were increased from 4.1-fold to 5.6-fold, 5.1-fold and 11.7-fold, respectively. The large error bar for 1 M NaBr might derive from the weak enzyme activity of free HG-XDH with high concentration of NaBr (Figure 2.24d).
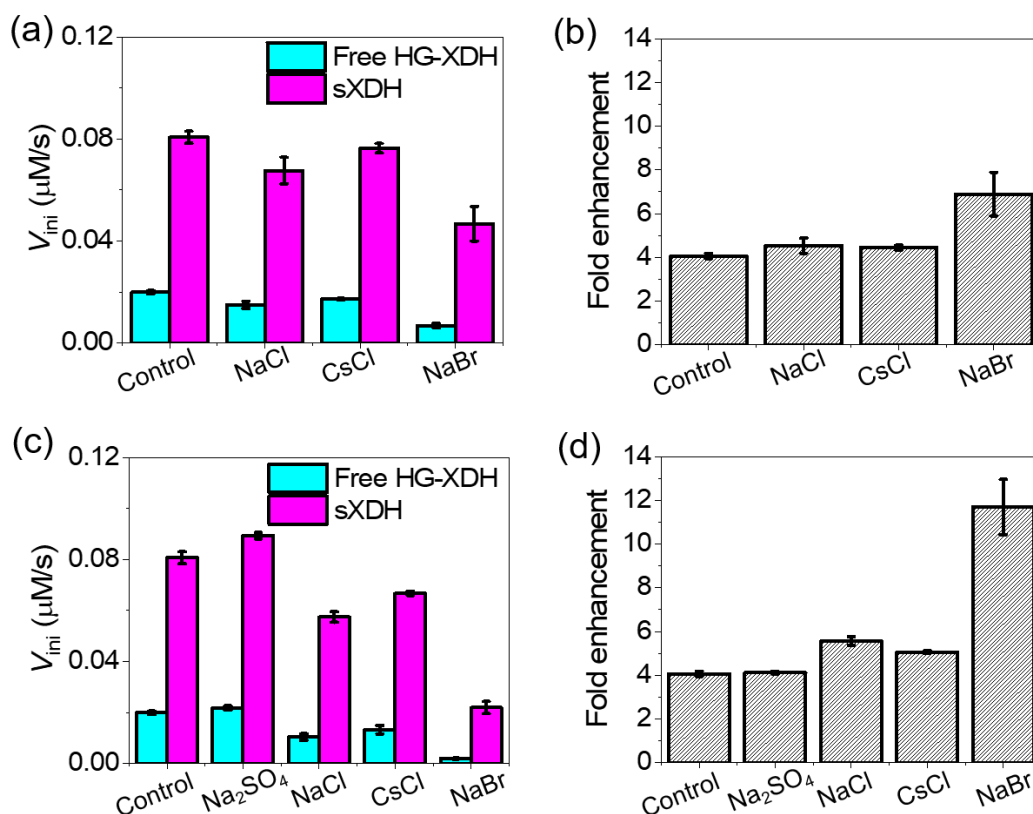
Figure 2.24. The effect of salts on free and scaffolded HG-XDH enzyme activity. (a) Initial reaction velocities of free HG-XDH or sXR enzyme reactions with 0.5 M salt, control indicated the reaction without the addition of salts. (b) Fold enhancement of sXDH activity over free HG-

XDH in the absence or presence of 0.5 M salt. (c) Initial reaction velocities of free HG-XDH or sXDH enzyme reactions with 1 M salt, control indicated the reaction without the addition of salts. (d) Fold enhancement of sXDH activity over free HG-XDH in the absence or presence of 1 M salt. Enzyme reactions were carried out by 2.5 nM (dimer) free HG-XDH or sXDH reacting with 300 mM xylitol and 2 mM NAD^+ in the buffer (pH 7.0) containing 40 mM Tris-HCl, 20 mM acetic acid, 12.5 mM $MgCl_2$, 5 μM BSA, 0.002% Tween20, 1 μM $ZnCl_2$ and 100 mM NaCl at 25 °C. Data were the averages of three independent repetitions, error bars indicated the S.D. of the repetitions.

sXDH showed an opposite tendency to sXR in the salt effect on the activity fold enhancement. One important factor is that the size of ZS-XR (69631 Da, monomer) is smaller than HG-XDH (164090 Da, dimer). The scaffolded HG-XDH will be affected to a lesser extent by reducing the packing of highly dense water in the presence of a high concentration of salt. Another important aspect is that ZS-XR and HG-XDH display different enzyme characteristics. Xylose reductase from *Pichia stipitis* is not a metalloenzyme,[45] while xylitol dehydrogenase from *Pichia stipitis* is a metalloenzyme containing catalytic Zn^{2+} in the catalytic domain, and Mg^{2+} far from the active site for stabilizing the multimeric structure.[24,46] In addition, ZS-XR and HG-XDH possess different isoelectric point (pI) value at 7.37 and 5.64, respectively. In this context, the charges carried by ZS-XR and HG-XDH might be very different in the enzyme reaction buffer (pH 7.0). By the addition of various salt with high concentration, the reduction of activity fold enhancement of sXR was observed, however, considering the opposite tendency displayed by sXDH and the different characteristics of enzymes, the proposed mechanism that the presence of salts in high concentration will destroy the ordered hydration layer on DNA scaffold surface and reduce the activity of scaffolded enzymes remains to be investigated.

2.3. Conclusion

In this chapter, two enzymes with different pH preferences, xylose reductase (XR) and xylitol dehydrogenase (XDH), were individually assembled on a square pyramidal DNA scaffold through the modular adaptor in high loading yield. The catalytic enhancements were observed for both the scaffolded XR (sXR) and scaffolded XDH (sXDH) over the respective free enzyme. The results from the dual-emission pH indicator indicated that the local pH change modulated by the highly negative charges on DNA scaffold surface is not the general factor to enhance the activity of scaffolded enzymes, ensuring that DNA nanostructures are applicable to the scaffolding of many types of enzymes. The preserved stability and the prevention of adsorption of DNA scaffolded enzyme could partly contribute to the catalytic enhancement. It was further hypothesized that the ordered hydration layer of DNA scaffold would increase the local concentration of hydrophilic substrate and enhance the activity of assembled enzymes. While the effect of various salts, and substrates with hydrophilicity or hydrophobicity were tested in this chapter, the further investigation of this mechanism would clarify the origin of scaffolding effect.

2.4. Materials and Methods

2.4.1. Materials

The single-stranded M13mp18 viral DNA (7249) was purchased from Guild Biosciences. pSNAP-tag (T7)-2 Vector, restriction enzymes (*Nde*I, *Hind*III and *Bam*HI), BG-GLA-NHS (S9151S) and bovine serum albumin (BSA, BS9000S) were purchased from New England Biolabs. pFN18A HaloTag® T7 Flexi® Vector and 5-chlorohexane (CH) derivative [HaloTag Succinimidyl Ester (O2) Ligand (P1691)] were purchased from Promega. Purified DNA origami staple strands, oligonucleotide

primers, and all other oligonucleotides were obtained from Sigma-Aldrich (St. Louis, MO), Japan Bio Services Co., LTD (Saitama, Japan) or Thermo Fisher Scientific (Tokyo, Japan). *Escherichia coli* BL21(DE3)pLysS competent cells were purchased from Invitrogen (Carlsbad, CA). *β*-Nicotinamide adenine dinucleotide in reduced (NADH) and oxidized (NAD$^+$) forms were obtained from Oriental Yeast (Tokyo, Japan). Xylose, xylitol and all other chemicals and reagents were purchased from Wako Chemicals (Tokyo, Japan) or Nacalai Tesque (Kyoto, Japan). 4-nitrobenzaldehyde, ethyl benzoylformate and *o*-chloroacetophenone were purchased from Sigma-Aldrich (St. Louis, MO). D,L-glyceraldehyde was purchased from Nacalai Tesque (Kyoto, Japan). Mini Elute Gel Extraction Kit was from QIAGEN (Tokyo, Japan). HisTrap HP column (5 mL), HiTrap SP XL column (5 mL), and Sephacryl S-400 were purchased from GE Healthcare Japan Inc. (Tokyo, Japan). PrimeSTAR HS DNA polymerase, T4 DNA ligase, and *E. coli* DH5α competent cells were obtained from TaKaRa Bio Inc. (Shiga, Japan). Toyopearl HW-55F was purchased from Tosoh Bioscience GmbH (Griesheim, Germany). Ultrafree-MC-DV column was obtained from Merckmillipore (Darmstadt, Germany). Low-binding microtube (BT-150L, 1.5 mL, nonpyrogenic & RNase- / DNase-free) was purchased from Ina OPTIKA CO., LTD (Osaka, Japan).

2.4.2 Preparation of enzyme ZS-XR and HG-XDH

Enzyme ZS-XR was prepared as previously reported.[26] Enzyme HG-XDH was prepared by the process shown followed.

2.4.2.1 Construction of an expression vector for HG-XDH

A gene encoding HG-XDH was constructed via overlapping PCR using p4LZ vector containing GCN4-XDH gene[47] and pFN18A HaloTag® T7 Flexi® Vector containing a Halo-tag gene. The primer pairs were shown in Table 2.3. The PCR products were run on a 1% agarose gel in 1× TAE buffer and purified by a Mini Elute

Gel Extraction Kit. The PCR products and pET-30a were digested with *Nde*I and BamHI and were purified in the same manner, separately. These products were incubated with T4 DNA ligase. The mixture was then transformed into E. coli DH5α competent cells for amplification. The purity and sequence of vector encoding HG-XDH (termed as pET-30a-HG-XDH) were checked and transformed into E. coli BL21(DE3)pLysS competent cells.

Table 2.3. Primer pairs for construction of an expression vector for enzyme HG-XDH

Primer	Sequence (from 5' to 3')
F-*Nde*-Halo	ATATATATATCATATGGCAGAAATCGGTACTGGCTTTC
R-GCN4-TEV	GAGCACGTTTCAGAGCAGCCGGGTCGGCGATCGCGTTAT C GCTCTGAAAG
F-TEV-GCN4	CTTTCAGAGCGATAACGCGATCGCCGACCCGGCTGCTCT GAAACGTGCTC
Rev-XDH-His-*Bam*HI	ATATATGGATCCTCAATGATGATGATGATGATGGCCGCC CTCAGG GCCGTCAAT

2.4.2.2 Overexpression and purification of HG-XDH

The transformed cells were grown at 37 °C until OD550 reached 0.45, and protein expression was induced with 1 mM IPTG for 24 h at 18 °C. The soluble fraction of the cell lysate containing HG-XDH was loaded on a HisTrap HP column in 50 mM phosphate buffer (pH 7.5) containing 200 mM NaCl, 1 mM dithiothreitol, and 10 mM xylitol and was eluted by imidazole gradient. The fractions containing HG-XDH were loaded on a HiTrap SP XL column in 20 mM phosphate buffer (pH 7.0) containing 1 mM dithiothreitol and 10 mM xylitol and eluted by NaCl gradient. The purified HG-XDH was dialyzed by using 50 mM phosphate buffer (pH 8.0), containing 0.5 M NaCl, 1 mM dithiothreitol, 2 mM $MgCl_2$, and 10 mM xylitol, and 50% glycerol and stocked at -20°C. The purity of HG-XDH was checked by SDS-polyacrylamide gel electrophoresis

(PAGE). The major band in SDS-PAGE corresponded to the calculated molecular weight of HG-XDH (82046 Da, monomer size) with purity over 95%.

2.4.3 Design of DNA scaffold

The DNA scaffold was designed in a honeycomb lattice using the open source software caDNAno (v 2.2.0.).[48] The caDNAno blueprints of the DNA scaffold with enzyme attachment sites and ODN-SNARF hybridization sites were shown in Figure 2.25 and Figure 2.26, respectively.
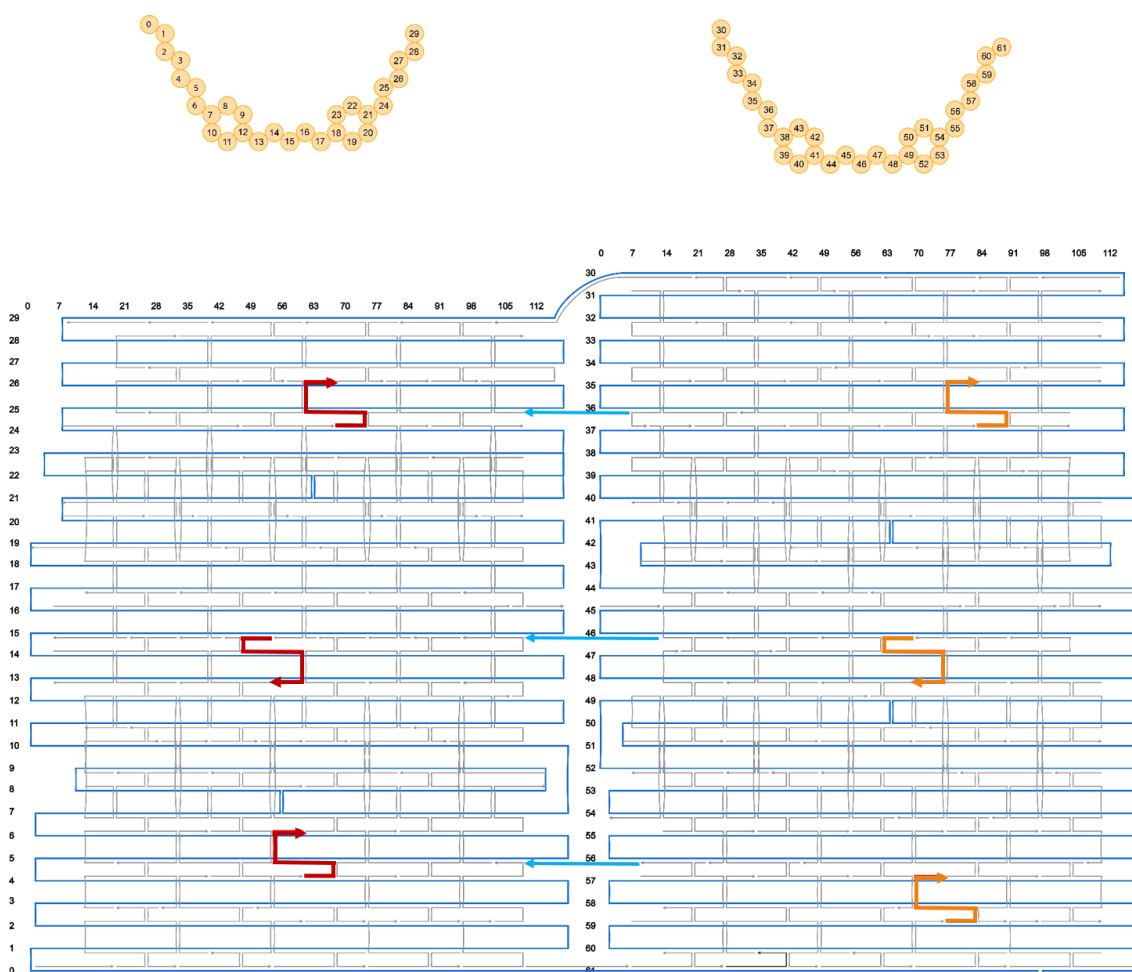
Figure 2.25. Blueprint modified from caDNAno[48] software interface of DNA scaffold (http://cadnano.org/). The staple strands in red represent enzyme ZS-XR attachment sites, staple strands in orange represent enzyme HG-XDH attachment sites, and staple strands in cyan represent the connecting hinges to fold the full open state of DNA scaffold.
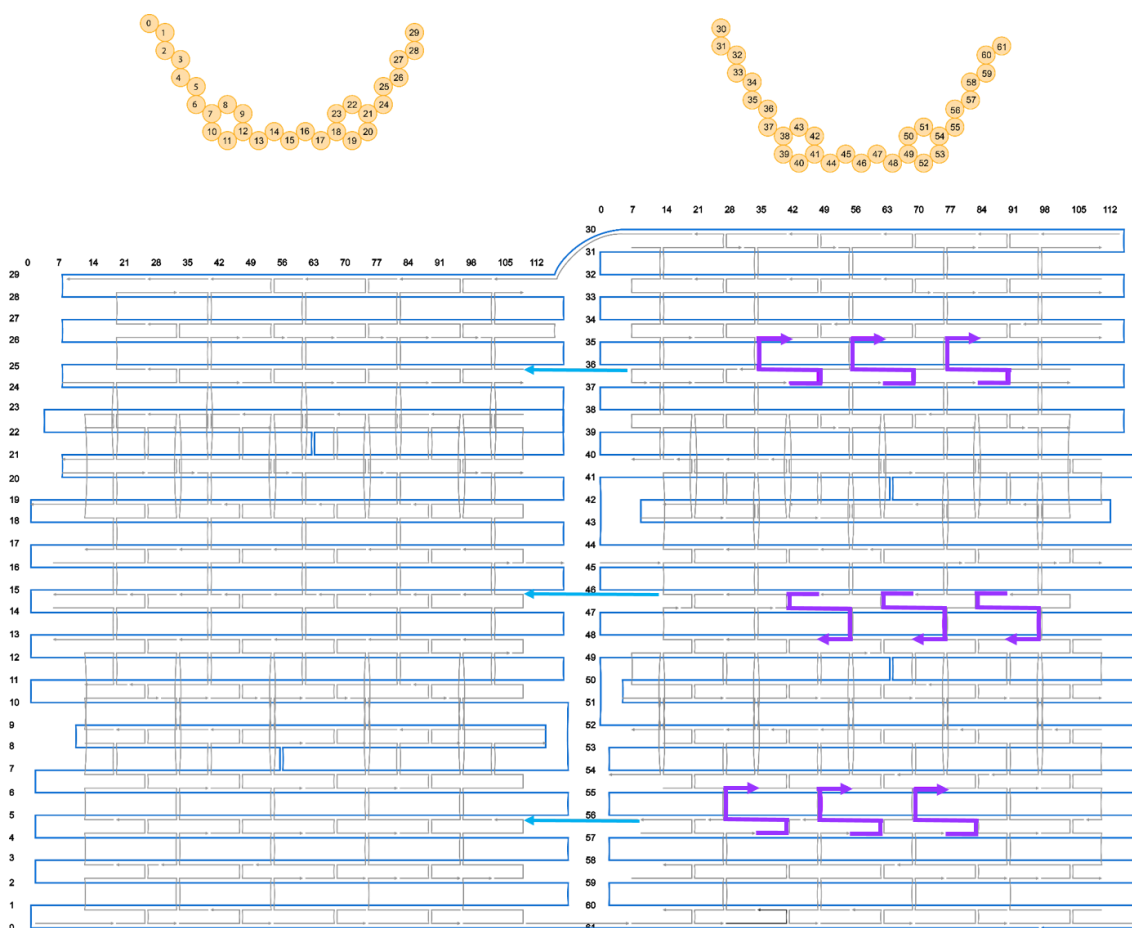
Figure 2.26. Blueprint modified from caDNAno[48] software interface of DNA scaffold (http://cadnano.org/). The staple strands in purple represent the hybridization sites of ODN-SNARF, and staple strands in cyan represent the connecting hinges to fold the full open state of DNA scaffold.

2.4.4. Preparation of DNA Scaffold

DNA scaffold was prepared by following the previous protocol.[21,49] A solution (50 μL) containing M13mp18 (20 nM) and staple DNA strands (10 equiv, 200 nM; nucleotide sequences for staple strands were shown in Table 2.7 and Table 2.8) in a DNA scaffold folding buffer (pH 8.0) containing 5 mM Tris-HCl, 1 mM EDTA and 8 mM $MgCl_2$, the mixture was subjected to a thermal-annealing ramp for folding with following program: 80 °C to 60 °C at 5 min/°C, 60 °C to 10 °C at 75 min/°C, and finally holding at 10 °C (C1000 Thermal Cycler, Bio-Rad). The sample was then purified by Sephacryl S-400 to remove the excess staple strands. The concentration of DNA

scaffold was quantified by the absorbance at 260 nm using the determined extinction coefficient of DNA scaffold.

The molar absorbance coefficient of DNA scaffold was determined as described previously.[26] The recovery yield of DNA scaffold after gel filtration was deduced by quantification of DNA in the agarose gel electrophoresis band (Figure 2.2) by following this equation:

$$\text{Recovery yield (\%)} = \frac{band\ intensity\ _{(after\ purification)}}{band\ intensity\ _{(before\ purification)}}$$

The recovery yield of DNA scaffold was 82%, from the starting concentration of DNA scaffold (20 nM), the concentration of DNA scaffold after the purification process was calculated to be 16.4 nM. From the absorbance spectrum of purified DNA scaffold measured by Nanodrop (Thermo Fisher Scientific Inc.), the average molar absorbance coefficient of DNA scaffold at 260 nm was determined ($\varepsilon = 1.2 \times 10^8$ M^{-1} cm^{-1}) (average value of three independent experiments). The determined molar extinction coefficient is consistent with that of a fully double-stranded M13mp18 molecules (the calculated molar absorbance coefficient is 1.17×10^8 M^{-1} cm^{-1} from the website http://www.molbiotools.com/dnacalculator.html).

2.4.5 Preparation of the DNA scaffold assembled with ZS-XR or HG-XDH

DNA scaffolds were constructed either containing the binding sites (hairpin DNA) with BG-GLA-NHS modification for ZS-XR attachment or the binding sites with 5-chlorohexane (CH) derivatives modification for HG-XDH attachment (Table 2.4).[27,28] 10 nM DNA scaffold with binding sites was incubated with 200 nM ZS-XR or HG-XDH in a buffer (pH 7.0) containing 40 mM Tris-HCl, 20 mM acetic acid, and 12.5 mM $MgCl_2$, 5 mM β-mecaptoethanol, 0.002% Tween20 and 1 μM $ZnCl_2$ at 4 °C for 1 h. The mixture was purified by gel filtration (500 μL in volume of Toyopearl HW55F)

in an Ultrafree-MC-DV column with a buffer (pH 7.0) containing 40 mM Tris-HCl, 20 mM acetic acid, and 12.5 mM MgCl$_2$ to remove the excess amount of unbound proteins.

Table 2.4. Nucleotide sequences for the staple strands containing the binding sites for ZS-XR with BG modification or the binding sites for HG-XDH with CH modification[27]

Oligo DNA	Sequence (from 5' to 3')
Binding site 1	GGGGGATCAGCCAGCTTACGCCCACGCGCGTT^{BG}TTCGCGCGTGG GCGTAAGCTTTCCGCAAACGG
Binding site 2	GGAAGCCGGAAGCACTTACGCCCACGCGCGTT^{BG}TTCGCGCGTGG GCGTAAGAACTCCAGTTGATT
Binding site 3	GCATAACAAATCTCCTTACGCCCACGCGCGTT^{BG}TTCGCGCGTGG GCGTAAGCAAAAAATTTCTGT
Binding site 4	TACCAGATTAAGACGT^{CH}TCATGAGTCATGAGTTTTCT^{CH}CATGAC TCATGAACTCCTTATCGATTGA
Binding site 5	TGTAAATGATAGCTGT^{CH}TCATGAGTCATGAGTTTTCT^{CH}CATGAC TCATGAACTAGATTATTAATTA
Binding site 6	ATAACATGCAACAGGT^{CH}TCATGAGTCATGAGTTTTCT^{CH}CATGAC TCATGAACGAAAAACGTAAGAA

Note

BG modified amino-C6-T was denoted as **T^{BG}**

CH modified amino-C6-T was denoted as **T^{CH}**

2.4.6 AFM imaging and statistical analyses

The sample was deposited on freshly cleaved mica (1.5 mm ϕ) surface and adsorbed for 5 min at ambient temperature, then washed three times with a buffer (pH 7.0) containing 40 mM Tris-HCl, 20 mM acetic acid, and 12.5 mM MgCl$_2$. The sample was scanned in tapping mode using a fast-scanning AFM system (Nano Live Vision, RIBM Co. Ltd., Tsukuba, Japan) with a silicon nitride cantilever (Olympus BL-AC10DS-A2). At least three independent preparations of each sample were analyzed by AFM, and several images were acquired from different regions of the mica surface. The total number of DNA scaffolds corresponded to the well-formed structures observed under AFM. The binding of ZS-XR or HG-XDH was counted for only ZS-XR or HG-

XDH bound to the perfectly folded DNA scaffold.

In the case of scaffolded ZS-XR, 253 well-formed DNA scaffolds were counted, in which DNA scaffolds with three molecules of ZS-XR (monomer) were 187 (73.9%), DNA scaffolds with two molecules of ZS-XR (monomer) were 28 (11.1%), DNA scaffolds with one molecule of ZS-XR (monomer) were 26 (10.3%), and empty DNA scaffolds were 12 (4.7%). The counting results indicated that 95.3% of DNA scaffolds were occupied with ZS-XR (P_{ZS-XR} = 95.3%). The average assembly numbers of ZS-XR on DNA was calculated as follow:

N_{ZS-XR} = 3 × 73.9% + 2 × 11.1% + 1 × 10.3% + 0 × 4.7% = 2.54 (molecules of ZS-XR monomer on each DNA scaffold)

In the case of scaffolded HG-XDH, 376 well-formed DNA scaffolds were counted, in which DNA scaffolds with three molecules of HG-XDH (dimer) were 295 (78.4%), DNA scaffolds with two molecules of HG-XDH (dimer) were 22 (5.8%), DNA scaffolds with one molecule of HG-XDH (dimer) were 16 (4.2%), and empty DNA scaffolds were 43 (11.4%). The counting results indicated that 88.4% of DNA scaffolds were occupied with HG-XDH (P_{HG-XDH} = 88.4%). The average assembly yield of HG-XDH on DNA was calculated as follow:

N_{HG-XDH} = 3 × 78.4% + 2 × 5.8% + 1 × 4.2% + 0 × 11.4% = 2.51 (molecules of HG-XDH dimer on each DNA scaffold)

2.4.7 Volume analysis of AFM images

For volume analysis, the AFM images were taken by using high-speed AFM system (Nano Live Vision, RIBM Co. Ltd., Tsukuba, Japan) with a silicon nitride cantilever (Olympus BL-AC10DS-A2). The volume of free enzyme XDH or XDH locating outside the DNA scaffold was analyzed by SPIP software (ver. 6.2.8, Image metrology), and the volume value was defined as the volume of all the pixels inside the shape's contour. The volume data were displayed as a histogram plot and fractions were

72

analyzed by means of a nonlinear curve fit by Origin Pro 2018 (ver. 9.5) software. The molecular volumes were converted to the number of enzyme molecules.

2.4.8 Calculation of the concentration of DNA-enzyme complexes

The concentration of DNA scaffold was quantitated by using a NanoDrop spectrophotometer (Thermo Fisher) at 260 nm and calculated by the determined extinction coefficient of DNA scaffold ($\varepsilon_{DNA\ scaffold} = 1.2 \times 10^8$ M^{-1}cm^{-1}). The concentration of scaffolded enzyme was calculated as followed:

$$[\text{ZS-XR}]\ (nM) = N_{\text{ZS-XR}} \times \frac{A_{260}}{\varepsilon_{DNA\ scaffold} \times l} \times 10^9$$

$$[\text{HG-XDH}]\ (nM) = N_{\text{HG-XDH}} \times \frac{A_{260}}{\varepsilon_{DNA\ scaffold} \times l} \times 10^9$$

Where $N_{\text{ZS-XR}}$ or $N_{\text{HG-XDH}}$ is the loading numbers of enzyme bound on the binding sites on the DNA scaffold by the statistical analysis of AFM images ($N_{\text{ZS-XR}} = 2.54$; $N_{\text{HG-XDH}} = 2.51$). A_{260} is the absorbance at 260 nm of sample after purification, and l is the pathlength (1 cm).

2.4.9 TEM characterization

DNA scaffold (2 to 3 nM, 2 μL) was placed onto a TEM grid and incubated for 2 minutes, then the extra sample was removed by filter paper. MilliQ water (15 to 20 μL) was used to wash the surface of TEM grid, followed by incubation with 2 μL 2% phosphotungstic acid (pH 1.0) for 2 min. The surface was washed by MilliQ water consecutively. Samples were visualized using a TEM microscope (JEOL JEM-2200FS + CETCOR) after the preparation. The sizes of DNA scaffold were analyzed by ImageJ 1.52a.

2.4.10 Enzyme assay of ZS-XR or HG-XDH

2.4.10.1 Enzyme assay of ZS-XR

Catalytic activity of ZS-XR was analyzed according to the previously reported methods by measuring the changes of absorbance at 340 nm (25 °C) derived from the oxidation of NADH in an Infinite 200 PRO microplate reader (TECAN).[26] In a typical experiment, a reaction was started with an addition of NADH (300 µM) to a mixture of ZS-XR (5 nM monomer) and xylose (200 mM) in a buffer (pH 7.0) containing 40 mM Tris-HCl, 20 mM acetic acid, 12.5 mM $MgCl_2$, 100 mM NaCl, 1 µM $ZnCl_2$, 5 µM BSA and 0.002% Tween20. Enzyme activities were measured on the microplate [Greiner Microplate, 655901, 96-well, PS, F-bottom (chimney well) clear, non-binding]. The turnover frequency was calculated from the initial reaction velocity divided by the concentration of ZS-XR.

2.4.10.2 Enzyme assay of HG-XDH

Catalytic activity of HG-XDH was measured by the changes of absorbance at 340 nm (25 °C) derived from the production of NADH in an Infinite 200 PRO microplate reader (TECAN). In a typical experiment, a reaction was started with an addition of NAD^+ (2 mM) to a mixture of HG-XDH (5 nM dimer) and xylitol (300 mM) in a buffer (pH 7.0) containing 40 mM Tris-HCl, 20 mM acetic acid, 12.5 mM $MgCl_2$, 100 mM NaCl, 1 µM $ZnCl_2$, 5 µM BSA and 0.002% Tween20. Enzyme activities were measured on the microplate [Greiner Microplate, 655901, 96-well, PS, F-bottom (chimney well) clear, non-binding]. The turnover frequency was calculated from the initial reaction velocity divided by the concentration of HG-XDH.

2.4.11 Enzyme stability against the pre-incubation time

For the investigation of ZS-XR stability, 6 nM free ZS-XR or scaffolded ZS-XR (sXR) was pre-incubated in the presence of 5 µM BSA and 0.002% Tween20 at 25

°C in the low-binding tube in a buffer (pH 7.0) containing 40 mM Tris-HCl, 20 mM acetic acid and 12.5 mM MgCl$_2$. The enzyme activities were measured at the interval of 15 min with the final enzyme concentration of 2.5 nM (monomer). For the HG-XDH stability, 6 nM free HG-XDH or scaffolded HG-XDH (sXDH) was incubated with 5 µM BSA and 0.002% Tween20 at 25 °C in the low-binding tube in a buffer (pH 7.0) containing 40 mM Tris-HCl, 20 mM acetic acid and 12.5 mM MgCl$_2$. The enzyme activities were measured at the interval of 12 h with the final enzyme concentration of 2.5 nM (dimer). The enzyme activities were measured as described above. To further verify the function of DNA scaffold, the experiments of enzyme stability were also conducted without the addition of BSA and Tween20 during the pre-incubation in the low-binding tube.

2.4.12 Local pH of the DNA scaffold analyzed by SNARF derivatives

2.4.12.1 Synthesis of SNARF derivative

The SNARF derivative (1)[33,50] was synthesized by a modified procedure of previous report.[34] The maleimide-modified SNARF derivative (SNARF-mal) was prepared by the following methods.
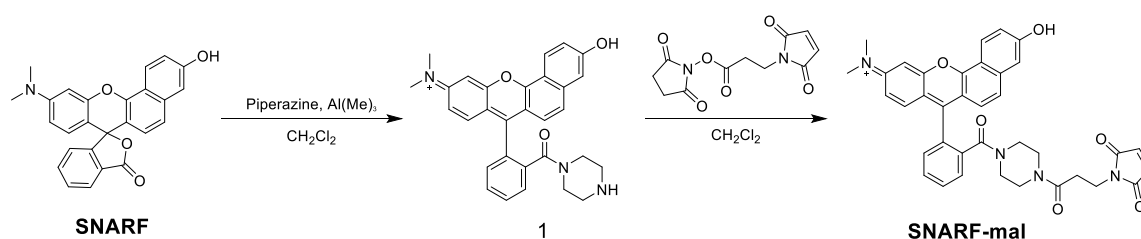
2.4.12.2 Synthesis of compound 1[51]

1.4 M trimethylaluminium in hexane (731 µL, 1.02 mmol) was added dropwise into a solution of piperazine (88 mg, 1.28 mmol) in CH$_2$Cl$_2$ (5 mL) and the solution was stirred at room temperature. After 1 h, SNARF (104 mg, 0.25 mmol) dissolved in CH$_2$Cl$_2$ (20 mL) was added dropwise. After stirring for 2 h under reflux, the reaction

solution was placed on ice bath and 0.1 M HCl was added dropwise until no gas was generated. The solution was filtered and the residue was washed twice by CH_2Cl_2 (25 mL) and once by CH_2Cl_2/MeOH (4: 1, 25 mL). The filtrate was concentrated and the residue was dissolved in CH_2Cl_2, the mixture was then filtered to remove insoluble salts and concentrated again. The resulting solid was dissolved in chloroform and washed by water. After concentration, the crude products were purified by column chromatography on amino-bonded silica gel [$CHCl_3$/MeOH: a linear gradient from 1: 0 to 10: 1 (*v/v*)] to give compound **1** in 48% yield (58 mg). ^{1}H NMR (600 MHz; DMSO): δ 8.72 (d, 1H, J_H = 9.0 Hz, Ar-H), 7.75 - 7.64 (m, 4H, Ar-H), 7.52 (d, 1H, J_H = 9.1 Hz, Ar-H), 7.37 - 7.28 (m, 5H, Ar-H), 7.09 (d, 1H, J_H = 9.0 Hz, Ar-H), 3.63 (s, 2H, CH_2), 3.32 - 3.27 (m, 8H, CH_2 and 2(CH_3)), 2.99 (s, 2H, CH_2), 2.84 (s, 2H, CH_2). ESI-TOF-MS *m/z* = 478.17 [M+H]$^+$ (calcd. for $C_{30}H_{28}N_3O_3$, 478.21).

2.4.12.3 Synthesis of SNARF-mal

Compound **1** (30 mg, 0.06 mmol) was dissolved in CH_2Cl_2 (5 mL). *N*-Succinimidyl 3-maleimidopropionate (33 mg, 0.12 mmol) and trimethylamine (18 μL, 0.12 mmol) were added to the solution. After stirring for 2 h, CH_2Cl_2 was removed and the crude was purified by a reverse phase column chromatography (ODS, H_2O/MeOH: a linear gradient from 9: 1 to 1: 9 (*v/v*)), then by HPLC (column: ULTRON VX-ODS ODS 20 mm × 150 mm / mobile phase 0.05% TFA with 33% to 45% acetonitrile) to give SNARF-mal in 17% yield (6.5 mg). ^{1}H NMR (600 MHz; Acetone-d6): δ 8.57 (d, 2H, J_H = 9.0 Hz, Ar-H), 7.71 - 7.68 (m, 3H, Ar-H), 7.59 (s, 1H, Ar-H), 7.52 (t, 1H, J_H = 4.5 Hz, Ar-H), 7.45 - 7.37 (m, 5H, Ar-H), 7.16 (d, 1H, J_H = 8.9 Hz, Ar-H), 6.70 (s, 2H, CH=CH), 3.52 - 3.16 (m, 16H, 5(CH_2), N(CH_3)$_2$), 2.45 (s, 2H, CH_2). ESI-TOF-MS *m/z* = 629.19 [M+H]$^+$ (calcd. for $C_{37}H_{33}N_4O_6$, 629.24).

2.4.12.4 Preparation of ODN-SNARF

Tris(2-carboxyethyl) phosphine (TCEP) was used to deprotect a thiol-modified oligo DNA (ODN-thiol, the sequence was shown in Table 2.5) at 30 °C for 1 h, then the mixture was first purified by the Bio-spin® 6 column with 50 mM PB buffer (pH 6.5), the concentration of oligo was measured by Nanodrop at 260 nm using the extinction coefficient (189600 $M^{-1}cm^{-1}$) of ODN-thiol. A coupling reaction between deprotected ODN-thiol and SNARF-mal was carried out by incubating ODN-thiol (100 µM) with SNARF-mal (500 µM) at 30 °C for overnight. Firstly, the reaction mixture was purified by Bio-spin® 6 column with 50 mM PB buffer (pH 8.0). Then, ODN-SNARF was purified by reversed-phase HPLC on a Cosmosil 5C18-MS II column (4.6 mm × 150 mm, elution with 100 mM triethylammonium acetate buffer, pH 7.0, linear gradient over 25 min from 30% to 80% acetonitrile at flow rate of 1.0 mL/min). ODN-SNARF was characterized by MALDI-TOF mass spectrometry (AXIMA-LNR, Shimadzu, HPA matrix). ODN-SNARF *m/z* calcd 6960, found 6960.

Table 2.5. Nucleotide sequence for the thiol modified ODN

Oligo DNA	Sequence (from 5' to 3')
ODN-thiol	**Thiol** – GGATTCGGCTCTTCAGCGAA

2.4.12.5 Preparation of sSNARF-n and sSNARF-f

ODN-SNARF was used for the further conjugation with DNA scaffold via hybridization with the protruding complementary sequence (ODN sequences were shown in Table 2.6). DNA scaffold was designed with 9 attachment sites (protruding single-stranded DNA) for the hybridization of the above prepared ODN-SNARF. In brief, ODN-SNARF was included at a molar ratio of 1:1.2 (SNARF binding sites: ODN-SNARF) in the annealing process of DNA scaffold for the hybridization.

Table 2.6. Nucleotide sequences incorporated in DNA scaffold used for the hybridization with ODN-SNARF

Oligo DNA	Sequence (from 5' to 3')
3SR-37-out1	GAAGCCCTACATACTTCGCTGAAGAGCCGAATCCTAATAATAA
3SR-36-in1	TTCGCTGAAGAGCCGAATCCATAAAGGATATGGT
4SR-37-out2	AAGCAGATATGTTATTCGCTGAAGAGCCGAATCCTAATAATAA
4SR-36-in2	TTCGCTGAAGAGCCGAATCCGCAAACGGACAAAA
5SR-37-out3	TACCAGATTAAGACTTCGCTGAAGAGCCGAATCCTAATAATAA
5SR-36-in3	TTCGCTGAAGAGCCGAATCCTCCTTATCGATTGA
3WX-46-out4	AATCGCATAGAATCTTCGCTGAAGAGCCGAATCCTAATAATAA
3WX-47-in4	TTCGCTGAAGAGCCGAATCCCTTGAAAATTTGAA
4WX-46-out5	TGTAAATGATAGCTTTCGCTGAAGAGCCGAATCCTAATAATAA
4WX-47-in5	TTCGCTGAAGAGCCGAATCCTAGATTATTAATTA
6WX-46-out6	AGGTTGGGAGAAGATTCGCTGAAGAGCCGAATCCTAATAATAA
6WX-47-in6	TTCGCTGAAGAGCCGAATCCGTCAATAACAAACA
3cb-57-out7	TCACGCATCAATCGTTCGCTGAAGAGCCGAATCCTAATAATAA
3cb-56-in7	TTCGCTGAAGAGCCGAATCCTCTGAAAACATTCT
4cb-57-out8	GCAATACGAAATACTTCGCTGAAGAGCCGAATCCTAATAATAA
4cb-56-in8	TTCGCTGAAGAGCCGAATCCCTACATTGAACCCT
5cb-57-out9	ATAACATGCAACAGTTCGCTGAAGAGCCGAATCCTAATAATAA
5cb-56-in9	TTCGCTGAAGAGCCGAATCCGAAAAACGTAAGAA

2.4.12.6 Preparation of SNARF-mal-ME

SNARF-mal (200 μM) was reacted with *β*-mercaptoethanol (200 μM) at 30 °C for 1 h in a 40 mM PB buffer (pH 6.5). The purity of SNARF-mal-ME was checked by reversed-phase HPLC with estimated purity of over 90%. SNARF-mal-ME was characterized by ESI-TOF-MS, SNARF-mal-ME *m/z* = 707.23 [M+H] [+] (calcd. for $C_{39}H_{38}N_4O_7S$, 706.81).

2.4.12.7 pH titration and fluorescence spectra measurement

Fluorescence emission spectra were measured by TECAN Infinite M Nano[+] by excitation at 534 nm in the 40 mM acetate, MES, HEPES or CHES buffer (pH 4.6 to 9.5). Fluorescence measurements were performed in the 96-plate [Greiner Microplate, 655906, 96-well, PS, F-bottom (chimney well) μCLEAR®, black, non-binding].

2.4.12.8 pKa values of SNARF-mal-ME, sSNARF-n and sSNARF-f

The dual-emission pH indicator follows a sigmoidal function described by equation (1).[52]

$$R = R_{min} + \frac{(R_{max} - R_{min})}{1 + 10^{pK_a - pH}} \qquad (1)$$

Where *R* is the ratio of fluorescence emission intensity at 600 nm over 652 nm (excited at 534 nm), R_{min} is the minimum ratio value (the ratio for the fully protonated form), R_{max} is the maximum ratio value (the ratio for the fully deprotonated form). The curves were fitted by Origin Pro 2018 (ver. 9.5) software using equation (1).

2.4.12.9 Estimation of local pH

The local pH near the surface or near the enzyme loaded position in the buffer (pH 7.0) was estimated by following methods.

For the local pH near the DNA scaffold surface, substitution of the estimated pK_a value of 7.1 for the SNARF derivative (sSNARF-n) and the pH of bulk solution (pH 7.0) to the equation (1) (Experimental methods) gave a ratio value ($R = 1.113$). This ratio value was then substituted to the above equation with the pK_a value of SNARF-mal-ME (6.3) to estimate the local pH near the DNA scaffold surface. The estimated pH at the location of sSNARF-f was obtained in a similar manner using the pK_a value of 6.8.

2.4.13. Enzyme reaction ZS-XR with various substrates

Enzyme reactions were carried out by 5 nM (monomer) free ZS-XR or sXR reacting with 500 μM NADH in the buffer (pH 7.0) containing 40 mM Tris-HCl, 20 mM acetic acid, 12.5 mM $MgCl_2$, 5 μM BSA, 0.002% Tween20, 1 μM $ZnCl_2$, 100 mM NaCl and 5% ethanol at 25 °C. The concentrations of substrates D-xylose, D,L-glyceraldehyde, 4-nitrobenzaldehyde, ethyl benzoylformate, and *o*-chloroacetophenone were 50 mM, 15 mM, 1 mM, 2 mM and 2 mM, respectively.

The measurement of kinetic parameters of free ZS-XR for substrate xylose was conducted at 25 nM ZS-XR and 300 μM NADH with the variation of xylose concentration from 25 mM to 500 mM. The kinetic parameters for substrate D,L-glyceraldehyde were measured at 20 nM ZS-XR and 500 μM NADH with the variation of D,L-glyceraldehyde concentration from 0.75 mM to 15 mM. The kinetic parameters for substrate 4-nitrobenzaldehyde were measured at 20 nM ZS-XR and 500 μM NADH with the variation of 4-nitrobenzaldehyde concentration from 10 μM to 2 mM. The kinetic parameters were obtained from Michaelis-Menten equation; the results were summarized in Table 2.2.

Table 2.7. Unmodified staple strands used for the assembly of the DNA origami scaffold

Oligo DNA	Sequence (from 5' to 3')
1	AAAATCCCTTATAATGCCAGCTGCATTACTCACTG
2	GATGGTGGTTCCGAGGCCAACGCGCGGGACTCACA
3	CAGCAGGCGAAAATGGTTTGCGTATTGGGGGTGCC
4	GAGAGTTTGAGACGGGCAACATCCACACAACATACGCTGTTT
5	TTTCTTTAAGCATAAAGTGTAGAATTCGTAATCATCTCTTCG
6	CCCGCTTACGGCCAGTGCCAAGCCAGGGTTTTCCCTGAGGGG
7	TTAATTGTGCCTGCAGGTCGAAAGGCGA
8	TAATGAGGGATCCCCGGGTACGGCGAAA
9	CTCAAGCCTGGCGCCAGTTTGCCC
10	ATAGAGCCGGTCACCAGGCAGCAA
11	CCTGTGTGGAAGGGCGATCGGAAAGCGC
12	TTAAGTTGGCCTCAGGAAGATTGGGATA
13	GGGGGATCAGCCAGCTTTCCGCAAACGG
14	CTATTACTTCTGGTGCCGGAACCGTCGG
15	ACGACGAAGATGGGCGCATCGGTTCTAGGATGAACGGTAA
16	CATTCGCTAAATGTGAGCGAGGCGTCTGATTCGCATTGTAAA
17	GGTCACGCCGGAGATCTGGAGGTACCCC
18	CGGATTGGAGAGATCTACAAAGTAATGT
19	ATTCTCCGAACGCCAATCAGCTTGTATA
20	GAGAATCCTGATAAGACAGTCAAATCACGGCAAAGAACA
21	CTGAGAGGGGTAGCAAAAGGGTGAGAAAAGCA
22	TATCAGGAAAGCCCCAAAAACGGGCGCGAATCGGTTGTACCATGCC
23	TGTTAAAGCCTTCCAAAATTTTTAGAACACTT
24	TCGTAAAACTAGCATGTCATAGCATTAATTAGCAAAATTAGGCC
25	GGTTGATCATCAATAAGCCTCAGAGCATAAG
26	AGCAAATGTTTAGCTATGACCCTGTAATCCT
27	CGTTAATTTCGCAACGGGAGA
28	GGAATTAATGTTGGTGTCAGTATCGGGTAACGCTTGCACGTTGCG
29	ATTCTATTTTTACCGTAACGCACTCGTGCTGCCTCTAGATGAGCTA
30	GTAGGTAAAAGCTAAGCTGAAGTGTCTGCCTTTAACAGA
31	TGACCAATAGGTGGGAAGCACCGCGCCAGCTCGAG
32	AATGCAAAAAACATTATATTTTATAACAACAGGTCCAAA
33	CATAATAATTCTAACAACACCAGGCTGCGGGCGGTC
34	ATATCTACTATAAATATAAGAGGTCTTT
35	TTGATGGTCACTGCGAACCAGACCCGAA
36	TCCATGCTGTGCTTAGAACCATAATTAA
37	CATGTTTATAGTAGATCATATCAAACAA
38	AAGTACGAAGGTGGAATCAGATCATTGC
39	CATTCCATCATTTGAGGAAGATCATTTTTTAAGGC
40	CCCAATTATAACCTATTTAAATTAAATTTTTGTTAATCAAAATATTTTA
41	AGCTTCAAAGCGAACGAGTAGATTTAGT
42	ATCAGGTCATTTTTGCGGATGAGCTCAA
43	ACCATTGAATAAGGAATGGTAGAAGACG
44	TTATAGTTTGCTCCTTTTGATGCAACTA
45	AGCGCGGAATAGAGCAATAACGGATAGT
46	ATTGCATAGGATTAGAGAGTAGAAGTTT
47	AAGGACTGGATCGTTTAATCTACGGTTT

48	GGAAGCCGGAAGCAAACTCCAGTTGATT
49	AGAGGGGTAAAAACCAAGTCAGGATTGTGAAAGATGAA
50	ACAAATGCAGAGATTTATCAGTGAAAATCAA
51	AAGTTTTGCCAGAGCTTCAAATATCGCG
52	ACGCCAACCCCCTCAAATGCTATCAAAA
53	CATAGTACGTCATAAATATTCCTGACTA
54	ATAACCCTAGCGTCCAATACTAAAGCGG
55	ACGATAATAGTAAATGTTTAATTAAGA
56	AGAAGAACCGGATATTCAGCGAAAACTTTTT
57	AAATCATCAAGAGTAATGAGGGTACAGAGGC
58	AATGGCGCATAGGCTGGGAACGAGCGACCTG
59	CCCATAAGGCTTGCCCTAGATTCAGAAGGCA
60	ACAAACACCAGAACGAGACAACATAAGAGGC
61	CCTTTGGGCTTGAGATGTTAATAAAAACACT
62	CCATTCAACTTTAATCACGTTGGGAGCGATT
63	CGGTGTATCATAAGGATAAAT
64	TTGAAAGAGGACTTACCTTATGCGATTTTAA
65	CATGAGGCCACTACTCAGTTGATACATA
66	TTTGAGGAAAACGATATTACATACGAGG
67	CTCCATGTACACTAAACGAACCACTATC
68	TGTGTCGGACCCCCAAGAAAACCAGACG
69	TTGTATCGCGCGAATATACCAAATAGCG
70	CGTAATGAAGTTTCTCGTCACGGAGTTA
71	CCAACCTACTAAAGGACAGCATTCGGTC
72	AAAAGAATTGGCTAGCAACACCGCCCAC
73	CATCTTTAAATCCGGCGCAGAGCCGACA
74	ATACCAAATCGCCTGGAACCGCAGCTTGATACCGATCGGTTT
75	GCTGAGGATAATAATTTTTTCAACAACT
76	GCATAACAAATCTCCAAAAAATTTCTGT
77	ATGACAACAAAAGGAGCCTTTTCCAGAC
78	GAATTTCTTAAAAACTGACCAACT
79	TAAAGGACGGAGTGAGAATAGACCCTCATTTTCAGGCCACCC
80	ATCAGCTGATCTAAAGTTTTGTGTAGCA
81	CAGATTGCGACTTGCAGCCTCAGCATTA
82	TTCAACAAAGCCCAATAGGAAAGAACCGCCACCCTTGAAACATGAAA
83	CTAACGTTGACGATATATCGGAACCTTG
84	ATGGGATACCGTAACACTGAGAGGTTTAGTACCGCGGCTGAG
85	GAATAAGGCTCCAACCATTTAGCCGCTGA
86	GTTAGTAACCAGTACAAACTAAGGTGTATCACCGTGGATTAGGATTA
87	TTCCACAGATATAAGTATAGC
88	CCGGAATCAACGCCTCGTCTTAATTGTATAGTTGCCGGTCAACAGA
89	ATTATTCCAGAACCGGATAGCGTTT
90	ATTAAGACACCCTCCCCATGTTTTG
91	AAGAGAAACTCAGGTTTCGTCAAT
92	ACAGGAGTGTACTGAATCCTCCTCCCTCCGGC
93	TGGCTTTGGAAAGCCAGAGCCCCTTATTCGTC
94	AGCCAGAACCCACCGTACAATGAATTATTTTCAAAGACGCAA
95	CAGCACCACCAATCAAGTAGCAAGAAAATTCTGGC
96	ATACAGAACCCAGACTGCACC

97	CCGCCACATTGACAGGAGGTTCGTATAA
98	TCAGAGCGTCAGACGATTGGCAGTGCCT
99	CCACCCTTTCACAAACAAATAGTAATAA
100	AAAATCACCGGAACGCAGTCTCTGAATT
101	ATTGGGAATTATTCAACTACGCAGTAGCCGAACAC
102	ATAGCCCACCACCGGAACCGCATTAAAG
103	AGTCGCCAAATAGAAAATTTTTAAGGTAATTTCCA
104	ACCAAGGTAAGGCATGAAGGAAACTTAGACGATAG
105	AGGTGAATTATCACAGCGTTTGCCATCT
106	TCAATAGGCCGGAAACGTCACATCAGTAGCGACAGCTCAGAG
107	TTACCAGAGCACCATTACCATTTTGCCTTTAGCGTGCCACCC
108	GGGCGACAGAGCCAGCAAAATTAGCGCGTTTTCATAGAGCCG
109	GGGAGGGGACTTGAGCCATTTTTCGGTC
110	AACATAGCTAGAGAGATCAGCCATCCTGAAT
111	AAGAACTATATTGACGGAAAT
112	GAAGAGTTAAATTTGCCCGAGCGT
113	AATAGCAATATAAAAGAAACGGTCACAA
114	GAAGCCCTACATACATAAAGGATATGGT
115	AAGCAGATATGTTAGCAAACGGACAAAA
116	TACCAGATTAAGACTCCTTATCGATTGA
117	CCTTGTTTAAAATCAAGATTAGTTTTCAATA
118	AATTGCACCCAGCTACAACGACGACGCCTGT
119	GATTTTTGAACAAACTTTCCTTATCATTCATTACC
120	AATGAAAGGAGAATCGGGTATTAAACCATTTT
121	CAGGCGGGAGGTTTTGATATAGAATTCATCG
122	TAAAGTTACAAAATAAAAACCCACCCTAATT
123	CTTACCAAGGTAAATAAGTCCTGAACAA
124	TATATTATTTATCCCAAGAGCGCTAACCAAT
125	GAACCTCTCTAAGAAACAAGCAAGCCGTAGTACCGAAGCGCACGAG
126	GCAAGCAGGGCTTAATTGAGAAAATAAGAATAAACAACTATA
127	TTATCAAATGTAGAAATATCATCTTACC
128	GCGCCCAGCTAATGCGGCTGTGTCAGAGGAAAAGT
129	TAGGAATCCAAGAATAACTGAACAAAGT
130	ATTGGCTTATTAAAGCCAACGCTCTCATAATTACTAGACCGGCTT
131	ATAATATCCCATAAGAATTACAATGA
132	TACGAGCCAATAGAGTAATTCAATTTAG
133	CAATAATCAGAACGCAATAAATATTTAA
134	GCAGAGGTTTAATGGTTTGAAGAACGCG
135	CAACGCCCCGTGTGATAAATACAAATCC
136	GCCACAACATGGCTATTTAAGAAAC
137	TTATACAAATTCTTTGTTTAG
138	GAAAACAGTAAATCAGAAGCCTTACGTCAAA
139	GCCACCAGTACCGGTATCCGACTTCCTTTAC
140	AGAAAACCGCTATTAATTAATGGAAACA
141	AATCGCATAGAATCCTTGAAAATTTGAA
142	TGTAAATGATAGCTTAGATTATTAATTA
143	AGGTTGGGAGAAGAGTCAATAACAAACA
144	CGTTTTTTCAACCTAAACATTTTCCGACAAAACGC
145	CCTAGACAAAATACCGAAACATGTTGTCCAGATTT

146	GTACATATTGAGTATGGCAATCTTCTGA
147	TTACCTTCGGAACAATATTCCAGAACCT
148	CATTTAAAGTTGCTCCTGAGAATTTGCA
149	TCAAGAAACAAAATGGAGAAAAAAGAAA
150	AAGAAGATTATTCAGTAACAGAGGTTTA
151	AGACAATTTCACATAGCGCTGATGAGGCGTTATC
152	TCGTTGAATAATAGATAATACATTATCAATACCAG
153	TACATCGCGCGCAGACTAATAGATTAGAAAATCAATTAA
154	GATTGTTTGGCCACGCTGAGA
155	ATAATGGATTAACACATCACCTTGCTGACTTT
156	ACCATATAACAGAGATATCAAACCCTCATGAGGATCACC
157	CGTAAAACGAACCATCTGGTCAGTTGGCGCCG
158	TTGCGTAATCGCCACAGTTGAAAGGAATACTA
159	CGACAACTCTAAAGCCGCCTGAAAAGGGTGGA
160	ACACATTTTGTTTTAATTTTC
161	TATTAGAACCTCAAGTGAGGCAGAGATATTGA
162	TCACCAAGTTAACAAAAAGACGCTGTTATATACCG
163	ACAAGGCGAATGATGAAGTGAATTTTAACCTAAAA
164	TAGGAGCTGAGGAAGATAGCCGCTATTAATCC
165	TGAAAAATCGTATTTAAAAGTAATCAATAAAT
166	CAGTGAAAGCGCTCATGTTCTTTGACAG
167	AAACACAGACAGCCATTCACTTGCTAGAATCTTAATGC
168	CAGTAATCAACAGTGATTATATCATCAATATAATCTTAATTTAAATCC
169	GGCCAACGGTCAGTAAGGGTTTGATTATCAGATGAACATTATAACAA
170	TCTGACCAAGATAACAAAATTGCGGAATTATCATCAAGAAACTTAGA
171	TACGTGGTACCGAACAGAAATCAATAACGGAT
172	TTGAATGCTAAAACGATTTTCTACCTTT
173	TTAAAGAGTCAGAATCCGGGCGCAGCCGGCGTTGTTC
174	CGCAATTAACTTTTAGAGTGTAGCGATTTAGAGTCCAC
175	AGATCAAACTCGTATAACGTACTA
176	GGCCACCGAGTATTTACATTGGCA
177	TCACGCATCAATCGTCTGAAAACATTCT
178	GCAATACGAAATACCTACATTGAACCCT
179	ATAACATGCAACAGGAAAAACGTAAGAA
180	GAAGAACACAATATTACCGCCAATATTT
181	GAGTAACCACGGAACCCGACTCCA
182	GAAAGCGAAAGGAGCTGAGAA
183	GCCGCGCAGAGCGGGAGCTAAATTAGTA
184	CAGGGCGCGTGCTTTCCTCGTCTGAGTA
185	CGGGGAATAGGGCGCTGGCAACAGGAACGGTACGCCTGTCCA
186	AGCCCCCGGTCACGCTGCGCGGCCGATTAAAGGGACGTTGTA
187	AGATAGGGTTGAGTGAACGTG
188	ACGTCAAAGGGCGATAAAGCACTAAATCCACACCC
189	TCTATCAGGGCGATTTTTTTGGGGTCGAGCCGCTA
190	TGAGTAACAGTGCCGAGG

Table 2.8. Nucleotide sequences of connecting hinges to stabilize the fully open state of DNA scaffold

Oligo DNA	Sequence (from 5' to 3')
Connecting hinge 1	ACATTGAATATATTTTAGTTTTTTACGAGAATG
Connecting hinge 2	ACATTGTCAGTGAGATTCACTTTTTCTGCCAGTT
Connecting hinge 3	ACATTGAATAAGAACCACGGTTTTAGGAACAAC

2.5. References

1. Di Cosimo, R., Mc Auliffe, J., Poulose, A. J. & Bohlmann, G. Industrial use of immobilized enzymes. *Chem. Soc. Rev.* **42**, 6437–6474 (2013).

2. Sheldon, R. A. Enzyme immobilization: the quest for optimum performance. *Adv. Synth. Catal.* **349**, 1289–1307 (2007).

3. Zhang, Y., Ge, J. & Liu, Z. Enhanced activity of immobilized or chemically modified enzymes. *ACS Catal.* **5**, 4503–4513 (2015).

4. Lim, S., Jung, G. A., Glover, D. J. & Clark, D. S. Enhanced enzyme activity through scaffolding on customizable self-assembling protein filaments. *Small* **15**, 1–11 (2019).

5. Tabaei, S. R., Rabe, M., Zetterberg, H., Zhdanov, V. P. & Höök, F. Single lipid vesicle assay for characterizing single-enzyme kinetics of phospholipid hydrolysis in a complex biological fluid. *J. Am. Chem. Soc.* **135**, 14151–14158 (2013).

6. Wang, Y. & Caruso, F. Mesoporous silica spheres as supports for enzyme immobilization and encapsulation. *Chem. Mater.* **17**, 953–961 (2005).

7. Lin, P. *et al.* Assembly of graphene oxide-formate dehydrogenase composites by nickel-coordination with enhanced stability and reusability. *Eng. Life Sci.* **18**, 326–333 (2018).

8. Virgen-Ortíz, J. J. *et al.* Polyethylenimine: a very useful ionic polymer in the design of immobilized enzyme biocatalysts. *J. Mater. Chem. B* **5**, 7461–7490 (2017).

9.   Rajendran, A., Nakata, E., Nakano, S. & Morii, T. Nucleic-acid-templated enzyme cascades. *ChemBioChem* **18**, 696–716 (2017).

10.   Rothemund, P. W. K. Folding DNA to create nanoscale shapes and patterns. *Nature* **440**, 297–302 (2006).

11.   Douglas, S. M. *et al.* Self-assembly of DNA into nanoscale three-dimensional shapes. *Nature* **459**, 414–418 (2009).

12.   Grossi, G., Dalgaard Ebbesen Jepsen, M., Kjems, J. & Andersen, E. S. Control of enzyme reactions by a reconfigurable DNA nanovault. *Nat. Commun.* **8**, (2017).

13.   Wilner, O. I. *et al.* Enzyme cascades activated on topologically programmed DNA scaffolds. *Nat. Nanotechnol.* **4**, 249–254 (2009).

14.   Ngo, T. A. *et al.* Protein adaptors assemble functional proteins on DNA scaffolds. *Chem. Commun.* **55**, 12428–12446 (2019).

15.   Zhao, Z. *et al.* Nanocaged enzymes with enhanced catalytic activity and increased stability against protease digestion. *Nat. Commun.* **7**, (2016).

16.   Rudiuk, S., Venancio-Marques, A. & Baigl, D. Enhancement and modulation of enzymatic activity through higher-order structural changes of giant DNA-Protein multibranch conjugates. *Angew. Chem., Int. Ed.* **51**, 12694–12698 (2012).

17.   Timm, C. & Niemeyer, C. M. Assembly and purification of enzyme-functionalized DNA origami structures. *Angew. Chem., Int. Ed.* **54**, 6745–6750 (2015).

18.   Lin, J. L. & Wheeldon, I. Kinetic enhancements in DNA-enzyme nanostructures mimic the sabatier principle. *ACS Catal.* **3**, 560–564 (2013).

19.   Zhang, Y., Tsitkov, S. & Hess, H. Proximity does not contribute to activity enhancement in the glucose oxidase-horseradish peroxidase cascade. *Nat. Commun.* **7**, (2016).

20.   Xiong, Y., Huang, J., Wang, S. T., Zafar, S. & Gang, O. Local environment affects the activity of enzymes on a 3D molecular scaffold. *ACS Nano* **14**, 14646–14654 (2020).

21.   Douglas, S. M., Bachelet, I. & Church, G. M. A logic-gated nanorobot for targeted transport of molecular payloads. *Science* **335**, 831–834 (2012).

22. Sander, B. & Golas, M. M. Visualization of bionanostructures using transmission electron microscopical techniques. *Microsc. Res. Tech.* **74**, 642–663 (2011).

23. Watanabe, S. *et al.* Ethanol production from xylose by recombinant *Saccharomyces cerevisiae* expressing protein-engineered NADH-preferring xylose reductase from *Pichia stipitis*. *Microbiology* **153**, 3044–3054 (2007).

24. Watanabe, S., Kodaki, T. & Makino, K. Complete reversal of coenzyme specificity of xylitol dehydrogenase and increase of thermostability by the introduction of structural zinc. *J. Biol. Chem.* **280**, 10340–10349 (2005).

25. Nakata, E., Dinh, H., Ngo, T. A., Saimura, M. & Morii, T. A modular zinc finger adaptor accelerates the covalent linkage of proteins at specific locations on DNA nanoscaffolds. *Chem. Commun.* **51**, 1016–1019 (2015).

26. Ngo, T. A., Nakata, E., Saimura, M. & Morii, T. Spatially organized enzymes drive cofactor-coupled cascade reactions. *J. Am. Chem. Soc.* **138**, 3012–3021 (2016).

27. Nguyen, T. M., Nakata, E., Saimura, M., Dinh, H. & Morii, T. Design of modular protein tags for orthogonal covalent bond formation at specific DNA sequences. *J. Am. Chem. Soc.* **139**, 8487–8496 (2017).

28. Nguyen, T. M. *et al.* Rational design of a DNA sequence-specific modular protein tag by tuning the alkylation kinetics. *Chem. Sci.* **10**, 9315–9325 (2019).

29. Ellenberger, T. E., Brandl, C. J., Struhl, K. & Harrison, S. C. The GCN4 basic region leucine zipper binds DNA as a dimer of uninterrupted α helices: crystal structure of the protein-DNA complex. *Cell* **71**, 1223–1237 (1992).

30. England, C. G., Luo, H. & Cai, W. HaloTag technology: a versatile platform for biomedical applications. *Bioconjug. Chem.* **26**, 975–986 (2015).

31. Eriksson, T., Börjesson, J. & Tjerneld, F. Mechanism of surfactant effect in enzymatic hydrolysis of lignocellulose. *Enzyme Microb. Technol.* **31**, 353–364 (2002).

32. Yang, B. & Wyman, C. E. BSA treatment to enhance enzymatic hydrolysis of cellulose in lignin containing substrates. *Biotechnol. Bioeng.* **94**, 611–617 (2006).

33. Whitaker, J. E., Haugland, R. P. & Prendergast, F. G. Spectral and photophysical studies of benzo[c]xanthene dyes: dual emission pH sensors. *Anal. Biochem.* **194**,

330–344 (1991).

34. Nakata, E. *et al.* A newly designed cell-permeable SNARF derivative as an effective intracellular pH indicator. *Chem. Commun.* **46**, 3526–3528 (2010).

35. Nakata, E. *et al.* A novel strategy to design latent ratiometric fluorescent pH probes based on self-assembled SNARF derivatives. *RSC Adv.* **4**, 348–357 (2014).

36. Chen, X., Zhou, Y., Peng, X., & Yoon, J. Fluorescent and colorimetric probes for detection of thiols. *Chem. Soc. Rev.* **39**, 2120-2135 (2010).

37. Langmuir, M. E., Yang, J. R., Moussa, A. M., Laura, R., & LeCompte, K. A. New naphthopyranone based fluorescent thiol probes. *Tetrahedron Lett.* **36**, 3989-3992 (1995).

38 Torrie, G. M., Kusalik, P. G. & Patey, G. N. Molecular solvent model for an electrical double layer: reference hypernetted-chain results for ion behavior at infinite dilution. *J. Chem. Phys.* **89**, 3285–3294 (1988).

39. Bérard, D. R., Kinoshita, M., Cann, N. M. & Patey, G. N. Structure of the metal-aqueous electrolyte solution interface. *J. Chem. Phys.* **107**, 4719–4728 (1997).

40. Kinoshita, M. Water structure and phase transition near a surface. *J. Solution Chem.* **33**, 661–687 (2004).

41. Kratzer, R. *et al.* Enzyme identification and development of a whole-cell biotransformation for asymmetric reduction of *o*-chloroacetophenone. *Biotechnol. Bioeng.* **108**, 797–803 (2011).

42. Kratzer, R., Wilson, D. K. & Nidetzky, B. Catalytic mechanism and substrate selectivity of aldo-keto reductases: insights from structure-function studies of *Candida tenuis* xylose reductase. *IUBMB Life* **58**, 499–507 (2006).

43. Drummond, C., Pérez-Fuentes, L. & Bastos-González, D. Can polyoxometalates be considered as superchaotropic ions? *J. Phys. Chem. C* **123**, 28744–28752 (2019).

44. Collins, K. D. Ions from the Hofmeister series and osmolytes: efects on proteins in solution and in the crystallization process. *Methods* **34**, 300–311 (2004).

45. Verduyn, C. *et al.* Properties of the NAD(P)H-dependent xylose reductase from the xylose-fermenting yeast *Pichia stipitis*. *Biochem. J.* **226**, 669–677 (1985).

46. Ehrensberger, A. H., Elling, R. A. & Wilson, D. K. Structure-guided engineering of xylitol dehydrogenase cosubstrate specificity. *Structure* **14**, 567–575 (2006).

47. Ngo, T. A., Nakata, E., Saimura, M., Kodaki, T. & Morii, T. A protein adaptor to locate a functional protein dimer on molecular switchboard. *Methods* **67**, 142–150 (2014).

48. Douglas, S. M. *et al.* Rapid prototyping of 3D DNA-origami shapes with caDNAno. *Nucleic Acids Res.* **37**, 5001–5006 (2009).

49. Amir, Y. *et al.* Universal computing by DNA origami robots in a living animal. *Nat. Nanotechnol.* **9**, 353–357 (2014).

50. Han, J. & Burgess, K. Fluorescent indicators for intracellular pH. *Chem. Rev.* **110**, 2709–2728 (2010).

51. Nguyen, T. & Francis, M. B. Practical synthetic route to functionalized rhodamine dyes. *Org. Lett.* **5**, 3245–3248 (2003).

52. Benjaminsen, R. V. *et al.* Evaluating nanoparticle sensor design for intracellular pH measurements. *ACS Nano* **5**, 5864–5873 (2011).

CHAPTER 3

Dynamic shape transformation of a DNA scaffold and its application for an enzyme nanocarrier

3. 1. Introduction

Enzymes are spatially organized in the cell to implement specific sequential reactions in the compartments, such as membrane-bound organelles, bacterial microcompartments, and multi-enzyme complexes.[1] Organization of such enzyme complexes often relies on the specific scaffolds of proteins or membrane to achieve the high efficiency and the specificity of enzymatic reactions.[2,3] Typical examples are found in the enzymes ribulose 1,5-bisphosphate carboxylase/oxygenase (RuBisCO) and carbonic anhydrase (CA) packed in carboxysome,[4] plant cytochrome P450 enzymes on the endoplasmic reticulum (ER) membrane,[5] and electron transport complexes arranged on the cyanobacterial thylakoid membrane.[6] Inspired by the nature systems, individual- or multi-enzyme have been encapsulated into a wide range of materials such as proteins,[7] lipid vesicles[8] and polymers.[9] However, applications of these carriers were limited due to the low enzyme loading yields and the difficulty in controlling the accurate locations and stoichiometry of enzymes. These obstacles were tackled by DNA nanotechnology. A typical example of DNA nanostructures, DNA origami,[10,11] folds a long single-stranded DNA into predesigned addressable 2D and 3D DNA structures through the hybridization of appropriate staple strands and provides ideal platforms for the assembly of various functional macromolecules.[12] Besides the static DNA structures, dynamic DNA structures induced by the hybridization of short DNA,[13] aptamer switches,[14] temperature[15] or pH[16] changes were constructed to exhibit controlled translational or rotational movement, providing a great potential for applications in drug delivery, biosensing and biocatalysis.[17]

The dynamic DNA devices for enzymes assembly have been constructed by altering the solution temperature,[18] pH,[19] or ion concentrations.[20] However, the variation of these factors at the same time modulates the enzyme activity and affects the stability of DNA origami, which was only applicable to the enzyme with high stability, such as

HRP. Compared to these external stimuli, the dynamic shape transformation triggered by the DNA hybridization, or the DNA fuels, would impact on the enzyme activity to a much lower extent, providing broader applications in biocatalysts. On the other hand, such DNA-fueled DNA origami devices faced the drawbacks of low enzyme loading yields[21] and less controllable spatial arrangements of enzymes,[22] limiting their application for a wide range of enzymes.[23] Therefore, there is still a demand on the design of reconfigurable DNA nanocarrier that enables the efficient shape transformation and the high enzyme encapsulation yield without showing a harmful effect on the enzyme activity.

In this chapter, a 3D DNA scaffold[24] was constructed to enable an efficient dynamic shape transition and applied for encapsulation of an enzyme xylitol dehydrogenase (XDH). The closing process was monitored by the changes of fluorescence resonance energy transfer (FRET)[25] with the variation in linker concentrations and hybridization temperatures. Typically, the DNA scaffold in open state was transformed to its closed state in over 90% yield at a 1:1 molar ratio of DNA scaffold to linkers at 25 ℃ for 12-h. This condition was applied for the encapsulation of enzyme. XDH was first assembled on the DNA scaffold in open state with a high enzyme loading yield, followed by the addition of the DNA closing keys to transform to the closed 3D scaffold. The enzyme encapsulated in the closed state exerted an activity comparable to that in the open state, ensuring that the catalytic activity of enzyme was maintained during the shape transformation process and upon encapsulation in the 3D DNA scaffold. The 3D DNA nanostructure with dynamic shape transformation would be applicable for the in vitro model of cellular dynamic process and the design of drug delivery, biosensing, biocatalytic and diagnostic tools.

3.2. Results and discussions

3.2.1. One-step folding and characterization of the open and closed states of 3D DNA scaffold

The open and closed states of a 3D DNA hexagonal prism (HP)[24] were constructed in one-step by DNA origami,[10,11] which consisted of two domains covalently attached in the rear by single-stranded scaffold hinges with a dimension of 35 nm × 35 nm × 45 nm in the closed state. Six types of single-stranded DNA linkers that hybridize with the complementary sequences spanning at both the edges of top and bottom domains of DNA scaffold were designed to fold the two domains together in the closed state (HPC). The six positions complementary to the linker sequences were left unhybridized for the open state (HPO) of DNA scaffold (Figure 3.1).
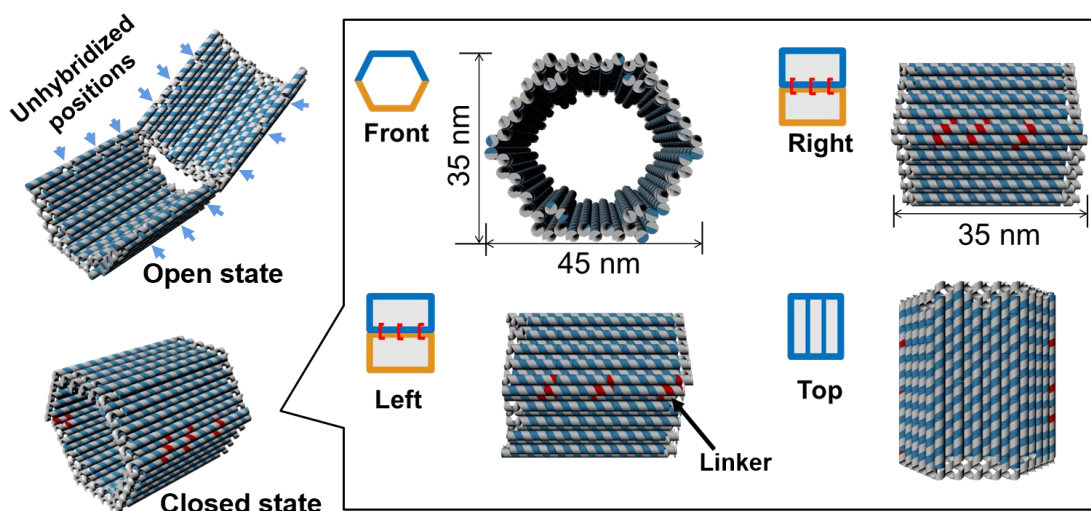
Figure 3.1. Scheme of DNA scaffold in open and closed states (HPO and HPC), the dimensions and different views of closed state were shown in the box.

The resulting DNA scaffolds HPC and HPO were purified by size exclusion chromatography (Sephacryl S-400) to remove the excess staple strands and characterized by means of atomic force microscopy (AFM) (Figure 3.2). HPC and HPO displayed comparable width, while the height of HPC was twofold of HPO. The well-formed yields of open and closed states were estimated to be 92% (276/300) and 96%

(600/624) by AFM images, respectively. The closed structures were easily, but systematically, broken by AFM cantilever during the measurement as illustrated in Figure 3.3, thus the systematically broken structures were counted as the closed structures. From the observation of transmission electron microscopy (TEM) images, the well-formed yield of HPC was estimated to be 92% (187/203). The sizes of HPO in TEM images were 69.7 ± 4.8 nm in length and 43.5 ± 4.2 nm in width, and HPC in rectangular form were 35.4 ± 1.7 nm in length and 46.2 ± 1.3 nm in width. The measured width and height of HPC in hexagonal form (front view) were 43.4 ± 2.7 nm and 33.8 ± 2.7 nm, respectively, which were well consistent with the designed dimensions (Figure 3.4).
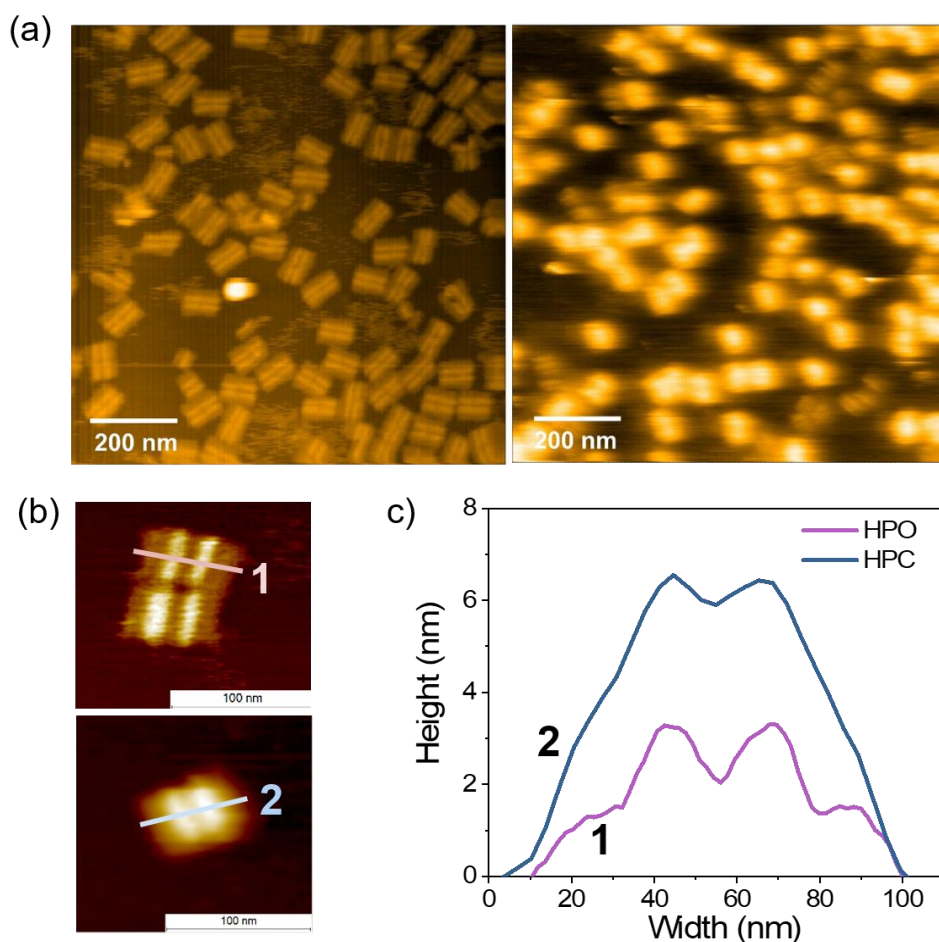
Figure 3.2. AFM images of DNA scaffolds and height analyses. (a) AFM images of DNA scaffold, scale bar: 200 nm. Left: open state; right: closed state. (b) Typical AFM images of DNA scaffold, scale bar: 100 nm. Top: open state; bottom: closed state. (c) Height analyses of DNA scaffold in open and closed states from (b).
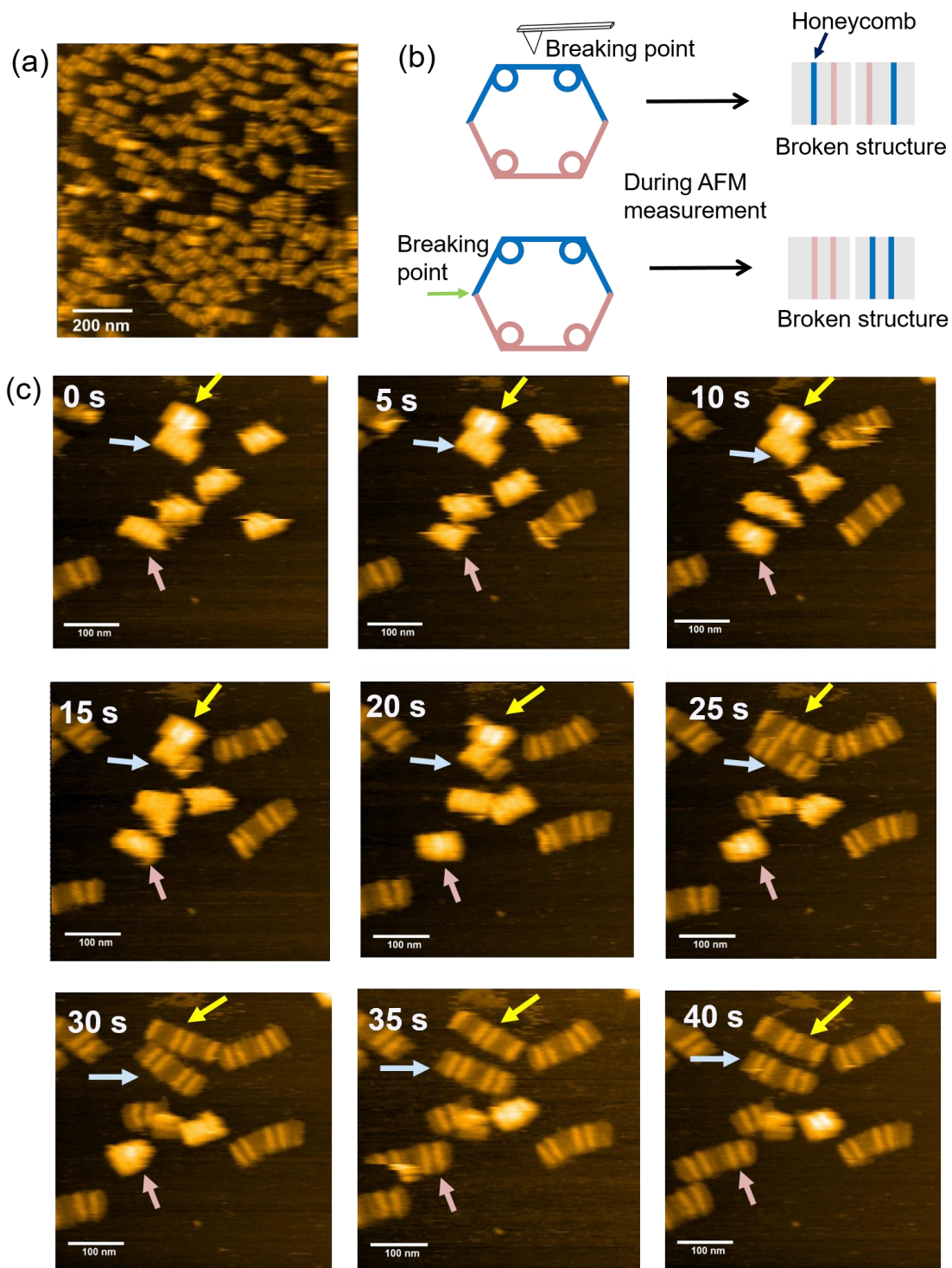
Figure 3.3. DNA scaffold in closed state broken by cantilever when measured by AFM. (a) Typical AFM image of HPC broken by cantilever when measured by AFM, scale bar: 200 nm. (b) Scheme presenting the breaking points and the resulting broken structures. (c) The process of AFM cantilever breaking the closed structures during measurement, scale bar: 100 nm. The arrows showed typical examples of the broken process.
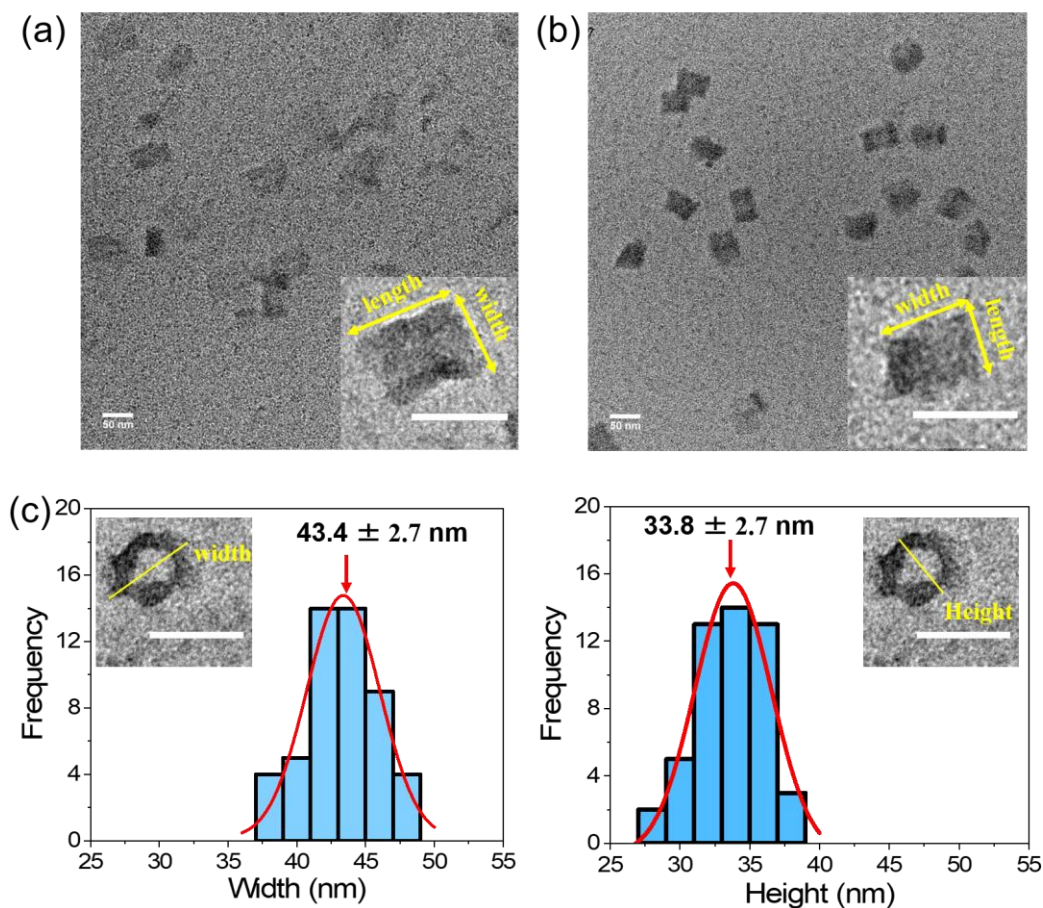
Figure 3.4. TEM analyses of DNA scaffold in open and closed states. (a) TEM image of open state HPO, scale bar: 50 nm. The enlarged typical HPO was shown inset, scale bar: 50 nm, the measured length and width were 69.7 ± 4.8 nm and 43.5 ± 4.2 nm, respectively. (b) TEM image of HPC, scale bar: 50 nm. The enlarged typical HPC was shown inset, scale bar: 50 nm. The measured length and width of HPC in rectangular form were 35.4 ± 1.7 nm and 46.2 ± 1.3 nm, respectively. (c) Size measurement of HPC in hexagonal form (front view), the measured width and height were 43.4 ± 2.7 nm and 33.8 ± 2.7 nm, respectively. The typical TEM image was shown inset, scale bar: 50 nm.

Fluorescence resonance energy transfer (FRET)[25] for each state was investigated to further identify the open and closed states of DNA scaffold. As shown in Figure 3.5a, a pair of Cy3 (donor fluorophore) and Cy5 (acceptor fluorophore) was attached at the edge of each domain of DNA scaffold with the theoretical distance of 25 nm in the fully open state and within 1 nm in the closed state. Fluorescence emission spectra of HPO (curve in green) and HPC (curve in red) upon the donor excitation (λ_{ex}

= 520 nm) at 25 °C were shown in Figure 3.5b. The primary fluorescence emission of donor (Cy3) alone at 570 nm in the open state indicated the far distance of two fluorophores, while the dominant peak at 670 nm in the closed state, corresponding the acceptor (Cy5) fluorescence emission, implied the efficient energy transfer between two dyes in the closed state.

The difference in the efficiency of FRET for both the states was also supported by the agarose gel electrophoretic analyses. The band corresponding to the open state showed a stronger band intensity than the closed state in the Cy3 channel ($\lambda_{ex} = 532$ nm, $\lambda_{em} = 605$ nm), conversely, the band corresponding to the closed state exhibited a stronger band intensity than the open state in the FRET channel ($\lambda_{ex} = 532$ nm, $\lambda_{em} = 695$ nm) under the gel scanner. Notably, HPC migrated faster than HPO possibly due to its compact closed structure (Figure 3.6).
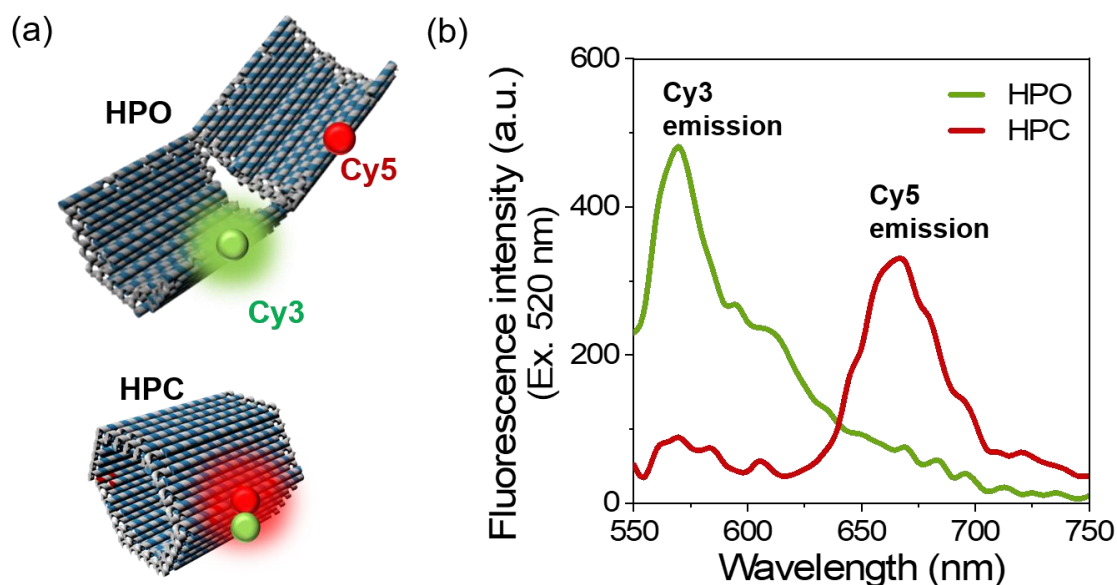
Figure 3.5. FRET analyses of DNA scaffold in open and closed states. (a) Scheme presenting the attachment sites of fluorophores Cy3 (donor, indicated in green) and Cy5 (acceptor, indicated in red) on open and closed states of DNA scaffold. (b) Fluorescence emission spectra of open and closed states of DNA scaffold excited at 520 nm, conditions: 5 nM HPO or HPC was scanned in the buffer (pH 7.0) containing 40 mM Tris-HCl, 20 mM acetic acid, 12.5 mM MgCl$_2$ and 0.002% Tween20 at 25 °C.
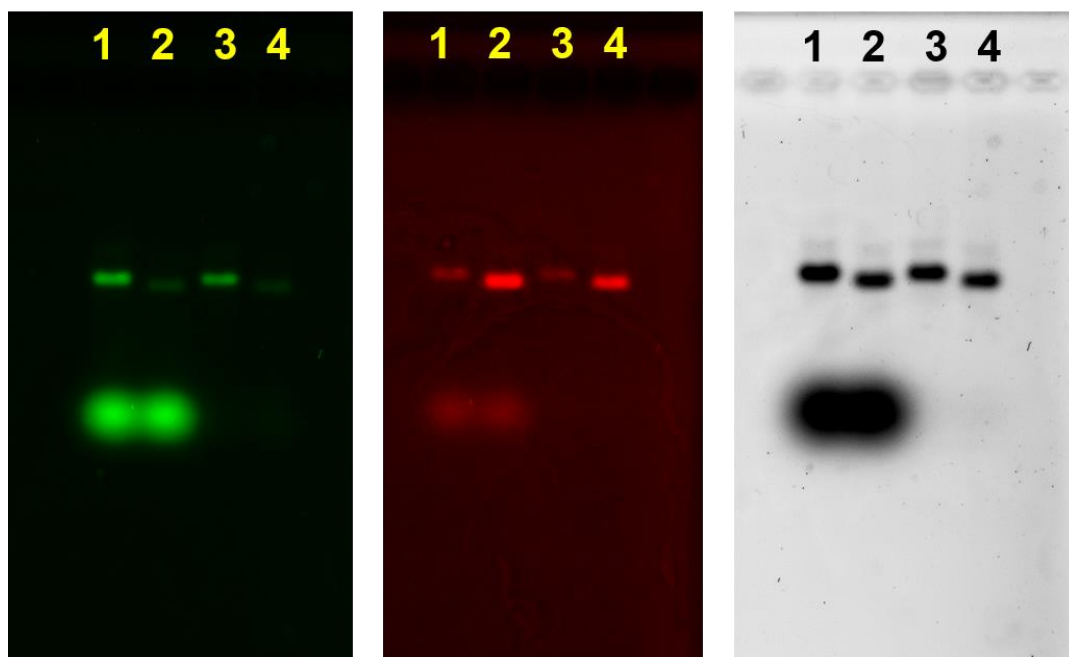
Figure 3.6. Agarose gel electrophoretic analyses of DNA scaffolds. Left: Cy3 channel (λ_{ex} = 532 nm, λ_{em} = 605 nm); middle: FRET channel (λ_{ex} = 532 nm, λ_{em} = 695 nm); right: EtBr channel (λ_{ex} = 532 nm, λ_{em} = 605 nm); Lane 1: Open state (HPO) before purification; Lane 2: Closed state (HPC) before purification; Lane 3: HPO after S-400 purification; Lane 4: HPC after S-400 purification. Agarose gel electrophoresis conditions: 1% agarose gel in $1 \times$ TAE (pH 8.0) containing 12.5 mM $MgCl_2$ at 50 V for 6 h.

3.2.2. Dynamic shape transformation from the open to closed state initiated by DNA linkers hybridizing to the two domains of DNA scaffold

The shape transformation of DNA scaffold from the open state (HPO) to the closed state (HPC) was initiated by an addition of six types of single-stranded short DNA strands (linkers) that hybridized to both the facing edges of two domains of the DNA scaffold (Figure 3.7a). FRET was used to trace the closing process (Figure 3.7b). The authentic open and closed states were prepared separately to apply for the control samples of HPO and HPC (HPO-control and HPC-control), respectively. The molar ratio of HPO to the DNA linkers was varied to investigate the efficiency of converting HPO to HPC. To study the closing kinetics, the time-course of fluorescence intensity change of 12-h was monitored. Upon addition of the DNA linkers, the Cy3 fluorescence

intensity (λ_{em} = 570 nm) was decreased with the increase of Cy5 fluorescence intensity (λ_{em} = 670 nm) when excited at 520 nm (Figure 3.8a and Figure 3.8b). The closing efficiency was estimated from the Cy5 fluorescence intensity in the fluorescence emission spectra after 12-h hybridization at 25 ℃ (Figure 3.8c). The optimal molar ratio (HPO: linkers) was found at 1:1, where the yield of closed state reached 91% at 25 ℃ for 12-h. In the molar ratio of 1:0.5, 1:2, 1:5 and 1:10, the closing yields were reduced to 62%, 76%, 69% and 61%, respectively (Figure 3.8d). With the higher molar ratio, the closing yield was lowered because each of the hybridizing sites in two domains was occupied by different molecules of the closing linker, and not shared by a single closing linker (Figure 3.9).
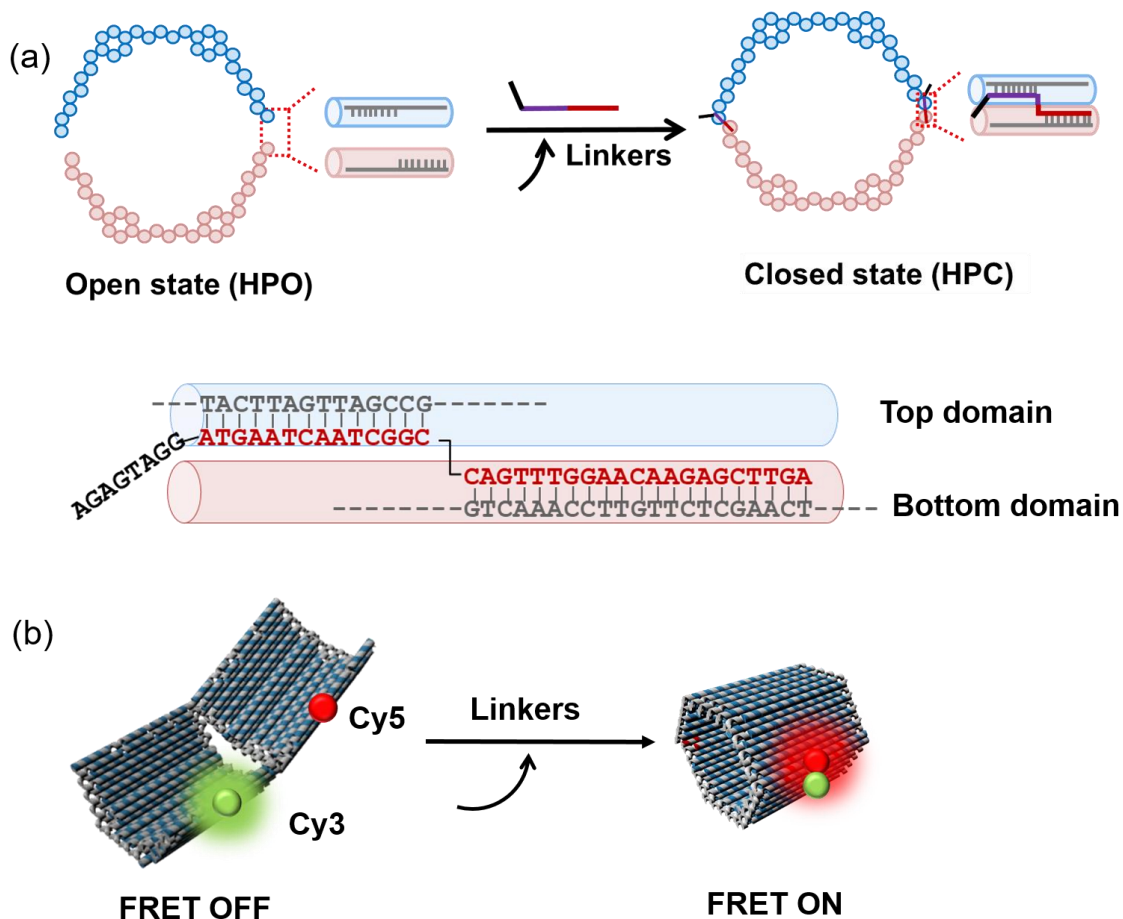
Figure 3.7. Scheme showing the closing process of DNA scaffold. (a) Scheme presenting one of the linkers hybridizing with the two domains of DNA scaffold. The cylinders indicated DNA helices, the sequences in grey, red and black indicated M13mp18 template sequence, linker sequence and the 8-based toehold of linker. (b) The closing process traced by FRET.
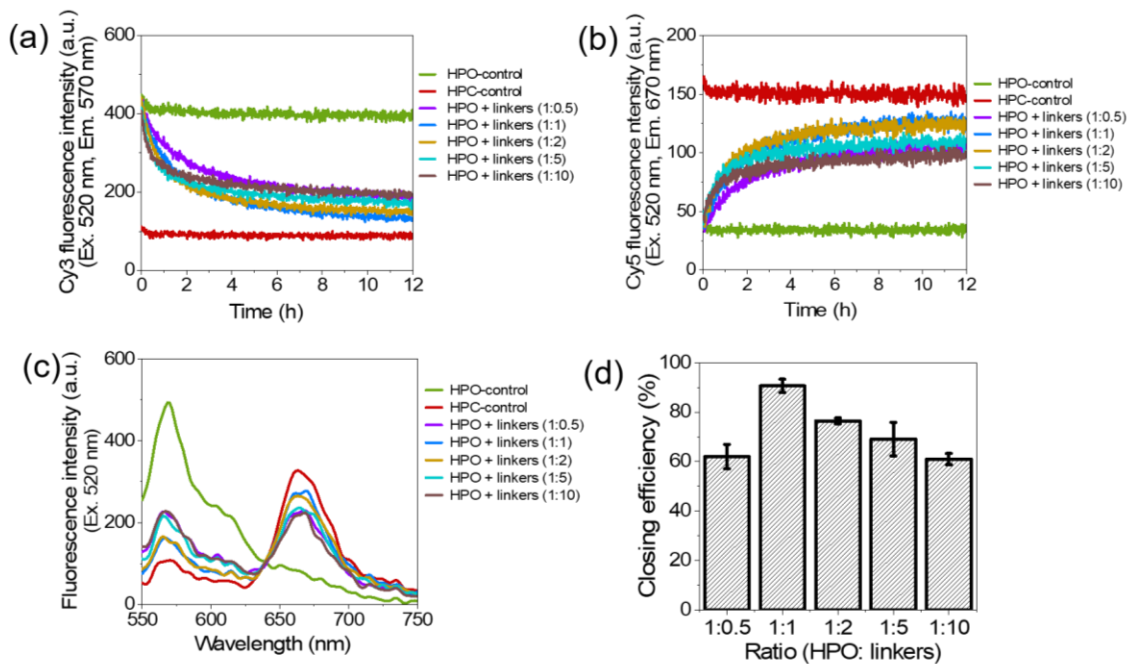
Figure 3.8. The effect of molar ratio (HPO: linkers) on closing efficiency. (a) Time course of the Cy5 fluorescence intensity (λ_{ex} = 520 nm, λ_{em} = 670 nm) during the closing process at various molar ratio of linkers. (b) Time course of the Cy5 fluorescence intensity (λ_{ex} = 520 nm, λ_{em} = 670 nm) in the closing process with various molar ratio of linkers. (c) Fluorescence emission spectra (λ_{ex} = 520 nm) after incubation for 12-h with various molar ratios of linkers. (d) Effect of molar ratio of HPO to linkers (HPO: linkers) on the closing efficiency. Hybridization conditions: 5 nM HPO was incubated with 2.5 nM to 50 nM linkers in the buffer (pH 7.0) containing 40 mM Tris-HCl, 20 mM acetic acid, 12.5 mM $MgCl_2$ and 0.002% Tween 20 at 25 ℃ for 12 h. Data in (d) were the averages of three independent repetitions, error bars indicated the S.D. of the repetitions.
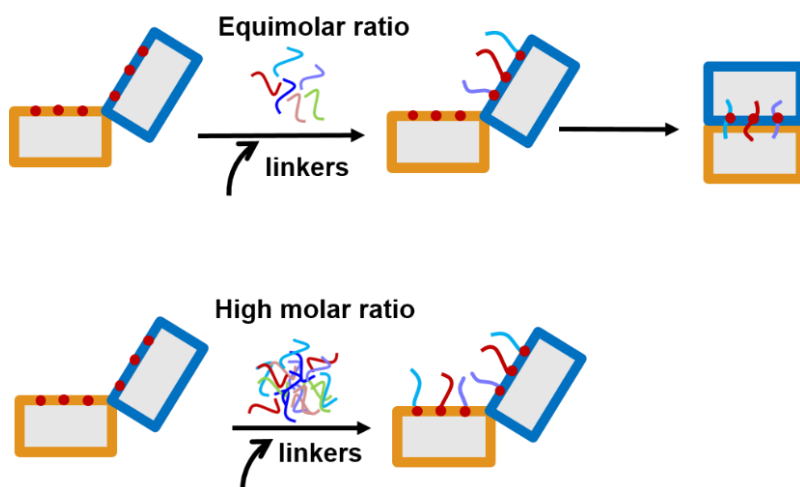
Figure 3.9. Scheme presenting the effect of molar ratio of DNA scaffold to linkers on the closing efficiency. In equimolar ratio, linkers were able to hybridize with of both domains and

100

reached high closing efficiency, by contrast, in high molar ratio, the binding sites of both domains were saturated with the linkers, the low closing yield was obtained. The red circles on DNA scaffold indicated the positions to hybridize with the linkers.

The kinetics of closing process with various molar ratio of DNA scaffold to linkers were investigated. The half time ($t_{1/2}$) for shape transformation was estimated from the time-course changes of Cy5 fluorescence intensity (Figure 3.8b and Figure 3.10a). Interestingly, $t_{1/2}$ gradually decreased with the molar ratio changed from 1:0.5 (105 min) to 1:2 (64 min) and kept in the similar value with 1:5, then slightly increased at 1:10 (68 min) (Figure 3.10b). These results suggested that the increase of molar ratio to a certain range enhanced the hybridization kinetics of closing process, but at the same time, impeded the yield of closed state. The result was consistent with the previous report that reducing the DNA concentration decreased the rate of duplex formation in DNA hybridization process.[26]
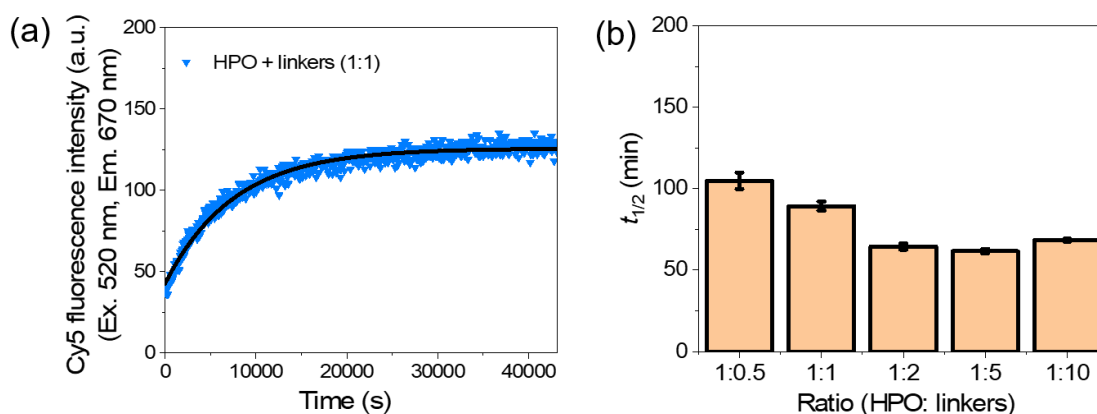
Figure 3.10. Kinetics of closing process induced by linkers. (a) Time course of Cy5 fluorescence intensity (λ_{ex} = 520 nm, λ_{em} = 670 nm) at the hybridization conditions: 5 nM HPO hybridized with 5 nM linkers at 25 °C in the buffer (pH 7.0) containing 40 mM Tris-HCl, 20 mM acetic acid, 12.5 mM MgCl$_2$ and 0.002% Tween20. The exponential curve fitting was conducted by Origin Pro 2018 (ver. 9.5) using one-phase function. (b) Half time ($t_{1/2}$) values of the closing process with different molar ratio (HPO: linkers) at 25 °C shown in Figure 3.8(b). Data in (b) were the averages of three independent repetitions, error bars indicated the S.D. of the repetitions.

The closing yield estimated from the fluorescence intensity was supported by AFM analyses of these samples (Figure 3.11). As described in Figure 3.3, the closed structures were easily, but systematically, broken by AFM cantilever during the measurement. The broken structures were counted as the closed structures. After 12-h incubation or hybridization at 25 °C, the percentages of closed structures of HPC-control, HPO + linkers (1:0.5), HPO + linkers (1:1), HPO + linkers (1:2) and HPO + linkers (1:5) were estimated to be 96% (624 closed structures/total of 650 structures), 73% (124/169), 86% (174/203), 81% (116/143), and 75% (103/138) by AFM images, respectively (Figure 3.11). These yields were consistent with the results obtained from the FRET analyses.
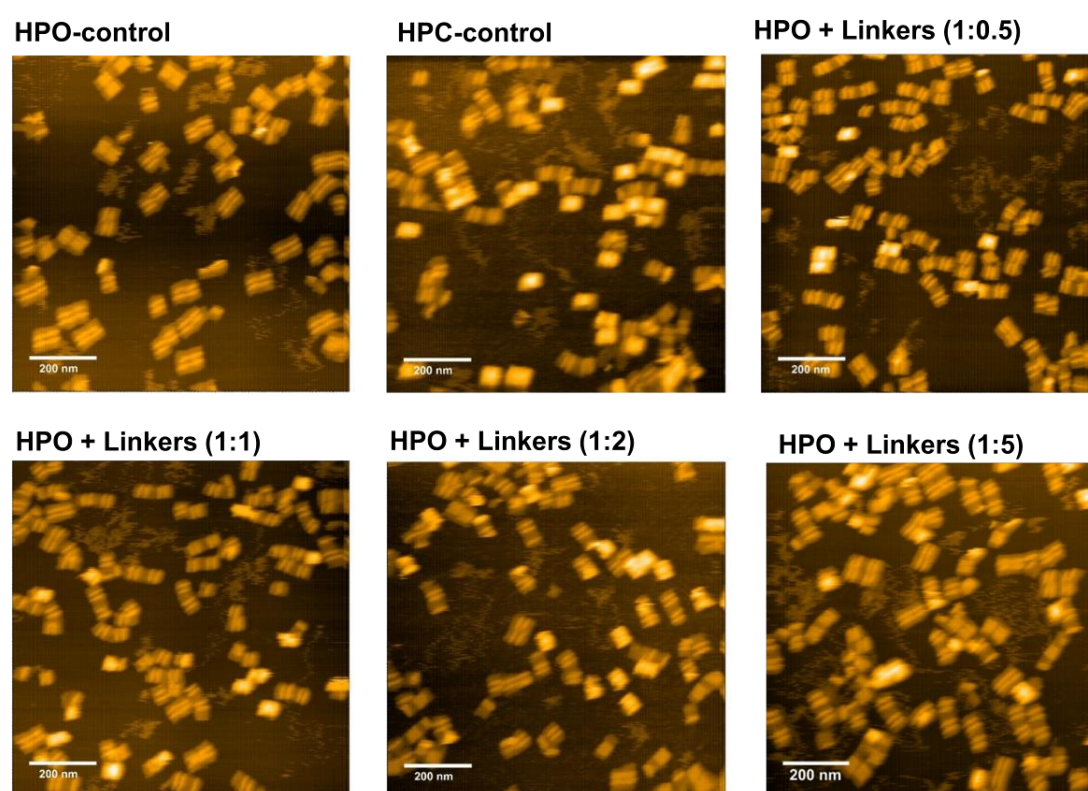
Figure 3.11. Characterization of the closing efficiency of DNA scaffold by AFM images. Typical AFM images of HPO-control, HPC-control, and HPO closed by linkers in the indicated molar ratio after 12-h incubation at 25 °C were shown, scale bar: 200 nm. The closing yields of HPO + linkers (1:0.5), HPO + linkers (1:1), HPO + linkers (1:2), HPO + linkers (1:5) were estimated to be 73% (124/169), 86% (174/203), 81% (116/143), and 75% (103/138) by AFM images, respectively.

The closing yields were also verified by agarose gel electrophoretic analyses. The sample of HPO + linkers (1:1) showed a comparable mobility and band intensities in both the Cy3 and FRET channels with those of HPC-control, indicating the almost quantitative yield for the transformation to the closed state of DNA scaffold (Figure 3.12). DNA origami comprises a high density of negatively charged phosphates on the DNA backbone. Upon addition of linkers, the closing process requires overcoming the electrostatic repulsion from the opposing domains of the DNA scaffold, which may explain the reason why the closing yield of HPO + linkers system was less than 100%.
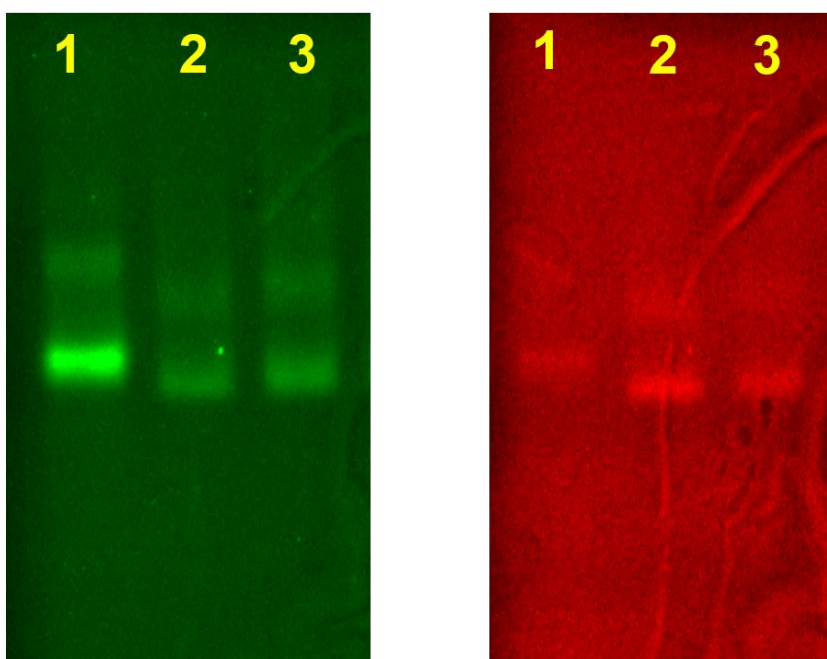
Figure 3.12. Agarose gel electrophoretic analysis of the DNA scaffolds. Left: Cy3 channel (λ_{ex} = 532 nm, λ_{em} = 605 nm); right: FRET channel (λ_{ex} = 532 nm, λ_{em} = 695 nm); Lane 1: HPO-control; Lane 2: HPC-control; Lane 3: HPO + linkers (1:1, after 12-h hybridization at 25 ℃). Agarose gel electrophoretic analyses were conducted with 1.5% agarose gel in 1 × TAE (pH 8.0) containing 12.5 mM $MgCl_2$ at 100 V for 6 h.

3.2.3. The effect of hybridization temperature on closing efficiency

The effect of temperature on the hybridization of linkers during the closing process was investigated at the optimal molar ratio of HPO to closing linkers (1:1) by varying the hybridization temperature from 20 ℃ to 30 ℃. The fluorescence emission spectra after 12-h incubation or hybridization at varied temperatures were shown in Figure 3.13a-c. It was found that the initial fluorescence intensities of control samples were slightly different due to the effect of temperature. The higher temperatures for hybridization resulted in the higher closing yields. By comparing the fluorescence emission spectra after 12-h hybridization at 20 ℃ and 30 ℃, the fluorescence emission spectrum of HPO + linkers at 30 ℃ was approached much more to that of HPC-control (Figure 3.13a-c). The closing yields at 20 ℃, 25 ℃ and 30 ℃ were 74%, 91% and 93%, as estimated by the Cy5 fluorescence intensity in the fluorescence emission. These results indicated that the effect of temperature on closing yield was more profound for the temperature change from 20 ℃ to 25 ℃ than that from 25 ℃ to 30 ℃ (Figure 3.13d).

The time courses changes of Cy5 fluorescence intensity at different hybridization temperatures were shown in Figure 3.14a-c. Elevating the temperature significantly accelerated the hybridization kinetics to shorten $t_{1/2}$ from 185 min at 20 ℃ to 89 min at 25 ℃, and to 43 min at 30 ℃ (Figure 3.14d), which is consistent with the previous reports.[26,27] These results suggested that the molar ratio and the hybridization temperature played critical roles in the closing yield and the kinetics of closing process induced by DNA linkers.
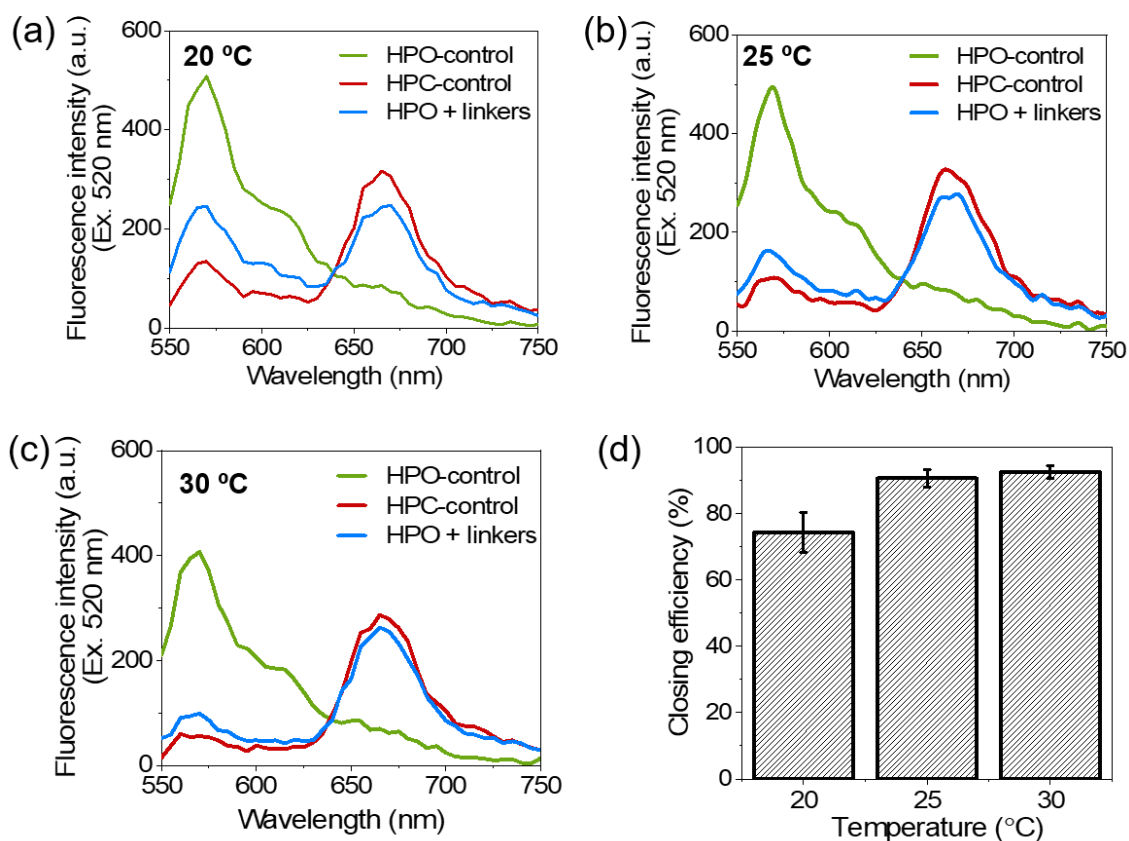
Figure 3.13. The effect of hybridization temperature on closing efficiency. (a) Fluorescence emission spectra (λ_{ex} = 520 nm) of HPO-control, HPC-control or HPO + linkers after the incubation or hybridization at 20 ℃ for 12-h. (b) Fluorescence emission spectra (λ_{ex} = 520 nm) of HPO-control, HPC-control or HPO + linkers after the incubation or hybridization at 25 ℃ for 12-h. (c) Fluorescence emission spectra (λ_{ex} = 520 nm) of HPO-control, HPC-control or HPO + linkers after the incubation or hybridization at 30 ℃ for 12-h. (d) Comparison of closing efficiency at different hybridization temperature. Hybridization conditions: 5 nM HPO was hybridized with 5 nM linkers in the buffer (pH 7.0) containing 40 mM Tris-HCl, 20 mM acetic acid, 12.5 mM $MgCl_2$ and 0.002% Tween 20 at corresponding temperature for 12-h. The closing efficiency was calculated from Cy5 fluorescence intensity in the fluorescence emission spectra after 12-h. Data in (d) were the averages of three independent repetitions, error bars indicated the S.D. of the repetitions.
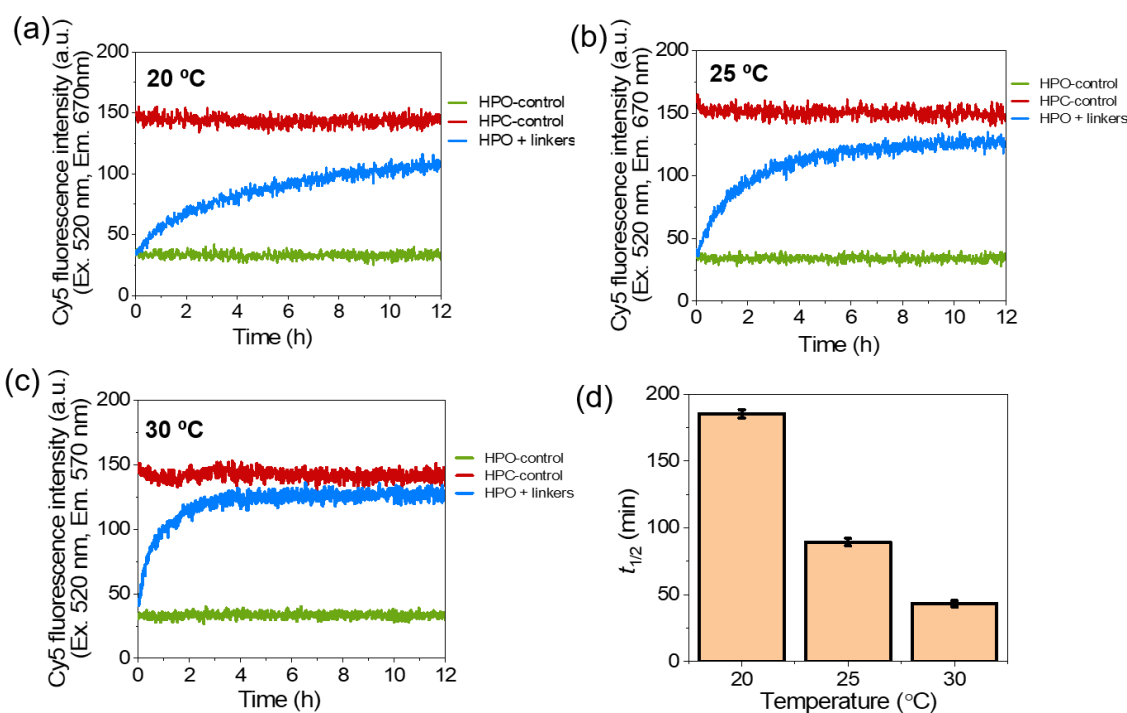
Figure 3.14. The effect of hybridization temperature on closing kinetics. (a) Time course of Cy5 fluorescence intensity (λ_{ex} = 520 nm, λ_{em} = 670 nm) in the closing process conducted at 20 °C. (b) Time course of Cy5 fluorescence intensity (λ_{ex} = 520 nm, λ_{em} = 670 nm) in the closing process conducted at 25 °C. (c) Time course of Cy5 fluorescence intensity (λ_{ex} = 520 nm, λ_{em} = 670 nm) in the closing process conducted at 30 °C. (d) Half time ($t_{1/2}$) of the closing process at various hybridization temperature. Hybridization conditions: 5 nM HPO was hybridized with 5 nM linkers in the buffer (pH 7.0) containing 40 mM Tris-HCl, 20 mM acetic acid, 12.5 mM MgCl$_2$ and 0.002% Tween 20 at corresponding temperature for 12-h. Data in (d) were the averages of three independent repetitions, error bars indicated the S.D. of the repetitions.

3.2.4. Assembly of XDH and quantification of the enzyme loading yield

Xylitol dehydrogenase (XDH),[28] the second enzyme in the D-xylose metabolic pathway that converts xylitol to xylulose by consuming a cofactor NAD⁺, was assembled on the DNA scaffold (Figure 3.15a and Figure 3.15b). The modular adaptor[29–32] stably locates an enzyme of interest at the specific position on DNA scaffold with a covalent linkage between the protein and the scaffold. As described in Chapter 2, XDH was fused to the C-terminal of modular adaptor consisting of the basic leucine zipper protein GCN4[33] and Halo-tag[34] (HG) to construct a fusion enzyme HG-

XDH as previously reported.[35] HG-XDH specifically reacts with the Halo-tag substrate 5-chlorohexane (CH) incorporated near the GCN4-binding DNA sequence.[31,32]

The dynamic DNA scaffold in the open state (HPO) was constructed with three hairpin DNAs containing the GCN4-binding DNA sequence modified with CH for HG-XDH. The DNA scaffold with the HG-XDH binding sites were incubated with excess amount of HG-XDH at a molar ratio of 1:10 at 4 ℃ for 1 h, then the binding reaction mixture was purified by size exclusion chromatography (Sephacryl S-400) to remove the unbound HG-XDH and to obtain the purified DNA-enzyme assembly (HPO/XDH).[35] The details of experimental procedure were described in the Materials and Methods. The assembly yield of HG-XDH on DNA scaffold was estimated from the AFM images for each preparation of the samples (Figure 3.15c). In a typical preparation, 2.53 molecules of HG-XDH dimer were loaded on the three loading sites of each DNA scaffold in the open state (HPO) as shown in Table 3.1.

(a) HG-XDH   **(b) HPO/XDH**   **(c)**
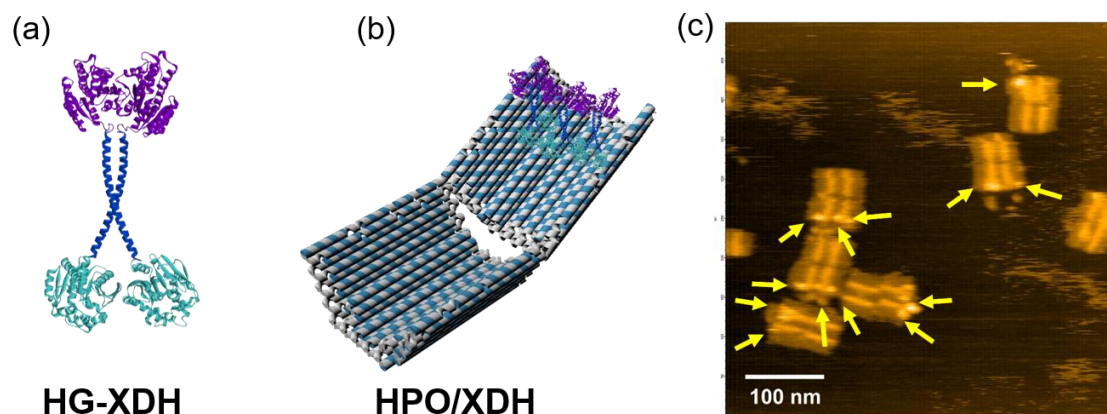
Figure 3.15. Assembly of HG-XDH on DNA scaffold. (a) Molecular model of enzyme HG-XDH. (b) Scheme presenting HG-XDH assembled on DNA scaffold with three binding sites in one domain (HPO/3XDH). (c) Typical AFM image of HPO/3XDH, scale bar: 100 nm, the arrows indicated enzyme HG-XDH. HG-XDH was assembled with average 2.53 molecule of dimer on each DNA scaffold, 250 well-formed DNA scaffolds were counted as shown in Table 3.1.

Table 3.1. Average number of assembled enzyme on DNA scaffold

Scaffolded enzyme	Modular adaptor enzymes	Number of well-formed DNA scaffold	Numbers of enzymes on modified sites [yield]				Average number of assembled enzyme
			Three-binding	Two-binding	One-binding	Empty	
HPO-XDH	HG-XDH	250	189 [75.6%]	21 [8.4%]	24 [9.6%]	16 [6.4%]	2.53[a]

[a] Calculated by the average assembly yield of HG-XDH on DNA scaffold

$N_{\text{HG-XDH}} = 3 \times 75.6\% + 2 \times 8.4\% + 1 \times 9.6\% + 0 \times 6.4\% = 2.53$ (molecules of HG-XDH dimer on each DNA scaffold)

3.2.5. Shape transformation of the HG-XDH loaded DNA scaffold by DNA linkers

The resulting HPO/XDH was incubated in the presence or absence of closing linkers (1:1) to obtain the closed state encapsulating the enzymes (HPC/XDH) or HPOa/XDH, a control sample for HG-XDH assembled on HPO treated with the same incubation time and temperature for the closing process (Figure 3.16a). The time-course of closing process for HPO/XDH monitored by the Cy5 fluorescence intensity indicated 92% closing yield after incubating for 12-h with a half-time value ($t_{1/2}$) of 88 min for closing (Figure 3.16b), which was similar to that of the HPO scaffold (89 min) at 25 ºC (Figure 3.14b). Formation of the closed structures after the hybridization process was independently verified by AFM images with the estimated closing yield of 90% (90 closed structures/100 counted structures) for HPO/XDH (Figure 3.16c). These results indicated that enzyme loaded HPO scaffold was efficiently transformed to the enzyme encapsulated HPC scaffold.
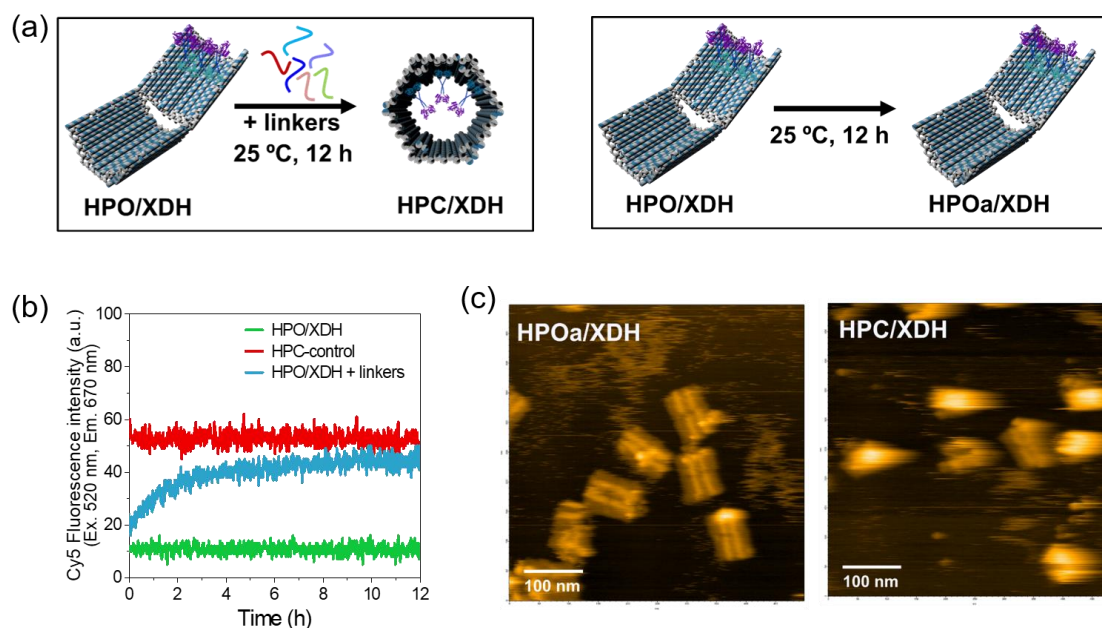
Figure 3.16. Shape transformation of HPO/XDH. (a) Schemes representing HPO/XDH was incubated in the presence or absence of closing linkers at 25 ºC for 12 h to obtain HPC/3XDH or a control sample for XDH assembled on the open state (HPOa/XDH). (b) Time course changes of the Cy5 fluorescence intensity (λ_{ex} = 520 nm, λ_{em} = 670 nm) for the HPO/XDH closing process. Hybridization conditions: 1.5 nM HPO/XDH (DNA scaffold concentration) was hybridized with 1.5 nM linkers in the buffer (pH 7.0) containing 40 mM Tris-HCl, 20 mM acetic acid, 12.5 mM $MgCl_2$, 0.002% Tween 20 and 5 μM BSA at 25 ºC for 12-h. (c) Typical AFM images of HPOa/XDH (left) and HPC/XDH (right). Scale bar: 100 nm. To obtain the AFM images with clean background, the samples for AFM measurement were independently prepared without the addition of BSA.

3.2.6. Comparison of enzyme activity in open and closed states

After the closing process, enzyme reaction was conducted for HPC/XDH, or HPOa/XDH, the control sample treated with the same incubation conditions. The reaction of HG-XDH on DNA scaffold was monitored spectrophotometrically by the production of NADH at 340 nm (Figure 3.17a). The comparable initial reaction velocities of HPOa/XDH and HPC/XDH indicated that HG-XDH encapsulated in the hexagonal prism nanocarrier HPC maintained a catalytic activity comparable to that assembled on the 2D-like DNA scaffold HPO (Figure 3.17b).

In the study of Chapter 2,[35] XDH or xylose reductase (XR) individually scaffolded on HPO fixed to the open state showed higher activity than the respective free enzyme. Indeed, the catalytic enhancements have been observed for a wide range of DNA-enzyme complexes with the proposed mechanisms of ordered hydration layer,[36] reduced adsorption[37] and substrate attraction[38] as discussed in Chapter 2. Besides, it has been proposed that the local pH change induced by the high, negative surface charge density of DNA nanostructures contributes the enhanced activity of enzyme scaffolded on DNA nanostructure.[39,40] While it was directly observed a slight pH change near the surface of DNA nanostructure, such local pH changes would not account for the higher activity of scaffolded enzymes because the optimal pH profiles of XDH and XR are pH 8.0 and pH 6.0, respectively (2.2.6 in Chapter 2). Likewise, contrary to the previous proposal, the neutral or net negative charge of substrates and cofactors for XDH and XR indicated that neither the HPO surface-substrate or the HPO surface-cofactor electrostatic attractive interaction contributed for the enhancement of catalytic activity (2.2.3 in Chapter 2). It was also observed the preserved stability and prevention of adsorption on the reaction vessel for the HPO scaffolded enzyme, but these are not the determining factors for enhancing the activity of scaffolded enzyme.

Instead, it is likely that the ordered hydration layer formed by the high, negative surface charge density of DNA nanostructure plays an important role. Zhao et al. have observed 4-10-fold higher turnover numbers of five DNA cage encapsulated enzymes (HRP, GOx, MDH, G6pDH and LDH) than the free enzymes with the hypothesis that the hydration layer stabilized the enzymes.[36] In addition to the stabilization effect, we further propose that the hydration layer enriches the local concentration of hydrophilic substrates. While the exact working mechanisms of catalytic enhancement of DNA scaffolded enzymes are still debating, it is believed scaffolds with high density of DNA helices create a favorable microenvironment for

enzymes.[41] Such local microenvironment has been recently demonstrated by different biomolecular interaction on DNA origami surface.[42,43]

Based on the design, the rigid 3D structure and large encapsulating capacity of the DNA scaffold in closed state provides a sufficient space for XDH. The enzyme would contact the assembled surface, but unlike the nanocage system,[36] the enzyme resided far away from the other surface of the DNA scaffold. Such an environment of HPC could account for the comparable activities of XDH assembled in the open state and that encapsulated in the closed state. The characteristics of HPO and HPC are quite useful for the applications of the dynamic DNA scaffold as the nanocarrier for enzymes or other macromolecules to maintain the catalytic activity of assembled enzyme during the shape transformation, in which the catalytic activity of enzyme on HPO is higher than its free form.[35] Moreover, the enhancement of catalytic activity would be further tuned by assembling the same type of enzyme in the packed state.[44]
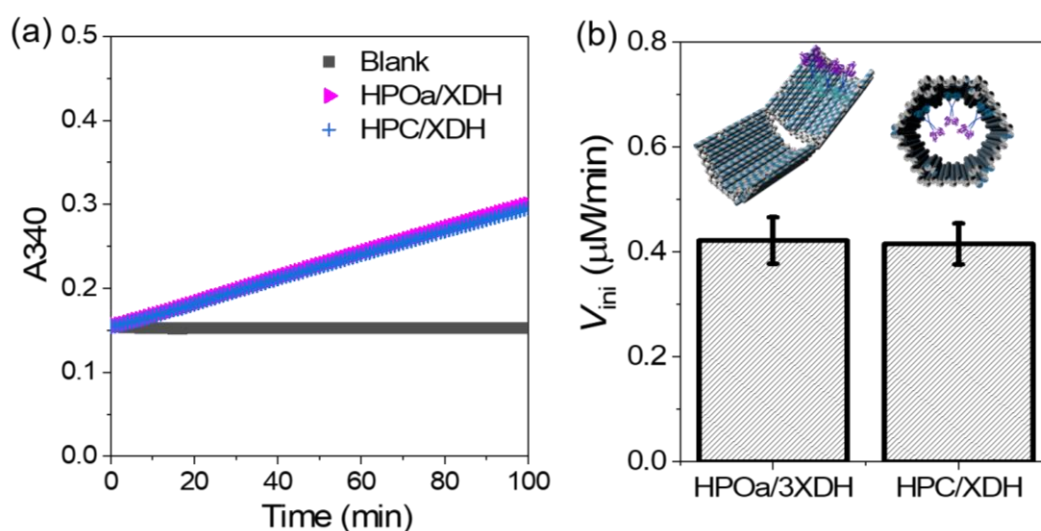
Figure 3.17. XDH encapsulated in HPC maintained its catalytic activity. (a) Time course changes of the absorbance at 340 nm (A340) for the enzyme reactions of HPOa/XDH and HPC/XDH. 2 nM HG-XDH (dimer) was reacted with 2 mM NAD$^+$ and 300 mM xylitol in the buffer (pH 7.0) containing 40 mM Tris-HCl, 20 mM acetic acid, 12.5 mM MgCl$_2$, 5 μM BSA, 1 μM ZnCl$_2$, 100 mM NaCl and 0.002% Tween 20 at 25 °C. (b) Comparison of the initial reaction velocities of HPOa/XDH and HPC/XDH in (a). Data in (b) were the averages of three independent repetitions, error bars indicated the S.D. of the repetitions.

3.3. Conclusions

In summary, this chapter presented the construction and characterization of a 3D DNA scaffold that undergoes a dynamic shape transition from the open state to the closed state induced by specific short DNA closing keys. Effects of the molar ratio for DNA scaffold to closing keys and the hybridization temperatures on the shape transformation were investigated. The optimal molar ratio of HPO to closing linkers was found at 1:1, where the closing state was obtained in over 90% yield at 25 °C. Hybridization at the higher temperature resulted in the higher closing yield with an acceleration of closing kinetics. The efficient shape transformation of DNA scaffold was applied for an enzyme encapsulation with high loading yield. The activity of efficiently encapsulated xylitol dehydrogenase in the closed state was comparable to that in the open state after the same closing process. The fact that the individual enzyme activity was maintained upon encapsulation in the hexagonal prism nanocarrier HPC supports further applications of the present system not only for the enzyme nanocarrier, but also for the drug delivery, biosensing and diagnostic tools.

3.4. Materials and Methods

3.4.1. Materials

The single-stranded M13mp18 viral DNA (7249) was purchased from Guild Biosciences. Bovine serum albumin (BSA, BS9000S) was purchased from New England Biolabs. 5-chlorohexane (CH) derivative [HaloTag Succinimidyl Ester (O2) Ligand (P1691)] was purchased from Promega. Purified DNA origami staple strands, and all other oligonucleotides were obtained from Sigma-Aldrich (St. Louis, MO), Japan Bio Services Co., LTD (Saitama, Japan) or Thermo Fisher Scientific (Tokyo, Japan). β-Nicotinamide adenine dinucleotide in oxidized form (NAD$^+$) was obtained from Oriental Yeast (Tokyo, Japan). Xylitol and all other chemicals and reagents were purchased from Wako Chemicals (Tokyo, Japan) or Nacalai Tesque (Kyoto, Japan).

3.4.2 Preparation of enzyme HG-XDH

Enzyme HG-XDH was prepared as the protocols shown in Chapter 2 (Materials and Methods).[35]

3.4.3 Design of DNA scaffold

The DNA scaffold was designed in a honeycomb lattice using the open source software caDNAno (v 2.2.0.).[45] The caDNAno blueprints of the DNA scaffold with enzyme HG-XDH attachment sites were shown in Figure 3.18. The sequences of six linker strands were shown in Table 3.2.

Table 3.2. Nucleotide sequences of linker strands of DNA scaffold

Oligo DNA	Sequence (from 5' to 3')
Linker strand 1	AGAGTAGGATGAATCAATCGGCCAGTTTGGAACAAGAGCTTGA
Linker strand 2	ACGGTGACGAGAGGCCCTGTTTTATTAAAGAACGTGTAAAGGG
Linker strand 3	CGTAGCAAGGAACCTACAGTTAATGCCCCCGCC
Linker strand 4	GCTTAATGACTCCTCGTTTTAACGGGGTCCTTG
Linker strand 5	AAGCCAACCCAGAATTGATGATGGGGTTTTGCTCAG
Linker strand 6	TTTAACAAGGTGCCGAAAACCGGCGGTCCACGCTGGGGTGGTT
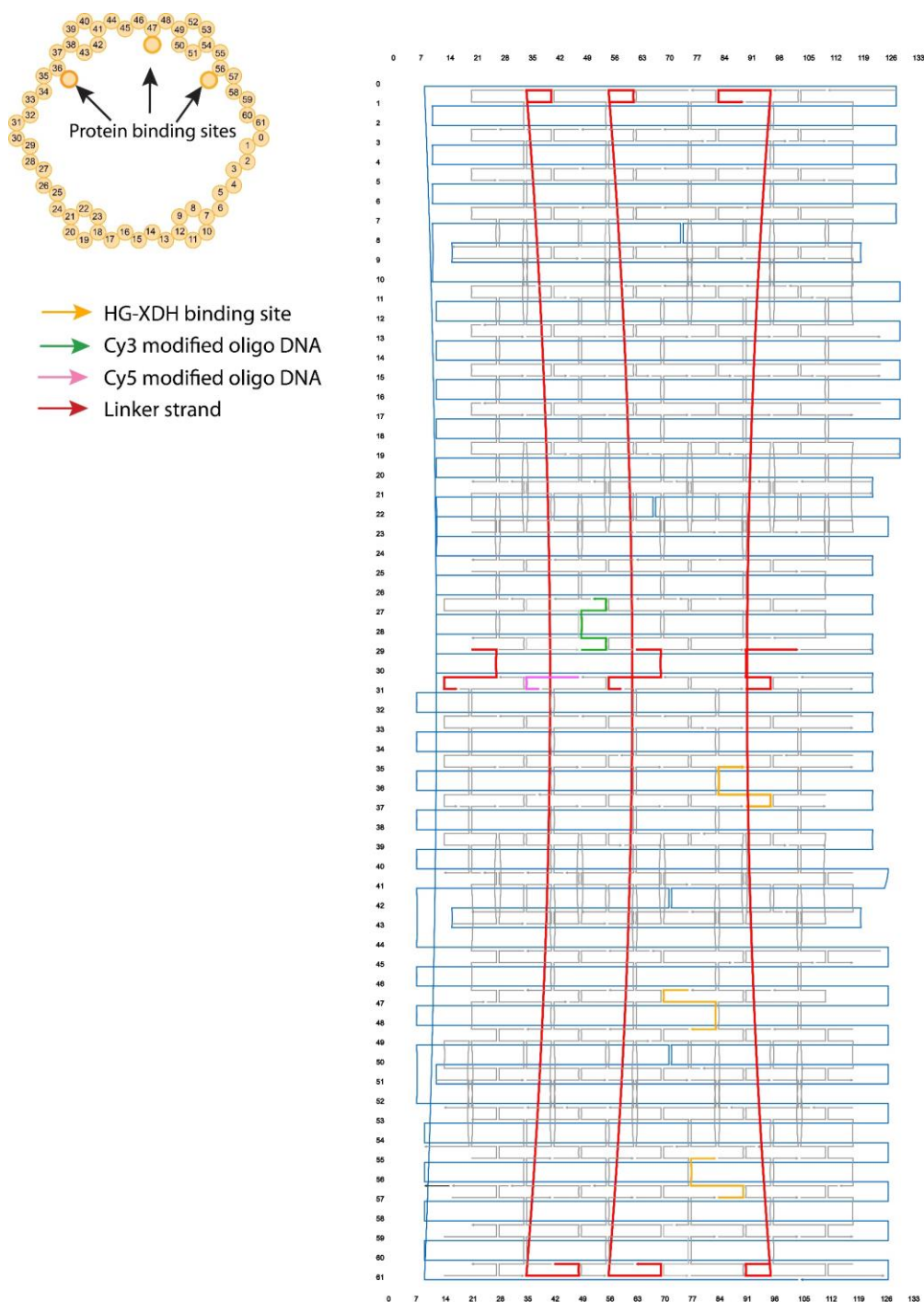
Figure 3.18. Front view and blueprint modified from caDNAno[45] software interface of DNA scaffold (http://cadnano.org/) with linkers. The staple strands shown in orange were HG-XDH binding sites. The staple strands shown in green and pink indicated Cy3-modified oligo and Cy5-modified oligo. The staple strands shown in red were linker strands of DNA scaffold.

3.4.4. Preparation of DNA Scaffold

DNA scaffold with HG-XDH binding sites was annealed by following the previous protocol.[24,46] The details of annealing process were shown in 2.4.4 in Chapter

2. Sephacryl S-400 was used to remove the excess staple strands. The concentration of DNA scaffold was quantified by the absorbance at 260 nm using the determined extinction coefficient of DNA scaffold (1.2×10^8 $M^{-1}cm^{-1}$).[35]

3.4.5 Preparation of the DNA Scaffold Assembled with HG-XDH

DNA scaffolds were constructed containing the binding sites (hairpin DNA) with 5-chlorohexane (CH) derivatives modification for HG-XDH attachment (Table 3.3).[31,32] 10 nM DNA scaffold with binding sites was incubated with 200 nM HG-XDH in a buffer (pH 7.0) containing 40 mM Tris-HCl, 20 mM acetic acid, and 12.5 mM $MgCl_2$, 5 mM β-mecaptoethanol, 0.002% Tween20 and 1 µM $ZnCl_2$ at 4 °C for 1 h. The mixture was purified by gel filtration (500 µL in volume of Toyopearl HW55F) in an Ultrafree-MC-DV column with a buffer (pH 7.0) containing 40 mM Tris-HCl, 20 mM acetic acid, and 12.5 mM $MgCl_2$ to remove the excess amount of unbound proteins.

Table 3.3. Nucleotide sequences for the staple strands containing the binding sites for ZS-XR with BG modification or the binding sites for HG-XDH with CH modification[31]

Oligo DNA	Sequence (from 5' to 3')
Binding site 1	TACCAGATTAAGACGT^{CH}TCATGAGTCATGAGTTTTCT^{CH}CATGACTCATGAACTCCTTATCGATTGA
Binding site 2	TGTAAATGATAGCTGT^{CH}TCATGAGTCATGAGTTTTCT^{CH}CATGACTCATGAACTAGATTATTAATTA
Binding site 3	ATAACATGCAACAGGT^{CH}TCATGAGTCATGAGTTTTCT^{CH}CATGACTCATGAACGAAAAACGTAAGAA

CH modified amino-C6-T was denoted as **T^{CH}**

3.4.6 AFM imaging and statistical analysis

The methods of AFM imaging and statistical analysis were shown in 2.4.6 in Chapter 2. The binding of HG-XDH was counted for only HG-XDH bound to the perfectly formed DNA scaffold. The direct counting result was shown in Table 3.1.

3.4.7 TEM characterization

The DNA scaffold (2 to 3 nM, 2 µL) was placed onto a TEM grid and incubated for 2 minutes, then the extra sample was removed by a filter paper. A MilliQ water (15 to 20 µL) was used to wash the surface of TEM grid, followed by the incubation with 10% TI Blue (4 µL) for 5 min. The surface was washed by the MilliQ water consecutively. Samples were analyzed by using a TEM microscope (JEOL JEM-2200FS + CETCOR).

3.4.8 Enzyme assay of HG-XDH

Catalytic activity of HG-XDH was measured by the changes of absorbance at 340 nm (25 °C) derived from the production of NADH in an Infinite 200 PRO microplate reader (TECAN). In a typical experiment, a reaction was started with an addition of NAD^+ (2 mM) to a mixture of HG-XDH (5 nM dimer) and xylitol (300 mM) in a buffer (pH 7.0) containing 40 mM Tris-HCl, 20 mM acetic acid, 12.5 mM $MgCl_2$, 100 mM NaCl, 1 µM $ZnCl_2$, 5 µM BSA and 0.002% Tween20. Enzyme activities were measured on the microplate [Greiner Microplate, 655901, 96-well, PS, F-bottom (chimney well) clear, non-binding].

3.4.9 Closing process of DNA scaffold

The open state of DNA scaffold was first constructed with the 6 positions of linker strands left unhybridized, then the corresponding 6 linker strands (Table 3.2) were added in a 1:1 molar ratio. Typically, 5 nM DNA scaffold in the open state was hybridized with 5 nM DNA linker strands in the Microplate [Greiner Microplate, 96-well, PS, F-bottom (chimney well) µCLEAR®, black, non-binding] in the buffer (pH 7.0) containing 40 mM Tris-HCl, 20 mM acetic acid, 12.5 mM $MgCl_2$ and 0.002% Tween 20 at 25 °C for 12 h.

3.4.10 Fluorescence measurements and FRET analyses

The nucleotide sequences of staple strands 5′-modified with Cy3 or Cy5 were shown in Table 3.4. Fluorescence measurements were carried out on a microplate reader (TECAN Infinite® 200Pro). Fluorescence spectra of the samples were measured from 550 nm to 750 nm upon the excitation at 520 nm in the 96-plate [Greiner Microplate, 96-well, PS, F-bottom (chimney well) μCLEAR®, black, non-binding] with 5 nm bandwidth. To study the kinetics of closing process, the time courses of Cy3 fluorescence intensity (λ_{em} = 570 nm) and Cy5 fluorescence intensity (λ_{em} = 670 nm) excited at 520 nm as the optimal excitation wavelength of Cy3 were monitored.

Table 3.4. Nucleotide sequences of staple strands modified with Cy3 or Cy5

Oligo DNA	Sequence (from 5' to 3')
Cy3-modification	ATTAAGACACCCTCCCCATGTTTTG
Cy5-modification	TGAGTAACAGTGCCGAGG

3.4.11 Calculation of closing efficiency (the percentage of closed structures)

The closing efficiency of DNA scaffold was estimated by the Cy5 fluorescence intensity upon excitation of donor Cy3 at 520 nm in the fluorescence emission spectra after the closing process for 12-h. The calculation followed the formula: $Y = (I_{HPO\text{-}control} - I_{HPO + linkers})/(I_{HPO\text{-}control} - I_{HPC\text{-}control})$. Here $I_{HPO\text{-}control}$, $I_{HPC\text{-}control}$ and $I_{HPO + linkers}$ indicated the Cy5 fluorescence intensity of HPO-control, HPC-control and HPO + linkers in the fluorescence emission spectra after 12-h incubation or hybridization, respectively. Y indicated the percentage of closed structures.

3.4.12 Agarose gel electrophoresis

Conditions for the agarose gel electrophoresis were described in the figure captions. Typically, the samples were run on a 1% agarose gel in 1 × TAE (pH 8.0) containing 12.5 mM $MgCl_2$ at 50 V for 6 h. The gel was visualized by using Molecular

Imager FX pro (Bio-Rad) under ethidium bromide (EtBr) channel (λ_{ex} = 532 nm, λ_{em} = 605 nm), Cy3 channel (λ_{ex} = 532 nm, λ_{em} = 605 nm), or FRET channel (λ_{ex} = 532 nm, λ_{em} = 695 nm).

3.5 References

1. Agapakis, C. M., Boyle, P. M. & Silver, P. A. Natural strategies for the spatial optimization of metabolism in synthetic biology. *Nat. Chem. Biol.* **8**, 527–535 (2012).

2. Küchler, A., Yoshimoto, M., Luginbühl, S., Mavelli, F. & Walde, P. Enzymatic reactions in confined environments. *Nat. Nanotechnol.* **11**, 409–420 (2016).

3. Conrado, R. J., Varner, J. D. & DeLisa, M. P. Engineering the spatial organization of metabolic enzymes: mimicking nature's synergy. *Curr. Opin. Biotechnol.* **19**, 492–499 (2008).

4. Bonacci, W. *et al.* Modularity of a carbon-fixing protein organelle. *Proc. Natl. Acad. Sci.* **109**, 478–483 (2012).

5. Gou, M., Ran, X., Martin, D. W. & Liu, C. J. The scaffold proteins of lignin biosynthetic cytochrome P450 enzymes. *Nat. Plants* **4**, 299–310 (2018).

6. Liu, L. N. Distribution and dynamics of electron transport complexes in cyanobacterial thylakoid membranes. *Biochim. Biophys. Acta-Bioenerg.* **1857**, 256–265 (2016).

7. Brasch, M. *et al.* Assembling enzymatic cascade pathways inside virus-based nanocages using dual-tasking nucleic acid tags. *J. Am. Chem. Soc.* **139**, 1512–1519 (2017).

8. Walde, P. & Ichikawa, S. Enzymes inside lipid vesicles: preparation, reactivity and applications. *Biomol. Eng.* **18**, 143–177 (2001).

9. Klermund, L., Poschenrieder, S. T. & Castiglione, K. Biocatalysis in polymersomes: improving multienzyme cascades with incompatible reaction steps by compartmentalization. *ACS Catal.* **7**, 3900–3904 (2017).

10. Rothemund, P. W. K. Folding DNA to create nanoscale shapes and patterns.

Nature **440**, 297–302 (2006).

11. Douglas, S. M. *et al.* Self-assembly of DNA into nanoscale three-dimensional shapes. *Nature* **459**, 414–418 (2009).

12. Hong, F., Zhang, F., Liu, Y. & Yan, H. DNA origami: scaffolds for creating higher order structures. *Chem. Rev.* **117**, (2017).

13. Simmel, F. C., Yurke, B. & Singh, H. R. Principles and applications of nucleic acid strand displacement reactions. *Chem. Rev.* **119**, 6326-6369 (2019).

14. Rangel, A. E., Hariri, A. A., Eisenstein, M. & Soh, H. T. Engineering aptamer switches for multifunctional stimulus-responsive nanosystems. *Adv. Mater.* (2020).

15. Turek, V. A. *et al.* Thermo-responsive actuation of a DNA origami flexor. *Adv. Funct. Mater.* **28**, 1–7 (2018).

16. Kim, S. H. *et al.* Reversible regulation of enzyme activity by pH-responsive encapsulation in DNA nanocages. *ACS Nano* **11**, 9352–9359 (2017).

17. Deluca, M., Shi, Z., Castro, C. E. & Arya, G. Dynamic DNA nanotechnology: toward functional nanoscale devices. *Nanoscale Horizons* **5**, 182–201 (2020).

18. Juul, S. *et al.* Temperature-controlled encapsulation and release of an active enzyme in the cavity of a self-assembled DNA nanocage. *ACS Nano* **7**, 9724–9734 (2013).

19. Ijäs, H., Hakaste, I., Shen, B., Kostiainen, M. A. & Linko, V. Reconfigurable DNA origami nanocapsule for pH-controlled encapsulation and display of cargo. *ACS Nano* **13**, 5959-5967 (2019).

20. Marras, A. E. *et al.* Cation-activated avidity for rapid reconfiguration of DNA nanodevices. *ACS Nano* **12**, 9484–9494 (2018).

21. Grossi, G., Dalgaard Ebbesen Jepsen, M., Kjems, J. & Andersen, E. S. Control of enzyme reactions by a reconfigurable DNA nanovault. *Nat. Commun.* **8**, (2017).

22. Xin, L., Zhou, C., Yang, Z. & Liu, D. Regulation of an enzyme cascade reaction by a DNA machine. *Small* **9**, 3088–3091 (2013).

23. Rajendran, A., Nakata, E., Nakano, S. & Morii, T. Nucleic-acid-templated enzyme cascades. *ChemBioChem* **18**, 696–716 (2017).

24. Douglas, S. M., Bachelet, I. & Church, G. M. A logic-gated nanorobot for targeted transport of molecular payloads. *Science* **335**, 831–834 (2012).

25. Roy, R., Hohng, S. & Ha, T. A practical guide to single-molecule FRET. *Nat. Methods* **5**, 507–16 (2008).

26. Markegard, C. B., Gallivan, C. P., Cheng, D. D. & Nguyen, H. D. Effects of concentration and temperature on DNA hybridization by two closely related sequences via large-scale coarse-grained simulations. *J. Phys. Chem. B* **120**, 7795–7806 (2016).

27. Groeer, S. & Walther, A. Switchable supracolloidal 3D DNA origami nanotubes mediated through fuel/antifuel reactions. *Nanoscale* **12**, 16995–17004 (2020).

28. Watanabe, S., Kodaki, T. & Makino, K. Complete reversal of coenzyme specificity of xylitol dehydrogenase and increase of thermostability by the introduction of structural zinc. *J. Biol. Chem.* **280**, 10340–10349 (2005).

29. Nakata, E., Dinh, H., Ngo, T. A., Saimura, M. & Morii, T. A modular zinc finger adaptor accelerates the covalent linkage of proteins at specific locations on DNA nanoscaffolds. *Chem. Commun.* **51**, 1016–1019 (2015).

30. Ngo, T. A., Nakata, E., Saimura, M. & Morii, T. Spatially organized enzymes drive cofactor-coupled cascade reactions. *J. Am. Chem. Soc.* **138**, 3012–3021 (2016).

31. Nguyen, T. M., Nakata, E., Saimura, M., Dinh, H. & Morii, T. Design of modular protein tags for orthogonal covalent bond formation at specific DNA sequences. *J. Am. Chem. Soc.* **139**, 8487–8496 (2017).

32. Nguyen, T. M. *et al.* Rational design of a DNA sequence-specific modular protein tag by tuning the alkylation kinetics. *Chem. Sci.* **10**, 9315–9325 (2019).

33. Ellenberger, T. E., Brandl, C. J., Struhl, K. & Harrison, S. C. The GCN4 basic region leucine zipper binds DNA as a dimer of uninterrupted α helices: crystal structure of the protein-DNA complex. *Cell* **71**, 1223–1237 (1992).

34. England, C. G., Luo, H. & Cai, W. HaloTag technology: a versatile platform for biomedical applications. *Bioconjug. Chem.* **26**, 975–986 (2015).

35. Lin, P. *et al.* Evaluation of the role of the DNA surface for enhancing the activity of scaffolded enzymes. *Chem. Commun.* **57**, 3925–3928 (2021).

36. Zhao, Z. *et al.* Nanocaged enzymes with enhanced catalytic activity and increased stability against protease digestion. *Nat. Commun.* **7**, (2016).

37. Timm, C. & Niemeyer, C. M. Assembly and purification of enzyme-functionalized DNA origami structures. *Angew. Chem., Int. Ed.* **54**, 6745–6750 (2015).

38. Lin, J. L. & Wheeldon, I. Kinetic enhancements in DNA-enzyme nanostructures mimic the sabatier principle. *ACS Catal.* **3**, 560–564 (2013).

39. Zhang, Y., Tsitkov, S. & Hess, H. Proximity does not contribute to activity enhancement in the glucose oxidase-horseradish peroxidase cascade. *Nat. Commun.* **7**, (2016).

40. Xiong, Y., Huang, J., Wang, S. T., Zafar, S. & Gang, O. Local environment affects the activity of enzymes on a 3D molecular scaffold. *ACS Nano* **14**, 14646–14654 (2020).

41. Rudiuk, S., Venancio-Marques, A. & Baigl, D. Enhancement and modulation of enzymatic activity through higher-order structural changes of giant DNA-Protein multibranch conjugates. *Angew. Chem., Int. Ed.* **51**, 12694–12698 (2012).

42. Huang, J. *et al.* Arranging small molecules with subnanometer precision on DNA origami substrates for the single-molecule investigation of protein-ligand interactions. *Small Structures* **1** : 2000038 (2020).

43. Zhang, P. *et al.* Quantitative measurement of spatial effects of DNA origami on molecular binding reactions detected using atomic force microscopy. *ACS Appl. Mater. Interfaces* **11**, 21973-21981 (2019).

44. Dinh, H. *et al.* Enhanced enzymatic activity exerted by a packed assembly of a single type of enzyme. *Chem. Sci.* **11**, 9088–9100 (2020).

45. Douglas, S. M. *et al.* Rapid prototyping of 3D DNA-origami shapes with caDNAno. *Nucleic Acids Res.* **37**, 5001–5006 (2009).

46. Amir, Y. *et al.* Universal computing by DNA origami robots in a living animal. *Nat. Nanotechnol.* **9**, 353–357 (2014).

CHAPTER 4

Inter-enzyme distance dependency of the efficiency of cascade reaction with a faster downstream enzyme

4. 1. Introduction

Cells have developed the systems capable of efficient enzyme cascade reactions to overcome the imbalanced fluxes.[1,2] Carbamoyl phosphate synthetase,[3] Malate dehydrogenase-citrate synthase (MDH-CS),[4] and RuBisCO/carbonic anhydrase are the typical examples.[5] Inspired by nature, the flux balancing was conducted on scaffolds with optimization of enzyme stoichiometry or spatial arrangement. The synthetic protein scaffolds were used to engineer metabolic path for the production of mevalonate, in which the stoichiometry of three enzymes ACAT, HMGR and HMGS was optimized.[6] Another example was the co-immobilization of xylose reductase (XR) and phosphite dehydrogenase (PTDH) on the spore surface with optimized stoichiometry, which resulted in the enhanced yields of xylitol.[7] However, the above carriers face the difficulties of spatial arrangement of enzymes.

The proximity effect of enzyme cascade reactions was extensively investigated on the static DNA scaffolds or simple dynamic DNA devices,[8–10] in which most of the studies depended on a pair of extremely stable enzymes GOx/HRP with balanced kinetic parameters, where the K_m values of GOx and HRP were determined to be 15 mM and 2.5 μM, respectively, and the k_{cat} values of the enzyme pairs were 250 s^{-1} and 32.7 s^{-1}, respectively.[11] However, cascaded enzymes involved in the cellular metabolic pathways may suffer from unfavourable kinetics of upstream and downstream enzymes. Kinetic parameters of those sequential enzymes are critical in considering the inter-enzyme distance dependency of sequential enzymes for designing an efficient artificial metabolic pathway.[12]

As reported previously, sequential enzymatic reactions from the initial reaction from the initial steps of xylose metabolic pathways, xylose reductase (XR) and xylitol dehydrogenase (XDH), were conducted on a 2D DNA scaffold with the variation of inter-enzyme distance from 98 nm to 10 nm. A clear dependency on the inter-enzyme

distance was observed with the best cascade reaction efficiency at 10 nm.[13] In this study, an enzyme cascade of XDH and xylulose kinase (XK) was constructed on a three-dimensional DNA scaffold[14] capable of dynamic shape transition via DNA hybridization. Cascaded enzymes were first assembled on the DNA scaffold in open state, followed by the addition of the DNA linkers to transform the scaffold to the closed 3D state in over 90% closing yield. The inter-enzyme distance was changed from 60 nm to 20 nm upon transforming the open state to the closed state. Evaluation of the sequential reaction of xylitol metabolism through the transport of intermediate xylulose from XDH to XK resulted in little or no evident distance dependency for the efficiency of cascade reaction by XDH and XK, in which the k_{cat} of XK was over 200-times higher than that of XDH. The result was consistent with the previous reports[15,16] that events occurring downstream do not have any effect on the overall output rate when the upstream enzyme is much slower than the downstream enzyme.

4.2. Results and discussions

4.2.1. Assembly of enzymes HG-XDH and AC-XK on the DNA scaffold and quantification of the enzyme loading yields

Xylitol dehydrogenase (XDH)[17] from *Pichia stipitis* and xylulose kinase (XK)[18] from *Saccharomyces cerevisiae* were chosen to build a xylitol metabolism pathway on the DNA scaffold. The modular adaptors[13,19-21] were used to stably locate the enzymes at specific positions on DNA scaffold with the covalent linkage between the protein and the scaffold. The upstream enzyme HG-XDH (modular adaptor Halo-GCN4 fused XDH) and downstream enzyme AC-XK (modular adaptor AZ-CLIP fused XK) were constructed as reported previously.[13,22] AZ-CLIP consists of zinc finger protein AZP4[23] recognizing the targeting DNA sequence, and a self-ligating tag protein CLIP-tag[24] reacting with its substrate benzylcytosine (BC) (Figure 4.1).[20] The model of HG-XDH

and its reaction to the substrate modified binding sequence were shown in Figure 2.5c-d.
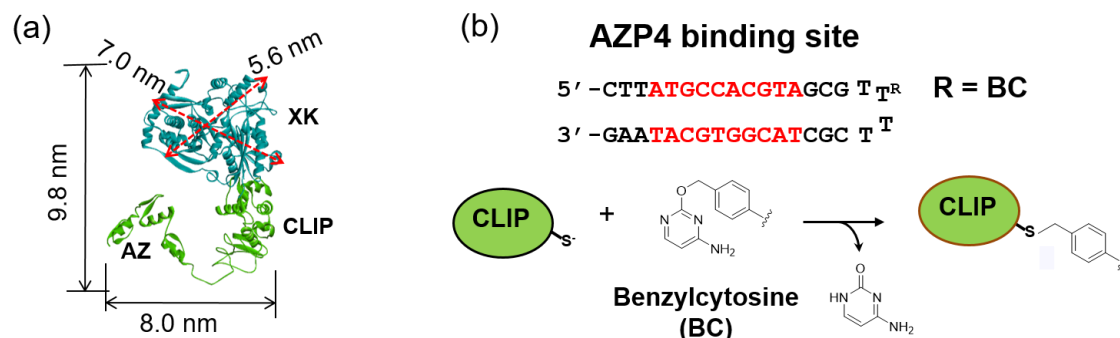

Figure 4.1. Molecular model of AC-XK and the modular adaptor binding reaction. (a) A molecular model for enzyme AC-XK (100.9 kDa) consisting of AZP4 (PDB: 1ZAA), CLIP-tag (PDB ID: 3KZY), and xylulose kinase (XK) (PDB ID: 2ITM).[20] The molecular model was constructed by using Discovery Studio (version 3.1, Accelrys Inc.). (b) AZP4 binding site (hairpin DNA) and CLIP-tag reacting with its substrate benzylcytosine (BC).[20]

DNA scaffold in the open state was designed with three hairpin DNAs with the target DNA sequences modified with CH for HG-XDH and/or single hairpin DNA with the target DNA sequence modified with BC for AC-XK.[20] The DNA scaffolds with the modular adaptor binding sites were incubated with HG-XDH and/or AC-XK at a molar ratio of 1:10 at 4 °C for 1 h. The binding mixture was purified by gel filtration to remove the unbound proteins to give purified DNA-enzyme assemblies, enzymes coassembled on the open state (HPO/3XDH-XK), individual assembly of XDH on the open state (HPO/3XDH) or individual assembly of XK on the open state (HPO/XK) (Figure 4.2).

The loading yields of enzymes on each DNA scaffold was quantitated by AFM images. It was observed that the AFM cantilever deformed the modular adaptor Halo-GCN4 and enzyme XDH during the analysis with the plausible XDH domain locating outside DNA scaffold. For HPO/3XDH-XK, enzymes were assembled with average 2.47 ± 0.11 molecules of HG-XDH (dimer) and 0.67 ± 0.06 molecules of AC-XK

(monomer) on each DNA scaffold (Figure 4.3). For HPO/3XDH, HG-XDH was loaded with average 2.53 ± 0.10 molecules of HG-XDH (dimer) on each DNA scaffold (Figure 4.4). In the case of HPO/XK, AC-XK was located with average 0.91 ± 0.02 molecules AC-XK (monomer) on each DNA scaffold (Figure 4.5). These counting results were obtained from three independent repetitions. Notably, the binding efficiency of AC-XK on the coassembled system was lower than the individual assembly system presumably due to the steric hindrance of two enzymes because HG-XDH is over 160 KDa (16 nm in length) in the dimeric form and AC-XK is over 100 KDa (10 nm in length) as a monomer (Figure 2.5 and Figure 4.1).

HPO/3XDH-XK **HPO/3XDH** **HPO/XK**
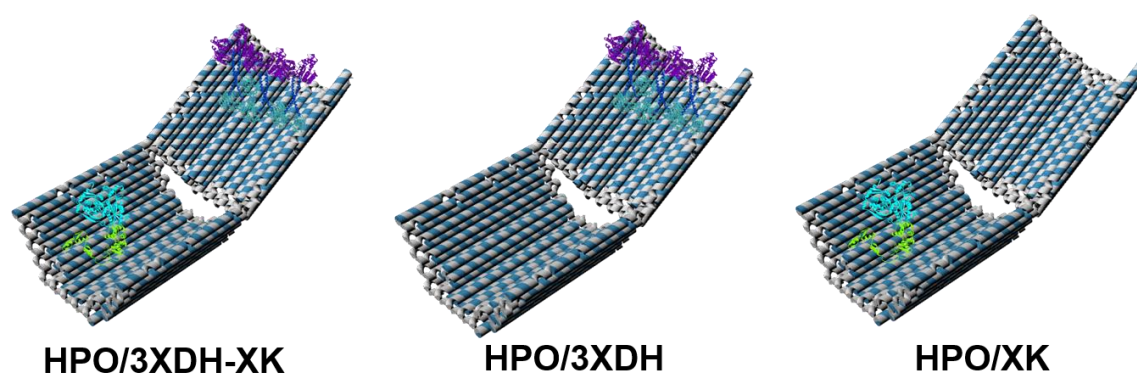
Figure 4.2. Scheme of DNA scaffolded enzymes HPO/3XDH-XK, HPO/3XDH and HPO/XK.
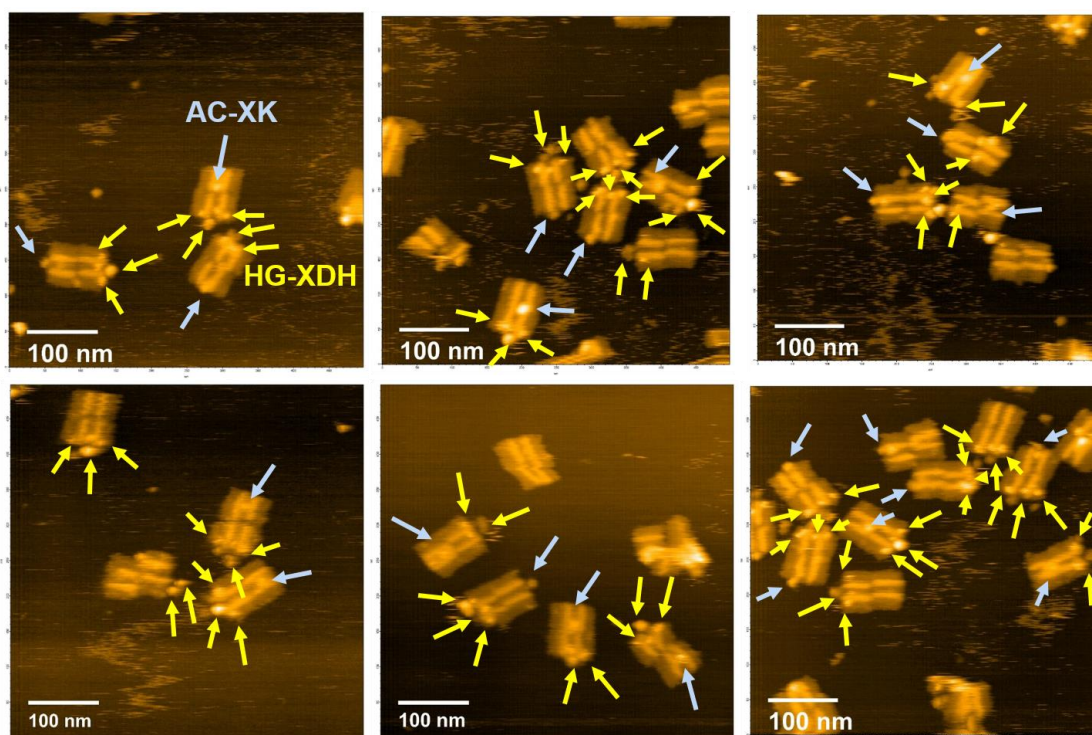
Figure 4.3 AFM images of HPO/3XDH-XK, scale bar: 100 nm. Enzymes were assembled with average 2.47 molecules of HG-XDH (dimer) and 0.67 molecules of AC-XK (monomer) on each DNA scaffold, the detail was shown in Table 4.1.
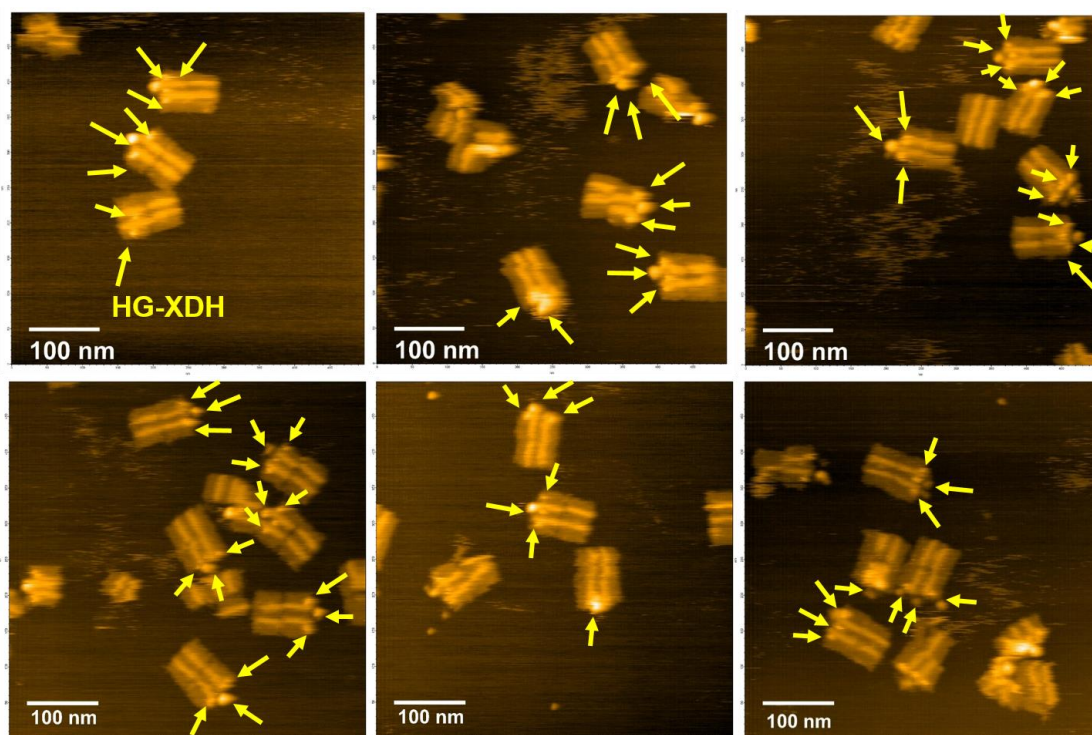
Figure 4.4 AFM images of HPO/3XDH, scale bar: 100 nm. HG-XDH was loaded with average 2.53 molecules of HG-XDH (dimer) on each DNA scaffold, the detail was shown in Table 4.1.

127
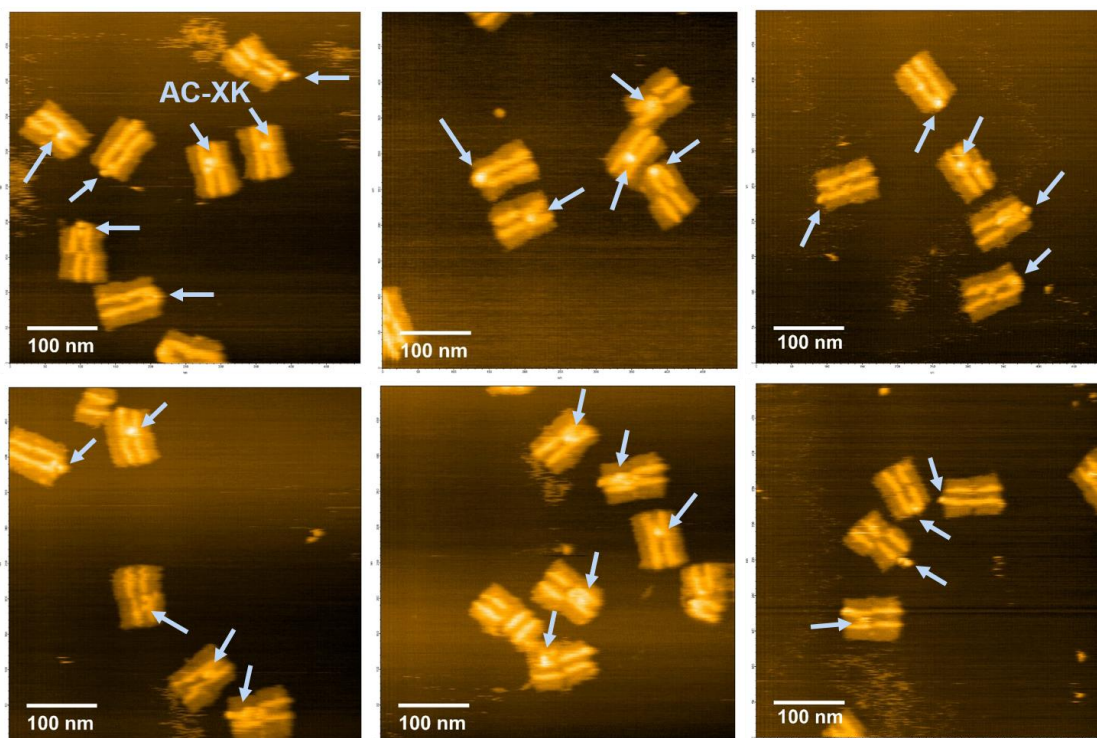
Figure 4.5 AFM images of HPO/XK, scale bar: 100 nm. AC-XK was located with average 0.91 molecules AC-XK (monomer) on each DNA scaffold, the detail was shown in Table 4.1.

Table 4.1 Average number of assembled enzyme on DNA scaffold

| DNA scaffold	Modular adaptor enzymes	Number of well-formed DNA scaffold	Numbers of enzymes on modified sites			Average number of assembled enzyme
			Three-binding	Two-binding	One-binding	
HPO/3XDH-XK	HG-XDH	250	178 [71.2%]	31 [12.4%]	21 [8.4%]	2.47*
	AC-XK				167 [66.8%]	0.67
HPO/3XDH	HG-XDH	225	68 [74.6%]	24 [10.6%]	18 [8.0%]	2.53
HPO/XK	AC-XK	375			347 [92.5]%	0.92

Note

* Calculated by the average assembly yield of HG-XDH on DNA scaffold

$N_{HG-XDH} = 3 \times 71.2\% + 2 \times 12.4\% + 1 \times 8.4\% = 2.47$ (molecules of HG-XDH dimer on each DNA scaffold)

4.2.2. Shape transformation of the enzyme loaded DNA scaffolds by DNA linkers

After the assembly of enzymes on the DNA scaffold in open state, the resulting HPO/3XDH-XK, HPO/3XDH and HPO/XK were incubated in the presence or absence of DNA linkers at a molar ratio of 1:1 to obtain the closed state encapsulating the enzymes (HPC/3XDH-XK, HPC/3XDH and HPC/XK). HPOa/3XDH-XK, HPOa/3XDH and HPOa/XK, the control samples of open state, were treated with the same incubation process in the absence of DNA linkers (Figure 4.6). The time-course of closing process for the open state of DNA scaffold assembled with enzymes was monitored by the Cy5 fluorescence intensity to give over 90% closing yields after incubating for 12-h (Figure 4.7). Formation of the closed structures was further verified by AFM images, in which HPO/3XDH-XK was closed with over 95% yield (Figure 4.8). These results indicated that the HPO scaffold was efficiently transformed to the HPC scaffold regardless of the assembly of enzymes.
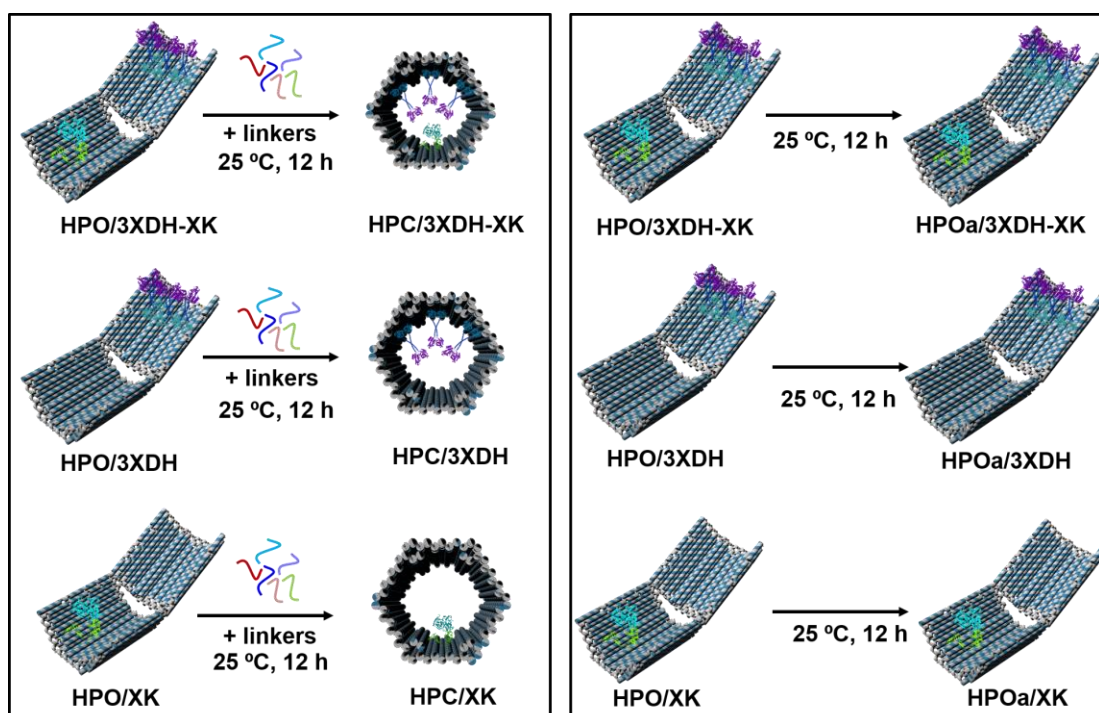
Figure 4.6. Scheme presenting the shape transformation of DNA scaffolded enzymes. DNA scaffolded enzymes HPO/3XDH-XK, HPO/3XDH and HPO/XK was incubated in the presence or absence of linkers to obtain HPC/3XDH-XK, HPC/3XDH and HPC/XK or the control samples HPOa/3XDH-XK, HPOa/3XDH and HPOa/XK. Hybridization conditions: 1.5 nM

DNA scaffold incubated 1.5 nM linkers in the buffer (pH 7.0) containing 40 mM Tris-HCl, 20 mM acetic acid, 12.5 mM MgCl$_2$, 5 µM BSA and 0.002% Tween20 at 25 ºC for 12-h.
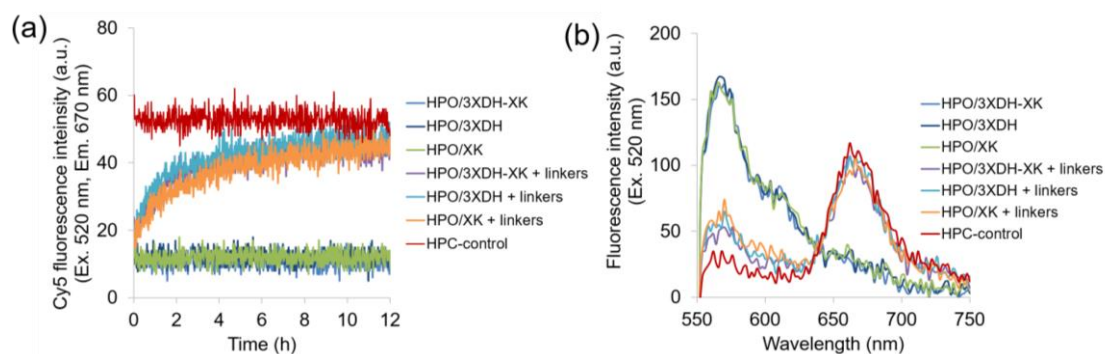
Figure 4.7. Closing process of DNA scaffolded enzymes. (a) Time course of Cy5 fluorescence intensity (λ_{ex} = 520 nm, λ_{em} = 670 nm) of the closing process of DNA scaffolded enzymes. (b) Fluorescence emission spectra (λ_{ex} = 520 nm) after 12-h incubation or hybridization at 25 ºC. Hybridization conditions: 1.5 nM DNA scaffold hybridized with 1.5 nM linkers in the buffer (pH 7.0) containing 40 mM Tris-HCl, 20 mM acetic acid, 12.5 mM MgCl$_2$, 5 µM BSA and 0.002% Tween20 at 25 ºC for 12-h.
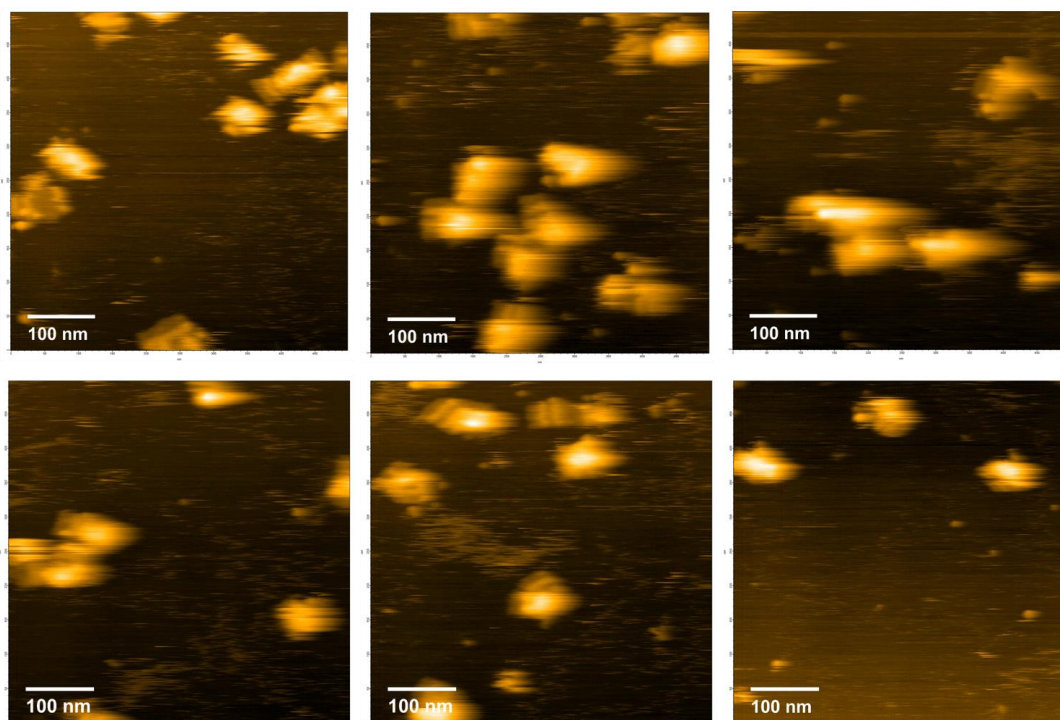
Figure 4.8. AFM images of HPC/3XDH-XK obtained from HPO/3XDH-XK hybridizing with linkers (1:1) at 25 ºC for 12-h, scale bar: 100 nm, the percentage of closed structures was estimated to be 95% (97/102). To obtain the AFM images with clean background, the samples for AFM measurement were independently prepared without the addition of BSA.

4.2.3. Measurement of the activity of first enzyme in the cascade reactions

Enzyme cascade reactions were investigated after the closing process. Besides the coassembled systems (HPOa/3XDH-XK or HPC/3XDH-XK), DNA scaffolds carrying either HG-XDH alone (HPOa/3XDH and HPC/3XDH) or AC-XK alone (HPOa/XK and HPC-XK) were utilized for control reactions. In the XDH/XK cascade reaction, the first enzyme HG-XDH converted xylitol into xylulose by consuming the cofactor NAD^+, the second enzyme AC-XK converts the resulting xylulose into xylulose-5-phosphate by consuming the cofactor ATP (Figure 4.9). In this study, excess amount of substrate xylitol (300 mM), cofactors NAD^+ (2 mM) and ATP (1 mM) were utilized for the enzyme cascade reactions to realize the unimolecular (xylulose) transport system.
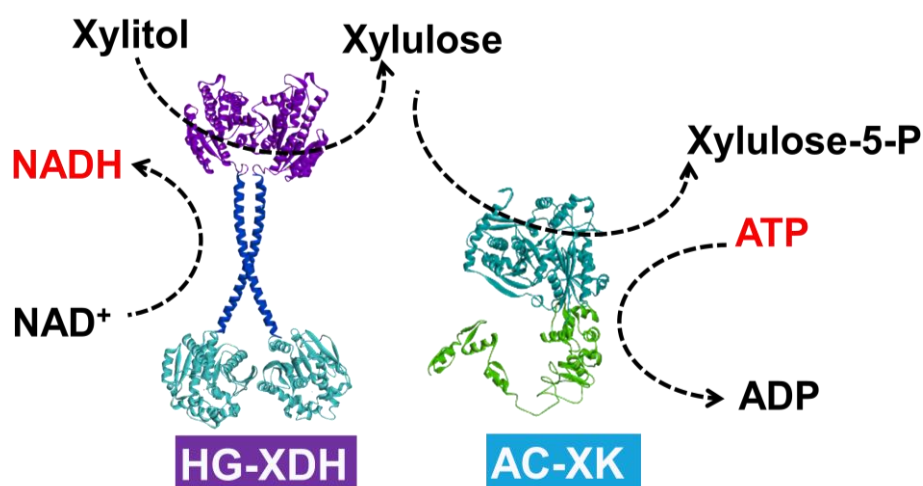
Figure 4.9. Scheme presenting the enzyme cascade reaction of HG-XDH and AC-XK. The produced intermediate (xylulose) by HG-XDH was utilized by second enzyme AC-XK to form xylulose-5-P.

Activity of the first enzyme HG-XDH alone in the cascade reactions was measured by spectrophotometrically monitoring the production of NADH at 340 nm as shown in Figure 4.10a. Comparable initial reaction velocities of HG-XDH were obtained for the coassembly systems (HPOa/3XDH-XK or HPC/3XDH-XK), and the equimolar mixture of two separate DNA scaffold assembling either HG-XDH or AC-XK (HPOa/3XDH + HPOa/XK or HPC/3XDH + HPC/XK) (Figure 4.10b), which further supported that the enzyme loading yields of HG-XDH on DNA scaffolds were similar to each other (Table 4.1).
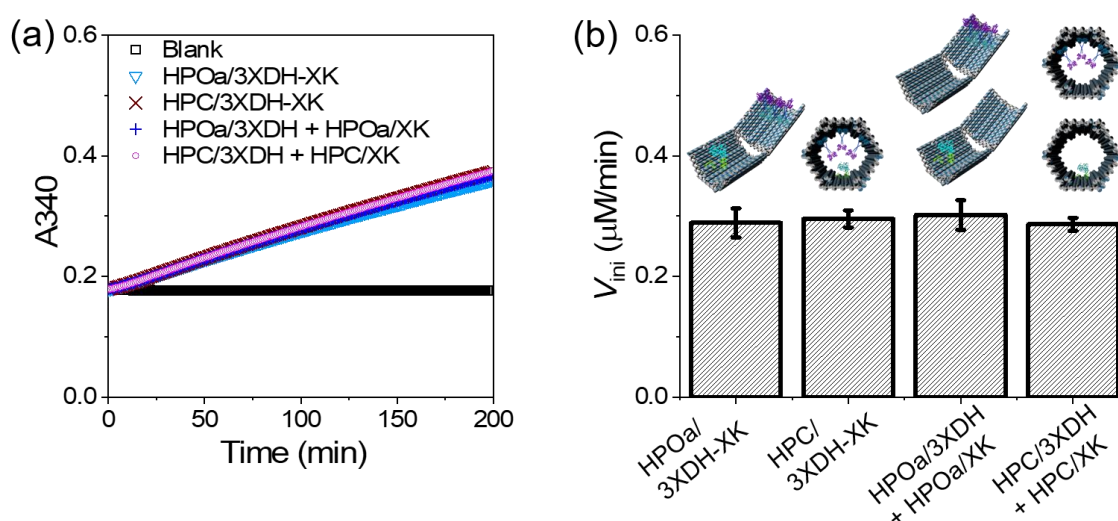
Figure 4.10. Activity of the first enzyme HG-XDH in the cascade reactions. (a) Time course of A340 of enzyme cascade reactions on DNA scaffold. (b) Comparison of initial reaction velocities of enzyme cascade reactions on DNA scaffold from (a). Assay condition: enzymes reacted with 300 mM xylitol, 2 mM NAD^+ and 1 mM ATP in the buffer (pH 7.0) containing 40 mM Tris-HCl, 20 mM acetic acid, 12.5 mM $MgCl_2$, 100 mM NaCl, 1 μM $ZnCl_2$, 0.002% Tween20, 5 μM BSA and 1 mM DTT at 25 ºC. In the reaction, each DNA scaffold concentration was fixed to 0.6 nM, which was equal to 1.5 nM HG-XDH and 0.4 nM AC-XK in the coassembly systems (HPOa/3XDH-XK or HPC/3XDH-XK), and 1.5 nM HG-XDH and 0.55 nM AC-XK in the separate systems (HPOa/3XDH + HPOa/XK or HPC/3XDH + HPC/XK) calculated based on the enzyme loading yields on DNA scaffold. Data in (b) were the averages of three independent repetitions, error bars indicated the S.D. of the repetitions.

4.2.4. Enzyme cascade reactions of XDH/XK monitored by HPLC

The enzyme cascade efficiencies were analyzed by high-performance liquid chromatography (HPLC) to quantitate the cofactors ATP, NAD^+, NADH, and ADP consumed or generated in the cascade reactions. Trifluoroacetic acid (TFA) was used to quench the enzyme reactions in a final concentration of 0.1%. To investigate the quenching ability of TFA and its effect on the stability of ADP and NADH, enzyme cascade reactions of free HG-XDH and AC-XK were conducted in the presence or absence of 0.1% TFA. The experimental details were shown in Figure 4.11a. By comparing Figure 4.11b, Figure 4.11c and Figure 4.11d, it was deduced that the enzymatic reaction was efficiently quenched by 0.1% TFA. By comparing Figure 4.11d and Figure 4.11e, it was found that ATP, ADP and NAD^+ were stable in 0.1% TFA, while NADH was decomposed in the acidic environment. It was reported that NADH is unstable in the acidic medium. It reacts with acid to yield a primary product whose spectrum possesses at 290 nm. The primary product undergoes a secondary reaction in the presence of acid yielding a product without absorbing at 290 nm or 340 nm. Besides, phosphate buffer resulted in a faster decomposition of NADH, which was attributed to the adduct formation between phosphate and the pyridine ring.[25–28]
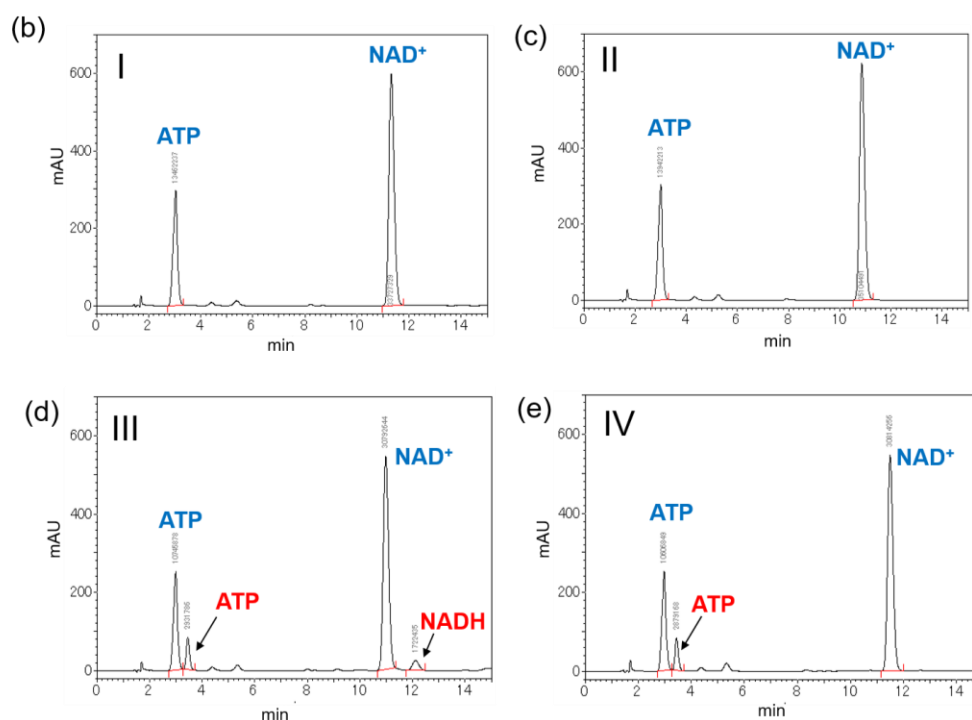
Figure 4.11. Quenching ability of 0.1% TFA and effect of TFA on the stability of cofactors. (a) Samples for investigating the effect of TFA. (b) HPLC graph of control sample (without enzyme) incubated with 0.1% TFA for 1 h. (c) HPLC graph of enzyme cascade reaction with 0.1% TFA for 1 h. (c) HPLC graph of enzyme cascade reaction proceeded without TFA, the reaction was quenched by 0.1% TFA after 1 h. (d) HPLC graph of enzyme cascade reaction proceeded without TFA, the reaction was quenched by 0.1% TFA after 1 h, then the mixture was incubated for another 4 h. Enzyme cascade reaction conditions: 45 nM free HG-XDH and 15 nM free AC-XK reacted with 300 mM xylitol, 2 mM NAD$^+$ and 1 mM ATP in the buffer (pH 7.0) containing 40 mM Tris-HCl, 20 mM acetic acid ,12.5 mM MgCl$_2$, 100 mM NaCl, 1 μM ZnCl$_2$, 0.002% Tween 20 and 1 mM DTT.

The enzyme cascade reactions of HG-XDH and AC-XK on DNA scaffold were monitored by HPLC under the steady-state conditions after 24-h reaction (Figure 4.12). The amount of ADP produced by the second enzyme AC-XK was used as a measurement of the efficiency of XDH/XK cascade reaction. By comparing the HPOa/3XDH-XK and HPC/3XDH-XK systems sharing the same assembly yield for HG-XDH and AC-XK, little or no enhancement of the ADP production was observed for the closed state over the open state. Without normalizing the loading yield of AC-XK to the DNA scaffold, it was found that the individually assembled systems (HPOa/3XDH + HPOa/XK or HPC/3XDH + HPC/XK) with the higher AC-XK assembly yield displayed the ADP production yields similar to the coassembled systems (Figure 4.13).

To compare the enzyme cascade reaction efficiency at the same AC-XK concentration, the turnover number was estimated from the amount of produced ADP divided by the concentration of the second enzyme AC-XK on DNA scaffold in the time unit (24 h). The loading yields of AC-XK in coassembly and separate systems are 0.67 and 0.91 molecules of protein monomer, respectively (Table 4.1). Compared with HPOa/3XDH-XK, the enhancement of turnover number of HPC/3XDH-XK was insignificant. The separate assembly systems (HPOa/3XDH + HPOa/XK or HPC/3XDH + HPC/XK) proceeded in lower turnover numbers as compared with that of coassembly systems (Figure 4.14).
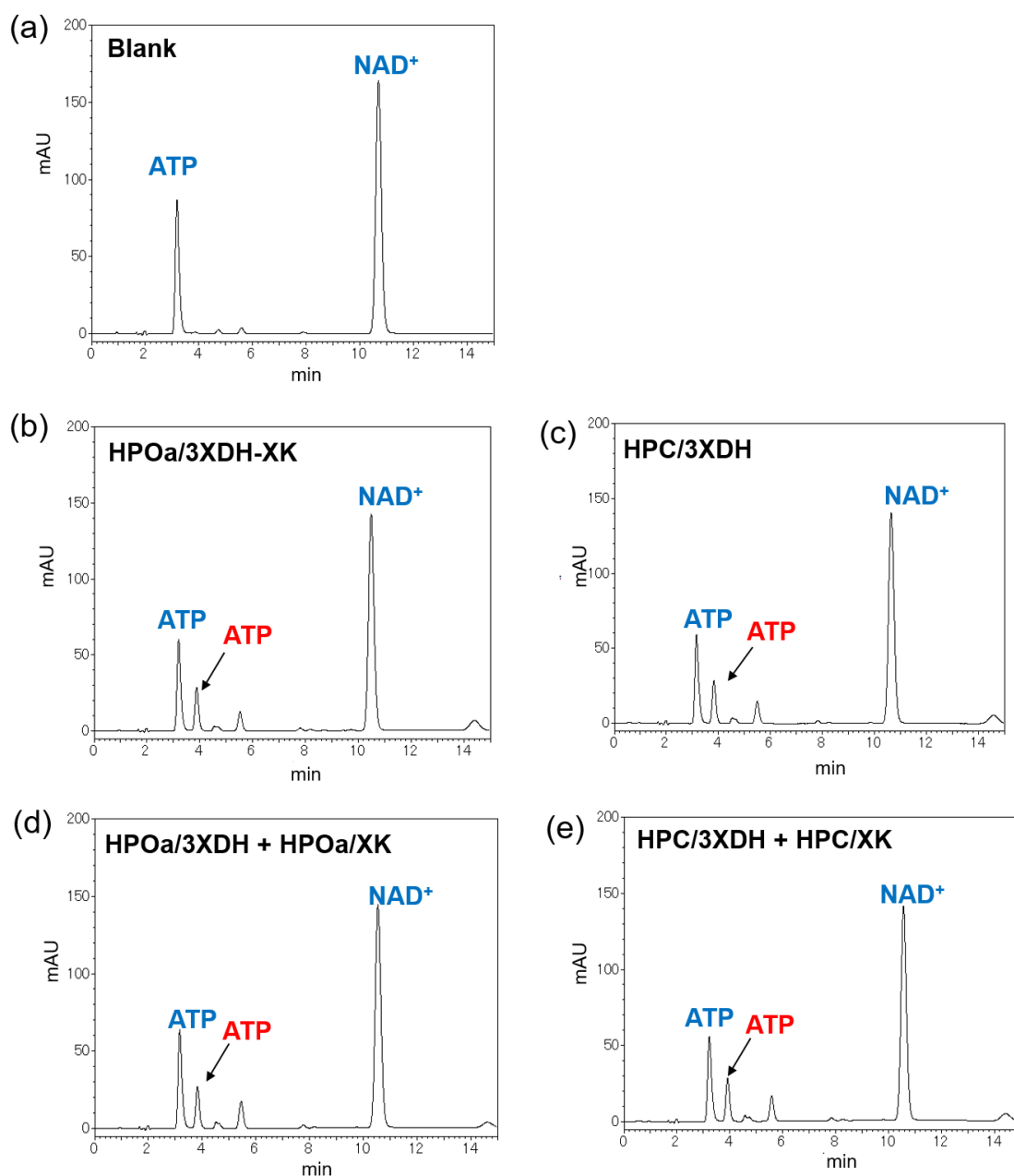
Figure 4.12. HPLC profiles of enzyme cascade reactions. (a) Blank (without enzyme); (b) HPOa/3XDH-XK; (c) HPC/3XDH; (d) HPOa/3XDH + HPOa/XK; (e) HPC/3XDH + HPC/XK. Enzymes were reacted with 300 mM xylitol, 2 mM NAD$^+$ and 1 mM ATP in the buffer (pH 7.0) containing 40 mM Tris-HCl, 20 mM acetic acid, 12.5 mM MgCl$_2$, 100 mM NaCl, 1 μM ZnCl$_2$, 0.002% Tween20, 5 μM BSA and 1 mM DTT at 25 ℃. In the reaction, DNA scaffold concentration was fixed to 0.6 nM, which corresponded to 1.5 nM HG-XDH and 0.4 nM AC-XK in the coassembly systems (HPOa/3XDH-XK or HPC/3XDH-XK), and 1.5 nM HG-XDH and 0.55 nM AC-XK in the separate systems (HPOa/3XDH + HPOa/XK or HPC/3XDH + HPC/XK) based on the enzyme loading yields on DNA scaffold. The peaks corresponding ATP, ADP and NAD$^+$ were indicated by arrows.

136
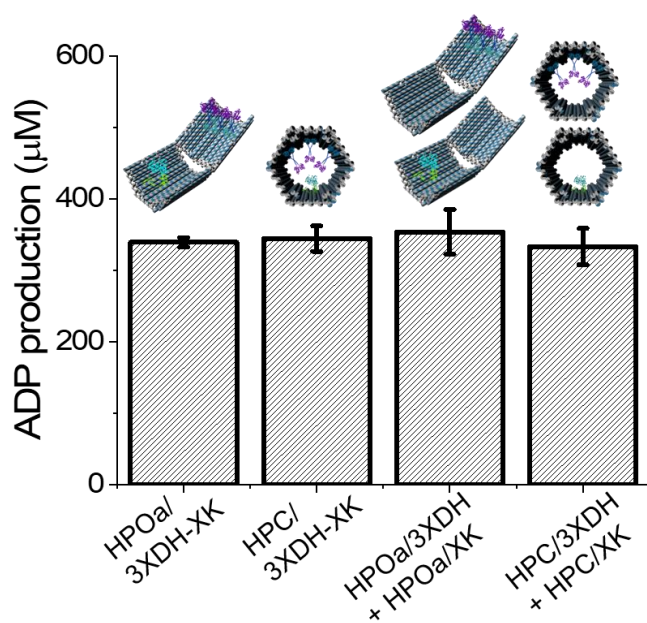
Figure 4.13. ADP production of enzyme cascade reactions on the DNA scaffold after 24-h reaction, ADP production was quantitated from Figure 4.12. Data were the averages of three independent repetitions, error bars indicated the S.D. of the repetitions.
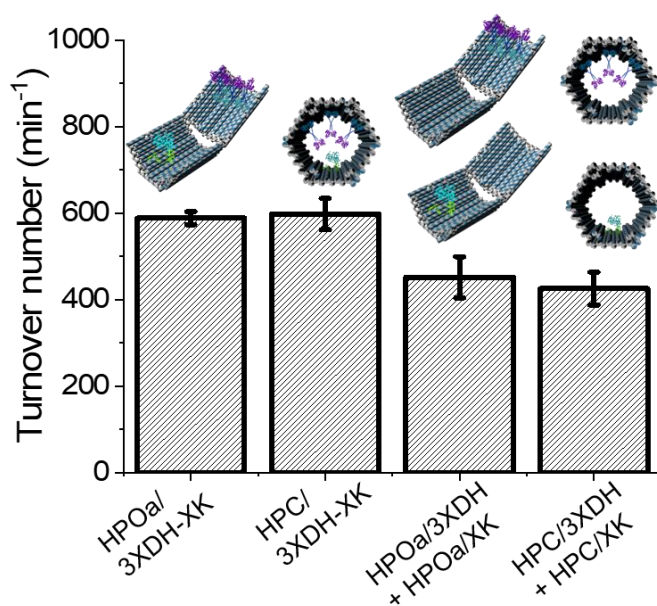
Figure 4.14. Turnover numbers of enzyme cascade reactions on the DNA scaffold. Turnover number of each reaction system was obtained from the amount of produced ADP divided by the concentration of the second enzyme AC-XK on DNA scaffold in the time unit (24 h). The loading yields of AC-XK in the coassembly and separate systems were 0.67 and 0.91 molecules of monomer, respectively. Data were the averages of three independent repetitions, error bars indicated the S.D. of the repetitions.

4.2.5. Inter-enzyme distance dependency of the XDH/XK cascade on DNA scaffold

The inter-enzyme distances of HG-XDH and AC-XK of HPOa/3XDH-XK in the fully open state and HPC/3XDH-XK were estimated to be 60 nm and 20 nm, respectively, while the inter-enzyme distance of the two enzymes in the separate systems (HPOa/3XDH + HPOa/XK or HPC/3XDH + HPC/XK) was estimated to be 1110 nm based on the concentration of DNA scaffold in the solution (Figure 4.15 a-c, Materials and Methods). The normalized turnover numbers were plotted against the inter-enzyme distances (Figure 4.15d). The turnover numbers were changed from 485 min^{-1} at 1110 nm to 580 min^{-1} at 60 nm to 600 min^{-1} at 20 nm, indicating that the inter-enzyme distance dependency was insignificant for the cascade reaction of XDH/XK on DNA scaffold.
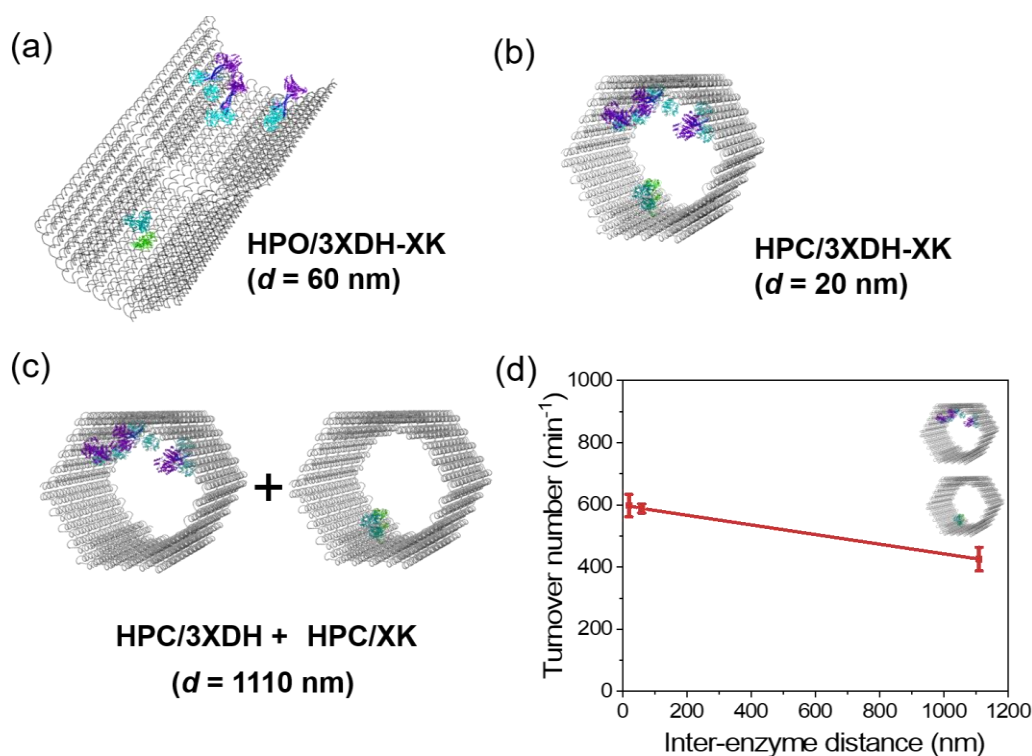
Figure 4.15. Estimation of inter-enzyme distance and inter-enzyme distance dependency. (a) Inter-enzyme distance of HPO/3XDH-XK. (b) Inter-enzyme distance of HPC/3XDH-XK. (c) Inter-enzyme distance of HPC/3XDH + HPC/XK (Materials and Methods). The molecular models were constructed by Discovery Studio (version 3.1, Accelrys Inc.). (d) The plot of normalized turnover number versus inter-enzyme distances. Data in (d) were the averages of three independent repetitions, error bars indicated the S.D. of the repetitions.

The K_m values of HG-XDH and AC-XK for xylitol and xylulose are 104 mM and 0.18 mM, respectively. The k_{cat} values of HG-XDH and AC-XK are 59 min^{-1} and 12600 min^{-1}, respectively, as shown in Table 4.2. Although enzyme cascade reactions by XDH/XK on the DNA scaffold were performed with the controlled stoichiometry of 3:1 (ratio of enzyme binding sites) for the HG-XDH dimer to the AC-XK monomer, the variation of the inter-enzyme distance from 60 nm to 20 nm was insufficient to obtain an evident distance dependency possibly due to the fast kinetics and the low K_m value of the second enzyme AC-XK.

In a sequential cascade with different reaction rates of V_{max1} and V_{max2} of the first and second enzymes, the final activity of all reactions will converge to the rate of the slower enzyme.[16] In the case of XDH-XK pair, the second enzyme XK is much faster than the first enzyme XDH, XK is the non-rate limiting enzyme. In the unimolecular system with the excess amount of ATP, the produced intermediate xylulose will be consumed by XK in a very efficient manner, the variation of distance from 60 nm to 20 nm will not affect the overall throughput.

Table 4.2. Kinetic parameters of HG-XDH and AC-XK

	HG-XDH[a]		AC-XK
	Xylitol [b]	NAD$^+$ [c]	Xylulose [d]
K_m (mM)	104.22 ± 16.26	0.358 ± 0.006	0.18
k_{cat} (min^{-1})	58.86 ± 2.63	50.10 ± 1.54	12600
k_{cat}/K_m (min^{-1}mM^{-1})	0.572 ± 0.070	140.0 ± 4.7	70000

[a] The enzyme assays were carried out at the enzyme concentration of 25 nM in a buffer (pH 7.0) containing 40 mM Tris-HCl, 20 mM acetic acid, 12.5 mM MgCl$_2$, 0.002% Tween20, 1 μM ZnCl$_2$ and 100 mM NaCl.

[b] Concentrations of xylitol were varied from 0 to 800 mM, and that of NAD$^+$ was kept at 2 mM for the assay. Data were the averages of three independent repetitions.

As previously reported in our lab, distinct inter-enzyme distance dependency on the cascade reaction efficiency was observed for the enzyme pair XR/XDH coassembled in the cavity of DNA scaffold with the variation of inter-enzyme distance from 98 nm to 10 nm.[13] First enzyme ZS-XR converts xylose to xylitol by consuming cofactor NADH, the resulting xylitol is then utilized by second enzyme G-XDH (GCN4 fused XDH) to produce xylulose with the regeneration of NADH (Figure 4.16a). The K_m value (for xylose) and k_{cat} value of ZS-XR were 256 mM and 125 min^{-1}, respectively (Table 4.3). The kinetic parameters for the enzymes in XR/XDH cascade are much more favourable than those for the XDH/XK cascade. In the bimolecular intermediates (xylitol and NAD⁺) transporting system, the clear inter-enzyme distance dependency of XR/XDH on DNA scaffold was observed shown in the NADH regeneration and turnover number (Figure 4.16b and Figure 4.16c).[13] The comparisons of enzyme pair XR/XDH and XDH/XK on DNA scaffold suggested that the dependency of inter-enzyme distance on the efficiency of cascade reaction only stands for the cascade enzymes with balanced kinetic parameters.

The effect of enzyme kinetics on the overall enzyme cascade efficiency have been well studied by Hess and coworkers.[15,16] By using the model enzyme GOx/HRP for simulation, it was proposed that if the second enzyme has a low K_m value, and the k_{cat} of the first enzyme is less than second enzyme (downstream enzyme faster), the probability of the waiting room (tunnel of intermediates) to be empty is high. Therefore, the downstream enzyme is not the rate-limiting enzyme. In the case that the upstream enzyme is much slower than the downstream enzyme, events occurring downstream do

not have any effect on the overall output rate.[15]
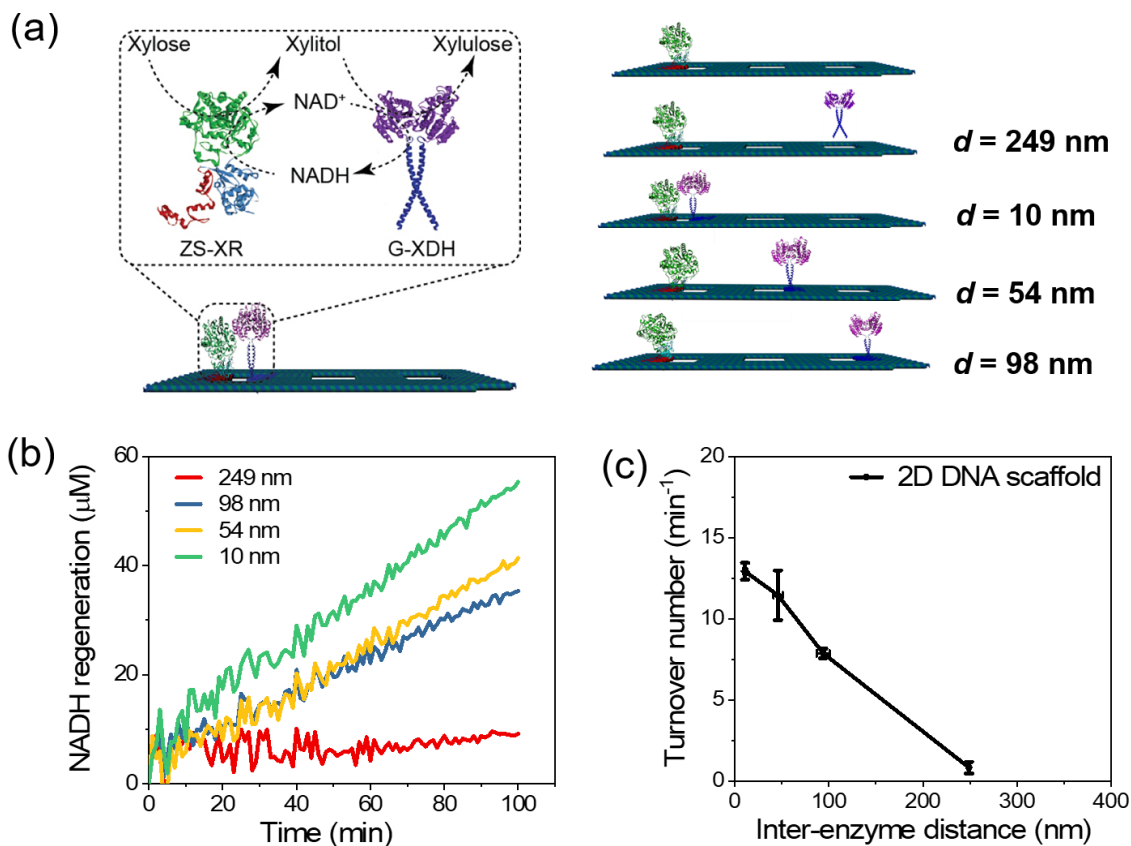
Figure 4.16. Inter-enzyme distance dependency of XR/XDH on a 2D DNA scaffold. (a) Scheme presenting XR/XDH enzyme cascade reactions on DNA scaffold with the variation of inter-enzyme distance from 98 nm to 10 nm. The inter-enzyme distance of DNA scaffolded ZS-XR and free G-XDH (GCN4 fused XDH) was estimated to be 249 nm base on the molecular concentration.[13] (b) NADH regeneration of XR/XDH enzyme cascade reactions on DNA scaffold in the first 100 min.[13] (c) A plot of turnover numbers of XR/XDH enzyme cascade reactions on the DNA scaffold against the inter-enzyme distance.[13] 85 nM ZS-XR and 85 nM G-XDH (monomer) were reacted with 12.5 mM xylose and 2 mM NADH in the buffer (pH 7.0) containing 40 mM Tris-HCl, 20 mM acetic acid, 12.5 mM $MgCl_2$, 0.02% Tween20, 1 μM $ZnCl_2$ and 100 mM NaCl. The turnover number for each system was calculated from the amount of product (regenerated NADH) divided by the concentration of the second enzyme G-XDH on DNA scaffold in the time unit (100 min). Data in (c) were the averages of three independent repetitions, error bars indicated the S.D. of the repetitions.

Table 4.3. Kinetic parameters of ZS-XR[a]

	ZS-XR	
	Xylose [b]	NADH [c]
K_m (mM)	256.4 ± 45.3	0.149 ± 0.011
k_{cat} (min^{-1})	124.6 ± 6.0	147.6 ± 0.8
k_{cat}/K_m (min^{-1}mM^{-1})	0.494 ± 0.072	994.3 ± 75.9

[a] The enzyme assays were carried out at the enzyme concentration of 25 nM in a buffer (pH 7.0) containing 40 mM Tris-HCl, 20 mM acetic acid, 12.5 mM MgCl$_2$, 0.002% Tween20, 1 μM ZnCl$_2$ and 100 mM NaCl. Data were the averages of three independent repetitions.

[b] Concentrations of xylose were varied from 0 to 500 mM, and that of NADH was kept at 300 μM for the assay.

[c] Concentrations of NADH were varied from 0 to 500 μM, and that of xylose was kept at 200 mM for the assay.

4.3. Conclusion

In summary, enzyme cascade XDH-XK was assembled on a 3D DNA scaffold with efficient dynamic shape transformation. The inter-enzyme distance was varied from 60 nm to 20 nm via the transition from open state to closed state of the DNA scaffold. The enzymes coencapsulated in the closed state displayed comparable overall cascade efficiency to that coassembled on the open state. These results indicate that the inter-enzyme distance is not the dominant factor for the cascade reaction where kinetic parameters of the cascade enzymes are imbalanced with the fast kinetics of second enzyme. Such an assumption is useful for the design of proximity for enzymes in efficient artificial metabolic pathway. The shape transformation of DNA nanostructure would be applicable for the construction of artificial metabolic pathway based on the consideration of enzyme kinetics.

4.4. Materials and Methods

4.4.1 Materials

The single-stranded M13mp18 viral DNA (7249) was purchased from Guild Biosciences. BC-GLA-NHS (S9237S), and bovine serum albumin (BSA, BS9000S) were purchased from New England Biolabs. 5-chlorohexane (CH) derivative [HaloTag Succinimidyl Ester (O2) Ligand (P1691)] was purchased from Promega. β-Nicotinamide adenine dinucleotide in oxidized form (NAD^+) was obtained from Oriental Yeast (Tokyo, Japan). Adenosine triphosphate (ATP) was obtained from Sigma-Aldrich (St. Louis, MO). Xylitol and all other chemicals and reagents were purchased from Wako Chemicals (Tokyo, Japan) or Nacalai Tesque (Kyoto, Japan). Sephacryl S-400 were purchased from GE Healthcare Japan Inc. (Tokyo, Japan). COSMOSIL packed column PBr (4.6 mm i.d. × 150 mm), and HPLC grade methanol were purchased from Nacalai tesque (Kyoto, Japan). Phosphate buffer (PB, pH 7.0) was prepared as 20 mM Na_2HPO_4 and 20 mM NaH_2PO_4.

4.4.2 Expression of enzymes HG-XDH and AC-XK

Construction of the expression vectors for HG-XDH and AC-XK, and overexpression and purification of enzymes were carried out as previously reported.[20,22]

4.4.3 Design of DNA scaffold

The DNA scaffold was designed in a honeycomb lattice using the open source software caDNAno (v 2.2.0.).[29] The caDNAno blueprints of the DNA scaffold with enzymes HG-XDH and AC-XK attachment sites were shown in Figure 4.17.
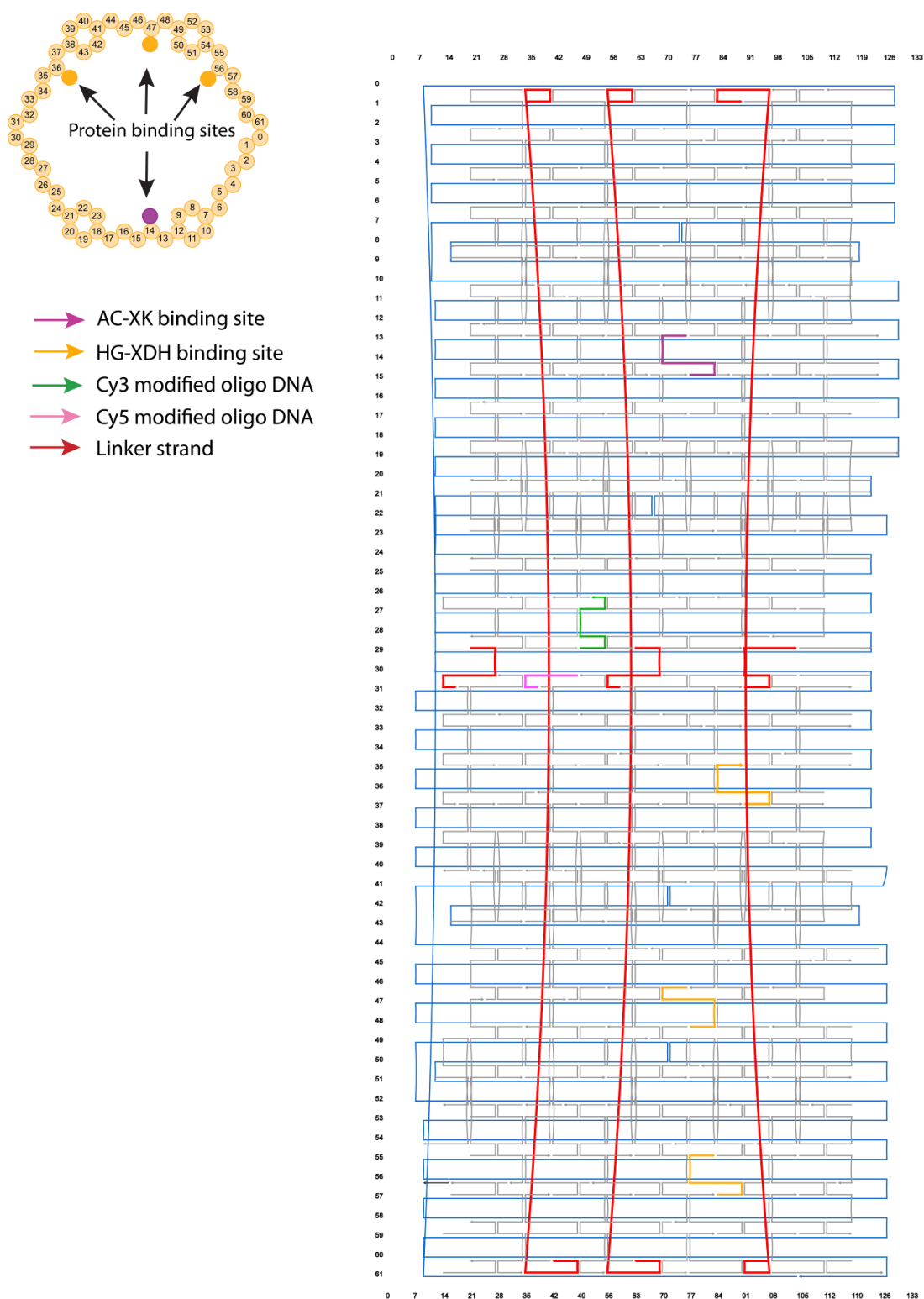
Figure 4.17. Front view and blueprint modified from caDNAno[29] software interface of DNA scaffold (http://cadnano.org/) with linker strands. The staple strand shown in purple was enzyme AC-XK binding site, staple strands shown in orange were enzyme HG-XDH binding sites. The staple strand shown in green shown in green was Cy3-modified oligo, the staple strand shown in pink was Cy5-modified oligo. The staple strands shown in red were linker strands of DNA scaffold.

4.4.4 Preparation of the DNA Scaffold

The open state of DNA scaffold was constructed with the 6 positions of linker strands left unhybridized. DNA scaffold was annealed as previously described.[14,30] The details of were shown in 2.4.4 in Chapter 2. The concentration of DNA scaffold was quantified by the absorbance at 260 nm (Nanodrop, Thermo Fisher Scientific Inc.) using the determined extinction coefficient of DNA scaffold ($1.2 \times 10^8 \, \text{M}^{-1}\text{cm}^{-1}$).[22]

4.4.5 Preparation of the DNA origami scaffold assembled with enzymes

DNA scaffolds were constructed with three hairpin DNA binding sites modified with 5-chlorohexane (CH) derivative for HG-XDH and/or one binding site modified with BC-GLA-NHS (BC) for AC-XK (Table 4.4). A 10 nM DNA scaffold with the binding sites was incubated with 200 nM HG-XDH and/or AC-XK in a buffer (pH 7.0) containing 40 mM Tris-HCl, 20 mM acetic acid, and 12.5 mM $MgCl_2$, 5 mM β-mercaptoethanol, 0.002% Tween 20 and 1 μM $ZnCl_2$ at 4 °C for 1 h. The mixture was purified by gel filtration (500 μL in volume of S-400) in an Ultrafree-MC-DV column with a buffer (pH 7.0) containing 40 mM Tris-HCl, 20 mM acetic acid, and 12.5 mM $MgCl_2$ to remove the unbound proteins. The concentration of DNA scaffold-protein assembly was estimated from the absorbance at 260 nm by using the extinction coefficient of DNA scaffold ($1.2 \times 10^8 \, \text{M}^{-1}\text{cm}^{-1}$).[22]

Table 4.4. Nucleotide sequences for the staple strands containing the binding sites for HG-XDH with CH modification and binding site for AC-XK with BC modification[20]

Oligo DNA	Sequence (from 5' to 3')
Binding site 1	TACCAGATTAAGACGT^{CH}TCATGAGTCATGAGTTTTCT^{CH}CATG ACTCATGAACTCCTTATCGATTGA
Binding site 2	TGTAAATGATAGCTGT^{CH}TCATGAGTCATGAGTTTTCT^{CH}CATG ACTCATGAACTAGATTATTAATTA
Binding site 3	ATAACATGCAACAGGT^{CH}TCATGAGTCATGAGTTTTCT^{CH}CATG ACTCATGAACGAAAAACGTAAGAA
Binding site 4	ATTGCATAGGATTACTTATGCCACGTAGCGTT^{BG}TTCGCTACGT GGCATAAGGAGAGTAGAAGTTT

CH modified amino-C6-T was denoted as **T^{CH}**

BC modified amino-C6-T was denoted as **T^{BC}**

4.4.6 Closing process of the DNA scaffold equipped with enzymes

The purified DNA scaffolded enzymes were incubated in the absence or the presence of DNA linkers to obtain the control samples or the closed state encapsulated with enzymes. The open state of DNA scaffold was first constructed with the 6 positions of linker strands left unhybridized, after the assembly of enzymes, the corresponding 6 linker strands (Table 4.5) were added in a 1:1 molar ratio. Typically, 5 nM DNA scaffold in the open state was hybridized with 5 nM linker strands in the Microplate (Greiner Microplate, 96-well, PS, F-bottom (chimney well) µCLEAR®, black, non-binding) in the buffer (pH 7.0) containing 40 mM Tris-HCl, 20 mM acetic acid, 12.5 mM MgCl$_2$, 5 µM BSA and 0.002% Tween 20 at 25 °C for 12 h.

Table 4.5. Nucleotide sequences of linker strands of DNA scaffold

Oligo DNA	Sequence (from 5' to 3')
Linker strand 1	AGAGTAGGATGAATCAATCGGCCAGTTTGGAACAAGAGCTTGA
Linker strand 2	ACGGTGACGAGAGGCCCTGTTTTATTAAAGAACGTGTAAAGGG
Linker strand 3	CGTAGCAAGGAACCTACAGTTAATGCCCCCGCC
Linker strand 4	GCTTAATGACTCCTCGTTTTAACGGGGTCCTTG
Linker strand 5	AAGCCAACCCAGAATTGATGATGGGGTTTTGCTCAG
Linker strand 6	TTTAACAAGGTGCCGAAAACCGGCGGTCCACGCTGGGGTGGTT

146

4.4.7 Fluorescence measurements and FRET analysis

Fluorescence measurements were carried out on a microplate reader (TECAN Infinite® 200Pro). Fluorescence spectra of the samples were measured from 550 nm to 750 nm upon excitation at 520 nm in the 96-plate [Greiner Microplate, 96-well, PS, F-bottom (chimney well) μCLEAR®, black, non-binding] with 5 nm bandwidth. To study the kinetics of closing process, the time courses of Cy3 fluorescence intensity ($\lambda_{ex} = 520$ nm, $\lambda_{em} = 570$ nm) and Cy5 fluorescence intensity ($\lambda_{ex} = 520$ nm, $\lambda_{em} = 670$ nm) were monitored.

4.4.8 Calculation of the closing efficiency

The closing efficiency of DNA scaffold was estimated by the Cy5 fluorescence intensity upon excitation of donor Cy3 at 520 nm in the fluorescence emission spectra after the closing process for 12-h. The calculation followed the formula: $Y = (I_{HPO-control} - I_{HPO + linkers})/(I_{HPO-control} - I_{HPC-control})$. Here $I_{HPO-control}$, $I_{HPC-control}$ and $I_{HPO + linkers}$ indicated the Cy5 fluorescence intensity of HPO-control, HPC-control and HPO + linkers in the fluorescence emission spectra after 12-h incubation or hybridization, respectively. Y indicated the percentage of closed structures.

4.4.9 AFM imaging and statistical analysis

The methods of AFM imaging and statistical analysis were shown in 2.4.6 in Chapter 2. The binding of HG-XDH and/or AC-XK was counted for only HG-XDH and/or AC-XK bound to the perfectly folded DNA scaffold.

4.4.10 Enzyme assay of HG-XDH

The methods of enzyme assay of HG-XDH were shown in 2.4.10.2 in Chapter 2. Enzyme activities were measured on the microplate [Greiner Microplate, 655901, 96-well, PS, F-bottom (chimney well) clear, non-binding].

4.4.11 Analysis of the enzyme cascade reaction

Enzymes HG-XDH and AC-XK reacted with 300 mM xylitol, 2 mM NAD$^+$ and 1 mM ATP in the buffer (pH 7.0) containing 40 mM Tris-HCl, 20 mM acetic acid, 12.5 mM MgCl$_2$, 100 mM NaCl, 1 μM ZnCl$_2$, 0.002% Tween20, 5 μM BSA and 1 mM DTT at 25 ℃. In the reaction, each DNA scaffold concentration was fixed to 0.6 nM, which was equal to 1.5 nM HG-XDH and 0.4 nM AC-XK in the coassembly systems (HPOa/3XDH-XK or HPC/3XDH-XK), and 1.5 nM HG-XDH and 0.55 nM AC-XK in the separate systems (HPOa/3XDH + HPOa/XK or HPC/3XDH + HPC/XK) calculated based on the enzyme loading yields on DNA scaffold. HPOa/3XDH-XK, HPOa/XDH and HPOa/XK denoted the samples of HPO/3XDH-XK, HPO/XDH and HPO/XK treated with the same incubation process in the absence of DNA linkers.

The amounts of cofactors (ATP, ADP, NADH, and NAD$^+$) were monitored by HPLC at 260 nm. HPLC conditions: COSMOSIL packed column PBr (4.6 mm i.d. × 150 mm); eluent A, 10% methanol in 20 mM phosphate buffer (pH 7.0); eluent B, 50% methanol in 20 mM phosphate buffer (pH 7.0); gradient of eluent B increased from 0% to 20% in 1 min and to 30% in 10 min at a flow rate of 1 mL/min. The enzyme reactions were quenched by an addition of TFA to the final concentration of 0.1%.

4.4.12 Calculation of the inter-enzyme distance of HPC/3XDH + HPC/XK

HPC/3XDH   HPC/XK
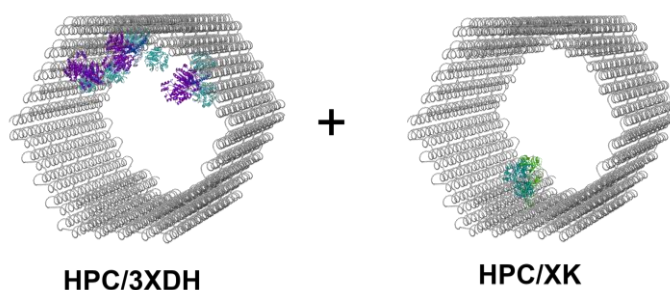
In a 1 M enzyme solution, there are 6×10^{23} molecules/liter (0.6 molecules/nm^3) or inverting, the volume per molecule is $V = 1.66$ nm^3/molecule at 1 M.[31] Therefore, for a concentration C, the volume per molecule is $V = 1.66/C$. If we

take the cube root of the volume per molecule, the average distance (d) will indicate in the equation: $d = 1.18/C^{1/3}$, where C is in molar and d is in nanometer. In a solution containing 0.6 nM DNA scaffold assembled with HG-XDH (HPC/3XDH) and 0.6 nM DNA scaffold assembled with AC-XK (HPC/XK), the total concentration of DNA scaffold was 1.2 nM. Based on the equation, the average separation of molecules was 1110 nm.

4.4.13 Turnover numbers normalized by the AC-XK concentrations

The produced ADP depends on the concentration of downstream enzyme AC-XK since the concentration of first enzyme HG-XDH was fixed to the same value. The turnover number for each system was calculated from the amount of products (ADP) divided by the concentration of the second enzyme AC-XK on DNA scaffold in the time unit (24 h). The calculation was shown as followed:

$$TN_{coassembly} = \frac{[ADP]_{cossembly}}{[AC-XK]_{coassembly} \times \Delta t} = \frac{[ADP]_{coassembly}}{0.6\ nM \times 0.67 \times 24\ h}$$

$$TN_{separate} = \frac{[ADP]_{separate}}{[AC-XK]_{separate} \times \Delta t} = \frac{[ADP]_{separate}}{0.6\ nM \times 0.91 \times 24\ h}$$

Here $TN_{coassembly}$ indicated the turnover number of coassembly system (HPOa/3XDH-XK or HPC/3XDH-XK), $TN_{separate}$ indicated the turnover number of separate system (HPOa/3XDH + HPOa/XK or HPC/3XDH + HPC/XK). In the reaction, each DNA scaffold concentration was fixed to 0.6 nM, the enzyme loading yields of AC-XK in coassembly systems and separate systems were 0.67 and 0.91 molecules of monomer, respectively.

4.5 References

1.   Wheeldon, I. *et al.* Substrate channelling as an approach to cascade reactions. *Nat. Chem.* **8**, 299–309 (2016).

2.   Conrado, R. J., Varner, J. D. & DeLisa, M. P. Engineering the spatial organization of metabolic enzymes: mimicking nature's synergy. *Curr. Opin. Biotechnol.* **19**, 492–499 (2008).

3.   Miles, E. W., Rhee, S. & Davies, D. R. The molecular basis of substrate channeling. *J. Biol. Chem.* **274**, 12193–12196 (1999).

4.   Wu, F. & Minteer, S. Krebs cycle metabolon: structural evidence of substrate channeling revealed by cross-linking and mass spectrometry. *Angew. Chemie., Int. Ed.* **54**, 1851–1854 (2015).

5.   Bonacci, W. *et al.* Modularity of a carbon-fixing protein organelle. *Proc. Natl. Acad. Sci.* **109**, 478–483 (2012).

6.   Dueber, J. E. *et al.* Synthetic protein scaffolds provide modular control over metabolic flux. *Nat. Biotechnol.* **27**, 753–759 (2009).

7.   Chen, L., Mulchandani, A. & Ge, X. Spore-displayed enzyme cascade with tunable stoichiometry. *Biotechnol. Prog.* **33**, 383–389 (2017).

8.   Xin, L., Zhou, C., Yang, Z. & Liu, D. Regulation of an enzyme cascade reaction by a DNA machine. *Small* **9**, 3088–3091 (2013).

9.   Wilner, O. I. *et al.* Enzyme cascades activated on topologically programmed DNA scaffolds. *Nat. Nanotechnol.* **4**, 249–254 (2009).

10.   Fu, J., Liu, M., Liu, Y., Woodbury, N. W. & Yan, H. Interenzyme substrate diffusion for an enzyme cascade organized on spatially addressable DNA nanostructures. *J. Am. Chem. Soc.* **134**, 5516–5519 (2012).

11.   Zhang, Y., Tsitkov, S. & Hess, H. Proximity does not contribute to activity enhancement in the glucose oxidase-horseradish peroxidase cascade. *Nat. Commun.* **7**, (2016).

12. Hinzpeter, F., Gerland, U. & Tostevin, F. Optimal compartmentalization strategies for metabolic microcompartments. *Biophys. J.* **112**, 767–779 (2017).

13. Ngo, T. A., Nakata, E., Saimura, M. & Morii, T. Spatially organized enzymes drive cofactor-coupled cascade reactions. *J. Am. Chem. Soc.* **138**, 3012–3021 (2016).

14. Douglas, S. M., Bachelet, I. & Church, G. M. A logic-gated nanorobot for targeted transport of molecular payloads. *Science.* **335**, 831–834 (2012).

15. Zhang, Y. & Hess, H. Toward rational design of high-efficiency enzyme cascades. *ACS Catal.* **7**, 6018–6027 (2017).

16. Tsitkov, S., Pesenti, T., Palacci, H., Blanchet, J. & Hess, H. Queueing theory-based perspective of the kinetics of 'channeled' enzyme cascade reactions. *ACS Catal.* **8**, 10721–10731 (2018).

17. Watanabe, S., Kodaki, T. & Makino, K. Complete reversal of coenzyme specificity of xylitol dehydrogenase and increase of thermostability by the introduction of structural zinc. *J. Biol. Chem.* **280**, 10340–10349 (2005).

18. Pival, S. L., Birner-Gruenberger, R., Krump, C. & Nidetzky, B. D-Xylulose kinase from *Saccharomyces cerevisiae*: isolation and characterization of the highly unstable enzyme, recombinantly produced in *Escherichia coli*. *Protein Expr. Purif.* **79**, 223–230 (2011).

19. Nakata, E., Dinh, H., Ngo, T. A., Saimura, M. & Morii, T. A modular zinc finger adaptor accelerates the covalent linkage of proteins at specific locations on DNA nanoscaffolds. *Chem. Commun.* **51**, 1016–1019 (2015).

20. Nguyen, T. M., Nakata, E., Saimura, M., Dinh, H. & Morii, T. Design of modular protein tags for orthogonal covalent bond formation at specific DNA sequences. *J. Am. Chem. Soc.* **139**, 8487–8496 (2017).

21. Nguyen, T. M. *et al.* Rational design of a DNA sequence-specific modular protein tag by tuning the alkylation kinetics. *Chem. Sci.* **10**, 9315–9325 (2019).

22. Lin, P. *et al.* Evaluation of the role of the DNA surface for enhancing the activity

of scaffolded enzymes. *Chem. Commun.* **57**, 3925–3928 (2021).

23. Greisman, H. A. & Pabo, C. O. A general strategy for selecting high-affinity zinc finger proteins for diverse DNA target sites. *Science* **275**, 657–661 (1997).

24. Gautier, A. et al. An engineered protein tag for multiprotein labeling in living cells. *Chem. Biol.* **15,** 128–136 (2008).

25. Burton, R. M. & Kaplan, N. O. The reaction of reduced pyridine nucleotides with acid. *Arch. Biochem. Biophys.* **101**, 150–159 (1963).

26. Wu, J. T., Wu, L. H. & Knight, J. A. Stability of NADPH: effect of various factors on the kinetics of degradation. *Clin. Chem.* **32**, 314–319 (1986).

27. Walsh, K. A., Daniel, R. M. & Morgan, H. W. A soluble NADH dehydrogenase (NADH: ferricyanide oxidoreductase) from *Thermus aquaticus strain* T351. *Biochem. J.* **209**, 427–33 (1983).

28. Rover, L. *et al.* Study of NADH stability using ultraviolet-visible spectrophotometric analysis and factorial design. *Anal. Biochem.* **260**, 50–55 (1998).

29. Douglas, S. M. *et al.* Rapid prototyping of 3D DNA-origami shapes with caDNAno. *Nucleic Acids Res.* **37**, 5001–5006 (2009).

30 Amir, Y., Ben-Ishay, E., Levner, D., Ittah, S., Abu-Horowitz, A., & Bachelet, I. Universal computing by DNA origami robots in a living animal. *Nat. Nanotechnol.* **9**, 353-357 (2014).

31. Erickson, H. P. Size and shape of protein molecules at the nanometer level determined by sedimentation, gel filtration, and electron microscopy. *Biol. Proced. Online* **11**, 32–51 (2009).

CHAPTER 5

A dynamic DNA scaffold with fast transformation kinetics and its application for the assembly of unstable enzyme

5.1. Introduction

The enzymatic cascade reactions embedded in the confined cellular environment implements complex biochemical processes. Multiple enzymes aligned on the cellular scaffold like membrane would benefit a direct transfer of intermediates and/or reactants in low concentrations that allows the high reaction velocity and selectivity.[1] Direct[2,3] and indirect[4] evidence are provided the transient assembly of metabolon by the sequential enzymes to facilitate channeling of intermediates, where the assembly and disassembly of the enzyme complexes regulate the cascade reaction. Featuring the structural programmability and accurate addressability, diverse DNA nanostructures have been created as the templates of enzymes with precise control over the nanoscale arrangement and the stoichiometry of them.[5–7] The dynamic DNA origami devices with controllable translational, rotational or more sophisticated movements triggered by DNA sequences,[8–11] aptamer,[12,13] ion,[14,15] pH,[16,17] temperature,[18,19] light,[20,21] or electric fields,[22] provide broad applications in different fields.

Dependency of the cascade reaction efficiency on the inter-enzyme distance, one of the spatial factors found in the assembly of enzyme, has been investigated extensively with the static DNA structures or the dynamic DNA devices. While the distance dependency of enzyme cascade reactions has been observed for several enzyme pairs,[23] the actual mechanism for the observed distance dependency of GOx/HRP cascade enzymes arouse much controversy. The observed distance dependency of GOx/HRP cascade enzyme reaction was questioned from the kinetic aspect of intermediate diffusion process, which led to a proposal that modulation of the local pH near enzyme contributed to the factor enhancing the efficiency of GOx/HRP system. However, this was not the case for the XR/XDH cascade reaction.[24] As speculated for the confined cellular environment, the confined 3D DNA space was suggested to provide a more favorable environment for enzyme cascade reactions, as proved for

GOx/HRP encapsulated into 3D tubular DNA reactor fabricated by gluing two tubular DNA origami units, one assembled with GOx and another with HRP. It was proposed the intermediates might be unable to diffuse through the barriers of the origami unit.[25] Similarly, as reported by Fu *et al.*, the cascade efficiency of GOx/HRP entrapped within a short nanotube was significantly higher than that on the planar rectangle.[26] The cascade reaction by the same enzyme pair positioned in an intact DNA cage was studied to suggest that the ordered hydration layer formed by the DNA nanocage enhance the stability of active enzyme conformations.[27] Despite these proposals, the role of the confined 3D DNA environment is still unclear.

In this study, a hexagonal prism DNA nanostructure was designed to transform its shape from the 2D-like open to the 3D closed state with fast kinetics induced by toehold-mediated strand displacement mechanism.[9,28] As a proof-of-principle application of the system, the cascade enzymes derived from the D-xylose metabolic pathway, XR and XDH, were assembled on the DNA scaffold.[12] The bimolecular transportation of xylitol and NAD^+ from XR to XDH with recycling of the cofactor NADH were investigated with the shape transformation of the scaffold from 2D to 3D. The closed state displayed a higher cascade reaction efficiency compared to the open state. The same cascade reaction was further verified by directly anchoring the enzymes to the open state or encapsulating into the closed state in the static form. The observed enhancement of cascade reaction efficiency exceeded that expected from the inter-enzyme distance on 2D scaffold, indicating that confined space of 3D DNA scaffold likely contributed further to the efficiency expected from the inter-enzyme distance-dependent effect. The 3D DNA nanostructure with the fast dynamic shape transition is useful for studying the temporal character of metabolon and in developing sophisticated metabolic pathways *in vitro*, and drug delivery systems and tools in synthetic biology.

5.2. Results and discussions

5.2.1. Construction and characterization of DNA scaffold

A 3D DNA hexagonal prism (HP) consisted of two square pyramidal domains which were fused in the rear single-stranded scaffold hinges with the dimensions of 35 nm × 35 nm × 45 nm was constructed in the open or the closed states with a slight modification of previous report.[12] The 2D-like open state (HPO_T) was designed with six protruding single-stranded long lock strands and six short lock strands in upper and lower domains, respectively. The long lock strands were pre-annealed with opening keys (OPK) applicable for the toehold-mediated strand displacement mechanism to keep the DNA scaffold open. The 3D closed state (HPC_T) of hexagonal prism was folded by the six corresponding side locks with long lock strands and short lock strands hybridized with each other (Figure 5.1).

Open state (HPO_T)　　　　**Closed state (HPC_T)**
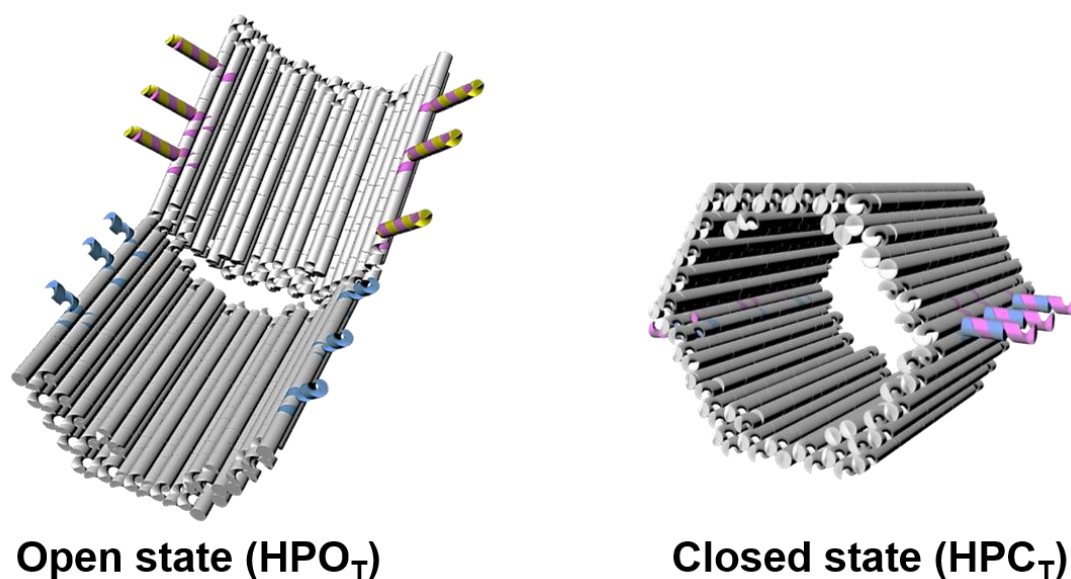
Figure 5.1. Models of DNA scaffold in the open state (HPO_T) and the closed state (HPC_T) for the toehold-mediated strand displacement. Open state (HPO_T) was folded with excess opening keys (1:10) and closed state (HPC_T) was folded with 6 side locks. The staple strands in gold, purple and blue indicated the opening key, long lock strand and short lock strand, respectively. The models were constructed by Autodesk Maya (Autodesk® Maya® 2020).

The resulting DNA scaffolds were characterized by means of atomic force microscopy (AFM), in which the yield of well-formed DNA scaffold in the open state (HPO$_T$) was estimated to be 92% (322/350). The closed structures were easily broken or opened by AFM cantilever, thus quantification of the yield of closed state (HPC$_T$) was difficult to estimate by AFM images (Figure 5.2, Figure 5.3 and Figure 5.4). The transmission electron microscopy (TEM) images of DNA scaffold in the open and the closed states were shown in Figure 5.5. The yield of well-formed closed state was estimated to be 92% (187/203) with the sizes measured by TEM being well consistent with the designed dimensions.
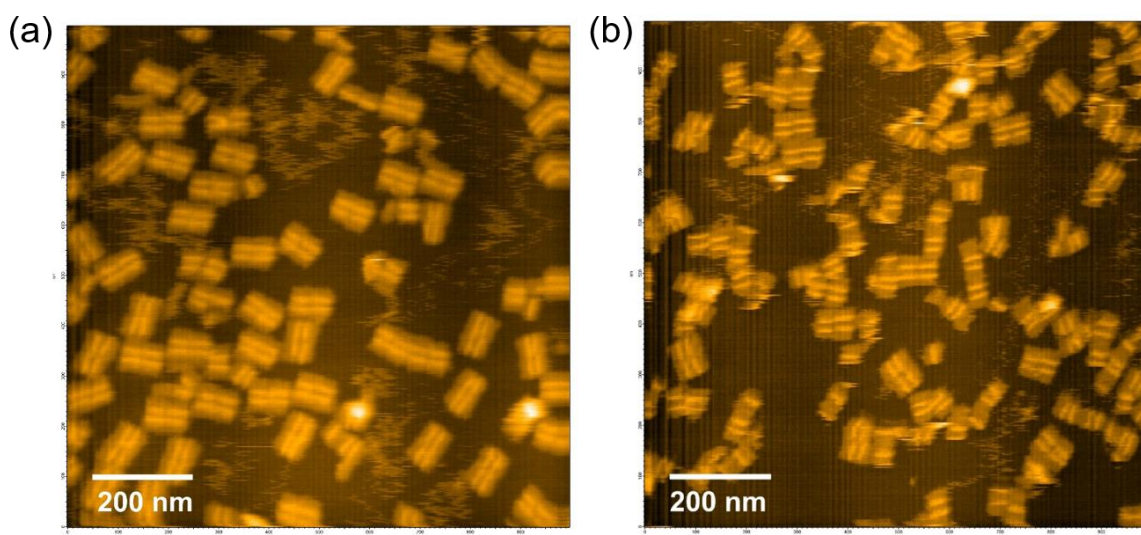
Figure 5.2. AFM images of DNA scaffold in the open and the closed states. (a) The open state annealed with 1: 10 OPK (HPO$_T$). The yield of well-formed DNA scaffold in the open state was estimated to be 92% (322/350). (b) The closed state constructed with 6 side locks designed for the toehold-mediated strand displacement mechanism (HPC$_T$). The closed structures were easily opened or broken by cantilever during the AFM measurements as shown in Figure 5.3 and Figure 5.4.

Figure 5.3. Schemes representing the closed structures (HPC$_T$) broken or opened during AFM measurements.

Figure 5.4. AFM images of closed structures (HPC$_T$) broken or opened during AFM measurements. The arrows indicated the typical images of broken or opened structures.

Figure 5.5. TEM images of the DNA scaffold. (a) TEM images of DNA scaffold in the open state (HPO$_T$), scale bar: 50 nm. The expanded images of typical open state were shown in right side, scale bar: 50 nm. (b) TEM images of DNA scaffold in th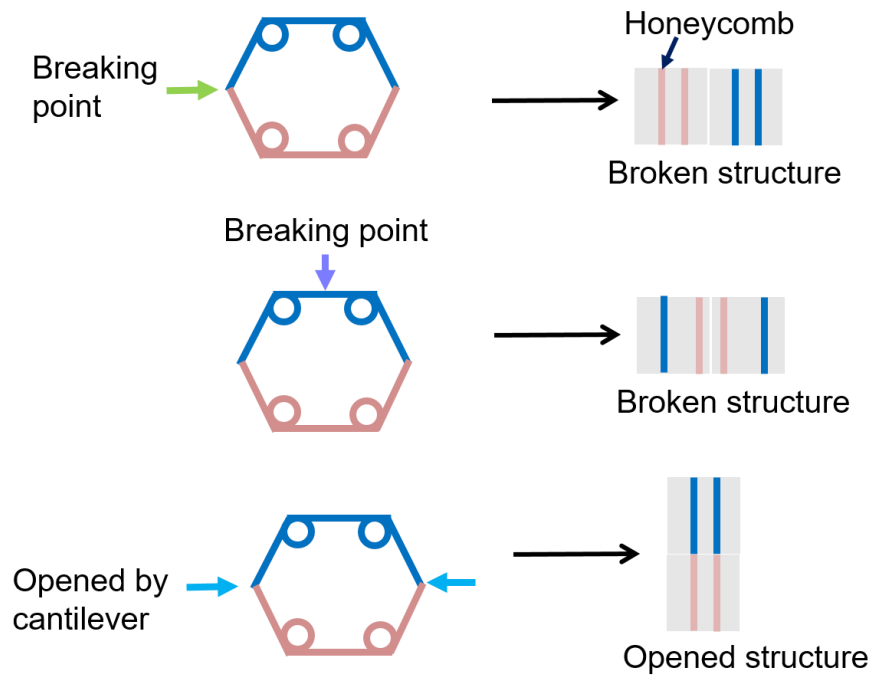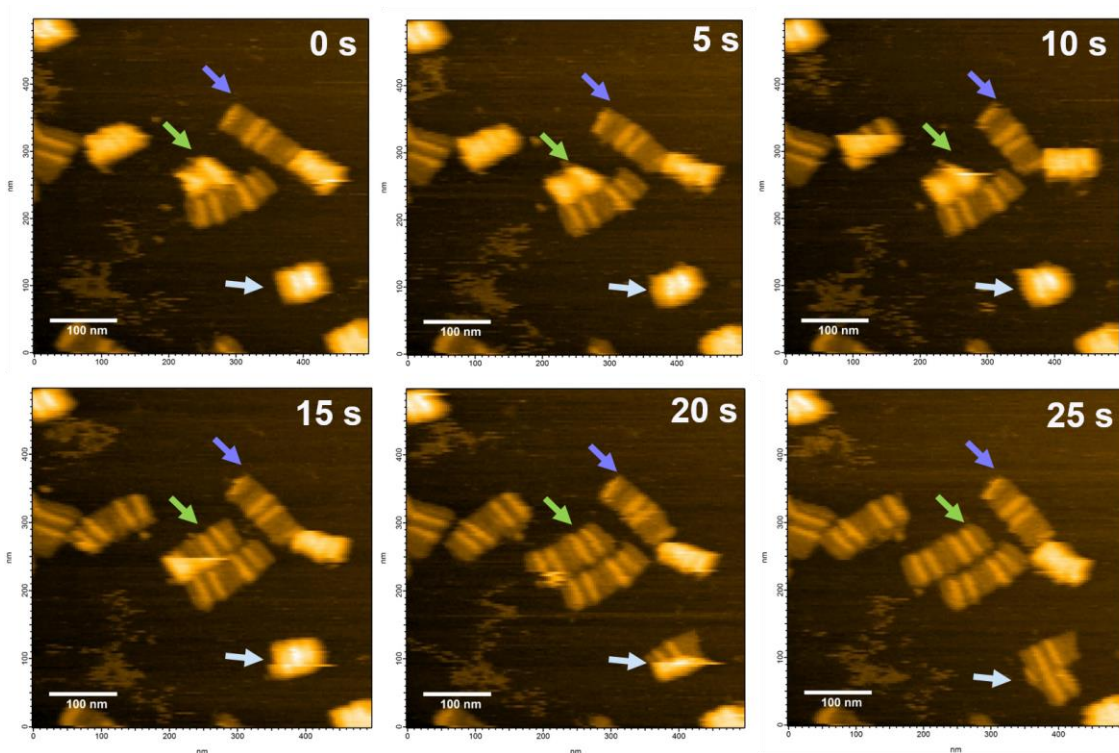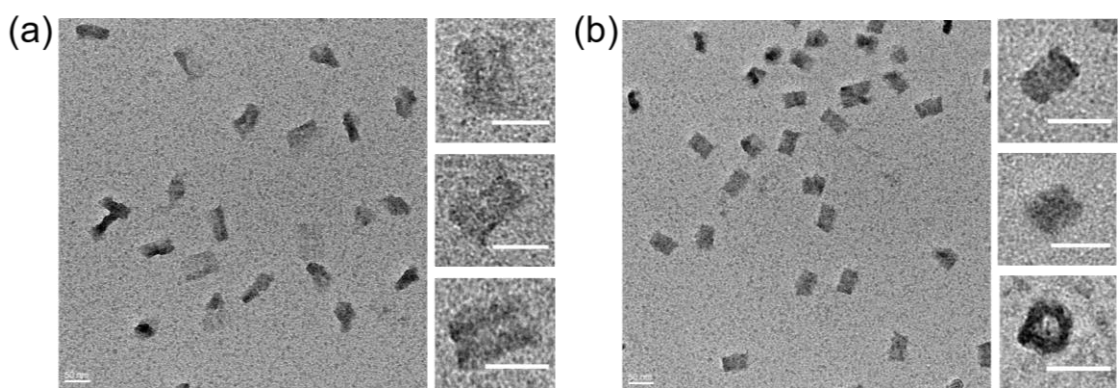e closed state (HPC$_T$), scale bar: 50 nm. The expanded images of typical closed state were shown in the right side, scale bar: 50 nm. The well-formed yield of closed state was estimated to be 92% (187/203) from TEM images.

Föster resonance energy transfer (FRET)[29] was used to further distinguish the open and closed states of DNA scaffold. One pair of Cy3 (donor fluorophore) and Cy5 (acceptor fluorophore) was attached at the edge of each square pyramidal domain with the theoretical distance of 25 nm in fully open HPO$_T$ and within 1 nm in HPC$_T$ (Figure 5.6a). The fluorescence spectra of HPO$_T$ (green curve) and HPC$_T$ (red curve) were obtained upon the donor excitation (λ_{ex} = 520 nm). The far distance of two fluorophores resulted in the primary emission of donor (Cy3) at 570 nm in the HPO$_T$, while the acceptor (Cy5) fluorescence emission peak at 670 nm implied the strong energy transfer between the two dyes in HPC$_T$ (Figure 5.6b).

The difference of fluorescence energy transfer was supported by gel electrophoretic analyses. HPO$_T$ displayed strong gel band intensity in Cy3 channel (λ_{ex} = 532 nm, λ_{em} = 605 nm), while HPC$_T$ displayed strong band intensity in FRET channel (λ_{ex} = 532 nm, λ_{em} = 695 nm) under gel imager. The faster mobility of HPC$_T$ over HPO$_T$ supported the more compact structure of HPC$_T$ in the closed state (Figure 5.7).
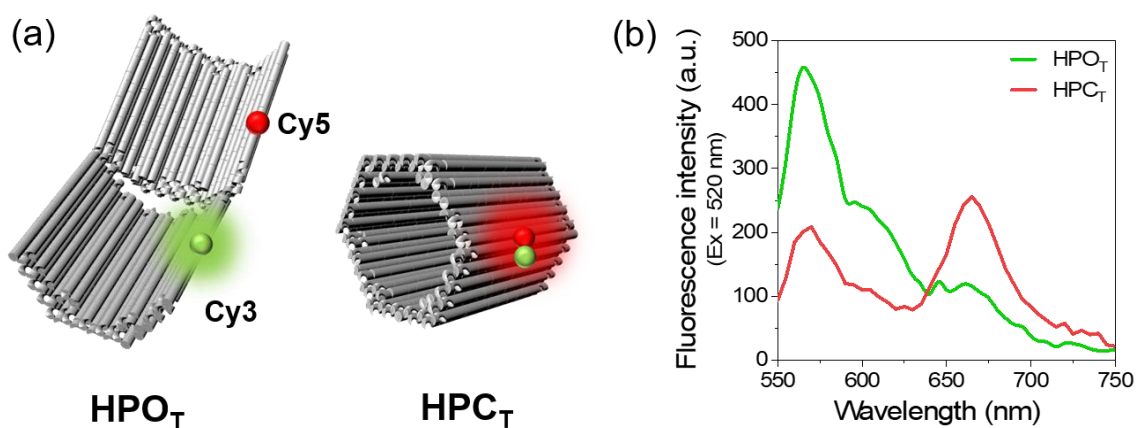
Figure 5.6. FRET analyses of DNA scaffold in the open and closed states (HPO_T and HPC_T). (a) Models representing the attachment sites of fluorophores Cy3 (donor, indicated in green) and Cy5 (acceptor, indicated in red) to the open and closed state of DNA scaffold. (b) Fluorescence emission spectra of the open state (HPO_T) and the closed state (HPC_T) excited at 520 nm. 5 nM HPO_T or HPC_T was scanned in the buffer (pH 7.0) containing 40 mM Tris-HCl, 20 mM acetic acid, 12.5 mM $MgCl_2$ and 0.002% Tween20 at 25 ℃.
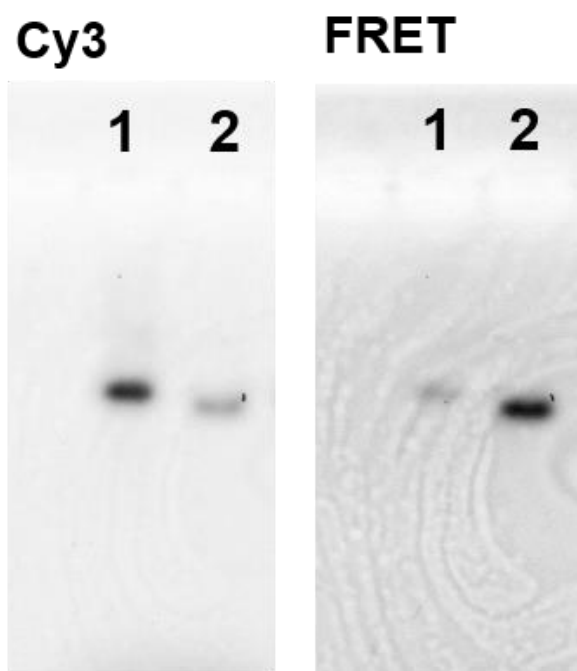
Figure 5.7. Agarose gel electrophoretic analyses of DNA scaffolds. Left: Cy3 channel (λ_{ex} = 532 nm, λ_{em} = 605 nm); right: FRET channel (λ_{ex} = 532 nm, λ_{em} = 695 nm). Lane 1: Open state (HPO_T); Lane 2: Closed state (HPC_T). Agarose gel electrophoresis conditions: 1% agarose gel in $1 \times$ TAE (pH 8.0) containing 12.5 mM $MgCl_2$ at 50 V for 6 h.

5.2.2 Dynamic shape transformation of the DNA scaffold from the open to closed state induced by the toehold-mediated strand displacement

The DNA scaffold[12] transforming from the open to closed states was constructed with a slight modification of previous report.[9] The dynamic shape transformation of DNA scaffold from HPO_T to HPC_T was induced by the toehold-mediated strand displacement mechanism to accelerate the shape transformation kinetics. Upon addition of closing keys (CLK, single-stranded DNA) sharing the complementary sequence with OPK, the long lock strands on the domain were released and hybridized with short lock strands on the other domain, enabling the open state (HPO_T) to transit to locked state (HPC_T) (Figure 5.8).


```
           5'-TGACAAACTGACACAACACCTC-3'  Closing key (CLK)
           3'-CATAAACTGTTTGACTGTGTTGTGGAG-5'  Opening key (OPK)
5'-CCAGAATTGATGATTGGGGTATTTGACAAACTGACA-3'  Long lock strand
3'-GACTCGTTTTGGGGACCCCATAAACTGT-5'  Short lock strand
```
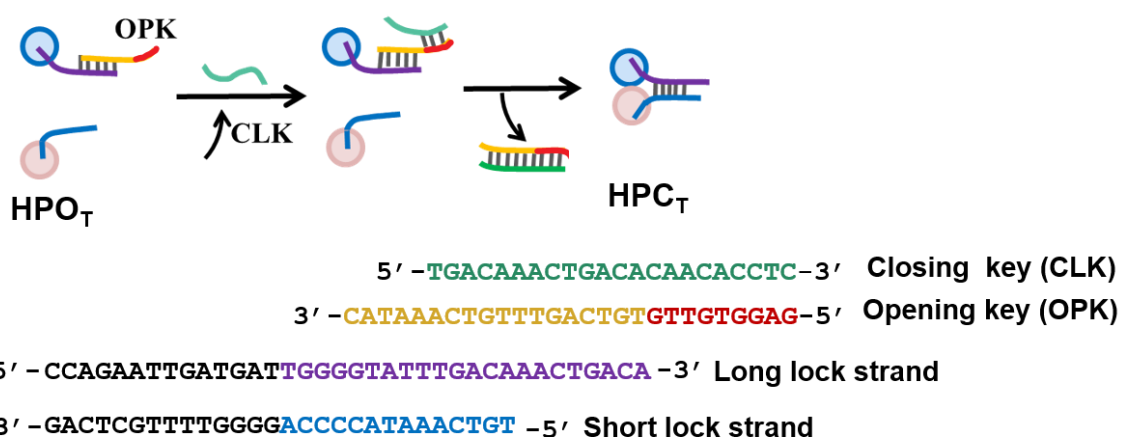
Figure 5.8. Scheme presenting the closing process of DNA scaffold initiated by the toehold-mediated strand displacement. The open state (HPO_T) was first folded with opening keys (OPK) in a molar ratio of 1:10 (HPO_T: OPK), after the gel purification to remove the excess amount of staple strands, 1:100 molar ratio of closing keys (CLK) were added to hybridize with OPK and remove OPK to obtain the closed state (HPC_T). The DNA scaffold was equipped with 6 side locks that underwent strand displacements as shown in the scheme. Nucleotide sequences in black, blue, purple, orange and green indicated the DNA template (M13mp18) sequence, the short lock strand, the long lock strand, OPK and CLK, respectively. The sequence in red indicated the toehold in OPK. The sequences of lock strands, OPK and CLK were designed as reported previously.[9]

FRET was utilized to trace the closing process, where the one-step annealed open state (HPO_T-control) and closed state (HPC_T-control) served as controls. Upon addition of CLK, the Cy3 fluorescence intensity decreased, while Cy5 fluorescence intensity increased (Figure 5.9a and Figure 5.9b). The effect of molar ratio of HPO_T to CLK on the closing process was investigated at 25 ℃. The closing efficiency was calculated by the Cy5 fluorescence intensity in the fluorescence emission spectra after 2-h hybridization (Figure 5.9c). It was found that the higher closing efficiency was achieved with higher concentration of CLK, the closing efficiency of 1:1, 1:5, 1:10, 1:50 and 1:100 molar ratios were 10%, 47%, 68%, 72% and 75%, respectively (Figure 5.9d).
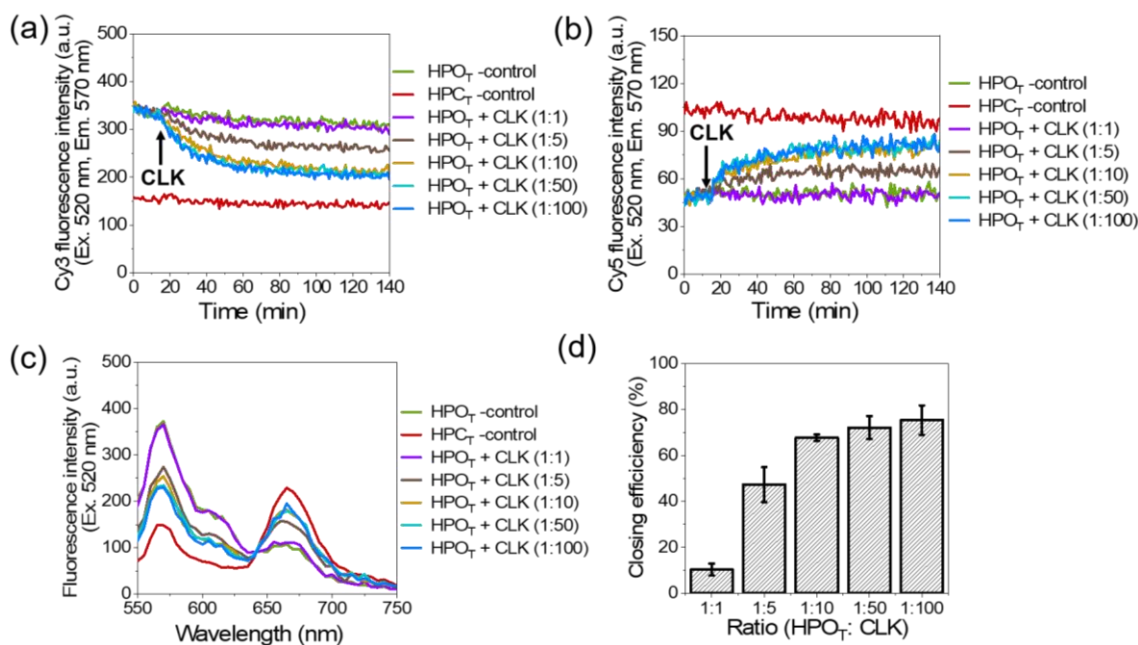
Figure 5.9. The effect of molar ratio (HPO_T: CLK) on the closing efficiency. (a) Time course changes of the Cy3 fluorescence intensity ($\lambda_{ex} = 520$ nm, $\lambda_{em} = 570$ nm) of closing procedure. (b) Time course of Cy5 fluorescence intensity ($\lambda_{ex} = 520$ nm, $\lambda_{em} = 670$ nm) of closing procedure. (c) Fluorescence emission spectra ($\lambda_{ex} = 520$ nm) after 2-h hybridization at 25 ℃. (d) Closing efficiency calculated from the Cy5 fluorescence intensity in the fluorescence emission spectra after 2-h hybridization at 25 ℃. 5 nM HPO_T was hybridized with 5 nM to 500 nM CLK in the buffer (pH 7.0) containing 40 mM Tris-HCl, 20 mM acetic acid, 12.5 mM $MgCl_2$ and 0.002% Tween20 at 25 ℃. Data in (d) were the averages of three independent repetitions, error bars indicated the S.D. of the repetitions.

The effect of hybridization temperature on the closing process was studied with a molar ratio (HPO$_T$: CLK) at 1:100. The fluorescence emission spectra after 2-h hybridization were shown in Figure 5.10a-c. The fluorescence intensities of control samples were different due to the effect of temperature. At the higher temperature, the fluorescence emission spectrum of HPO$_T$ + CLK approached more to HPC$_T$-control. The closing efficiencies at 20 °C, 25 °C and 30 °C were 48%, 75% and 88%, respectively, suggesting that the closing efficiency was increased with the rising temperature (Figure 5.10d).
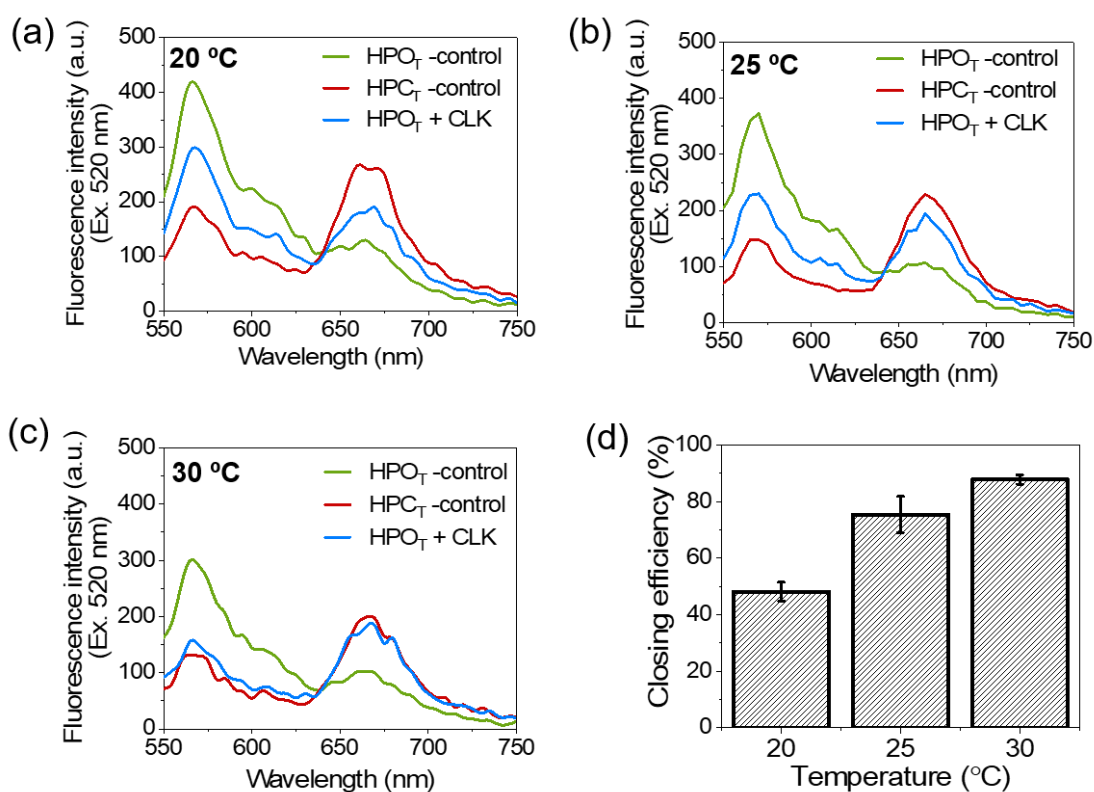
Figure 5.10. Effect of hybridization temperatures on the efficiency of closing process induced by the toehold-mediated strand displacement. (a) Fluorescence emission spectra (λ_{ex} = 520 nm) after 2-h hybridization at 20 °C. (b) Fluorescence emission spectra (λ_{ex} = 520 nm) after 2-h hybridization at 25 °C. (c) Fluorescence emission spectra (λ_{ex} = 520 nm) after 2-h hybridization at 30 °C. (d) Closing efficiency at various temperatures. 5 nM HPO$_T$ was hybridized with 500 nM CLK in the buffer (pH 7.0) containing 40 mM Tris-HCl, 20 mM acetic acid, 12.5 mM MgCl$_2$ and 0.002% Tween20 at the respective temperature. Data in (d) were the averages of three independent repetitions, error bars indicated the S.D. of the repetitions.

The faster closing kinetics was observed with elevating the hybridization temperature as shown in the time courses of Cy5 fluorescence intensity changes (Figure 5.11a-c). The time course profiles of HPO_T + CLK were used to estimate the halve time values ($t_{1/2}$) with 24.6 min at 20 ℃, 14.5 min at 25 ℃, and 4.5 min at 30 ℃ (Figure 5.11d). The higher temperature resulted in the higher closing efficiency and accelerated closing kinetics, which might be due to the increased dynamics for staple strands, increasing the chance of forming duplex by OPK and CLK.
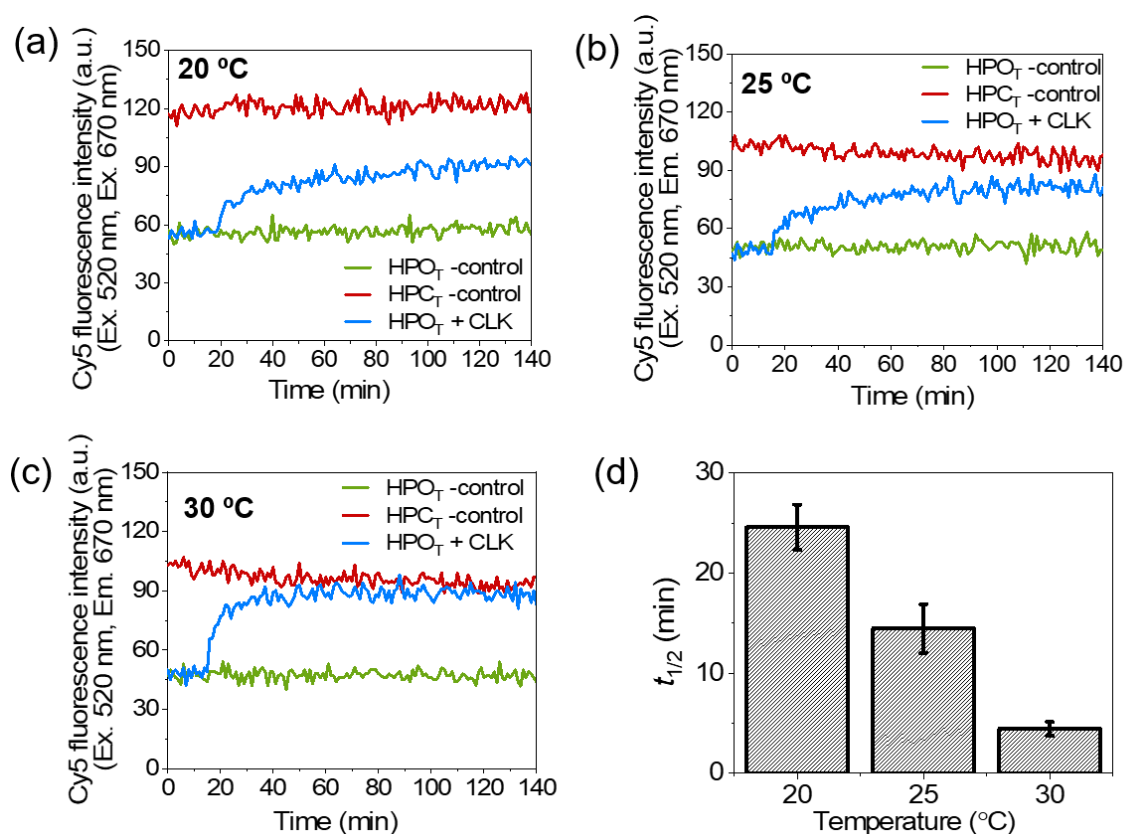
Figure 5.11. The effect of hybridization temperature on closing kinetics. (a) Time course changes of the Cy5 fluorescence intensity (λ_{ex} = 520 nm, λ_{em} = 670 nm) at 20 ℃. (b) Time course of Cy5 fluorescence intensity (λ_{ex} = 520 nm, λ_{em} = 670 nm) at 25 ℃. (c) Time course changes of Cy5 fluorescence intensity (λ_{ex} = 520 nm, λ_{em} = 670 nm) at 30 ℃. (d) Half time ($t_{1/2}$) of closing process estimated at various temperatures. 5 nM HPO_T was hybridized with 500 nM CLK at 30 ℃ in the buffer (pH 7.0) containing 40 mM Tris-HCl, 20 mM acetic acid, 12.5 mM $MgCl_2$ and 0.002% Tween20. Data in (d) were the averages of three independent repetitions, error bars indicated the S.D. of the repetitions.

Several methods were utilized to confirm the closing efficiency estimated from fluorescence intensity changes. After 2-h incubation or hybridization, the percentages of closed structure of HPC_T-control, HPO_T + CLK (1:100, 25 °C) and HPO_T + CLK (1:100, 30 °C) were 60% (222 closed structures/370 counted structures), 59% (117/200), and 60% (119/200), respectively (Figure 5.12). Due to the flexibility of the side locks, the closed structures were easily opened by cantilever during AFM imaging as mentioned in Figure 5.3, thus the quantitation by AFM images did not provide reliable yields of the closed structure.
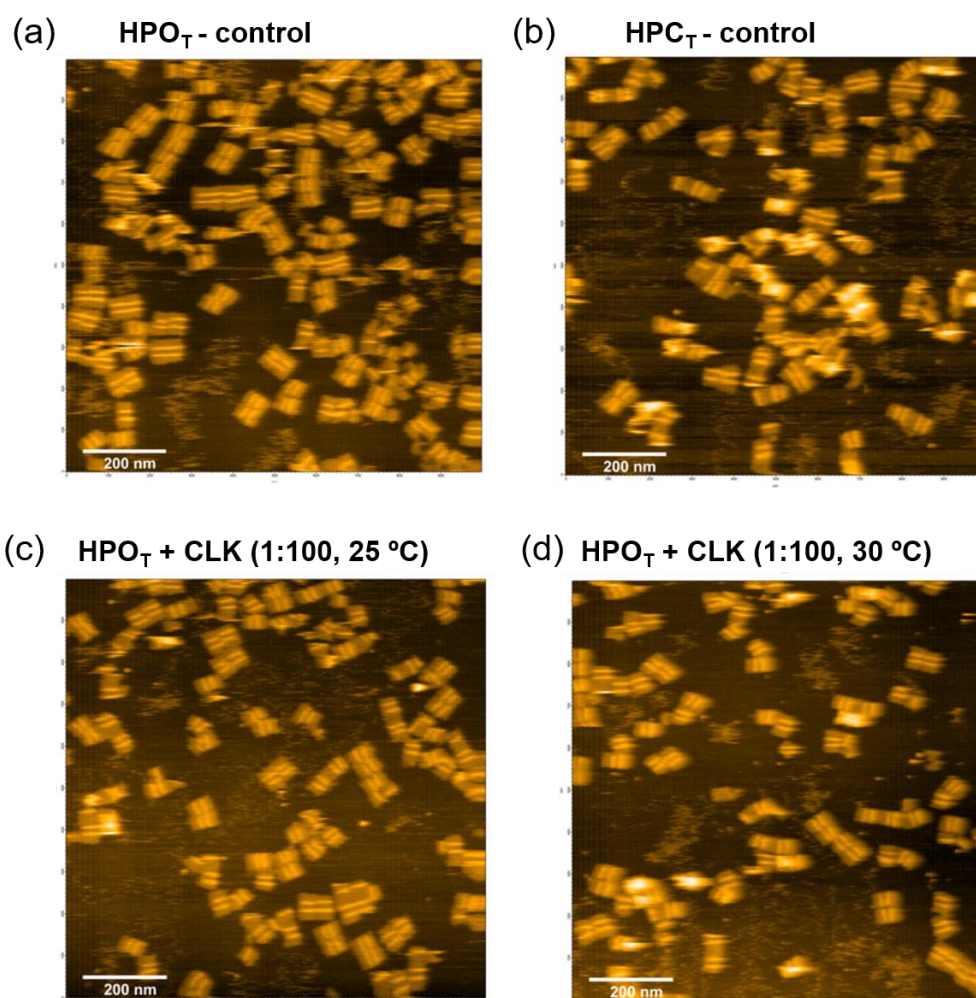
Figure 5.12. AFM images of DNA scaffold. (a) HPO_T-control (after 2-h incubation at 25 °C). (b) HPC_T-control (after 2-h incubation at 25 °C), the percentage of closed structures were estimated to be 60% (222/370). (c) HPO_T + CLK (1:100, after 2-h hybridization at 25 °C), the closing efficiency was estimated to be 59% (117/200) by AFM images. (d) HPO_T + CLK (1:100, after 2-h hybridization at 30 °C), the closing efficiency was estimated to be 60% (119/200) by AFM images.

Instead, in the TEM images, closed state appeared as uniform rectangles or hexagons, which were easily quantitated. Compared with the HPO_T-control, the percentage of closed structures of HPC_T-control after 2-h incubation at 25 °C, HPO_T + CLK (1:100) after 2-h hybridization at 25 °C and HPO_T + CLK (1:100) after 2-h hybridization at 30 °C were 93% (196/210), 93% (265/285), and 95% (247/260), respectively (Figure 5.13). These results indicated that DNA scaffolds were closed in high yields.
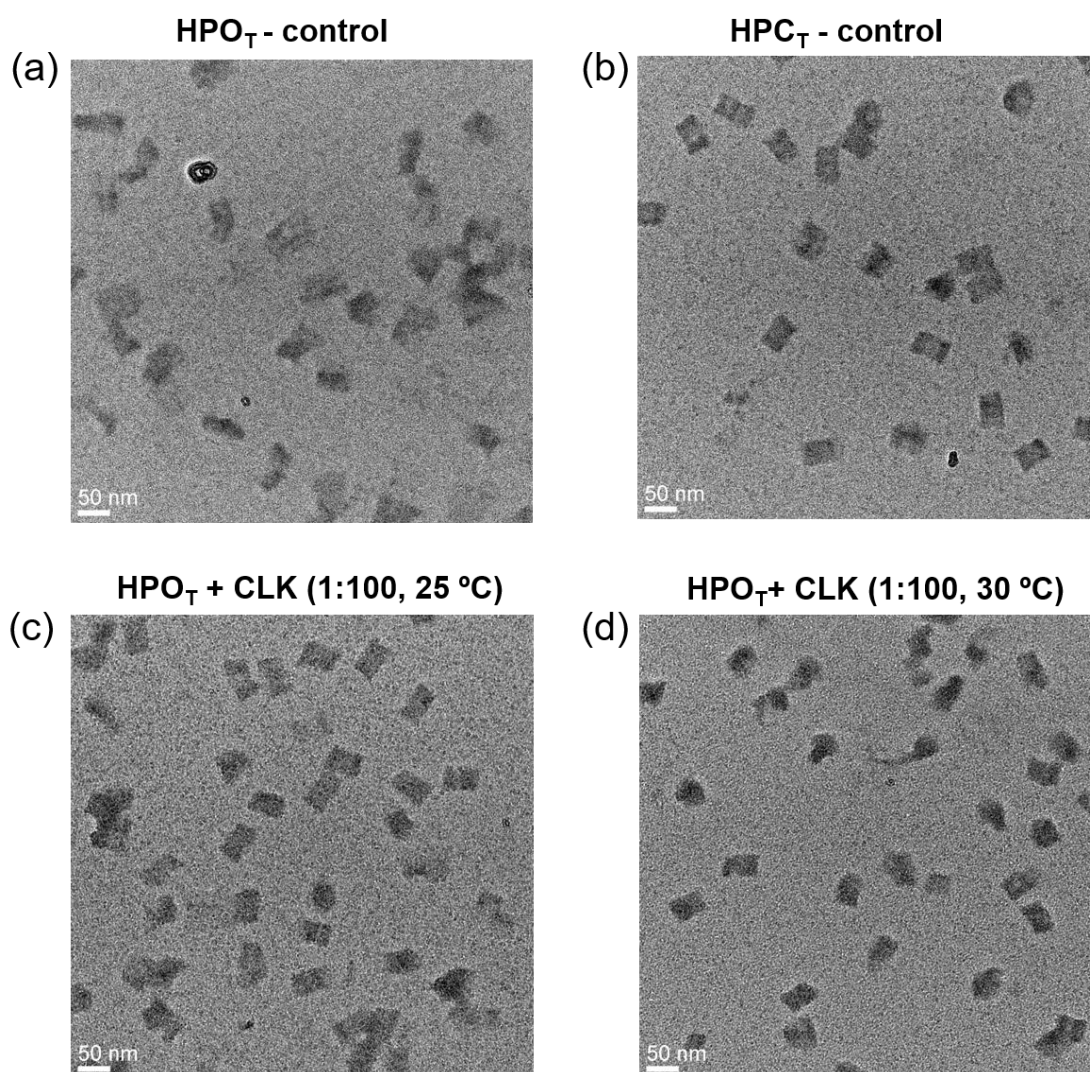
Figure 5.13. TEM images of the DNA scaffolds. (a) HPO_T-control (after 2-h incubation at 25 °C). (b) HPC_T-control (after 2-h incubation at 25 °C): the percentage of closed structures were estimated to be 93% (196/210). (c) HPO_T + CLK (1:100, after 2-h hybridization at 25 °C): the closing efficiency was estimated to be 93% (265/285). (d) HPO_T + CLK (1:100, after 2-h hybridization at 30 °C): the closing efficiency was estimated to be 95% (247/260).

Moreover, in the agarose gel electrophoresis, the band mobility of HPO_T was approached to that of HPC_T-control with increasing the concentration of CLK, indicating that HPO_T was closed to HPCT in high yield at 1:100 molar ratio of CLK (Figure 5.14). The closing process initiated by the addition of closing keys and the hybridization of long lock strands and short lock strands gave resulted in the weaker fluorescence energy transfer compared with that of HPC_t-control. However, from that estimated from TEM images and the gel electrophoretic analyses, the closing efficiency estimated from fluorescence intensity could be under-estimated.

Compared with the closing process triggered by DNA linkers that hybridized to both the facing edges of two domains of DNA scaffold (Chapter 3), the closing process proceeded by the toehold-mediated strand displacement resulted in a comparable closing efficiency with the remarkably accelerated hybridization kinetics. The half time value ($t_{1/2}$) was shortened from 89 min in the closing process with DNA linkers to 14 min in the process triggered by the toehold-mediated strand displacement under the conditions of optimal molar ratio and 25 °C.

Figure 5.14. Agarose gel electrophoresis of the DNA scaffolds. Lane M: 1kb DNA marker. Lane 1: HPO_T + CLK (1:50), after 2-h hybridization at 25 °C; Lane 2: HPO_T + CLK (1:100),

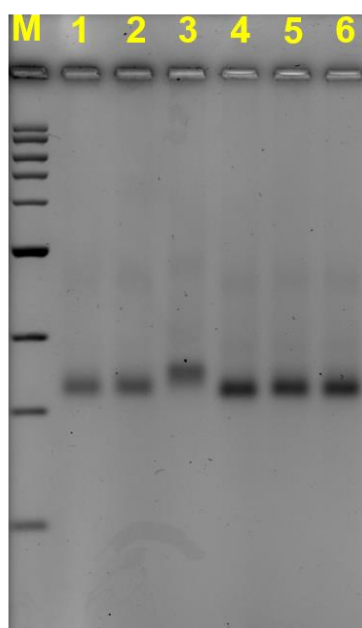after 2-h hybridization at 25 ℃; Lane 3: HPO$_T$-control; Lane 4: HPC$_T$-control; Lane 5: HPO$_T$ + CLK (1:50), after 2-h hybridization at 30 ℃; Lane 6: HPO$_T$ + CLK (1:100), after 2-h hybridization at 30 ℃. The samples were run on a 2% agarose gel with 0.5 × TB containing 5 mM MgCl$_2$ at 104 V for 10 h. The gel stained with EtBr was scanned under EtBr channel (λ_{ex} = 532 nm, λ_{em} = 595 nm).

5.2.3 Assembly of enzymes ZS-XR and HG-XDH on the DNA scaffold

The cascade enzymes XR[30] and XDH[31] were assembled on HPO$_T$ to investigate the cascade reaction coupled with the dynamic shape transformation of the enzyme-assembled scaffold. The modular adaptor method[32–35] was used to stably locate the enzymes at specific positions on the DNA scaffold through the covalent linkage. The modular adaptor fused enzymes ZS-XR and HG-XDH were constructed as previously reported.[24, 33] The molecular models of ZS-XR and HG-XDH were shown in Figure 2.5 (Chapter 2).

Three hairpin DNA sites containing the target sequences modified with BG for ZS-XR and three sites modified with CH for HG-XDH were introduced on each floor of HPO$_T$. The different DNA binding structures of modular adaptors rendered the different location geometries. ZF-SNAP snugly fits into the stem of hairpin with residing XR near its loop region, while Halo-GCN4 perpendicularly crips the stem with locating XDH around the midpoint of the stem region. HPO$_T$ possessing these modular adaptor binding sites was incubated with ZS-XR and HG-XDH at 4 °C for 1 h. The binding mixture was purified by gel filtration to remove the unbound proteins to obtain purified HPO$_T$/XR-XDH. For the detailed experimental procedure, see the Materials and Methods. The binding efficiency of enzymes to DNA scaffold was quantitated by AFM images (Figure 5.15).[24] For HPO$_T$/3XR-XDH, enzymes were assembled on the DNA scaffold with average 2.50 molecules of ZS-XR monomer and 2.53 molecules of HG-XDH dimer bound on each DNA scaffold. For HPO$_T$/3XDH, HG-XDH was loaded with

average 2.54 molecules of dimer on each scaffold. For HPO_T/3XR, ZS-XR was loaded with average 2.45 molecules of monomer on each scaffold (Table 5.1).
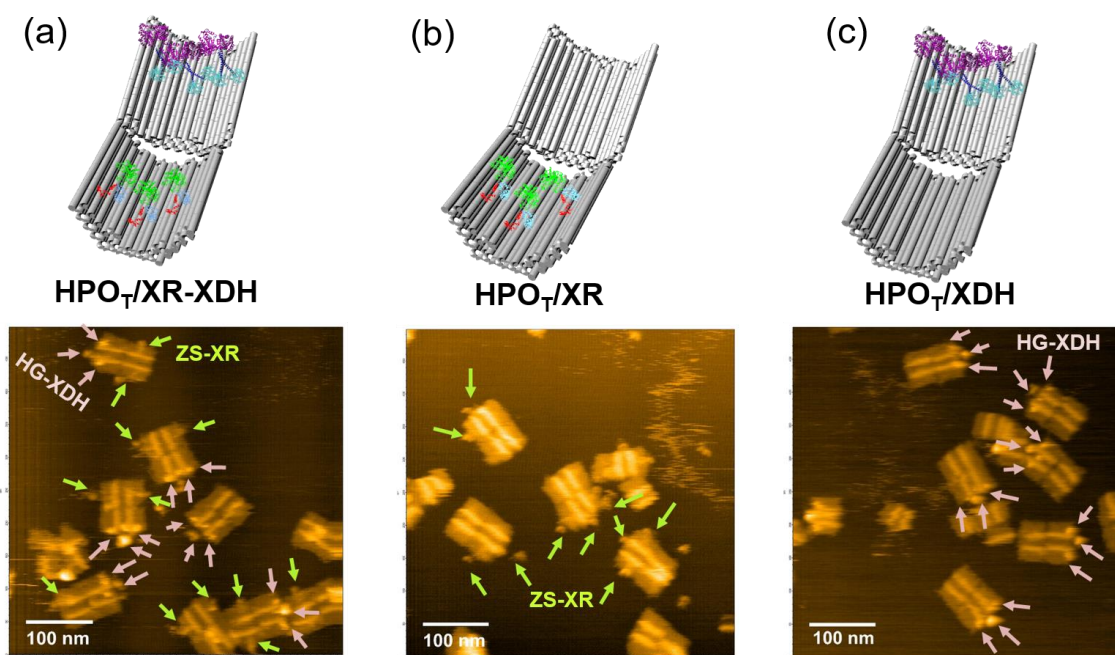
Figure 5.15. Assembly of enzymes on the DNA scaffold. (a) An illustration and typical AFM image of HPO_T/XR-XDH, scale bar: 100 nm. (b) An illustration and typical AFM image of HPO_T/XR, scale bar: 100 nm. (c) An illustration and typical AFM image of HPO_T/XDH, scale bar: 100 nm. The arrows in pink indicated the loaded HG-XDH, and the arrows in green indicated the loaded ZS-XR. The quantifications of enzyme loading yields on the DNA scaffold were shown in Table 5.1.

Table 5.1. Average number of assembled enzyme on DNA scaffold

DNA scaffold	Modular adaptor enzymes	Number of well-formed DNA scaffold	Numbers of enzymes on modified sites [yield]			Average number of assembled enzyme
			Three-binding	**Two-binding**	**One-binding**	
HPO_T/XR	ZS-XR	219	156 [71.2%]	25 [9.9%]	26 [11.9%]	2.45[a]
HPO_T/XDH	HG-XDH	303	218 [71.9%]	48 [15.8%]	20 [6.6%]	2.54
HPO_T/XR-XDH	ZS-XR	218	158 [72.5%]	27 [10.7%]	23 [10.6%]	2.50
	HG-XDH		166 [76.1%]	22 [10.1%]	10 [4.6%]	2.53

[a] Calculated from the average yield (HPO_T/XR as an example):

The average number of ZS-XR (monomer) on each DNA scaffold: $3 \times 0.712 + 2 \times 0.990 + 1 \times 0.119 + 0 \times 0.047 =$ **2.45** molecules

5.2.4 Enzyme cascade reactions by scaffolded XR-XDH upon the shape transformation of DNA scaffold

The DNA scaffolded enzymes HPO_T/XR-XDH and HPO_T/XR were incubated in the presence or absence of closing keys (CLK) to obtain the closed state entrapped with enzymes (HPC_T/XR-XDH) or the control samples HPO_Ta/XR-XDH and HPO_Ta/XR underwent the same incubation process within 2-h at 25 ℃ (Figure 5.16a). The closing process was traced by the changes of Cy3 fluorescence intensity and Cy5 fluorescence intensity (Figure 5.16b and Figure 5.16c), suggesting that DNA scaffold was efficiently closed regardless of the assembly of both enzymes.
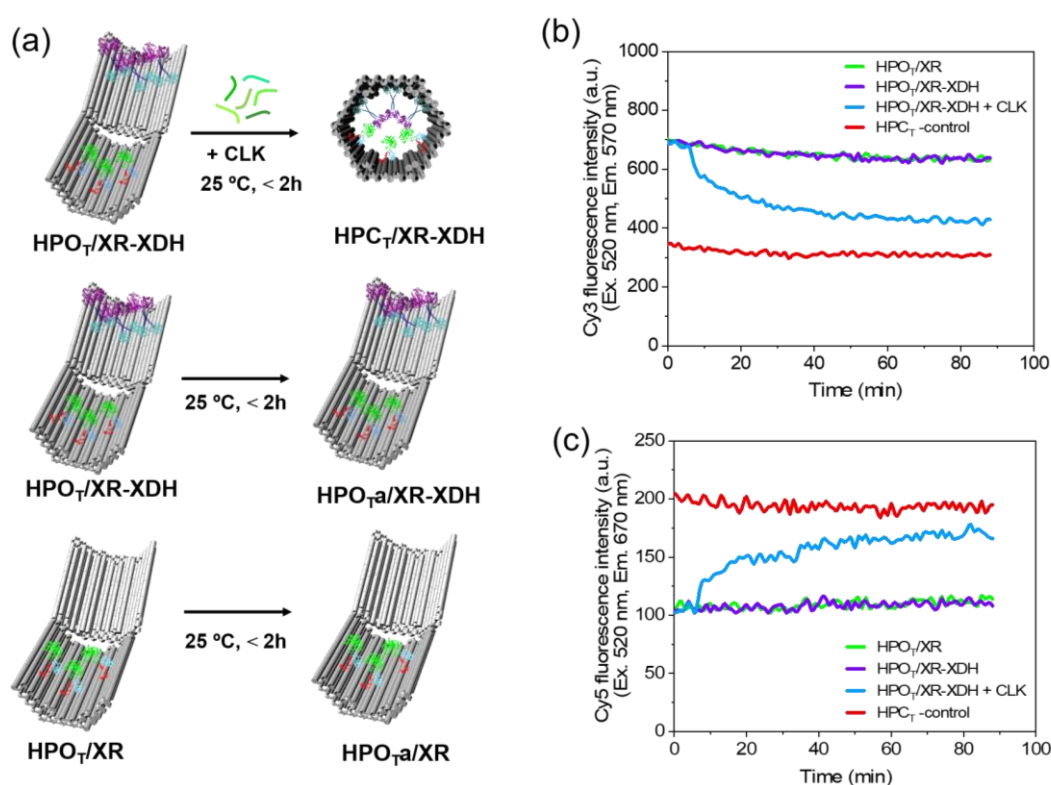
Figure 5.16. Shape transformation of the enzyme loaded DNA scaffolds. (a) Schemes illustrating enzyme loaded DNA scaffolds incubated in the presence of closing keys to obtain HPC_T/XR-XDH. HPO_Ta/XR-XDH and HPO_Ta/XR were the control samples treated with same incubation process in the absence of closing keys. (b) Time course changes of the Cy3 fluorescence intensity (λ_{ex} = 520 nm, λ_{em} = 570 nm). (c) Time course changes of the Cy5 fluorescence intensity (λ_{ex} = 520 nm, λ_{em} = 670 nm). 7 nM DNA scaffold was hybridized with 700 nM closing keys in the buffer (pH 7.0) containing 40 mM Tris-HCl, 20 mM acetic acid, 12.5 mM $MgCl_2$, 5 µM BSA and 0.002% Tween20 at 25 ℃ for 80 min.

After the closing process, the sequential reactions of xylose metabolism through the simultaneous bimolecular transport of xylitol and NAD^+ from XR to XDH with recycling the cofactor NADH were investigated by monitoring the change of NADH absorption at 340 nm. The amount of NADH in the solution was equal to the total of NADH remaining after the first ZS-XR reaction and NADH regenerated by the second enzyme HG-XDH at any given point, thus the NADH regenerations of HPC_T/XR-XDH and HPO_Ta/XR-XDH were obtained by subtracting the NADH consumption of control HPO_Ta/XR. The enhancement of NADH regeneration was observed for the cascade on the shape-transformed scaffold (HPC_T/XR-XDH) despite the instability of XR (Figure 5.17).[24]
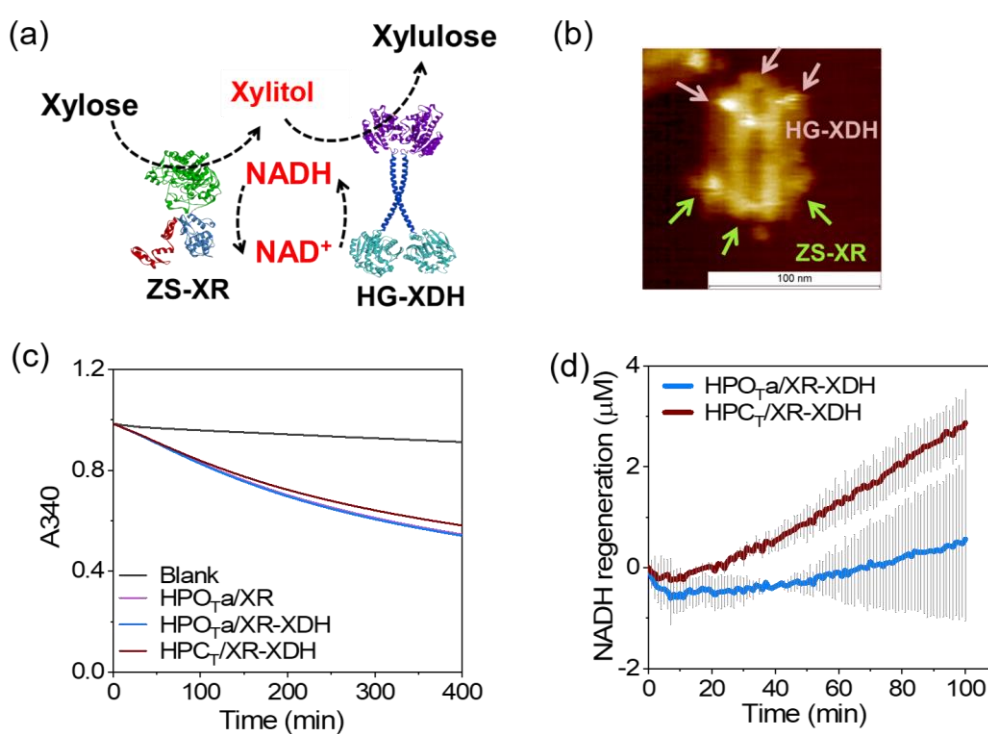
Figure 5.17. (a) A scheme illustrating the enzyme cascade reaction by ZS-XR and HG-XDH. (b) Typical AFM image of enzymes coassembled on the DNA scaffold in open state (HPO_T/XR-XDH), scale bar: 100 nm. (c) XR-XDH cascade reactions monitored by the time course changes of NADH absorbance at 340 nm. 7 nM ZS-XR and 7 nM HG-XDH were reacted with 200 mM xylose and 300 μM NADH in the buffer (pH 7.0) containing 40 mM Tris-HCl, 20 mM acetic acid, 12.5 mM $MgCl_2$, 5 μM BSA, 0.002% Tween20, 1 μM $ZnCl_2$ and 100 mM NaCl. (d) Time course for the NADH regeneration by HPC_T/XR-XDH or HPO_Ta/XR-XDH. Data in (d) were the averages of three independent repetitions, error bars indicated the S.D. of the repetitions.

171

Cy3 and Cy5 were designed to locate on the opposing domains of DNA scaffold with the distance of 25 nm in the fully open state of HPO_T, where the fluorescence energy transfer would not be observed theoretically.[29] However, as shown in Figure 5.18, the fluorescence emission peak at 670 nm of HPO_T indicated a certain degree of fluorescence energy transfer for HPO_T. Because the DNA origami is flexible in solution, HPO_T would exist in various status, such as the fully open, partially open or closed status. The closed fraction of HPO_Ta/XR-XDH was estimated to be 22% from FRET using the rigid fully open state (HPO_T + connecting hinges) as a control (Table 5.2). To better compare the enzyme cascade efficiencies in open and closed states, a DNA scaffold with a statically open configuration was designed.
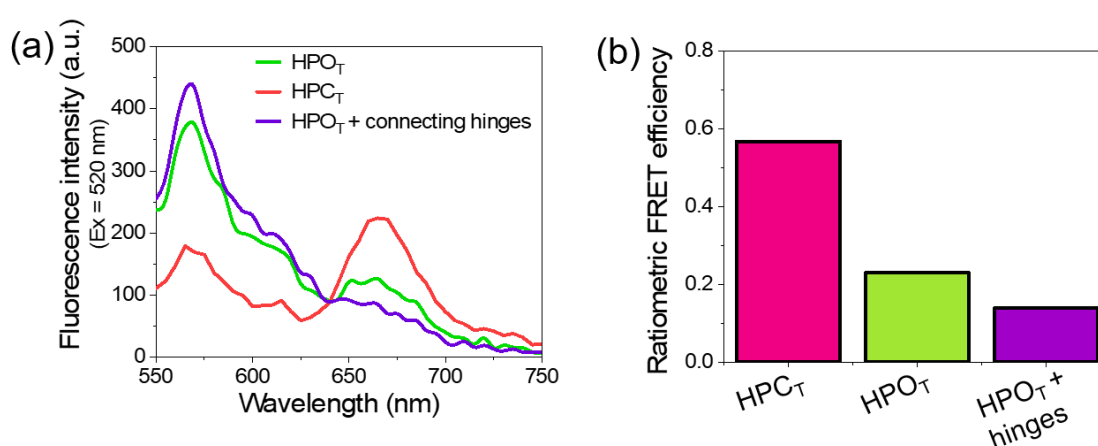
Figure 5.18. Estimation of closed fraction of flexible HPO_T in solution. (a) Fluorescence emission spectra of HPC_T, HPO_T in the flexible open state and HPO_T in the fully open state (HPO_T + connecting hinges) after 2 h incubation at 25 °C in the buffer (pH 7.0) containing 5 nM DNA scaffold, 40 mM Tris-HCl, 20 mM acetic acid, 12.5 mM $MgCl_2$, and 0.002% Tween20. (b) Comparison of the ratiometric FRET efficiency of DNA scaffold. The ratiometric FRET efficiencies were calculated by use the formula ($E_r = I_{DA}/(I_{DD}+I_{DA})$), in which I_{DA} was the acceptor (Cy5) fluorescence intensity, and I_{DD} was the donor (Cy3) fluorescence intensity upon the donor excitation ($\lambda_{ex} = 520$ nm) in the fluorescence emission spectra.

Table 5.2 Estimation of closed fraction of flexible HPO_T

	Er	Closed fraction (%) [a]
HPC_T	0.57	
HPO_T	0.23	22
HPO_T + hinges	0.14	

[a] Closed fraction (%) was obtained as follow: $(0.23 - 0.14) \times 100/(0.57 - 0.14) = 22\%$

5.2.5 Enzyme cascade reactions on the statically open and closed states of DNA scaffold

To verify the enzyme cascade reaction efficiency in the closed state of DNA scaffold, the one-step prepared HPO in the statically open state and HPC in the statically closed state were prepared to assemble the cascade enzymes XR and XDH. The one-step preparation of these scaffold is also advantageous to preserve the stability of XR in the reaction. Three connecting hinges were introduced between the two domains to keep the fully open state HPO_h[24] and six linker strands spanning and hybridizing to the two domains of DNA scaffold were used to maintain the rigid closed state of HPC (Figure 5.19). HPC in the closed state was prepared as described in Chapter 3.
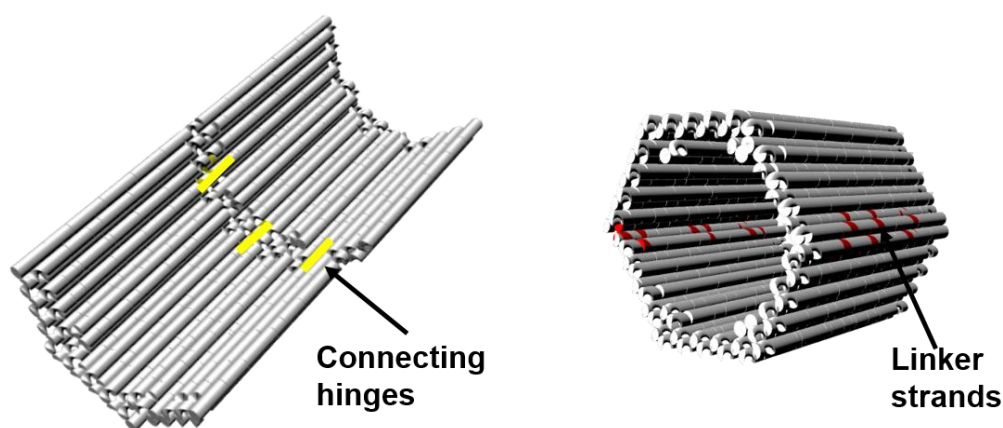
Figure 5.19. Three connecting hinges (single-stranded DNA shown in golden) were introduced to maintain the fully open state (HPO_h). Six linker strands (single-stranded DNA shown in red) spanning and hybridizing to the two domains of scaffold were used to fold the rigid closed state (HPC).

Enzymes were directly co-assembled on the open state to give HPO$_h$/XR-XDH or coencapsulated in the closed state to obtain HPC/XR-XDH. The binding efficiencies of enzymes were quantitated by AFM images, in which HPC/XR-XDH was quantitatively transformed to the open state by adding the removers (single-stranded DNA) that removed linkers (Figure 5.20, Figure 5.21 and Figure 5.22). HPO$_h$/XR-XDH was prepared with average 2.49 molecules of ZS-XR and 2.51 molecules of HG-XDH assembled on each DNA scaffold. HPC/XR-XDH was constructed with average 2.55 molecules of ZS-XR and 2.49 molecules of HG-XDH encapsulated in each scaffold. ZS-XR was loaded 2.48 molecules and 2.51 molecules on each HPO$_h$ and HPC, respectively, which was supported by the comparable enzyme activities of HPO$_h$/XR and HPC/XR. HG-XDH was loaded on HPO$_h$ and HPC with 2.50 molecules and 2.53 molecules, respectively, on each scaffold (Table 5.3). The statistical analyses depicted that enzymes were efficiently loaded in HPO$_h$ and HPC. The results indicated that 3D hexagonal prism provided sufficient space for the encapsulation of both enzymes as predicted from the sizes of enzymes and the high reactivity of modular adaptors.
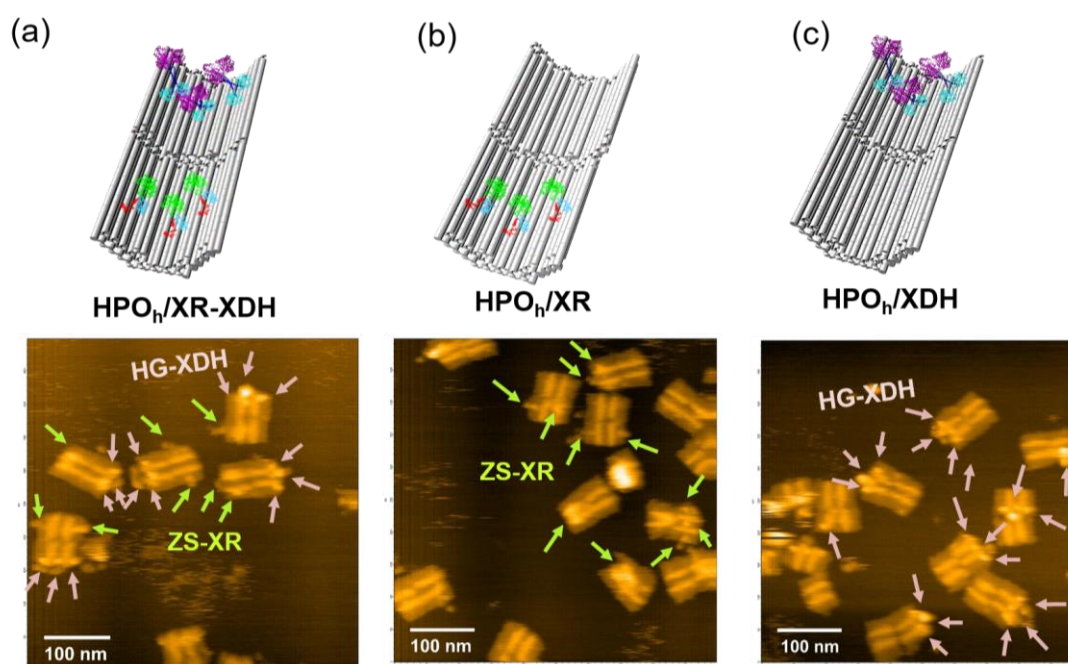
Figure 5.20. Assembly of enzymes on the statically open state of DNA scaffold (HPO$_h$). (a) An illustration and typical AFM image of HPO$_h$/XR-XDH, scale bar: 100 nm. (b) An illustration

and typical AFM image of HPO$_h$/XR, scale bar: 100 nm. (c) An illustration and typical AFM image of HPO$_h$/XDH, scale bar: 100 nm. The arrows in pink and green indicated the immobilized HG-XDH and ZS-XR, respectively.
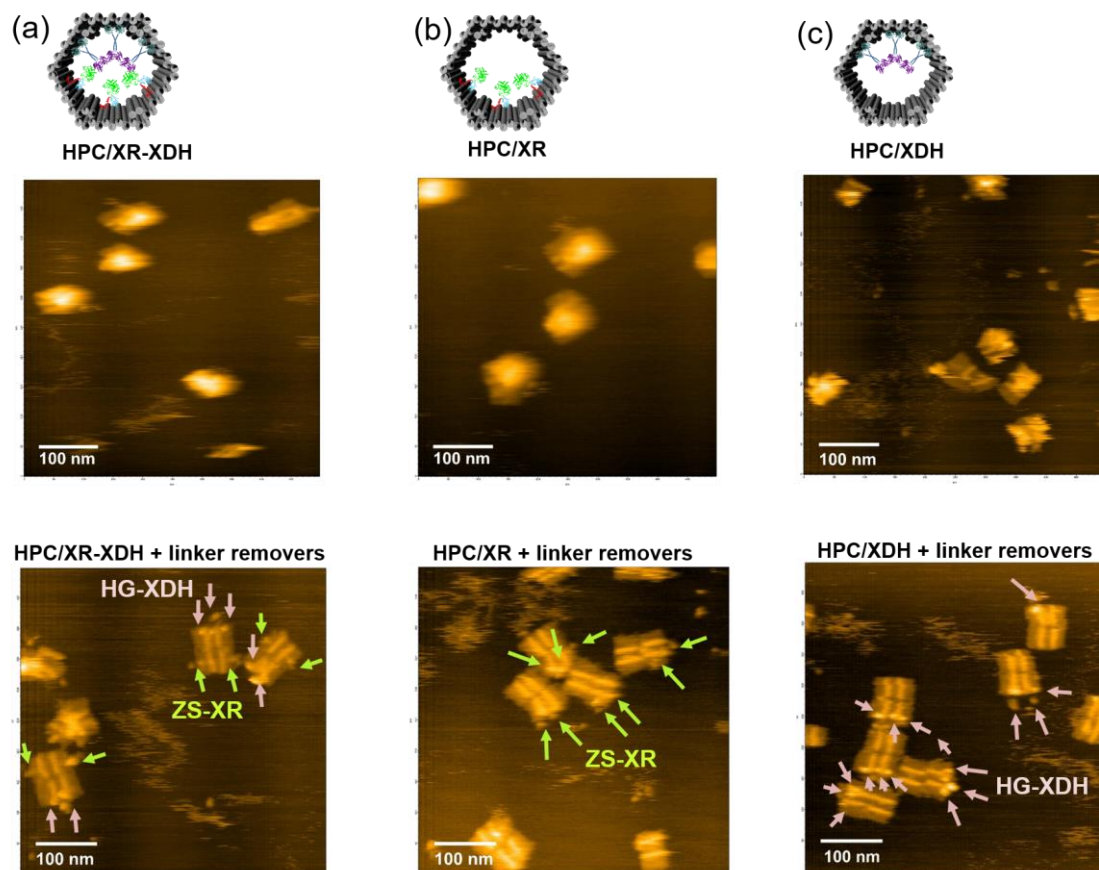
Figure 5.21. Assembly of enzymes on the statically closed state of DNA scaffold HPC. (a) Top: an illustration of HPC/XR-XDH; middle: typical AFM image of HPC/XR-XDH, scale bar: 100 nm; bottom: typical AFM image of HPC/XR-XDH opened by removing linkers, scale bar: 100 nm. (b) Top: an illustration of HPC/XR; middle: typical AFM image of HPC/XR, scale bar: 100 nm; bottom: typical AFM image of HPC/XR opened by removing linkers, scale bar: 100 nm. (c) Top: an illustration of HPC/XDH; middle: typical AFM image of HPC/XDH, scale bar: 100 nm; bottom: typical AFM image of HPC/XDH opened by removing linkers, scale bar: 100 nm. HPC/XR-XDH, HPC/XR and HPC/XDH were incubated with 1: 200 molar ratio of the removers at ambient temperature for overnight to open the closed structure and quantitate enzyme numbers. The arrows in pink and green indicated the immobilized HG-XDH and ZS-XR, respectively.
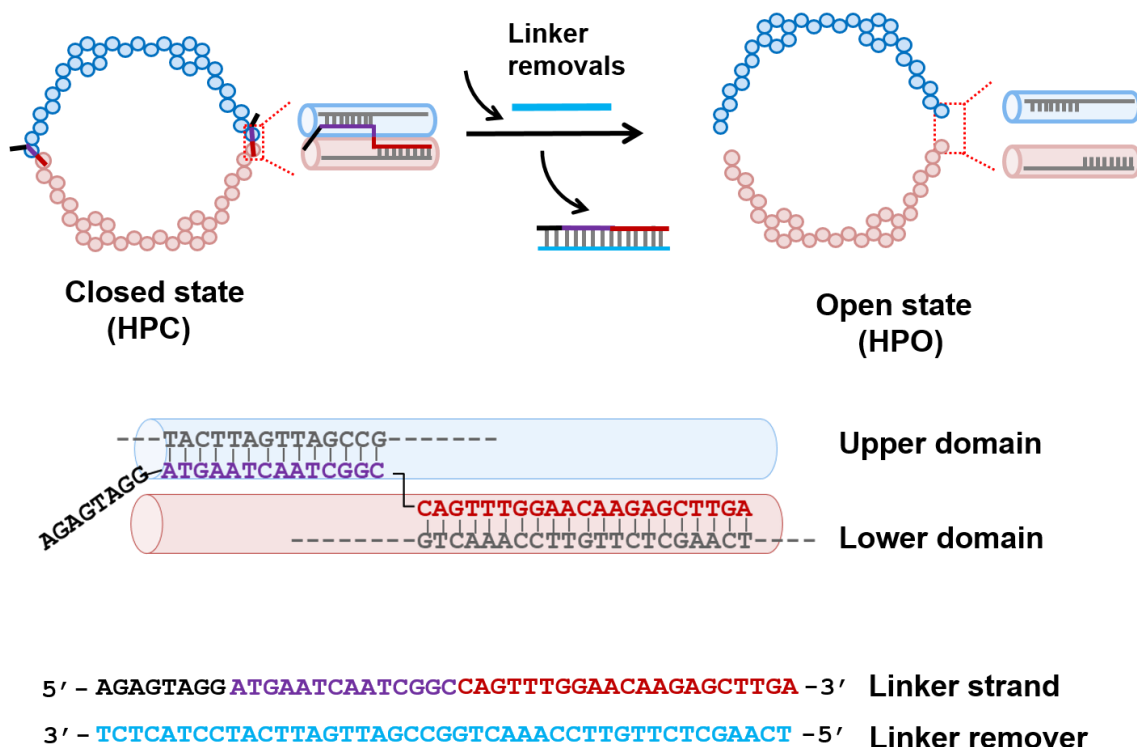
Figure 5.22. Scheme presenting the reopening process of DNA scaffold. To quantitate the enzyme loading yields encapsulated into rigid closed state (HPC), six linker removers (single-stranded DNA) complementary to linker strands were added to remove the linker strands and open the closed structures.

Table 5.3. Average number of assembled enzyme on DNA scaffold

DNA scaffold	Modular adaptor enzymes	Number of well-formed DNA scaffold	Numbers of enzymes on modified sites			Average number of assembled enzyme[a]
			Three-binding	Two-binding	One-binding	
HPO$_h$/XR	ZS-XR	202	146 [72.4%]	20 [10.1%]	22 [10.8%]	2.48
HPO$_h$/XDH	HG-XDH	245	176 [71.8%]	37 [15.1%]	11 [4.5]%	2.50
HPO$_h$/XR-XDH	ZS-XR	279	201 [72.0%]	31 [11.1%]	31 [11.1%]	2.49
	HG-XDH		205 [73.5%]	32 [11.5%]	22 [7.9%]	2.51
HPC/XR	ZS-XR	315	236 [74.9%]	26 [8.2%]	32 [10.2%]	2.51
HPC/XDH	HG-XDH	250	182 [72.0%]	39 [15.6%]	14 [5.6%]	2.53
HPC/XR-XDH	ZS-XR	274	211 [77.0%]	20 [7.3%]	26 [9.5%]	2.55
	HG-XDH		201 [73.4%]	29 [10.6%]	22 [8.0%]	2.49

[a] Calculated by average assembly yield.

HPC/XR as an example:

$3 \times 0.749 + 2 \times 0.082 + 1 \times 0.102 = 2.51$ molecules of ZS-XR (monomer) on each DNA scaffold

The enzyme cascade reaction of the individually assembled system (HPO_h/XR + HPO_h/XDH or HPC/XR + HPC/XDH) or the coassembled system (HPO_h/XR-XDH or HPC/XR-XDH) (Figure 5.23) was started by the addition of NADH (500 μM) to a mixture of the substrate xylose (12.5 mM) and the enzyme-loaded DNA scaffold, and monitored by the time-course changes of NADH absorption at 340 nm. (Figure 5.24a). The regeneration of NADH by HPO_h/XR-XDH or HPC/XR-XDH was estimated by subtracting the consumption of NADH by HPO_h/XR or HPC/XR, respectively. The co-assembled enzyme cascade exhibited evidently higher NADH regeneration than the reaction by HPO_h/XR and HPO_h/XDH or the reaction by HPC/XR and HPC/XDH (Figure 5.24b). The initial velocity of NADH production ($V_{ini-NADH}$) was estimated from the slope of plot for the time-dependent regeneration of NADH for the reactions within the initial reaction state up to 100 min. Notably, the $V_{ini-NADH}$ of HPC/XR-XDH was two-fold higher than HPO_h/XR-XDH, and five-fold higher than the separate system (HPC/XR + HPC/XDH) (Figure 5.24c).
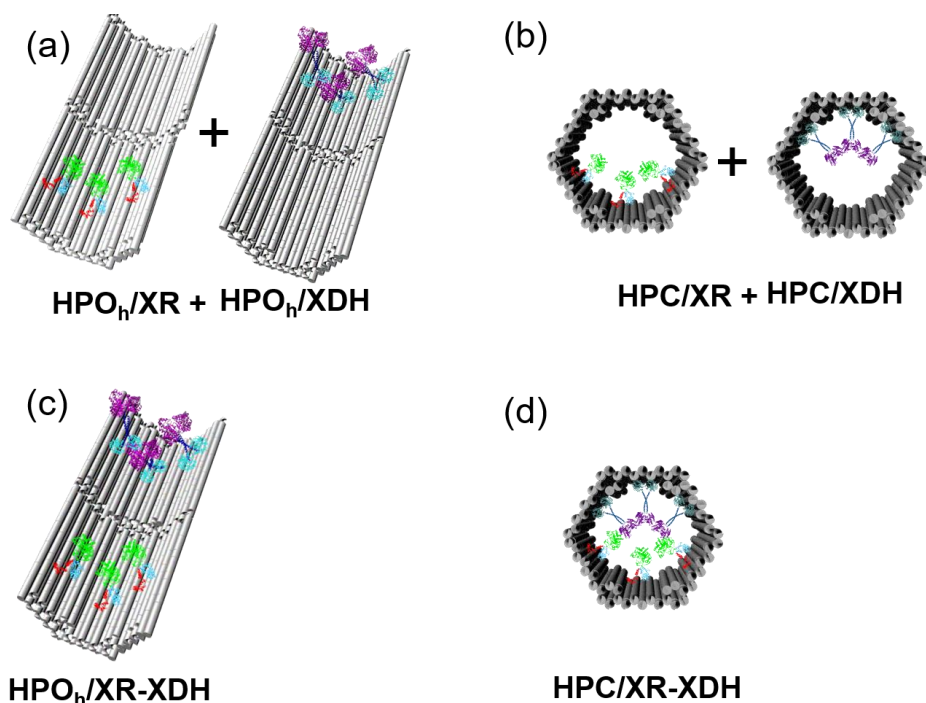
Figure 5.23. Illustrations of the individually assembled systems (a) HPO_h/XR + HPO_h/XDH and (b) HPC/XR + HPC-XDH, and the coassembly systems (c) HPO_h/XR-XDH and (d) HPC/XR-XDH.

177
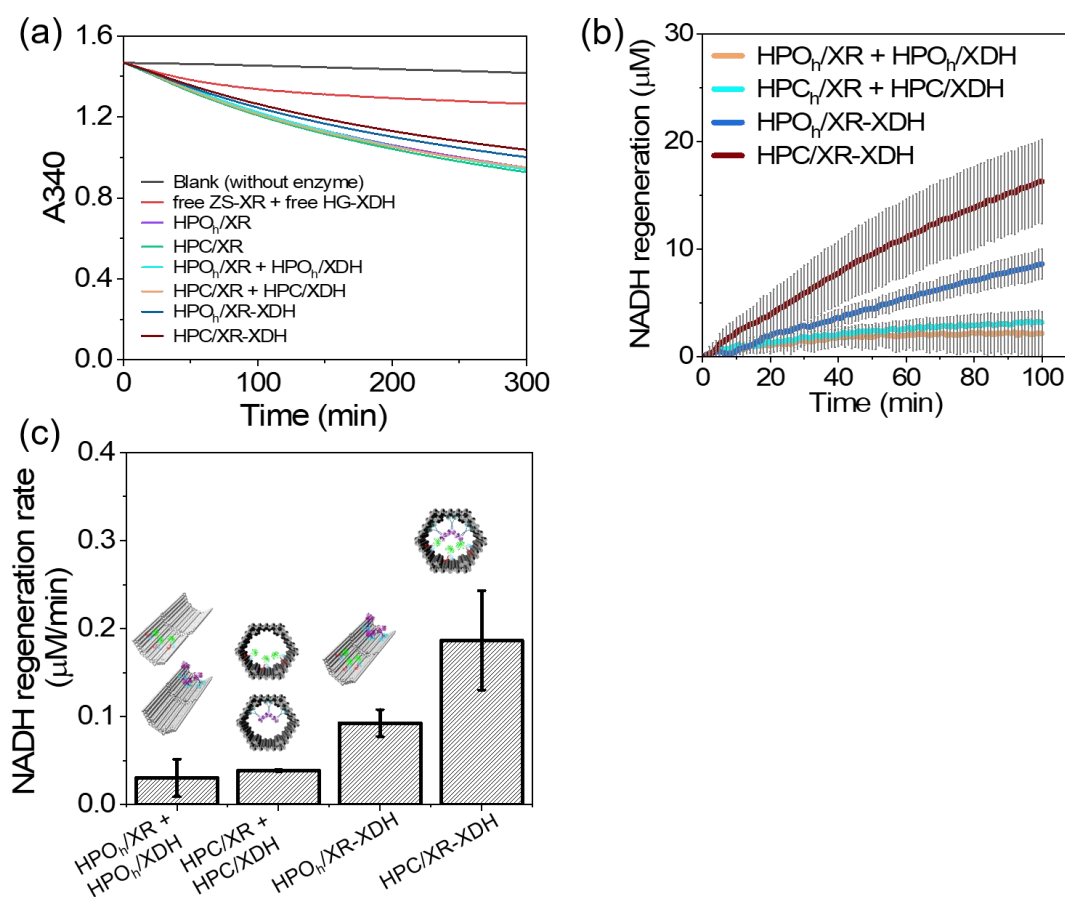
Figure 5.24. Enzyme cascade assembled on the DNA scaffold in statically open or closed state. (a) The time course changes of NADH absorbance at 340 nm for the cascade reactions by HPO$_h$/XR-XDH, HPC/XR-XDH, a mixture of HPO$_h$/XR and HPO$_h$/XDH and a mixture of HPC/XR and HPC/XDH. 8 nM ZS-XR and 8 nM HG-XDH were reacted with 12.5 mM xylose and 500 µM NADH in the buffer (pH 7.0) containing 40 mM Tris, 20 mM acetic acid, 12.5 mM MgCl$_2$, 5 µM BSA, 0.002% Tween20, 1 µM ZnCl$_2$ and 100 mM NaCl. (b) NADH regeneration by the cascade reactions by HPO$_h$/XR-XDH, HPC/XR-XDH, a mixture of HPO$_h$/XR and HPO$_h$/XDH and a mixture of HPC/XR and HPC/XDH. (c) Initial reaction velocity for the NADH regeneration by the enzyme cascade reactions. Data were the averages of three independent repetitions, error bars indicated the S.D. of the repetitions.

178

After 6-h reaction, HPC/XR-XDH and HPO$_h$/XR-XDH regenerated 31 μM and 17 μM NADH, respectively, while the reaction by HPC/XR and HPC/XDH regenerated 4 μM NADH (Figure 5.25). The higher regeneration yields by the coassemblies of XR-XDH were well explained by considering the K_m values of HG-XDH for substrate xylitol (104 mM) and cofactor NAD$^+$ (358 μM) (Table 5.4). The concentrations of intermediates (xylitol and NAD$^+$) produced by HPO$_h$/XR or HPC/XR were not sufficient for the individually scaffolded downstream enzyme HPO$_h$/XR or HPC/XDH for the far inter-enzyme distance. The observed higher NADH regeneration yield by HPO$_h$/XR-XDH or HPC/XR-XDH over the one observed by HPC$_T$/XR-XDH (closed state obtained from the closing process, Figure 5.17d) could reflect the higher remaining activity of XR for HPO$_h$/XR-XDH or HPC/XR-XDH by applying the DNA scaffolds prepared in one-step.
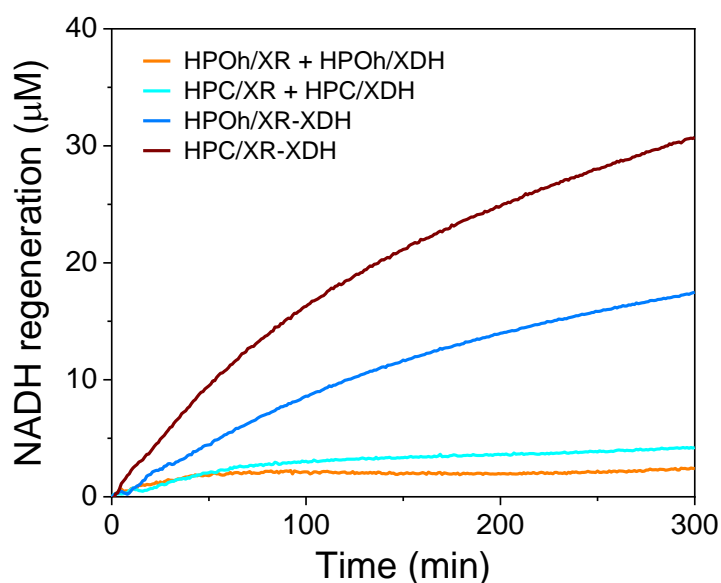
Figure 5.25. Time course changes of NADH regeneration of the cascade reactions by HPO$_h$/XR-XDH, HPC/XR-XDH, an equimolar mixture of HPO$_h$/XR and HPO$_h$/XDH and an equimolar mixture of HPC/XR and HPC/XDH.

Table 5.4. Kinetic parameters of ZS-XR and HG-XDH[a]

	ZS-XR		HG-XDH	
	Xylose [b]	NADH [c]	Xylitol [d]	NAD$^+$ [e]
K_m (mM)	256.4 ± 45.3	0.149 ± 0.011	104.22 ± 16.26	0.358 ± 0.006
k_{cat} (min^{-1})	124.6 ± 6.0	147.6 ± 0.8	58.86 ± 2.63	50.10 ± 1.54
k_{cat}/K_m (min^{-1}mM^{-1})	0.494 ± 0.072	994.3 ± 75.9	0.572 ± 0.070	140.0 ± 4.7

[a] The enzyme assays were carried out at the enzyme concentration of 25 nM in a buffer (pH 7.0) containing 40 mM Tris-HCl, 20 mM acetic acid, 12.5 mM MgCl$_2$, 0.002% Tween20, 1 µM ZnCl$_2$ and 100 mM NaCl. Data were the averages of three independent repetitions.

[b] Concentrations of xylose were varied from 0 to 500 mM, and that of NADH was kept at 300 µM for the assay.

[c] Concentrations of NADH were varied from 0 to 500 µM, and that of xylose was kept at 200 mM for the assay.

[d] Concentrations of xylitol were varied from 0 to 800 mM, and that of NAD$^+$ was kept at 2 mM for the assay.

[e] Concentrations of NAD$^+$ were varied from 0 to 2 mM, and that of xylitol was kept at 200 mM for the assay.

5.2.6 Inter-enzyme distance dependency of XR/XDH cascade reactions on the DNA scaffold

The estimated average inter-enzyme distances (*d*) of HPO$_h$/XR-XDH and HPC/XR-XDH were 60 nm and 18 nm, respectively. The inter-enzyme distance of the separate system (HPC/XR + HPC/XDH) was estimated to be 601 nm based on the DNA scaffold concentration (Figure 5.26a-c) (Materials and Methods). The turnover number of each system was estimated from the amount of product (regenerated NADH in first 100 min) divided by the concentration of second enzyme HG-XDH in the time unit (100 min). The turnover numbers were plotted against inter-enzyme distances of ZS-XR and HG-XDH (Figure 5.26d). A clear inter-enzyme distance dependency was observed. The shorter inter-enzyme distance of coassembly system in the closed state facilitated the

transportation of intermediates (xylitol and NAD$^+$) from first enzyme to second enzyme. The enzyme cascade reaction by the individually assembled system (HPC/XR + HPC/XDH) proceeded with much lower cascade efficiency due to the large inter-enzyme distance.
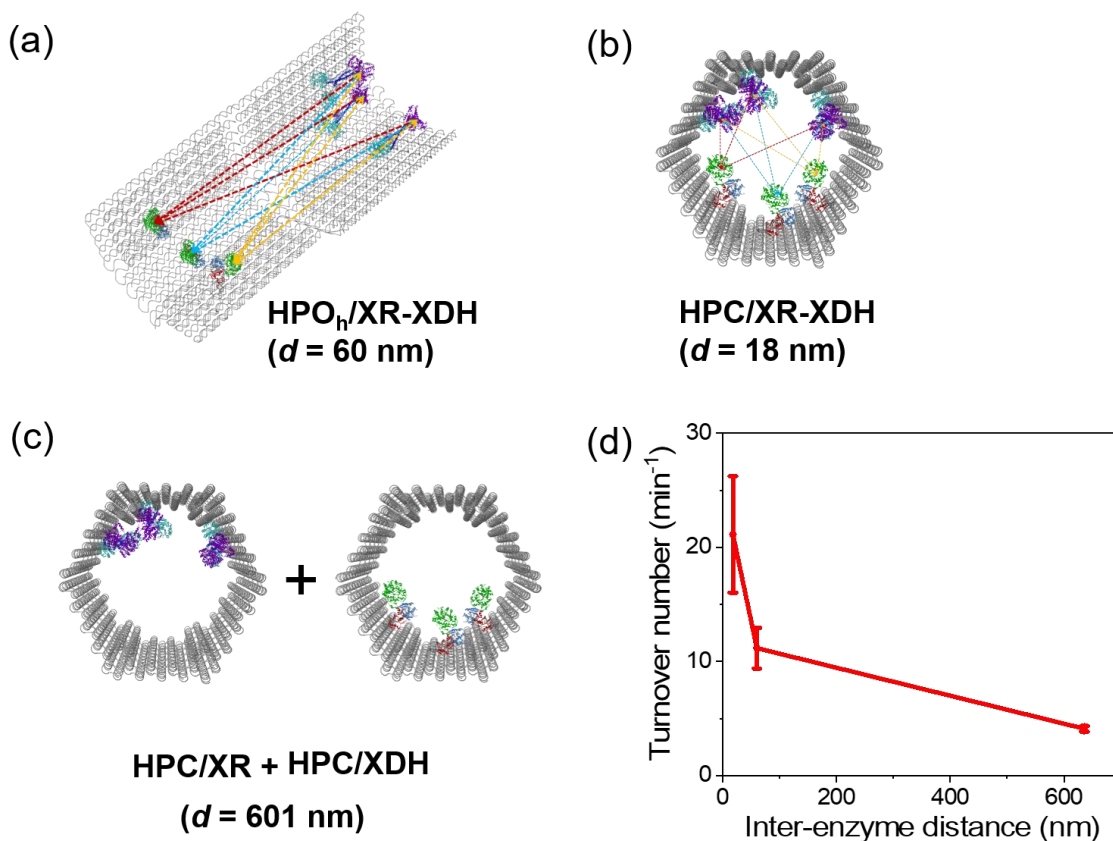
Figure 5.26. Inter-enzyme distance dependence of the XR-XDH enzyme cascade reactions on the 3D DNA scaffold. An illustration showing the average inter-enzyme distance of (a) HPO$_h$/XR-XDH, (b) HPC/XR-XDH, and (c) HPC/XR + HPC/XDH. The molecular models were constructed by Discovery Studio (version 3.1, Accelrys Inc.). (d) The plot of turnover numbers of XR/XDH enzyme cascade reactions on the 3D DNA hexagonal prism (HP) against the inter-enzyme distance of ZS-XR and HG-XDH. 8 nM ZS-XR and 8 nM HG-XDH were reacted with 12.5 mM xylose and 500 µM NADH in the buffer (pH 7.0) containing 40 mM Tris-HCl, 20 mM acetic acid, 12.5 mM MgCl$_2$, 5 µM BSA, 0.002% Tween20, 1 µM ZnCl$_2$ and 100 mM NaCl. Data in (d) were the averages of three independent repetitions, error bars indicated the S.D. of the repetitions.

181

To further investigate the effect of inter-enzyme distance and 3D DNA space on the efficiency of cascade reaction, distance dependence of the turnover numbers for enzyme cascade reactions by XR and XDH were compared with those obtained by using 2D DNA scaffold as previously reported from Morii Lab.[33] The turnover number for the cascade reactions on the hexagonal prism and on the 2D DNA scaffold were similar with each other for HPO_h/XR-XDH with the inter-enzyme distance of 60 nm (11.2 min^{-1}) and 2D DNA scaffold with that of 54 nm (11.4 min^{-1}).[33] Interestingly, the turnover number of HPC/XR-XDH with the inter-enzyme distance of 18 nm (21.1 min^{-1}) was much higher than that expected from the plot for 2D DNA scaffold or that for 10 nm (12.9 min^{-1}). The results indicated that besides the inter-enzyme distance effect, the confined space in 3D DNA hexagonal prism provided a more favorable environment to enhance the efficiency of cascade reaction (Figure 5.27).
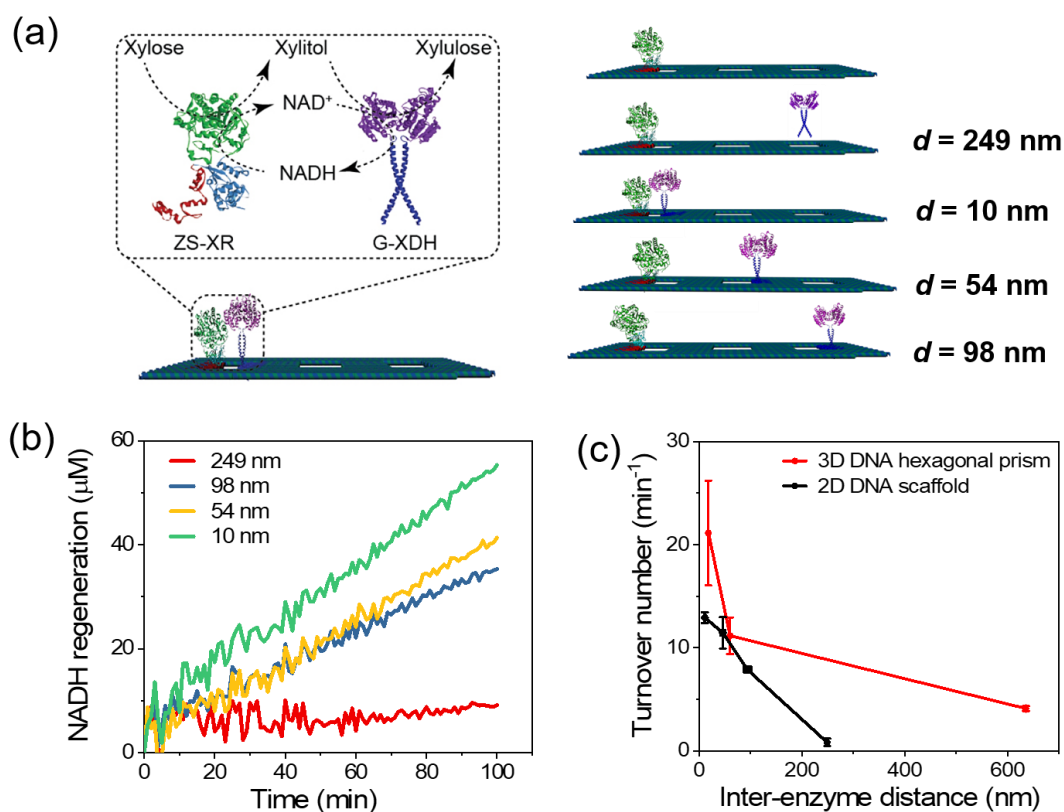
Figure 5.27. Comparison of the enzyme cascade reactions XR/XDH on 2D DNA scaffold with three cavities and in the 3D DNA hexagonal prism. (a) Illustrations showing XR/XDH enzyme cascade reactions on the 2D DNA scaffold with the variation of inter-enzyme distance from 98

nm to 10 nm. [33] The inter-enzyme distance of DNA scaffolded ZS-XR and free G-XDH (GCN4 fused XDH) was estimated to be 249 nm base on the molecular concentrations. (b) NADH regeneration of the XR/XDH enzyme cascade reactions on DNA scaffold in the first 100 min.[33] (c) Comparison of turnover numbers of enzyme cascade reactions on the 2D DNA scaffold and in the 3D DNA hexagonal prism in the first 100 minutes.[33] The turnover number for each system was estimated from the amount of product (regenerated NADH) divided by the concentration of the second enzyme G-XDH (or HG-XDH) on DNA scaffold in the time unit (100 min). The cascade reaction by ZS-XR and G-XDH on 2D DNA scaffold was carried out by 85 nM ZS-XR and 85 nM G-XDH (monomer) reacted with 12.5 mM xylose and 2 mM NADH in the buffer (pH 7.0) containing 40 mM Tris, 20 mM acetic acid, 12.5 mM $MgCl_2$, 0.02% Tween20, 1 µM $ZnCl_2$ and 100 mM NaCl. Data in (d) were the averages of three independent repetitions, error bars indicated the S.D. of the repetitions.

5.2.7 Mechanistic insights into the enhancement of enzyme cascade reactions inside the 3D DNA scaffold

The observed enhanced efficiency of XR/XDH cascade reaction inside the closed state of 3D DNA hexagonal prism could be attributed to the cooperation of the proximity effect, the scaffolding effect and the effects of confined environment. Indeed, the controversy exits whether the inter-enzyme distance affects for the cascade reaction and how it works. Idan *et al.* used the theoretical calculation to illustrate the activity enhancement of enzyme cascade was limited to less than 1 s when the inter-enzyme distance was less than 10 nm.[36] And the GOx/HRP simulation results of Chado *et al.* showed that the overall cascade activity was only weakly dependent on spatial arrangement under diffusion-limited conditions.[37] However, as previously reported, the distance dependence of enzyme cascade reactions has been observed by test tube and simulation experiments.[38-40] In the present study, the inter-enzyme distance of XR and XDH was varied from 60 nm to 18 nm with twofold enhancement of enzyme cascade efficiency. The result was well explained by the assumption that proximity facilitated the efficient transportation of intermediates from XR to XDH.

Besides the proximity effect, a scaffold with high density of DNA helix was beneficial for the immobilized enzymes. Enhanced activities of DNA scaffolded enzymes have been reported for various DNA-enzyme complexes to propose the contribution of ordered hydration layer, substrate affinity, lower local pH environment, reduction of absorption or favorable microenvrioment.[27, 41–45] In Chapter 2, the enhanced activities of individual DNA scaffolded ZS-XR and scaffolded HG-XDH on the open state of the 3D DNA hexagonal prism were observed. The different optimal pH profiles of XR (pH 6.0) and XDH (pH 8.0), and the neutral or net negative charge of their substrates and cofactors of the experimental conditions indicated that neither the local pH change nor the surface-substrate or -cofactor electrostatic attractive interaction accounted for the increase in activities of assembled enzymes. It was also indicated that the improved stability or reduced adsorption of scaffolded enzymes alone would not account for the enhanced activity of enzyme on the DNA scaffold.[24] In the present case, cascaded enzymes would benefit the stabilization and the protection against adsorption by the DNA scaffold, which could be reflected by the result that enzyme cascade in the diffusion form (free ZS-XR + free HG-XDH) reacted with lower efficiency than the enzyme cascades on DNA scaffold.

It was further suggested that the confined environments of DNA scaffold prevented the intermediates from escaping to the bulk solution and increased the local concentration of intermediates. Linko *et al.* compartmentalized GOx/HRP inside a tubular DNA origami to suggest that the intermediates might be unable to diffuse through the barriers of the origami unit.[25] Similarly, Fu *et al.* suggested that GOx and HRP entrapped within short nanotube was significantly higher than that on the planar rectangle. It was proposed that H_2O_2 could not diffuse out of the diffusion layer that was much thicker than the diameter of DNA nanotubes (20 nm).[26] However, the intermediates would not be kept inside the confined DNA structures by considering the

pore sizes of DNA origami.[46] Instead, the ordered hydration layer formed by the highly charged DNA scaffold surface might increase the local concentration of hydrophilic substrates and intermediates as proposed in Chapter 2. In the present study, the local concentration of xylitol was increased within the ordered hydration layer, which in turn increased the reaction velocity of enzyme to enhance the cascade reaction efficiency.

5.3 Conclusion

In summary, a three-dimensional DNA hexagonal prism was developed with a fast dynamic transition from the open to closed state induced by a toehold-mediated strand displacement. Effects of the stoichiometry of closing keys and the hybridization temperature on the closing efficiency were systematically investigated. By the reconfiguration of DNA scaffold, the enzyme cascade reaction xylose reductase/xylitol dehydrogenase was regulated. The overall reaction efficiency in the closed state was higher than that of the open state, which was contributed by synergy of the proximity effect, scaffolding effect and the environment the confined 3D DNA space with higher local concentration of the hydrophilic intermediate. Herein, an enzyme cascade reaction with tunable efficiency was constructed based on the natural metabolic pathway. As one of the possible applications of this reconfigurable 3D DNA structure, the origin of catalytic enhancement of enzyme cascade reaction on the DNA scaffold was studied to provide insights into the working mechanisms of for metabolic reactions in cells. This system is expected to be employed for the further construction of more sophisticated metabolic pathway in vitro or vivo, drug delivery and biosensor. The reconfigurable 3D DNA scaffold would also act as a smart tool to explore the allosteric switches of proteins or other biomolecules, which exhibit highly potential applications in the field of bio-nanotechnology.

5.4 Materials and Methods

5.4.1 Materials

The single-stranded M13mp18 viral DNA (7249) was purchased from Guild Biosciences. BG-GLA-NHS (S9151S) and Bovine Serum Albumin (BSA, BS9000S) were purchased from New England Biolabs. 5-chlorohexane (CH) derivative [HaloTag Succinimidyl Ester (O2) Ligand (P1691)] were purchased from Promega. β-Nicotinamide adenine dinucleotide in reduced (NADH) and oxidized (NAD$^+$) forms were obtained from Oriental Yeast (Tokyo, Japan). Xylose, xylitol, and all other chemicals and reagents were purchased from Wako Chemicals (Tokyo, Japan) or Nacalai Tesque (Kyoto, Japan). Toyopearl HW-55F was purchased from Tosoh Bioscience GmbH (Griesheim, Germany). Amicon® Ultra-0.5 Centrifugal Filter Device (100 KDa).

5.4.2. Design of DNA scaffold

The DNA scaffold was designed in a honeycomb lattice using the open source software caDNAno (v 2.2.0.).[47] The caDNAno blueprints of the DNA scaffold with enzymes HG-XDH and ZS-XR attachment sites were shown in Figure 5.28.

5.4.3 Preparation of DNA Scaffold

The DNA scaffolds were prepared by following the previous report.[12,48] The samples were purified by Sephacryl S-400 to remove the excess staple strands. The concentration of DNA scaffold was quantified by the absorbance at 260 nm using the determined extinction coefficient of DNA scaffold (1.2×10^8 M^{-1}cm^{-1}).[24]
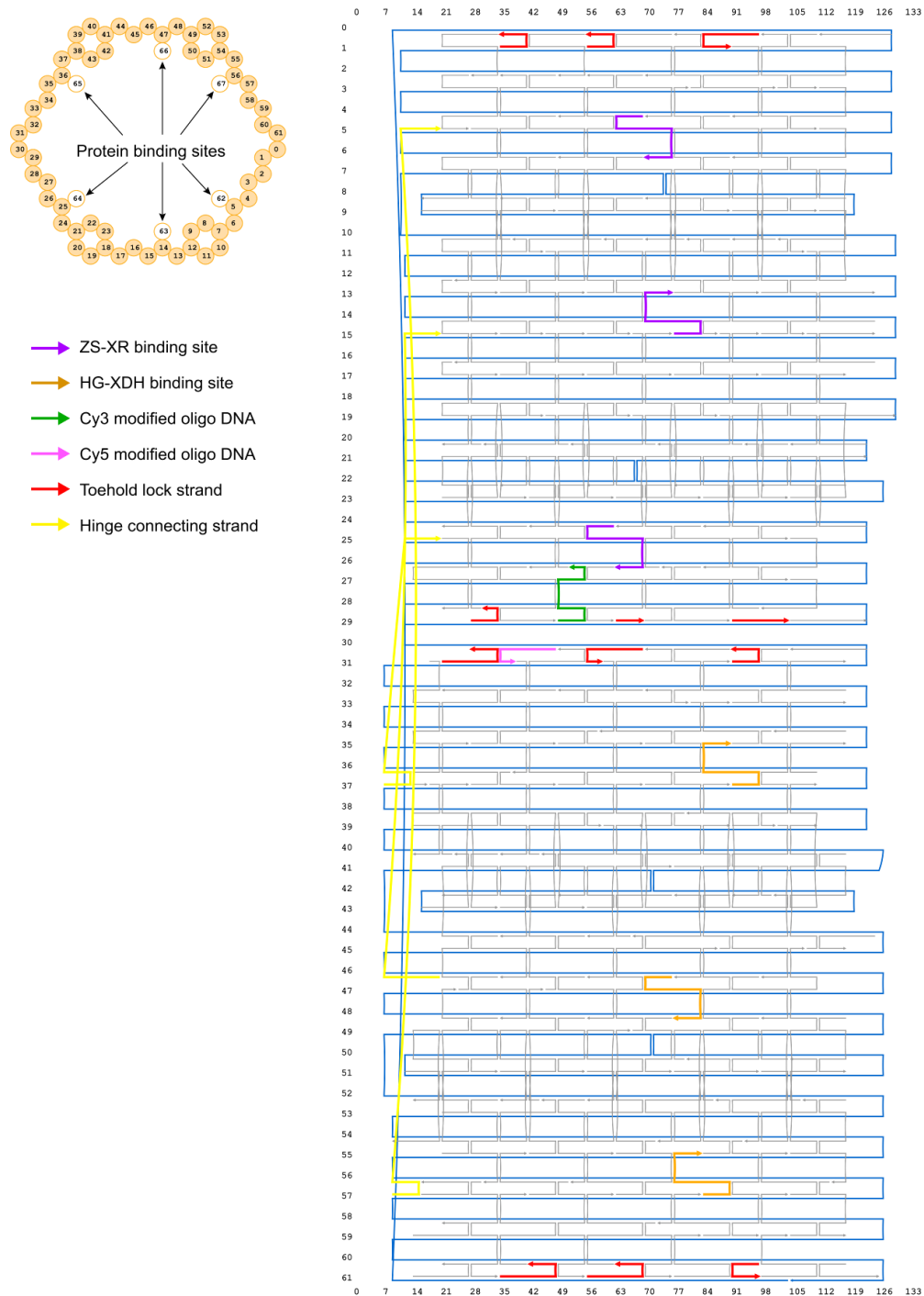
Figure 5.28. Front view and blueprint modified from caDNAno[47] software interface of DNA scaffold (http://cadnano.org/) with the extension positions of toehold locks. The staple strands in purple and orange indicated enzyme ZS-XR and HG-XDH attachment sites, respectively. The staple strands in green and pink were Cy3-modified oligo and Cy5-modified oligo, respectively. The staple strands in red were the positions for the extension positions of toehold lock sequences. The staple strands in yellow were connecting hinges when used for the folding of DNA scaffold in open sate in 180º.

5.4.4 Closing process of DNA scaffold

The open state of DNA scaffold was first folded with 1:10 molar ratio of opening keys, then 1:100 molar ratio of closing keys were added to hybridize with the opening keys. Typically, 5 nM DNA scaffold in open state closed by 500 nM closing keys in 96-plate (Greiner Microplate, 96-well, PS, F-bottom (chimney well) µCLEAR®, black, non-binding) in the buffer (pH 7.0) containing 40 mM Tris, 20 mM acetic acid, 12.5 mM $MgCl_2$ and 0.002% Tween20 at 25 °C. The nucleotide sequences of long lock strands, short lock strands, opening keys and closing keys were shown in Table 5.5.

Table 5.5. Nucleotide sequences of staple strands used for toehold locks, opening keys and closing keys

Oligo DNA	Sequence (from 5' to 3')
Toehold-Lock-1a	ATTGACAGGAGGTTCGTATAATGGTATAAACATCAGTGTAGGA
Toehold-Lock 1b	TGATGTTTATACCAATTATTCCAGA
Toehold-Lock 2a	ACTCCTCTCAACATCAGTCTGATAAGCTA
Toehold-Lock 2b	CAGACTGATGTTGAGTTTTAACGGGGTCCTTG
Toehold-lock 3a	CCAGAATTGATGATTGGGGTATTTGACAAACTGACA
Toehold-Lock 3b	TGTCAAATACCCCAGGGGTTTTGCTCAG
Toehold-Lock 4a	ATGAATCAATCGGCCAGCTGCTTTTGGGATTCCGTTG
Toehold-Lock 4b	CCCAAAAGCAGCTGCAGTTTGGAACAAGAGCTTGA
Toehold-Lock 5a	GAGAGGCCCTGTTTTCAGCCGCTGTCACACGCACAG
Toehold-Lock 5b	GTGACAGCGGCTGATATTAAAGAACGTGTAAAGGG
Toehold-Lock 6a	GGTGCCGAAAACCGACTCACCGACAGCGTTGAATGTT
Toehold-Lock 6b	CGCTGTCGGTGAGTGCGGTCCACGCTGGGGTGGTT
Toehold Lock-OPK	ATCCTCGTAATCCTACACTGATGTTTAT
Toehold Lock-OPK	AAGATTCAGTAGCTTATCAGACTGATG
Toehold Lock-OPK	GAGGTGTTGTGTCAGTTGTCAAATAC
Toehold Lock-OPK	AATCTATAACAACGGAATCCCAAAAGCA
Toehold Lock-OPK	TAGAATTGTCTGTGCGTGTGACAGCGG
Toehold Lock-OPK	CCGGCTTAAAACATTCAACGCTGTCGGT
Toehold Lock-CLK	CATCAGTGTAGGATTACGAGGAT
Toehold Lock-CLK	GTCTGATAAGCTACTGAATCTT
Toehold Lock-CLK	TGACAAACTGACACAACACCTC
Toehold Lock-CLK	TTGGGATTCCGTTGTTATAGATT
Toehold Lock-CLK	GTCACACGCACAGACAATTCTA
Toehold Lock-CLK	CAGCGTTGAATGTTTTAAGCCGG

5.4.5 Fluorescence measurement and FRET analysis

Fluorescence measurements were performed on microplate reader (TECAN Infinite® 200Pro). The fluorescence spectra of the samples were collected from 550 nm to 750 nm upon the excitation wavelength of 520 nm in the 96-plate [Greiner Microplate, 96-well, PS, F-bottom (chimney well) μCLEAR®, black, non-binding] with 5 nm bandwidth. Ratiometric FRET efficiency values were calculated as $E = I_{DA}/(I_{DA}+I_{DD})$, where I_{DD} and I_{DA} are the donor fluorophore (Cy3) and acceptor fluorophore (Cy5) fluorescence intensity, respectively, upon donor excitation ($\lambda_{ex} = 520$ nm). To study the kinetics of closing process, the time courses of Cy3 fluorescence intensity ($\lambda_{ex} = 520$ nm, $\lambda_{em} = 570$ nm) and Cy5 fluorescence intensity ($\lambda_{ex} = 520$ nm, $\lambda_{em} = 670$ nm) were monitored.

5.4.6 Calculation of closing efficiency

The closing efficiency was calculated by the Cy5 fluorescence intensity ($\lambda_{ex} = 520$ nm, $\lambda_{em} = 670$ nm) of the fluorescence emission spectra after closing process based on the formula $(I_{HPO_{T}\text{-control}} - I_{HPO_{T} + CLK})/(I_{HPO_{T}\text{-control}} - I_{HPC_{T}\text{-control}})$ for the closing process.

5.4.7 TEM Characterization

DNA scaffold (2 to 3 nM, 2 μL) was placed onto a TEM grid and incubated for 2 minutes, then the extra sample was removed by filter paper. MilliQ water (15 to 20 μL) was used to wash the surface of TEM grid, followed by incubation with 4 μL 10% TI Blue for 2 min or 5 min. The surface was then washed by MilliQ water consecutively. Samples were visualized using a TEM microscope (JEOL JEM-2200FS + CETCOR) after the preparation.

5.4.8 Agarose gel electrophoresis

The agarose gel electrophoresis conditions were specified in the captions of figures. Typically, the samples were run on a 2% agarose gel ($0.5 \times$ TB + 5 mM MgCl$_2$) with the following conditions: $0.5 \times$ TB + 5 mM MgCl$_2$, 104 V for 10 h. The gel was visualized by using Molecular Imager FX pro (BioRad) under ethidium bromide (EtBr) channel (λ_{ex} = 532 nm, λ_{em} = 605 nm), Cy3 channel (λ_{ex} = 532 nm, λ_{em} = 605 nm), or FRET channel (λ_{ex}= 532 nm, λ_{em} = 695 nm).

5.4.9 Preparation of ZS-XR and HG-XDH

The construction of expression vectors, overexpression and purification of enzymes ZS-XR and HG-XDH were conducted as previously reported.[24,33]

5.4.10 Preparation of the DNA scaffold assembled with ZS-XR and/or HG-XDH

Amicon® Ultra-0.5 Centrifugal Filter Device (100 KDa) was used to remove the excess amount of staple strands and concentrate DNA scaffold. Each of the concentrated DNA scaffolds containing either the binding sites with BG-GLA-NHS modification for ZS-XR and/or the binding sites with 5-chlorohexane (CH) derivatives modification for HG-XDH was incubated with ZS-XR and/or HG-XDH in a buffer (pH 7.0) containing 40 mM Tris-HCl, 20 mM acetic acid, and 12.5 mM MgCl$_2$, 5 mM β-Mecaptoethanol, 0.002% Tween20 and 1 μM ZnCl$_2$ at 4 °C for 1 h. The mixture was purified by gel filtration (500 μL in volume of Toyopearl HW55F) in an Ultrafree-MC-DV column with a buffer (pH 7.0) containing 40 mM Tris-HCl, 20 mM acetic acid, and 12.5 mM MgCl$_2$ to remove the excess amount of unbound proteins. The concentration of DNA scaffold-protein complexes was quantified by the absorbance at 260 nm and calculated by using the determined extinction coefficient of DNA scaffold (1.2×10^8 M^{-1}cm^{-1}).[24] The nucleotide sequences for the staple strands containing the binding sites were shown in Table 5.6.

Table 5.6. Nucleotide sequences for the staple strands containing the binding sites for ZS-XR with BG modification or the binding sites for HG-XDH with CH modification[34]

Oligo DNA	Sequence (from 5' to 3')
Binding site 1	GGGGGATCAGCCAGCTTACGCCCACGCGCGTT^{BG}TTCGCGCGTGGG CGTAAGCTTTCCGCAAACGG
Binding site 2	GGAAGCCGGAAGCACTTACGCCCACGCGCGTT^{BG}TTCGCGCGTGGG CGTAAGAACTCCAGTTGATT
Binding site 3	GCATAACAAATCTCCTTACGCCCACGCGCGTT^{BG}TTCGCGCGTGGG CGTAAGCAAAAAATTTCTGT
Binding site 4	TACCAGATTAAGACGT^{CH}TCATGAGTCATGAGTTTTCT^{CH}CATGACT CATGAACTCCTTATCGATTGA
Binding site 5	TGTAAATGATAGCTGT^{CH}TCATGAGTCATGAGTTTTCT^{CH}CATGACT CATGAACTAGATTATTAATTA
Binding site 6	ATAACATGCAACAGGT^{CH}TCATGAGTCATGAGTTTTCT^{CH}CATGACT CATGAACGAAAAACGTAAGAA

BG modified amino-C6-T was denoted as **T^{BG}**

CH modified amino-C6-T was denoted as **T^{CH}**

5.4.11 AFM imaging and statistical analysis

The methods of AFM imaging and statistical analysis were shown in 2.4.4 in Chapter 2. The binding of ZS-XR and/or HG-XDH was counted for only ZS-XR and/or HG-XDH bound to the perfectly folded DNA scaffold. The average numbers of ZS-XR and/or HG-XDH were quantitated as previously report.[24]

5.4.12 Enzyme assays in the presence of both ZS-XR and HG-XDH

The bimolecular intermediates (xylitol and NAD$^+$) transporting system of ZS-XR and HG-XDH was investigated in this study. For the enzyme cascade reactions after the shape transformation of DNA scaffold, the reactions were carried out by 7 nM ZS-XR and 7 nM HG-XDH reacting with 200 mM xylose and 300 μM NADH in the buffer (pH 7.0) containing 40 mM Tris-HCl, 20 mM acetic acid, 12.5 mM MgCl$_2$, 5 μM BSA, 0.002% Tween20, 1 μM ZnCl$_2$ and 100 mM NaCl. For the enzyme cascade reactions on statically open and closed states of DNA scaffold, the reactions were carried out by 8

nM ZS-XR and 8 nM HG-XDH reacted with 12.5 mM xylose and 500 µM NADH in the buffer (pH 7.0) containing 40 mM Tris-HCl, 20 mM acetic acid, 12.5 mM MgCl$_2$, 5 µM BSA, 0.002% Tween20, 1 µM ZnCl$_2$ and 100 mM NaCl. The progress of reaction was monitored by the time-course changes of absorbance at 340 nm (25 °C). Enzyme activities were measured on the microplate [Greiner Microplate, 655901, 96-well, PS, F-bottom (chimney well) clear, non-binding].

5.4.13 Constructions of statically open and closed states of scaffold

Three connecting hinges were used to fold the fully open state of DNA scaffold (the nucleotide sequences were shown in Table 5.7). Six DNA linker strands hybridizing the two domains of DNA scaffold were used to fold the rigid closed state (the nucleotide sequences of linkers were shown in Table 5.8). To quantitate the enzyme loading numbers encapsulated into the rigid closed state, six linkers removers complementary with the linkers were used to remove the linkers (the nucleotide sequences of linker removers were shown in Table 5.9). HPC/XR-XDH, HPC/XR and HPC/XDH were incubated with 1: 200 molar ratio of linker removers at ambient temperature for overnight to open the closed structure and quantitate enzyme numbers.

Table 5.7. Nucleotide sequences of connecting hinges to stabilize the fully open state of DNA scaffold

Oligo DNA	Sequence (from 5' to 3')
Connecting hinge 1	ACATTGAATATATTTTAGTTTTTTACGAGAATG
Connecting hinge 2	ACATTGTCAGTGAGATTCACTTTTTCTGCCAGTT
Connecting hinge 3	ACATTGAATAAGAACCACGGTTTTAGGAACAAC

Table 5.8. Nucleotide sequences of linker strands of DNA scaffold

Oligo DNA	Sequence (from 5' to 3')
Linker strand 1	AGAGTAGGATGAATCAATCGGCCAGTTTGGAACAAGAGCTTGA
Linker strand 2	ACGGTGACGAGAGGCCCTGTTTTATTAAAGAACGTGTAAAGGG
Linker strand 3	CGTAGCAAGGAACCTACAGTTAATGCCCCCGCC
Linker strand 4	GCTTAATGACTCCTCGTTTTAACGGGGTCCTTG
Linker strand 5	AAGCCAACCCAGAATTGATGATGGGGTTTTGCTCAG
Linker strand 6	TTTAACAAGGTGCCGAAAACCGGCGGTCCACGCTGGGGTGGTT

Table 5.9. Nucleotide sequences of linker strand removers

Oligo DNA	Sequence (from 5' to 3')
Linker remover 1	TCAAGCTCTTGTTCCAAACTGGCCGATTGATTCATCCTACTCT
Linker remover 2	CCCTTTACACGTTCTTTAATAAAACAGGGCCTCTCGTCACCGT
Linker remover 3	GGCGGGGGCATTAACTGTAGGTTCCTTGCTACG
Linker remover 4	CAAGGACCCCGTTAAAACGAGGAGTCATTAAGC
Linker remover 5	CTGAGCAAAACCCCATCATCAATTCTGGGTTGGCTT
Linker remover 6	AACCACCCCAGCGTGGACCGCCGGTTTTCGGCACCTTGTTAAA

5.5 References

1. Agapakis, C. M., Boyle, P. M. & Silver, P. A. Natural strategies for the spatial optimization of metabolism in synthetic biology. *Nat. Chem. Biol.* **8**, 527–535 (2012).

2. Pareek, V., Tian, H., Winograd, N. & Benkovic, S. J. Metabolomics and mass spectrometry imaging reveal channeled de novo purine synthesis in cells. *Science* **368**, 283–290 (2020).

3. Bulutoglu, B., Garcia, K. E., Wu, F., Minteer, S. D. & Banta, S. Direct evidence for metabolon formation and substrate channeling in recombinant TCA cycle enzymes. *ACS Chem. Biol.* **11**, 2847–2853 (2016).

4. Sweetlove, L. J. & Fernie, A. R. The role of dynamic enzyme assemblies and substrate channelling in metabolic regulation. *Nat. Commun.* **9**, (2018).

5. Rothemund, P. W. K. Folding DNA to create nanoscale shapes and patterns. *Nature* **440**, 297–302 (2006).

6.   Douglas, S. M. *et al.* Self-assembly of DNA into nanoscale three-dimensional shapes. *Nature* **459**, 414–418 (2009).

7.   Saccà, B. *et al.* Orthogonal protein decoration of DNA origami. *Angew. Chem., Int. Ed.* **49**, 9378–9383 (2010).

8.   Yurke, B., Turber, A. J., Jr, A. P. M., Simmel, F. C. & Neumann, J. L. A DNA-fuelled molecular machine made of DNA. *Nature* **406**, 605–608 (2000).

9.   Grossi, G., Dalgaard Ebbesen Jepsen, M., Kjems, J. & Andersen, E. S. Control of enzyme reactions by a reconfigurable DNA nanovault. *Nat. Commun.* **8**, (2017).

10.   Andersen, E. S. *et al.* Self-assembly of a nanoscale DNA box with a controllable lid. *Nature* **459**, 73–76 (2009).

11.   Zadegan, R. M. *et al.* Construction of a 4 Zeptoliters switchable 3D DNA box origami. *ACS Nano* **6**, 10050–10053 (2012).

12.   Douglas, S. M., Bachelet, I. & Church, G. M. A logic-gated nanorobot for targeted transport of molecular payloads. *Science* **335**, 831–834 (2012).

13.   Li, S. *et al.* A DNA nanorobot functions as a cancer therapeutic in response to a molecular trigger in vivo. *Nat. Biotechnol.* **36**, 258–264 (2018).

14.   Marras, A. E. *et al.* Cation-activated avidity for rapid reconfiguration of DNA nanodevices. *ACS Nano* **12**, 9484–9494 (2018).

15.   Kuzuya, A., Sakai, Y., Yamazaki, T., Xu, Y. & Komiyama, M. Nanomechanical DNA origami 'single-molecule beacons' directly imaged by atomic force microscopy. *Nat. Commun.* **2**, (2011).

16.   Ijäs, H., Hakaste, I., Shen, B., Kostiainen, M. A. & Linko, V. Reconfigurable DNA origami nanocapsule for pH-controlled encapsulation and display of cargo. *ACS Nano* **13**, 5959–5967 (2019).

17.   Kim, S. H. *et al.* Reversible regulation of enzyme activity by pH-responsive encapsulation in DNA nanocages. *ACS Nano* **11**, 9352–9359 (2017).

18.   Turek, V. A. *et al.* Thermo-responsive actuation of a DNA origami flexor. *Adv. Funct. Mater.* **28**, 1–7 (2018).

19.   Juul, S. *et al.* Temperature-controlled encapsulation and release of an active

enzyme in the cavity of a self-assembled DNA nanocage. *ACS Nano* **7**, 9724–9734 (2013).

20. Kohman, R. E. & Han, X. Light sensitization of DNA nanostructures via incorporation of photo-cleavable spacers. *Chem. Commun.* **51**, 5747–5750 (2015).

21. Feng, Y., Tohgasaki, T., Shitomi, Y., Sugiyama, H. & Endo, M. A photocaged DNA nanocapsule for delivery and manipulation in cell*s*. *Methods Enzymol.* **641**, 329-342 (2020).

22. Kopperger, E. *et al.* A self-assembled nanoscale robotic arm controlled by electric fields. *Science* **359**, 296–301 (2018).

23. Linko, V. *et al.* DNA-based enzyme reactors and systems. *Nanomaterials* **6**, 139 (2016).

24. Lin, P. *et al.* Evaluation of the role of the DNA surface for enhancing the activity of scaffolded enzymes. *Chem. Commun.* **57**, 3925–3928 (2021).

25. Linko, V., Eerikäinen, M. & Kostiainen, M. A. A modular DNA origami-based enzyme cascade nanoreactor. *Chem. Commun.* **51**, 5351–5354 (2015).

26. Fu, Y. *et al.* Single-step rapid assembly of DNA origami nanostructures for addressable nanoscale bioreactors. *J. Am. Chem. Soc.* **135**, 696–702 (2013).

27. Zhao, Z. *et al.* Nanocaged enzymes with enhanced catalytic activity and increased stability against protease digestion. *Nat. Commun.* **7**, (2016).

28. Zhang, D. Y. & Winfree, E. Control of DNA strand displacement kinetics using toehold exchange. *J. Am. Chem. Soc.* **131**, 17303–17314 (2009).

29. Roy, R., Hohng, S. & Ha, T. A practical guide to single-molecule FRET. *Nat. Methods* **5**, 507–516 (2008).

30. Watanabe, S. *et al.* Ethanol production from xylose by recombinant *Saccharomyces cerevisiae* expressing protein-engineered NADH-preferring xylose reductase from *Pichia stipitis*. *Microbiology* **153**, 3044–3054 (2007).

31. Watanabe, S., Kodaki, T. & Makino, K. Complete reversal of coenzyme specificity of xylitol dehydrogenase and increase of thermostability by the introduction of structural zinc. *J. Biol. Chem.* **280**, 10340–10349 (2005).

32. Nakata, E., Dinh, H., Ngo, T. A., Saimura, M. & Morii, T. A modular zinc finger adaptor accelerates the covalent linkage of proteins at specific locations on DNA nanoscaffolds. *Chem. Commun.* **51**, 1016–1019 (2015).

33. Ngo, T. A., Nakata, E., Saimura, M. & Morii, T. Spatially organized enzymes drive cofactor-coupled cascade reactions. *J. Am. Chem. Soc.* **138**, 3012–3021 (2016).

34. Nguyen, T. M., Nakata, E., Saimura, M., Dinh, H. & Morii, T. Design of modular protein tags for orthogonal covalent bond formation at specific DNA sequences. *J. Am. Chem. Soc.* **139**, 8487–8496 (2017).

35. Nguyen, T. M. *et al.* Rational design of a DNA sequence-specific modular protein tag by tuning the alkylation kinetics. *Chem. Sci.* **10**, 9315–9325 (2019).

36. Idan, O. & Hess, H. Origins of activity enhancement in enzyme cascades on scaffolds. *ACS Nano* **7**, 8658–8665 (2013).

37. Chado, G. R., Stoykovich, M. P. & Kaar, J. L. Role of dimension and spatial arrangement on the activity of biocatalytic cascade reactions on scaffolds. *ACS Catal.* **6**, 5161–5169 (2016).

38. Fu, J., Liu, M., Liu, Y., Woodbury, N. W. & Yan, H. Interenzyme substrate diffusion for an enzyme cascade organized on spatially addressable DNA nanostructures. *J. Am. Chem. Soc.* **134**, 5516–5519 (2012).

39. Lim, S., Kim, J., Kim, Y., Xu, D. & Clark, D. S. CRISPR/Cas-directed programmable assembly of multi-enzyme complexes. *Chem. Commun.* **56**, 4950–4953 (2020).

40. Cao, Y. *et al.* Investigating the origin of high efficiency in confined multienzyme catalysis. *Nanoscale* **11**, 22108–22117 (2019).

41. Lin, J. L. & Wheeldon, I. Kinetic enhancements in DNA-enzyme nanostructures mimic the sabatier principle. *ACS Catal.* **3**, 560–564 (2013).

42. Zhang, Y., Tsitkov, S. & Hess, H. Proximity does not contribute to activity enhancement in the glucose oxidase-horseradish peroxidase cascade. *Nat. Commun.* **7**, (2016).

43. Zhang, Y. & Hess, H. Toward rational design of high-efficiency enzyme

cascades. *ACS Catal.* **7**, 6018–6027 (2017).

44. Timm, C. & Niemeyer, C. M. Assembly and purification of enzyme-functionalized DNA origami structures. *Angew. Chem., Int. Ed.* **54**, 6745–6750 (2015).

45. Rudiuk, S., Venancio-Marques, A. & Baigl, D. Enhancement and modulation of enzymatic activity through higher-order structural changes of giant DNA-protein multibranch conjugates. *Angew. Chem., Int. Ed.* **51**, 12694–12698 (2012).

46. Wu, N. *et al.* Molecular threading and tunable molecular recognition on DNA origami nanostructures. *J. Am. Chem. Soc.* **135**, 12172–12175 (2013).

47. Douglas, S. M. *et al.* Rapid prototyping of 3D DNA-origami shapes with caDNAno. *Nucleic Acids Res.* **37**, 5001–5006 (2009).

48. Amir, Y. *et al.* Universal computing by DNA origami robots in a living animal. *Nat. Nanotechnol.* **9**, 353–357 (2014).

CHAPTER 6

Conclusions

In this thesis, to understand and mimic the spatial organization of enzymes in cells, a 3D DNA scaffold was constructed to assemble individual- or multi-type of enzymes. The chemical mechanisms of DNA scaffolding effect on the catalytic enhancement of assembled enzymes were explored. The dynamic shape transformation of DNA scaffold from the open state to the closed state was efficiently achieved by two strategies, which were applied for the investigation of metabolic reactions to provide insights into the effects of enzyme kinetics, spatial arrangement and confined 3D DNA environment on the enzyme cascade reaction efficiency.

Chapter 1 described the research background of this thesis. Cells have developed the systems capable of efficient enzyme cascade reactions to achieve biochemical transformation by organelles, bacterial compartments or multi-enzyme complexes. Inspired by nature, artificial metabolic pathways have been constructed on a wide range of carriers, such as proteins, lipids, polymersomes and DNA-based materials, among which, DNA scaffolds attract great interest as the ideal enzyme platforms for the predominant advantages of structural programmability and accurate addressability. Besides the static DNA scaffolds, dynamic DNA scaffolds would provide broader applications in drug delivery, biosensing and biocatalysis. To attach enzymes on the DNA scaffold, several strategies such as biotin-avidin, chemical modification and modular adaptor have been developed. The current progress in the regulation of individual or multiple enzyme reactions on DNA scaffolds and the proposed mechanisms for the catalytic enhancement on DNA scaffolds are also discussed. At the end of this chapter, the aim and significance of this thesis are highlighted.

In Chapter 2, the mechanisms of catalytic enhancement of DNA scaffolded enzymes were studied. Two enzymes with different pH preferences, xylose reductase (XR) and xylitol dehydrogenase (XDH), were individually assembled on the fully open state of 3D DNA scaffold through the modular adaptor in high loading yield. The

catalytic enhancements were observed for both the scaffolded XR (sXR) and scaffolded XDH (sXDH) over the respective free enzyme. The neutral or net negative charge of their substrates and cofactors indicated that the electrostatic attractive interaction between the DNA scaffold surface and the substrate or the cofactor could not account for the increase in activities of assembled enzymes. The observed enhanced enzyme stability and the reduction of absorption could partly contribute to the catalytic enhancement of scaffolded enzymes. The local pH near the enzyme loaded position in the reaction buffer (pH 7.0) was deduced to be 6.5 via the SNARF pH indicator. Such a local pH shift would result in at most 25% enhancement of the catalytic activity for sXR and 30% reduction for sXDH since XR and XDH displayed the optimal pH at 6.0 and 8.0, respectively. Therefore, the postulated modulation of enzyme activity by the lower pH shift near DNA scaffold surface unlikely explains the catalytic enhancements of both scaffolded enzymes. Instead, an increase of the hydrophilic substrate concentration at the ordered hydration layer on the DNA surface was a plausible candidate for the factor to enhance the catalytic activity of the enzyme scaffolded on DNA nanostructure. This hypothesis was supported by the fact that the reaction of the same enzyme with hydrophobic substrates did not show marked enhancement.

In Chapter 3, the open and closed states of 3D DNA hexagonal prism (HP) were constructed by DNA origami. Six types of single-stranded DNA linkers that hybridized with the complementary sequences spanning at both the edges of top and bottom domains of DNA scaffold were designed to fold the two domains together in the closed state (HPC). The six positions complementary to the linker sequences were left unhybridized for the open state of DNA scaffold (HPO). The resulting DNA scaffolds were characterized by means of AFM and TEM with estimated yields over 90%. The dynamic shape transformation of 3D DNA scaffold from the open state to the closed state was induced by the addition of six types of DNA linkers. FRET was used to trace

the closing process and to estimate the closing yield. The optimal molar ratio of DNA scaffold to linkers was found at 1:1, where the closed state was obtained in over 90% yield at 25 ℃ for 12-h. Hybridization at the higher temperature resulted in the higher closing yield with an acceleration of closing kinetics. The closing yield was also verified by AFM images and agarose gel electrophoretic analyses. Then the efficient shape transformation of DNA scaffold was applied for an enzyme encapsulation with high loading yield. The activity of xylitol dehydrogenase (XDH) in the closed state was comparable to that in the open state after the closing process. The fact that the individual enzyme activity is maintained upon encapsulation in the hexagonal prism nanocarrier supports further applications of the present system not only for the enzyme nanocarrier, but also for the drug delivery, biosensing and diagnostic tools.

In Chapter 4, the dynamic transformation of DNA scaffold triggered by DNA linkers constructed in Chapter 3 was applied to investigate an enzyme cascade reaction by xylitol dehydrogenase (XDH) and xylulose kinase (XK). Modular adaptor fused enzymes, HG-XDH (Halo-GCN4 fused XDH) and AC-XK (AZP4-CLIP fused XK), were assembled on the open state of DNA scaffold in high enzyme assembly yield (HPO/3XDH-XK). The addition of linkers at 1:1 molar ratio provided the closed state of enzyme assembly (HPC/3XDH-XK). Time-course of the closing process of DNA scaffold assembled with enzymes was monitored by the Cy5 fluorescence intensity indicated over 90% closing yield after incubating for 12-h at 25 ℃. Formation of the closed states was further verified by AFM images, in which HPO/3XDH-XK in the closed state was observed over 95% yield. These results indicated that the HPO scaffold was efficiently transformed to the HPC scaffold regardless of the coassembly of the enzymes. The cascade reaction efficiency was analyzed by HPLC to quantitate the produced ADP after 24-h reaction at 25 ℃. The inter-enzyme distances of XDH-XK were varied from 60 nm in the open state to 20 nm in the closed state. An insignificant

inter-enzyme distance dependence was observed, which might be due to the far fast kinetics and low K_m value of the second enzyme XK. The k_{cat} values of HG-XDH and AC-XK are 59 min^{-1} and 12600 min^{-1}, respectively. Compared with the obvious inter-enzyme distance dependence observed for the XR-XDH cascade reaction reported previously in our laboratory,[1] it was suggested that the balanced enzyme kinetic parameters played important roles to exert the inter-enzyme distance dependency of cascade reaction efficiency.

In Chapter 5, a new strategy for the dynamic shape transformation of DNA scaffold was explored to accelerate the closing kinetics and applied for the enzyme cascade reaction consisting of an unstable enzyme XR. The transformation of DNA scaffold was induced by a toehold-mediated strand displacement mechanism. The open state (HPO$_T$) was stabilized by annealing with an excess amount of opening keys (OPK). Addition of the closing keys (CLK) that contained complementary sequences to OPK and removed OPK from the long lock strands in one domain by the duplex formation. The resulting free long lock strands hybridized with the short lock strands in another domain to transform the open state to the closed state (HPC$_T$). The higher closing efficiency was achieved with the higher molar ratio (HPO$_T$: CLK). The faster closing kinetics and the improved closing yield were obtained by elevating the hybridization temperature. Typically, the closing yield of DNA scaffold estimated by TEM images reached 93% with the molar ratio of 1:100 at 25 °C for 2-h.

The cascade enzymes XR and XDH were separately assembled on each domain of HPO$_T$ to investigate the cascade reaction upon the dynamic shape transformation of the enzyme-assembled DNA scaffold. Enhancement of the NADH regeneration was observed for the cascade upon the shape transformation of HPO$_T$ to HPC$_T$ despite the instability of XR. This enhancement was further verified by conducting enzyme cascade reactions on the statically open and closed states. Variation

of the inter-enzyme distance from 60 nm in the open state to 18 nm in the closed state resulted in an evident increase of the overall throughput by the proximity effect. A higher turnover number of XR-XDH cascade reaction was observed in the 3D DNA scaffold over that on the cavity of 2D DNA scaffold in the previous study of our laboratory.[1] The confined space in 3D DNA hexagonal prism provided a more favorable environment in enhancing the overall efficiency possibly due to the higher concentration of hydrophilic intermediates in the ordered hydration layer of the DNA scaffold surface.

In summary, a DNA scaffold was constructed to undergo dynamic shape transformation by two strategies. Characterization of the structures and the shape transformation processes demonstrated a promising potential of the DNA scaffold as a nanocarrier for enzymes. Understanding of the origin of enhanced activity of immobilized enzymes accelerated the logical design of effective catalysts. Investigation of two types of enzyme cascades with different enzyme pairs derived from the D-xylose metabolic pathway on the dynamic DNA scaffold indicated that the enzyme kinetics were the critical parameters in exerting the inter-enzyme distance dependency of enzyme cascade efficiency. Such assumption is quite useful in the design of efficient artificial compartmentalization. The achievement of this work provides insights into the working mechanisms of cells in the perspective of enzyme kinetics, proximity and scaffolding effect.

Reference

1. Ngo, T. A., Nakata, E., Saimura, M. & Morii, T. Spatially organized enzymes drive cofactor-coupled cascade reactions. *J. Am. Chem. Soc.* **138**, 3012–3021 (2016).

List of publications

Publications directly related to the contents of this thesis

1. Enzyme cascade reactions on DNA origami scaffold

Eiji Nakata, Huyen Dinh, <u>Peng Lin</u>, Takashi Morii

Methods Mol. Biol. **2021**, in press.

(Chapter 1)

2. Evaluation of the role of DNA surface for enhancing the activity of scaffolded enzyme

<u>Peng Lin</u>, Huyen Dinh, Yuki Morita, Zhengxiao Zhang, Eiji Nakata, Masahiro Kinoshita, Takashi Morii

Chem. Commun. **2021**, *57*, 3925-3928.

(Chapter 2)

3. Dynamic shape transformation of a DNA scaffold applied for an enzyme nanocarrier

<u>Peng Lin</u>, Huyen Dinh, Eiji Nakata, Takashi Morii

Front. Chem. **2021**, *9*, 697857.

(Chapters 3)

4. Effect of enzyme kinetics on the inter-enzyme distance dependency of cascade reaction

<u>Peng Lin</u>, Huyen Dinh, Eiji Nakata, Takashi Morii

Manuscript to be submitted

(Chapter 4)

5. Dynamic assembly of multi-enzymatic cascade by shape transformation of DNA scaffold

Peng Lin, Huyen Dinh, Yuki Morita, Eiji Nakata, Takashi Morii

Manuscript to be submitted

(Chapter 5)

Publications not directly related to the contents of this thesis

1. Reaction of ribulose biphosphate carboxylase/oxygenase assembled on a DNA scaffold

Huyen Dinh, Eiji Nakata, Peng Lin, Masayuki Saimura, Hiroki Ashida, Takashi Morii

Bioorg. Med. Chem. **2019**, *27*, 115120.

List of Presentations

International Conferences

1. Assembling cascade enzymes on a 3D DNA nanostructure

Peng Lin, Huyen Dinh, Thang Minh Nguyen, Eiji Nakata, Takashi Morii, the 45th International Symposium on Nucleic Acids Chemistry, November 7–9, **2018**, Kyoto, Japan

2. Reaction of enzyme cascade assembled on a 3D DNA structure

Peng Lin, Huyen Dinh, Eiji Nakata, Takashi Morii, the 46th International Symposium on Nucleic Acids Chemistry, October 29–31, **2019**, Tokyo, Japan

Domestic Conferences

1. Efficiency of the enzyme cascade reaction on a DNA scaffold

Peng Lin, Thang Minh Nguyen, Huyen Dinh, Eiji Nakata, Takashi Morii, the 98th CSJ Annual Meeting, March 20–23, **2018**, Tokyo, Japan

2. Construction of a 3D DNA nanostructure for assembling enzyme cascade reaction

Peng Lin, Huyen Dinh, Thang Minh Nguyen, Eiji Nakata, Takashi Morii, the 12th Symposium on Biorelevant Chemistry, September 9–11, **2018**, Osaka, Japan

3. Reaction of enzyme cascades assembled on 3D DNA structure

Peng Lin, Huyen Dinh, Thang Minh Nguyen, Eiji Nakata, Takashi Morii, the 99th CSJ Annual Meeting, March 16–19, **2019**, Kobe, Japan

4. A dynamic DNA scaffold for enzyme cascade reaction

Peng Lin, Huyen Dinh, Yuki Morita, Eiji Nakata, Takashi Morii, the 100th CSJ Annual Meeting, March 22–25, **2020**, Tokyo, Japan